Proceedings e report

50

Impact of climate change on agricultural and natural ecosystems

edited by
MARCO BINDI, GIADA BRANDANI, CAMILLA DIBARI,
ALESSANDRO DESSÌ, ROBERTO FERRISE,
MARCO MORIONDO AND GIACOMO TROMBI

Progetto grafico di Alberto Pizarro Fernández

TABLE OF CONTENTS

PREFACE

Climate change is evidently affecting the whole biosphere, as already illustrated by hundreds of publications and research projects under the most important scientific organizations (EC, FAO, WMO, IPCC, etc.). Natural ecosystems, as well as human-made ones (agroecosystems) are changing so fast that planning the use of natural resources, both for development and protection, requires tools and technologies able to understand and take into account complex relations, at Regional and Global scale.

Moreover, these ecosystems and large natural areas do not have only a passive role in climate change issue, since they also play an active role in the emission and balance of greenhouse gasses (carbon dioxide, methane, nitrogen oxides, etc.). In particular is fundamental to determine the role of these ecosystems in areas such the South American Continent, due to the relevance of its natural resources, the mitigation and adaptation strategies may have global level repercussions.

To face such a problem, communication and experience sharing is needed between Research Groups from different Countries. Indeed, knowledge flow is a key to satisfy the need for supporting a sound and sustainable development, based on strong scientific results. This must be based on an interdisciplinary approach, integrating atmospheric physics, remote sensing, eco-physiology, modelling. Thus, very often the usual university backgrounds are not sufficient to work on these aspects.

This book describes the main results obtained within the Impact of Climate change On agricultural and Natural Ecosystems (ICONE) Project funded by the ALFA Programme of the EC. This project aims at strengthening the relations between the scientific communities from different Countries within Latin America and with European ones working on the same topics, beginning from seminars, students and researchers interchange, to help the development of common research ideas; within them, a special focus was given to trends and models at Regional and Global scale, for a general improvement of educational offer and academic activities between all the members of the Network.

The editors

DEVELOPMENT OF A WEB BASED MODEL TO PROCESS AND ANALYSE REMOTELY SENSED DATA SETS

Alberto Ramirez
Facultad de Ciencias y Tecnología
Universidad Católica Nuestra Señora de la Asunción
Paraguay

Tutors: Prof. M. Danson and Dr. Richard Armitage
School of Environment and Life Sciences
University of Salford
United Kingdom

1. Introduction

The aim of the research to be carried out was the development of a Web based model to process and analyse remotely sensed data sets, adopting the approach of a user friendly interface which allows scientists to access a wide range of analytical tools, as well as different sources of information.

As a case study, we agreed to study the clouds conditions over Greater Manchester in the year 2005. Specifically, we were working with the Modis Cloud Mask Product (MOD35_L2), which combines infrared and visible techniques to determine both physical and radiative cloud properties. The presence or absence of cloudiness is critical to retrieve properly many atmospheric and surface parameters.

2. The Web based Model

Environmental scientists often need to interpret a large amount of data to draw a conclusion about certain phenomena. This interpretation process requires the use of different computer based tools. Addressing a particular research topic demand not only the use of existing tools, but also the production of programming solutions in order to complement what was already developed. At this point it is clear the necessity of a framework which allows integration of both available sources of data and analytical tools.

2.1 Objective

The Web based model, which is being introduced, allows the scientists to focus on data analysis and interpretation, without worrying about how the data are managed or formatted. The model has been implemented for the analysis of MODIS time series data sets in the first instance, but can be adapted for other applications.

2.2 Components of the Web based Model

The schematic diagram shown in Figure 1 identifies the components of the Web-based Model proposed and the interaction among them. The scientists and programmers can interact with both the database and the web based interface in order to prepare the data and add the

required functionalities according to a given research topic. The integration of external sources of data, as well as existing data processing and analysis tools is also allowed.

Figure 1. Schematic diagram of the Web-based Model
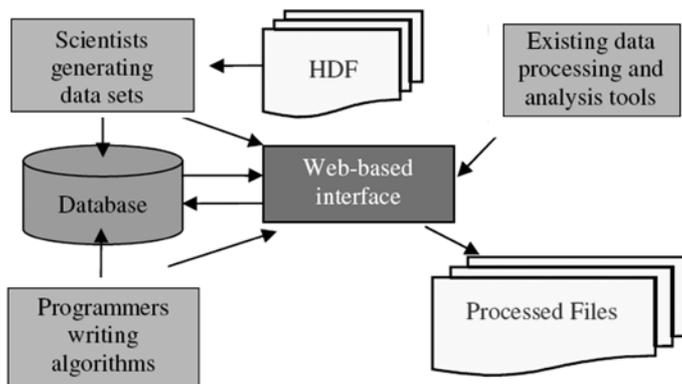
2.3   *A Database Approach*

Relational Database Systems provide a method for storing data in an independent manner, which means that the data is held in such a way that modifications to the structure of the database will not affect any of the programs used to access the data. In a different approach, the same information may be held on several files and directories. Apart from wasting disk space, this makes the operations on the data more time consuming.

The idea behind using a Database System for storing, MODIS data relies on the fact that within a database the data is stored in a way that makes it easily accessible. Another key concept of this approach is flexibility, as developments can progress around a database in an incremental way.

2.3.1 Building Datasets

The model presented in this work allows scientists to produce their own datasets, which can be processed at any time from its creation. Metadata are used to describe the information associated to these datasets. In fact, metadata describe how and where a particular set of data was acquired, and how the data are formatted. This gives relevant information not only to the scientists, but also to the programmers, who are developing the different functionalities within the model, in order to interact with the data. As an example, an image can be a series of numbers that does not make sense without associated metadata describing what is being represented by this information.

According to the needs of the scientists, who are working on MODIS Cloud Mask Product, a structure for the associated metadata was developed. Changes to this structure will not modify the behaviour of the current algorithms used to process the collected data. In other words, this highlights the concept of flexibility, which was mentioned before. The Metadata Structure used is shown in Table 1.

The Relational Database System chosen for this work was Oracle 10g Express Edition (Oracle Database XE), which is free to develop, deploy and distribute. The database was tested in both, Windows XP and Unix-based operative systems. Additional tests were made using

Table 1. Metadata Structure

OWNER_ ATTRIBUTES	DATASET_ ATTRIBUTES	FILE_ ATTRIBUTES
OWN_USERNAME	DST_NAME	FILE_NAME
OWN_PASSWORD	DST_DESCRIPTION	FILE_DESCRIPTION
OWN_EMAIL	DST_SOURCE	FILE_LASTUPDATE
	DST_LASTUPDATE	FILE_VERSION
	DST_VERSION	FILE_DATASET
	DST_OWNER	FILE_TYPE

Table 2. Functionalities of the Web based Model

FUNCTIONALITY	STATUS
Database creation and maintenance	The creation of data sets is already available, whereas the developing of maintenance features is still in progress.
Integration of existing data and processing tools	The automated generation of scripts for the Modis Reprojection Tool (MRT) is already implemented and the integration of other ancillary tools is still in progress.
Modis data edition	Basic edition capabilities are already implemented for the Modis Cloud Mask Product.
Modis data analysis and processing	Analysis and processing of Modis Cloud Mask Product is already implemented.
Report generation with graphs, charts and tables	The developing of report generation capabilities is still in progress.

MySQL and PostgreSQL. The migration process from Oracle to MySQL and PostgreSQL was made as part of the activities of this work.

2.4 Functionalities of the Web based Model

The functionalities of the model presented in this work and their current status are depicted in Table 2.

3. The Modis Cloud Mask Product

As a working example, we focused on the Modis Cloud Mask Product which indicates whether a given view of the earth surface is obstructed by clouds or optically thick aerosol. All Modis Standard Products are in the Hierarchical Data Format (HDF) which is a physical file format for storing and sharing scientific data (Weaver and Singh, 2002). The Cloud Mask Product is generated at 1 kilometre and 250 metres spatial resolutions. There are two Modis Cloud Mask data product files: MOD35_L2, containing data collected from the terra platform, and MYD35_L2, containing data collected from the Aqua platform (Modis 2007).

3.1 Modis Data Processing Tools

Tools for working with Modis data are freely available from the Internet. A number of these tools were integrated into the framework being developed (Table 3).

Table 3. MODIS Data Processing Tools used in this research

Tool	Description	Limitations
Modis Reprojection Tool (MRT)	Tool for reprojecting Modis images into standard map projections.	Not suitable for processing a large amount of images at once.
HDF View	Tool for browsing and editing HDF files.	Very basic editing capabilities.
HDF Tool	Multifunctional data processing and visualization tool for Modis data.	Not suitable for processing a large amount of images at once.

3.2   *Cloud Mask Scientific Data Set*

Environmental Scientists are often interested in identifying some pieces of information, which are stored in individual bits or groups of bits within a HDF file. For this reason, a bit-level analysis of the product is necessary in order to extract the right elements to produce significant results.

In order to establish the certainty of clear sky from a MODIS Cloud Mask product file, it is necessary to understand the format of it.

In this document, we are not going to give a detailed description of the file format. Instead of that, we are just going to focus on the Cloud Mask Scientific Data Set (SDS), which is part of the Science Parameters within the MODIS Cloud Mask file and contains the cloudiness information.

Each pixel in the Cloud Mask SDS is assigned a 6 byte (48 bit) array. Individual bits or group of bits are set to denote various cloud conditions and characteristics for that pixel.

We want to determine for each pixel in the image, if it refers to a Confident Cloudy, Probably Cloudy, Probably Clear or Confident Clear condition. This information is coded using the second and third bit within the first of the six bytes mentioned before. Hence we are interested in the Byte #0, as all bit and byte numbering, in the Cloud Mask Scientific Data Set (Table 4), start with 0. A description of the Byte #0 is given below.

The information encoded in the Unobstructed FOV Quality Flag has four possible combinations, as can be seen in Table 5. This information indicates the probability of clear sky for every pixel in the image.

3.3   *Cloud Mask Bit-field Interpretation*

An algorithm was written to perform the bit extraction. It takes Modis Cloud Mask Product file as an input, while the output overwrites the value of the first byte of the Cloud Mask SDS for every pixel in the image, taking into account only the values of the second and third bit which have the relevant information.

The image in Figure 2 covers the United Kingdom and surrounding areas and shows the information stored in the first byte of the Cloud Mask SDS (Table 4) which corresponds to a Modis Cloud Mask Product HDF file. The resulting image after performing the bit extraction is shown in Figure 3.

4.   *Data analysis*

After processing a set of images corresponding to a given year, two stacks of binary files were produced with the intention of calculating the cloud cover probability in a given region. The pixel values of the images within the first stack indicate whether the Cloud Mask Algorithm was executed or not. Whereas, the pixels values of the images within the second stack indicate cloudy areas or a high probability of clear sky. The analysis process is shown in Figure 4.

Table 4. Cloud Mask Bit-field Interpretation (Byte #0)

Bits	Field Description	Bit Interpretation Key
0	Cloud Mask Flag	0 = Not Determined 1 = Determined
1-2	Unobstructed FOV Quality Flag	0 = Confident Cloudy 1 = Probably Cloudy 2 = Probably Clear 3 = Confident Clear
3	Day / Night Flag	0 = Night 1 = Day
4	Sunglint Flag	0 = Yes 1 = No
5	Snow / Ice Background Flag	0 = Yes 1 = No
6-7	Land / Water Background Flag	0 = Water 1 = Coastal 2 = Desert 3 = Land

Table 5. Possible Values for the Unobstructed FOV Quality Flag

Value of Bit #1	Value of Bit #2	Bit Interpretation Key
0	0	Confident Cloudy
1	0	Probably Cloudy
0	1	Probably Clear
1	1	Confident Clear

Figure 2. Image before performing the bit extraction

Figure 3. Image after performing the bit extraction
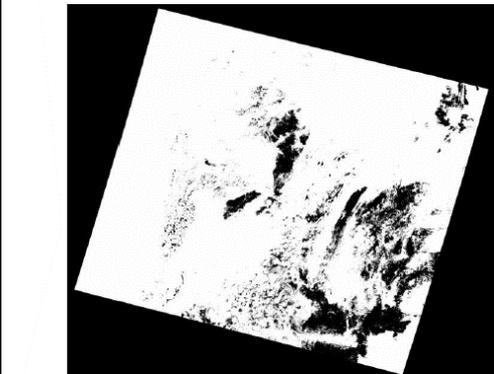
Confident Clear	Probably Clear	Probably Cloudy	Confident Cloudy

Figure 4. Data analysis process

STACK #1
Under certain conditions, the Cloud Mask Algorithm is not executed and the pixels are set to 0.

0 – Not determined
1 – Determined

STACK #2

STACK #1

STACK #2
This stack indicates whether a pixel presents 100 percent probability of clear or not.

0 – Not Cloud Free
1 – Cloud Free

After calculating the ratio between the two stacks, a single file is produced showing the certainty of clear sky for every pixel.

Figure 5. January 2005

Probability of clear sky

Low   High

Figure 6. June 2005

Probability of clear sky

Low   High

5. Results

The values of the pixels in the images (Figure 5, Figure 6) show the percentage of cloudy days across England, Scotland and Wales corresponding to January and June 2005. The darker areas suggest higher probability of clouds, while the brighter areas indicate higher probabilities of clear sky. The range for January 2005 is 0–41% and the range for June 2005 is 0–65%.

6. Conclusions

After processing remotely sensed data within the framework proposed, the following advantages are noted:

- Easy creation and maintenance of large data sets.
- Faster processing of data sets.
- Flexibility for integrating existing ancillary tools.
- Easily adaptable programming solutions to existing processes.

   The model proposed in this work has some limitations that are being addressed in order to improve the overall performance. The redundancy in the information stored in the database will be reduced after optimizing the data analysis process. The integration of existing data processing and analysis tools has also to be improved.

   Further work will expand the model in order to perform the processing of other Modis product files. We will continue to test the bit-extraction algorithm on other years, and we will also work on speeding up the processing time of the images which will allow faster processing of data for longer periods of time.

References

Weaver R., Singh S. (2002). Extracting and Viewing Bit-Level Metadata in EOS Files. Earth Science Technology Conference – Pasadena, CA (USA).

Internet References

Modis Atmosphere. <http://modis-atmos.gsfc.nasa.gov/MOD35_L2/index.html> (accessed 7th June 2007).

MESOSCALE STUDY OF THE CLIMATIC PARAMETERS IN THE EASTERN REGION OF PARAGUAY

Pedro Domaniczky, Maria Amparo Gilabert Navarro, Beatriz Martínez
Facultad de Ciencias y Tecnología
Universidad Católica Nuestra Señora de la Asunción
Paraguay

Tutor: Prof. M.A. Gilabert Navarro
Departament de Física de la Terra i Termodinàmica
Universidad de València
Dr. Moliner, 50. 46100-Burjassot (Spain)

1. Introduction

The United Nations Conference on the Human Environment, held in Stockholm from June 5 to 16 of 1972 proclaimed that: «Man has constantly to sum up experience and go on discovering, inventing, creating and advancing. In our time, man's capability to transform his surroundings, if used wisely, can bring to all people the benefits of development and the opportunity to enhance the quality of life. Wrongly or heedlessly applied, the same power can do incalculable harm to human beings and the human environment» (UNEP 1972).

At present – more than three decades after that declaration – modifications of the environment on the planetary scale are being perceived as originate both from natural causes and from human ones. The scientific community accepts, practically without exception, that changes in the atmospheric abundance of greenhouse gases and aerosols, in the solar radiation and in land surface properties can introduce significant variations in the terrestrial climate, with the consequent repercussions for the human being (IPCC 2007). These processes can be attributed to the energy use activities related to man and given the concern generated by the perception of an eventual climatic change over the short term, mainly academic organizations are expressing the need for studying the different energy sources utilized by men and which could be associated with these modifications. Certainly, the climatic change constitutes a permanent concern for different academic organizations and institutions, both at the local and the international level (see Figure 1)

These anthropogenic activities could be considered to be recent, since man, by means of different technological advances, can now produce significant changes over large extensions of the earth's surface, both in the atmospheric component and in that of the soil, over relatively short periods of time.

Data collected through WMO's GOS (Global Observing System) give a clear indication that globally averaged surface temperatures have increased since the beginning of instrumental records in 1861. Over the 20th century, this increase was about 0.74°C; however, the linear warming trend over the last 50 years is nearly twice that for the last 100 years. Moreover, analyses of indirect data for the Northern Hemisphere indicate that the late 20th century warmth was unprecedented for at least the past millennium. Over the same period, the 1990s was the warmest decade, 1998 the warmest year with 2005, the second warmest. Whereas Atmospheric concentrations of greenhouse gases have increased significantly since industrial revolution and they are projected to reach double pre-industrial levels towards the end of the present century, the projected temperature rise would likely be around 3°C (WMO, 2007).

The World Meteorological Organization, in its declaration on the state of the climate in 2006 (WMO, 2006), places in evidence that the above year has been the sixth hottest since record-

Figure 1. Evaluation of the relative importance of the radiative forcing originated by natural and by anthropogenic factors (IPCC, 2007).
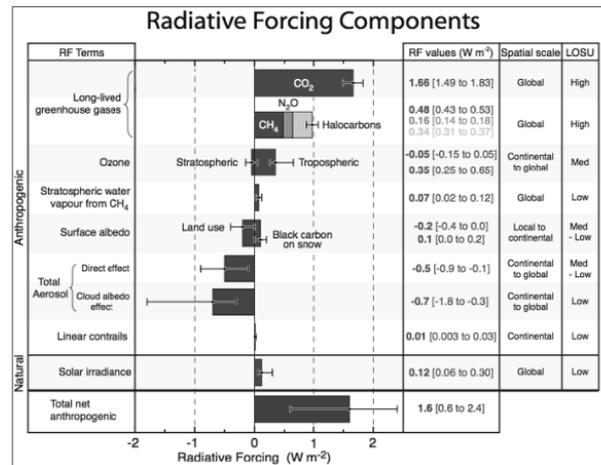

Figure 2. Deviation of the mean temperature of the terrestrial surface in relation to the mean value corresponding to the period of 1961–1990
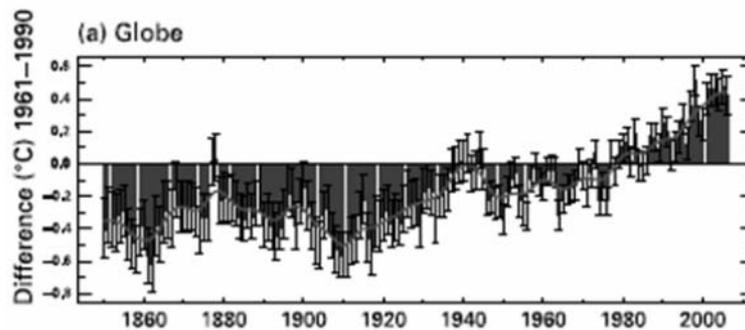
ings began (with a temperature between 0.42 °C and 0.54 °C, depending on the month, above the mean corresponding to the period of 1961–1990). Figure 2 shows the deviation of the mean temperature of the world's surface in relation to the mean value corresponding to the period of 1961–1990, showing the appreciable temperature increase being recorded in recent years.

According to the predictions being produced by the climatic models for the different scenarios (IPPC, 2007), the tendency for the temperature to rise is not only going to hold, but will also be greater in the present XXI century than what observed during the past century.

It should be remembered that the climate of a particular region, or of the planet as a whole, is defined on the basis of the different parameters that characterise the physical state of the atmosphere. Its study requires taking into account the mean value of these measurements and also the variability associated with them. Consequently the spatial and temporal distributions of the elements of the climate are not fixed, but instead oscillate year after year around an average curve. It may occur that at some period of this distribution the values stray notably from the mean. This displacement may be abrupt or progressive, and can subsist for more or less time, before returning to the average value. It also may occur that this climatic fluctuation is sufficiently great as to exert influence upon an average of 30 years. Under these circumstances it can be stated to be a climatic variation (Hufty 1984).

This natural variability of the elements of the climate causes difficulties in the task of detecting and differentiating the alterations of the system and the changes or trends that they may indicate.

For this reason, in order to analyze the climate of a particular region it is necessary to possess data that characterise both spatially and temporally the state of the atmosphere. Also, obviously, it is essential to have a methodology for the analysis of temporal series that helps to discern circum-stantial changes that maintain the climate within its essential characteristics of continual trends (towards increase or decrease) that can be associated with long-term changes (climatic changes).

Based on the above, and within the framework of the ALFA programme of the European Union, and specifically in the ICONE project (Impact of climatic change upon natural and agricultural ecosystems), this report presents a methodology suitable for the mesoscale study, and over the last 40 years, concerning the behaviour of the principal climatic parameters of a zone situated in the Eastern region of Paraguay; a zone that results of particular interest due to the transformations registered in it during the period analysed.

2. Study Area

We will briefly run through some features of the study area in relation to its geographical location and climate. Anthropogenic changes in land surface properties (modifications in land use and the construction of the Itaipú reservoir) are also discussed.

2.1 Geographical framework

The study will be carried out in the area of influence of the Itaipú Reservoir, transversally encompassed by the axis of the lake and the contour of its watershed on the Paraguayan side, i.e., between the latitudes 24º 05' S and 25º 30' S and longitudinally by the cities of Salto del Guairá and Ciudad del Este, located between the longitudes 54º 15' W and 55º 30' W, with an elevation in the contour of the watershed of close to 400 m above sea level. The elevation of the reservoir is 219.6 m above sea level. The study area is located in the Eastern region of Paraguay, in the Departments of Alto Paraná and Canindeyú (see Figure 3).

Figure 3. Geographical location of the study zone (dotted line in the image on the right)
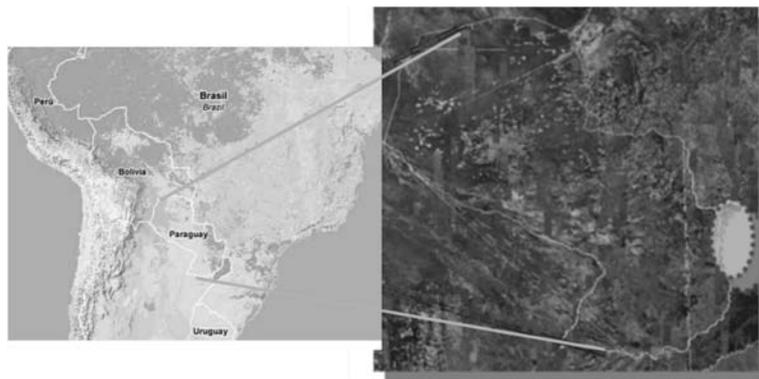
2.2 Climate

The mean annual temperature of the region is 21.5 °C, while the mean annual precipitation is 1690 mm. The seasonal variation in the mean temperature is 9.8 °C, with the recording of 16.3 °C in June and 26.1 °C in January as monthly averages. The extreme absolute tempera-

tures in the aforementioned periods vary from –3 °C in July up to 40.2 °C in December. The average number of rainy days is 101 days. The precipitation exceeds the evaporation during the whole year (National Weather Service of Paraguay DMH–DINAC).

2.3 *Anthropogenic activity*

In the region under consideration there have been three significant occurrences from the viewpoint of the possible human pressure upon the ecosystems:

- the expansion of the agricultural border, linked to a regional policy of expanding the cultivated areas;
- the increase in population caused by the frontier commerce both in the southern and in the northern parts of the area being studied;
- the construction of the Itaipú Hydroelectric Power Plant, which not only introduced a new element into the landscape, but also led to an increase in population (the labour force involved about 24 000 people, of which 90% immigrated to the zone). This increase in population led in turn to further landscape modifications through the creation of urban zones and the necessary infrastructures to shelter this population.

2.3.1 *Changes in the land use*

The change in the land use of this region is show in the Figures 4, 5 and 6, where the evolution of the forested region is observed in two periods: from 1945 to 1991 and from 1990 to 2002, respectively, and in greater detail from 1973 to 2003. In recent decades there has been a gradual decrease in the forests in favour of the implantation of diverse agrarian cultures.

2.3.2 *Dam and reservoir*

The zone being studied presents a singular feature that must also be considered within the complex of the analysis: it contains the largest Hydroelectric Power Plant in operation in the world (Itaipú 2000).

From a technical point of view, the hydroelectric power plants are works of engineering that address the generation of energy and the utilization of the water. Two of its principal elements are the dam and the reservoir: the first impounds the water and the second refers to the volume of water stored (Chow *et al.* 1994).

On April 26 of 1973, the Treaty of Itaipú was signed between Paraguay and Brazil, which dealt with the development of the hydraulic resources of the Paraná River, belonging in condominium to both countries, from the Guairá Falls to the mouth of the Yguazú River, having as its principal objective the production of electrical energy (Itaipú 1973).

The Itaipú hydroelectric power plant, the first in energy production in the world: 12.600 kW (Itaipú 2000) is located on the frontier between Paraguay and Brazil, in the Paraná River, which has an average flow of 17.300 m3/s at its mouth, which is the seventh greatest volume in the world (Mataix 1983). The hydrographical basin of the Paraná River belongs to the River Plate watershed with a surface area of 3.100.000 km². In Figure 7, the contour of the River Plate watershed is visible.

The Paraná River basin, upstream of the axis of the Itaipú dam, encompasses a surface of 820 000 km², with only the 2.5% of this area corresponding to the basin of this artificial lake, from the Itaipú dam until the foot of the reservoir (Saltos de Guairá). This lake was created

Figure 4. Spatial and temporal evolution of the Atlantic Forest in the Oriental Region of Paraguay from 1945 to 1991
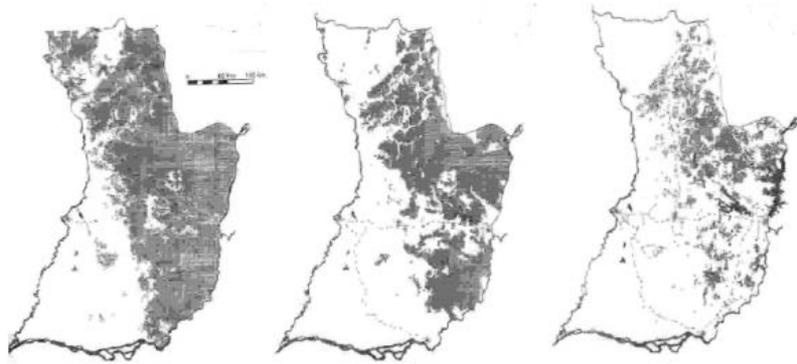

Figure 5. Left: Vegetation cover in the region designated as the Atlantic Forest in Paraguay referred to the year 2000. Right: Satellite image (Landsat MSS) referred to the year 1974. (Adapted from Huang *et al.* 2007)
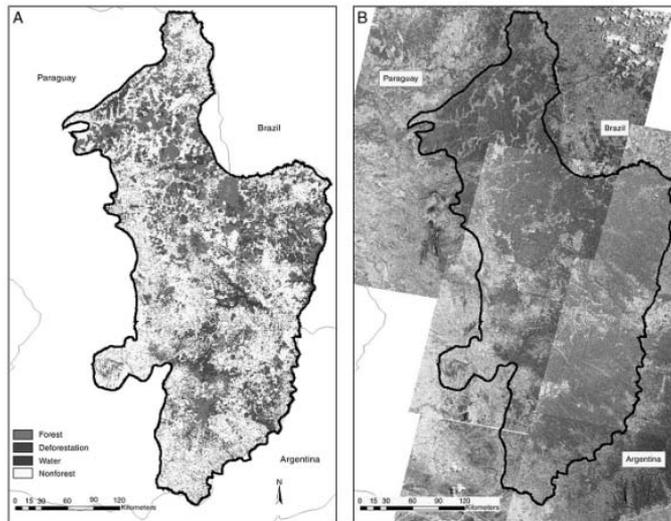

Figure 6. Changes in the land use at the junction of Paraguay, Brazil and Argentina from 1973 to 2003 (from UNEP: http://www.grid.unep.ch/activities/global_change/atlas)
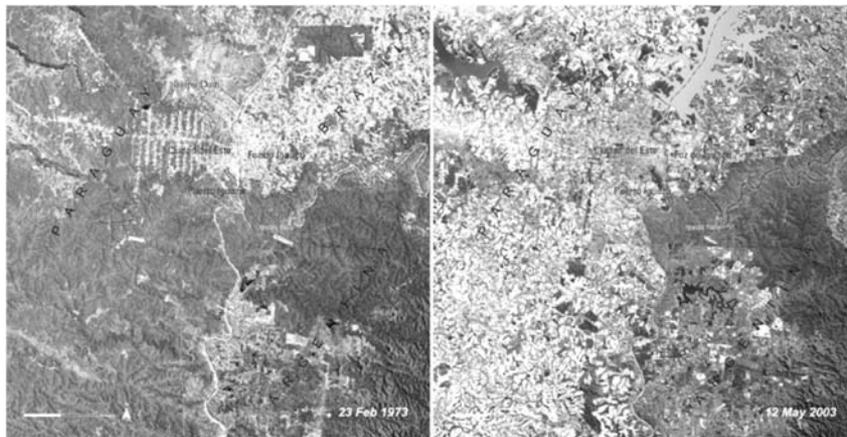
Figure 7. The Plate Watershed (http://www.ciudaddeleste.galeon.com/cvitae250727.html)
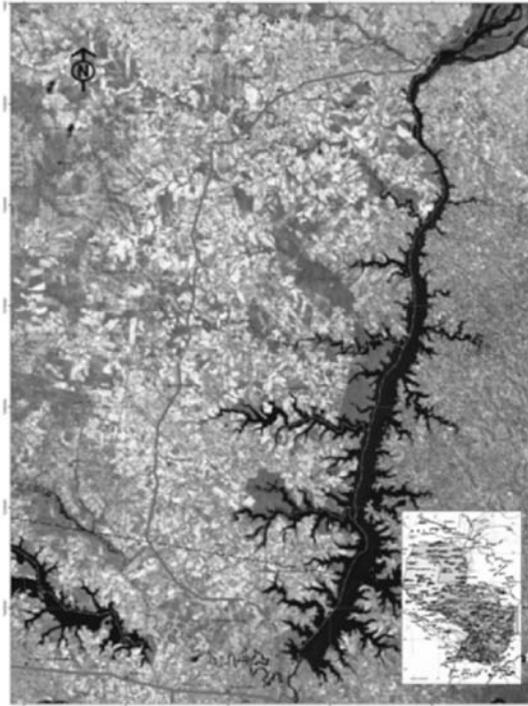
in two stages, the first –until elevation 205.81 m– started on October 13 of 1982, culminating on November 23 of the same year, the second, up to the operating elevation of 219.6 m, on June 5 of 1984 (Müller, 1987).

The reservoir constitutes an artificial lake of significant dimensions (Brunkow *et al.*, 1987; Itaipú, 2000): the surface is 1460 km2 (835 km2 in Brazil and 625 km2 in Paraguay) the volume is 29 billion cubic metres, with maximum depths of up to 170 m and an average depth of 21.5 m. The longitude along the axis is 164.6 km, and the average width is 7.5 km.

The filling of the reservoir took place in December of 1982.

3. Data

In order to consider the mesoclimatic effects upon the area under study, it was decided to utilize the data recorded by 6 meteorological stations located in Paraguayan territory:

- Ciudad del Este (CDE)
- Encarnación (EN)
- Villa Rica (VR)
- Concepción (CON)
- Salto del Guairá (SDG)
- Capitán Meza (CM)

It should be noted that although on a global scale they all present a similar climate, they can be considered independent on the local scale, since they are more than 100 km distant from

Figure 8. Location of the meteorological stations considered in the study. (The contour of Paraguay appears in yellow).

each other, in accordance with the technical standard established by the WMO (1990). Figure 8 shows the location of the stations.

The CDE and SDG stations are representative of the region under study. The stations EN, VR and CON do not present significant changes in land use from 1965 to 2006.

The data recorded by all the stations consists on refined and adequately prepared statistical series and covers the period 1965-2006, with the exception of the CM station, where the data from the first decades are not available due to technical problems.

The meteorological stations of reference utilized for the study correspond to those of the National Weather Service of Paraguay (DMH-DINAC), whose data are recorded in the format standardised by the World Meteorological Organization (WMO). All the stations are of conventional type, i.e., requiring the assistance of a meteorologist observer to read and record the different parameters. The stations are equipped with the following instruments:

- a meteorological hut comprising a dry and wet thermometer, a maximum thermometer, a minimum thermometer, a daily recording thermo-hydrograph and a Piché evaporimeter;
- pluviometer;
- pluviograph;
- wilde-type wind vane for estimating the direction and velocity of the wind;
- heliograph.

The Itaipú Binacional meteorological stations are also conventional and they also fulfil the recommendations of the WMO.

The records utilized correspond to the parameters of average monthly temperature (maximum, mean and minimum), accumulated-monthly precipitation and average monthly relative humidity, between 1965 and 2006.

The process of control, validation and homogenization of the data was executed and verified based on the recommendations of the guide for climatological practices of the WMO (WMO, 1990). The temperatures were recorded during four daily collections: 09:00, 12:00, 18:00 and 00:00 GWT or TCU, and from those values first daily averages and then monthly averages (mean monthly temperatures) were obtained. By using a similar procedure and only

considering the maximum and minimum daily values, it was possible to obtain the monthly maximum and minimum temperatures respectively. Regarding the precipitation data, the procedure followed was similar to that indicated in the above paragraph, obtaining values for monthly-accumulated and annual precipitation. The monthly relative humidity was obtained in an identical manner.

The data set employed for the present study was provided by the Dirección Nacional de Meteorología e Hidrología del Paraguay and by the Itaipú Binacional Hydroelectric Power Plant, through the Universidad Católica Ntra. Sra. de la Asunción.

4. Methods: the wavelet analysis

In climate analysis, it is common to differentiate four scales: macroclimatic, mesoclimatic, local climate and microclimatic. The present study considers the mesoscale analysis, which is defined as the zonal climate of variable linear dimensions between 200 and 2000 km (Cuadrat and Pita 1997).

The knowledge of the spatial and temporal distribution of the climatic variables is essential for carrying out any analysis of the climate. The spatial feature is covered by the network of stations. The temporal feature is also sufficiently covered by the available data bases throughout the last 41 years. The length of this period is enough to evaluate the methodology we propose, but not to establish strength conclusions in relation to the climatic variability.

As previously mentioned, the object of this study is to present a methodology for the study of temporal series of data mainly devoted to detect trends towards change. These series present a high variability at different temporal scales and, therefore, it is important to determine if the detected modifications constitute a long-term change, or if they only respond to variations, fluctuations or to thermal or pluviometric cycles.

When studying temporal series of data, it is frequent to use the Fourier transform (FT). Its use presupposes the admission that the data is stationary and proceeds from linear systems. However, the data we are working with is of finite duration, is not stationary and proceeds from non-linear systems, either intrinsically or through interactions with imperfect sensors or numerical designs. Under these conditions, FT is of limited use and can lead us to physically false results, which must be kept in mind in its interpretation (Gimeno 2003). The reason for the existence of these limitations in the Fourier analysis is that the functions that form the orthogonal base upon which to expand a series of data are sinusoidal functions with an infinite temporal support, so that a small disturbance of the series in any point of its domain influences all the points in the space of the frequencies and vice versa.

For this reason, for the analysis of non-stationary temporal series (such as those considered in the present work), we must use another type of mathematical instruments. The choice here is based upon the wavelet transform (WT).

The WT is a method of spectral analysis in the time-frequency space that presents some interesting features that convert it into a very useful mathematical instrument (Gimeno 2003). It has become enormously popular in recent years among the scientific community due, among other reasons, to the wavelets being the result of a multidisciplinary effort with the participation of mathematicians, physicists and engineers who, independently, had been developing similar ideas in each of their fields of research, fundamentally in the 1980s decade (Trenas 2000). The WT has already been used for remote sensing applications such as image registration (Fonseca *et al.* 1998), spatial and spectral fusion (Zhou 1998), feature extraction (Simhadri *et al.* 1998), speckle reduction (Horgan 1998), texture classification (Zhu and Yang 1998), and crop phenology detection (Galford *et al.* 2008; Sakamoto *et al.* 2005). Particularly, the WT has proven quite useful to the study of multiscale and non-stationary processes over finite spatial and temporal domains (Furon *et al.* 2008; Sakamoto *et al.* 2005).

The fundamental idea behind wavelets is to analyze the signal according to different scales or resolutions. A WT uses local basis functions (wavelets) that can be stretched and translated with a flexible resolution in both frequency and time domains. The WT can be understood as a technique that looks at different sections of the time series with a window adjusted according to scale. A wide window can be used to capture the presence of short lived events (high frequency variability), such as abrupt changes, while resolving processes which show low frequency variability in time scale. Therefore, one of the principal advantages of this method is that it permits isolating the seasonal changes inherent in the data, leaving uncovered another possible variability in them, in order to expose the existence of any marked trend towards change.

4.1 The wavelet transform

Generally, the idea of the WT is the decomposition of a signal at different spatial or time scales onto a set of basis functions. For the sake of brevity and clarity the theory is presented in one dimension (λ). That set of basis functions, $\{\Psi_{a,b}(\lambda)\}$, can be generated by translating and scaling the basic or mother wavelet, $\Psi(\lambda)$, according to the following

$$\varnothing_{a,b}(\lambda) \equiv \frac{1}{\sqrt{a}} \varnothing \left(\frac{b \pm \lambda}{a} \right) \qquad a > 0, b \in R \qquad (1)$$

where a is the scale parameter which adjusts the dilation of the wavelet and b determines the location of the wavelet. R denotes the set of real number. The mother wavelet is translated in the spatial or time domain to select the different portions of signal, and dilated and contracted to analyze different scale variations (Meyer 1993; Mallat 1989).

The name of wavelet suggests a small wave, in contrast with a wave such as a sinusoid, with an infinite temporal support. It is, by definition, any function whose integer is null and which is an integrable square, without this necessarily demanding that the function be defined as real. Nevertheless, for a wavelet to be of practical utility, it is necessary to impose some additional conditions. Among these, what stands out is the "condition of admissibility" (Percival and Walden 2000; Daubechies 1992), which permits the reconstruction of a signal. More details associated with the mathematical treatment of wavelets can be found in Gimeno (2003).

The continuous wavelet transform (CWT), denoted by $W_f(a,b)$, of a one dimension signal, $f(\lambda)$, with respect to the wavelet basis function $\psi_{a,b}(\lambda)$, can be defined as:

$$W_f(a,b) \equiv \int_{-\infty}^{\infty} f(\lambda) \bar{\psi}_{a,b}(\lambda) d\lambda \qquad (2)$$

where $\bar{\psi}$ denotes the mother wavelet complex conjugation. The result of the WT is a set of coefficients; each set is associated with a scale and each element in a set is associated with a particular location (Lindsay et al. 1996). For a uniquely defined scale a_0 and location b_0, a coefficient is obtained for that specific point in the time frequency domain. If the spectral component of the signal around location b_0 is comparable to the wavelet defined at the scale a_0, the wavelet coefficient calculated will have a relatively large value. This is repeated for other combinations of b and a (i.e. other basis functions) resulting in a set of coefficients (the wavelet transform) representing the decomposition of the signal into time-frequency space.

The wavelets coefficients can be interpreted as proportional to the differences between temporally adjacent averages of portions of a time series. This physical interpretation has rendered the WT useful not only for the information provided on the time series average values but also for evaluating how stable such averages are over time (Percival et al. 2004).

An alternative approach when dealing with discrete signals is to define discrete wavelet transform (DWT) specifically adapted for sampled values (Daubechies 1992; Lindsay *et al.* 1996). Let the discrete signal be defined as the multi-temporal satellite-sensor-acquired data, it can be expressed as a vector of finite set of N observations $f(t_i)$, i=1…N, where:

$t_i = t_0 + i\Delta t$
t_0 is an offset, and Δt is the sample interval.

The DWT is performed by scaling the *mother* wavelet by powers of two, $a = 2^j$, and translating by integers, $b = k2^j$. This sampling of the coordinates (a, b) is referred to as *dyadic sampling* because consecutive values of the discrete scales differ by a factor of 2. The scale index j runs from 0 to J, where J is the total number of scales used. k is a location index that runs from 1 to $2^{-j}N$ and typically indicates where the non zero portion of each wavelet basis vector occurs.

Thus a discretely scaled and translated wavelet in the time domain is:

$$\psi_{j,k}(t) = 2^{-j/2}\psi\left(2^{-j}t - k\right) \tag{3}$$

where the DWT coefficients are obtained by the inner product of the signal and the mother wavelet function

$$W_{j,k} = \left\langle f(t), \psi_{j,k} \right\rangle = \sum_{i=1}^{N} f\left(t_i\right)\psi_{j,k}\left(t_i\right) \tag{4}$$

and the discrete signal, $f(t)$, can be represented by a linear combination of the product of wavelets $_{j,k}(t)$ and wavelet coefficient $W_{j,k}$, i.e.:

$$f(t) = \sum_{j=1}^{J}\sum_{k=1}^{n_j} W_{j,k}\psi_{j,k}(t) \tag{5}$$

where $n_j = 2^{-j}N$ is the number of locations for scale j.

4.2   The multi-resolution analysis (MRA)

One of the most important applications of the DWT is the so-called *multi-resolution analysis* (MRA), which constitutes a form of visualizing a function at different levels of proximity or resolution (Mallat 1989; Meyer 1993). By means of this analysis we can decompose a complicated signal into various simpler functions and study them separately. In order to perform the MRA, the DWT can be implemented in a hierarchical algorithm, well known as *pyramid algorithm* (Mallat 1989). This decomposition of the signal into different scales is simply obtained by successive translating and convolving the elements of a high-pass filter and low-pass scaling filter associated to the *mother* wavelet. These filters retain the small and large-scale components of the signals also known as *detail (D)* and *approximation (A)* functions.

For a particular decomposition level m of the *pyramid algorithm,* the evaluation of the sum of the products of the wavelets and their coefficients over all locations but for one value of the scale parameter, 2^m, results in the detail component of the discretely sampled for that scale parameter, D_m,

$$D_m(t) = \sum_{k=1}^{n_j} W_{m,k}\psi_{m,k}(t) \tag{6}$$

This component is an N dimensional vector that depends upon just the wavelets coefficients $W_{m,k}$. Beside the detail component, it also resulted in a smoothed representation of the signal

for scale 2^m, denoted by A_m. The smoothed representation also known as approximation component is described as:

$$A_m(t) = \sum_{k=1}^{n_j} V_{m,k} \; {}_{m,k}(t) \tag{7}$$

where ${}_m(t)$ is a scaled and translated basis function called the *scaling* function and are the scaling coefficients.

As a result of the MRA, our signal $f(t)$ can be reconstructed from the approximation and detail components as:

$$f(t) = A_m(t) + \sum_{j=1}^{m} D_j(t) \tag{8}$$

where m is the highest decomposition level considered. In the first step of the decomposition,

$f(t) = A_1 + D_1,$

the signal has a low pass filtered component, the A_1, and a high pass filtered component, the level D_1.

In a next step, the approximation itself is split in a second level approximation,

$A_1 = A_2 + D_2,$

and so on.

Each successive recursion represents the highest to lowest frequency component of the signal. Figure 9 shows the scheme of a multi-resolution analysis, in which a signal is decomposed into functions of approximation and detail in successive levels.

In summary, the fundamental utility of the MRA is that it presents certain information about the temporal signal in a new manner. The detail component D_j is an N dimensional vector that depends upon just the wavelets coefficients ($W_{j,k}$) and hence is associated with changes on averages in a scale j. The final term in the MRA is A_m, which again is an N dimensional vector, but this depends just on the scaling coefficients. The approximation vector is associated with averages over scales 2^m and longer and hence captures the slowly varying portion of the original signal (Percival and Walden 2000). A more detailed theory of the scale wavelet transform can be found in (Percival and Walden 2000; Lindsay *et al.* 1996; Burke-Hurbbard 1998).

The objective of the application of this multi-resolution wavelet analysis is to identify long-term changes and assess the trend of the series. For this purpose, the original signal is decomposed in two components: (i) the intra-annual component, which may be related with the seasonal variability of the data and can be derived from the *detail component*, and (ii) the inter-annual component, which can be related with low frequency variability events in time scale and can be derived from the *approximation component*. According to the WT theory (Percival *et al.* 2004), the WT can be interpreted in terms of differences between temporally adjacent averages over the studied period at different scales. Thus, the *approximation* function would give us information about how stable these averages at the one-year scale are over the considered period, i.e., the inter-annual variability over the considered period.

In practice, the MRA scheme cannot be applied to any wavelet function because not all of them have an associated *scaling* function. In this work, the Meyer discrete wavelet function is proposed since it is an orthonormal transform which has a *scaling* function besides the *mother* wavelet. It provides an easy implementation and low cost computation for decomposing a signal into orthonormal frequency levels (Daubechies 1992).

In order to select the most appropriate scales for deriving the inter-annual component, the scale and frequency need to be connected. A convenient way is to characterize the dominant

Figure 9. Scheme of a multi-resolution analysis in which the signal is decomposed into functions of approximation (or trends) and detail (or variability) in successive levels
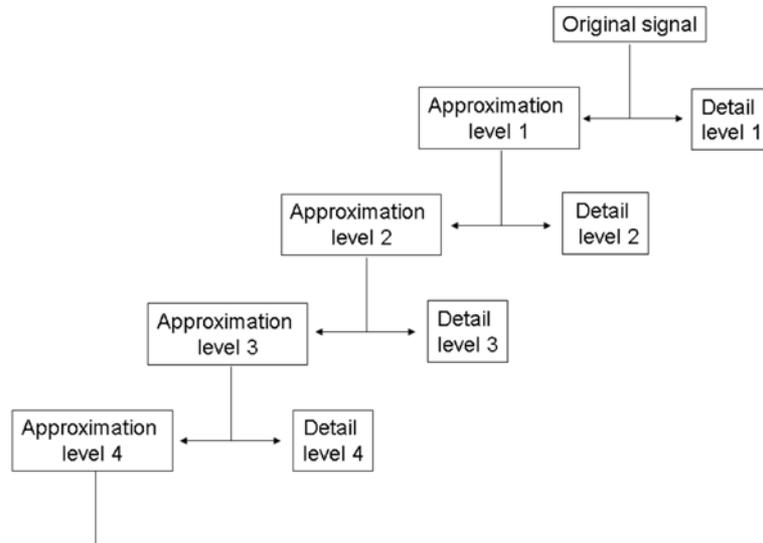
frequency of the wavelet by defining a purely periodic signal of frequency f_p (pseudo–frequency) or period $p = 1/f_p$. This periodic signal allows wavelet decomposition to be related to the more traditional Fourier decomposition (Meyer 1993; Abry 1997).

Pseudo–frequency corresponding to the scale of wavelet decomposition is calculated as:

$$f_p = \frac{f_c}{a} \tag{9}$$

where a is a scale, Δ is the sampling period, and f_c is the center frequency of the wavelet in Hz (i.e., the frequency corresponding to the spectral peak of the wavelet). For the Meyer function the center frequency is equal to 0.67213.

In our case, the level 4 with a semi–period of 356 days (almost the year) has been selected to derive the inter–annual component of the signal. On the other hand, the component derived from the level 6 (semi–period around four years) is used as a «smoothed inter–annual component» that sometimes reveals better some interesting features observed in the trends.

5. Results

5.1 Mean temperature analysis

To provide an example, we are going to illustrate the procedures indicated in section 4 with the monthly mean temperature data of the stations: Ciudad del Este (CDE), Encarnación (EN), Villarica (VR), Concepción (CON) and Salto del Guairá (SDG). As aforementioned, the stations CDE and SDG are close to the reservoir of the Itaipú dam and they are located in areas that have undergone significant changes in land use. For this first analysis, data from 1965 to 2002 have been considered.

In order to report trends in the data series, the slope from a linear regression analysis can be obtained. If this parameter is significantly different from zero, there exists a trend in the data. It is noticeable that both the uncertainty of the slope and the overall error of the linear–

regression model have to be reported. These uncertainties are partly dependent on the data dispersion and therefore, the trend identification can be improved by reducing the dispersion.

As an example, Figure 10 shows graphs for January and for June. The most relevant feature in these graphs is the positive slope for the linear regressions of the data in the case of the CDE station (increase of its mean temperature in both months) and negative for the station VR (decrease of its mean temperature). However, both statements are very doubtful if we observe the uncertainty assigned to the slopes (around 100%). The summary for the values found in all the months is presented in Table 1.

The qualitative analysis of these data indicates that both the CDE and the SDG stations register positive slopes throughout the greater part of the months, and EN, VR and CON on–

Figure 10. Evolution of the average monthly temperature corresponding to the months of January (dots) and June (crosses), from 1965 to 2002, for the stations of Ciudad del Este (a) and Villa Rica (b). The uncertainties assigned to the fitting parameters are given as standard errors

Table 1. Signs of the slope of the monthly mean temperature evolution during the last years for the five stations: Ciudad del Este, Encarnación, Villa Rica, Concepción and Salto del Guairá

	Jan	Feb	Mar	Apr	May	Jun	Jul	Aug	Sep	Oct	Nov	Dec
CDE	+	–	+	+	–	+	+	+	+	+	+	+
EN	–	–	+	+	–	+	–	+	–	+	–	–
VR	–	–	+	+	–	+	–	+	–	+	–	–
CON	+	–	+	+	–	+	–	+	–	+	–	–
SDG	+	+	+	+	+	+	+	+	+	+	+	+

Figure 11. Evolution of the moving average of the mean monthly temperature in all the months, from 1965 to 2006, for the Ciudad del Este station
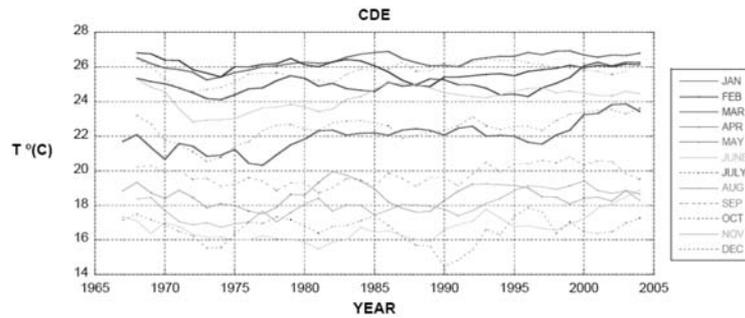
Figure 12. Evolution of the mean monthly temperature from 1965 to 2006, for the stations of Ciudad del Este, Encarnación and Villa Rica
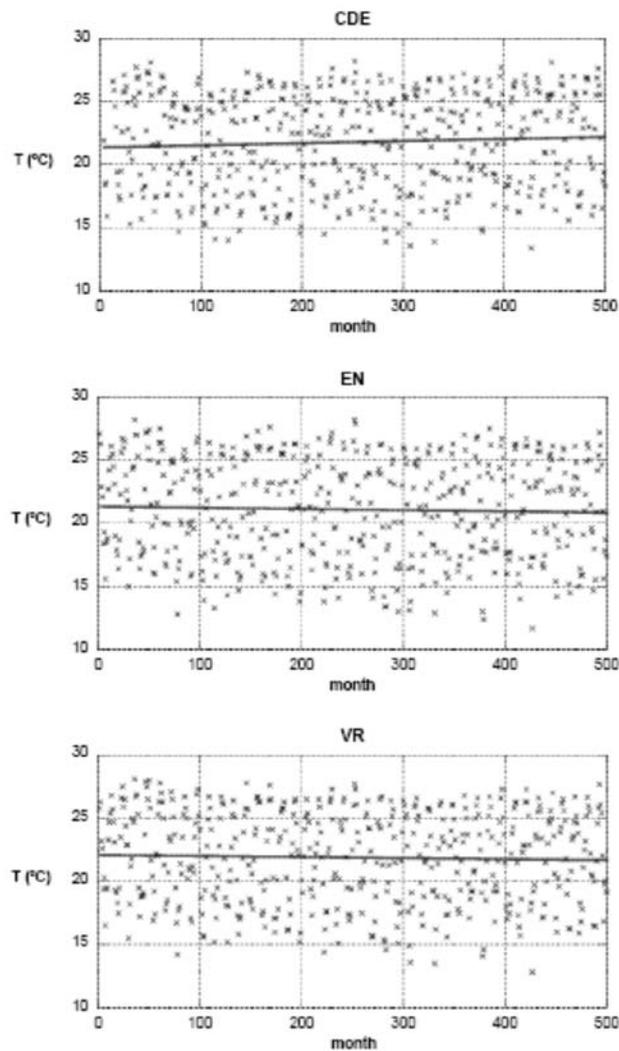
ly during a few of them. The qualitative analysis indicates that the annual thermal amplitude may have suffered alteration, but not much more can be concluded.

A procedure commonly used in climatology to reduce the typical dispersal inherent to its variables is the moving average. A *simple moving average*, SMA, consists of calculating the average value of the series contained in a window of size "*n*" that is being displaced along the length of the series. In this context, a SMA has been applied to smooth the temperature data series. The first question that arises at the moment of applying this procedure is the choice of the value for *n*, that is, the number of years providing the average. To this effect, several tests were conducted on the January data of the stations CDE, EN, VR, CON and SDG with values of $n = 3, 5, 10$ and 12. It was found that averaging over 5 years conserved the trends presented by the data at the same time as a reduction in the dispersion was obtained.

As an example, Figure 11 shows the evolution of the moving average for the mean monthly temperature of the CDE station in all the months. Analyses have been made, by means of linear regressions, of the slopes of all the curves, with the result that they are positive in all months except in February and March. But it is necessary, once again, to stress the high dispersion of the data. The same study at other stations showed both positive and negative trends.

When considering all the data available (502 data, from January of 1965 to October of 2006), the high dispersion is again the most noticeable feature observed. This is shown in Figure 12.

Once again, the linear regression makes evident the trend of the data by means of the sign of the slope, but the associated uncertainty (of up to 100% in some cases) is too high to establish strength conclusions. Even so, it is observed – when the analysis is applied to all the stations – that Ciudad del Este and Salto del Guairá are the only ones that have increased their mean monthly temperature through time, while the exhibit a slight decrease. However, these variations are very small and the errors, as previously mentioned, are high.

These results reveal the need of a procedure capable to identify both the intrinsic variability of the data (seasonal change) and trends due to long-term variations.

For example, if this variability is assumed to be of the sinusoidal type, instead of a linear regression a sinusoidal adjustment of the temperature (variable *y*) in function of time (variable *x*) could be carried out:

$$y = m_1 + m_2 \sin \left(2\pi \; \frac{x}{12} \right) + m_3 \tag{5}$$

where m_1 is the mean value of the temperature, m_2 the thermal amplitude and m_3 the phase displacement.

The Figure 13 presents an example for the Ciudad del Este station.

The 'theoretical' series can be calculated with the adjustment equation in order to see how much the real series diverges from the adjusted series. If we define $\Delta T = T_{teorethical} - T_{real}$. The representation of ΔT with respect to time is another form of analysing the trend towards change of the temperature. For example, for the CDE station (Figure 14).

The same trend as before can be observed, that is, an increase of the mean temperature. What is most relevant is that the error of the slope has been considerably reduced (it has gone from 100% to 60%) although it continues being high.

As mentioned before, there is another procedure to perform a similar analysis, the multi-resolution analysis (MRA) based on the wavelet transform (as explained in section 4.). The main advantage of the MRA in relation to trend identification is its capacity to split the original signal in two components: the intra-annual component, which is related to the seasonal variability of the data, and the inter-annual component, which may be related to long-term changes. If the trend analysis is performed in the inter-annual component of the data series, which is not affected by the «noise» introduced by the seasonal variability of the data, an important reduction of the dispersion and hence of the associated uncertainties is expected.

Figure 13. Sinusoidal analysis of the mean temperature data corresponding to Ciudad del Este
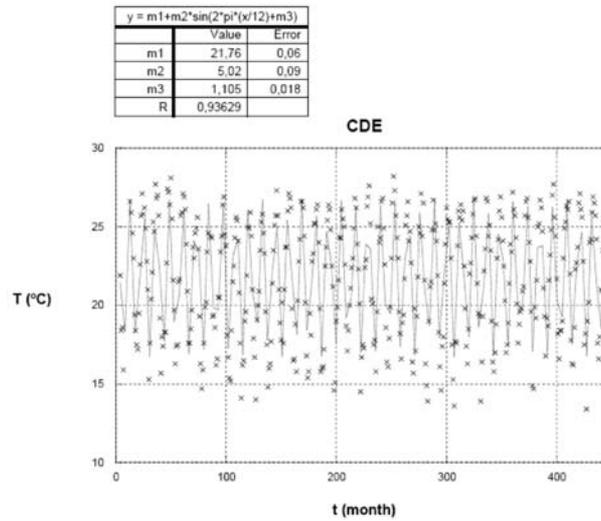

Figure 14. Difference between the real temperature and the "theoretical" temperature calculated through the sinusoidal function (see in the text)
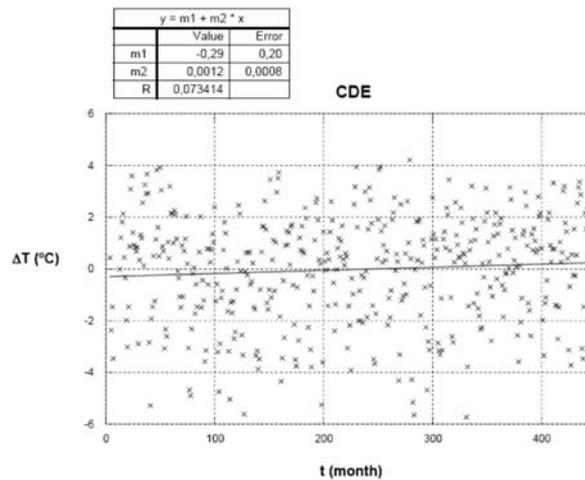

Figure 15(a) shows the inter-annual component for the monthly mean temperature corresponding to the CDE, VR and EN stations for all the considered period. As shown, an oscillating behaviour is observed for the three stations. A linear regression has been applied only to this component of the signal. It is observed again the positive trend towards change experimented by the temperature in Ciudad del Este and the negative trend in the other stations. The errors in the slopes have decreased (38, 10 and 12% in CDE, VR and EN, respectively). This decrease is still larger when the «smoothed inter-annual component» is considered. In this case, the slope uncertainties are 25, 7 and 10% for CDE, VR and EN, respectively.

The influence of the episodes of El Niño / La Niña upon the values of the meteorological variables in Paraguay and in other countries of the Centre-South part of South America has been suggested in different studies (Berri and Bertossa 2004; Grassi 2007). As a general rule,

Figure 15. Inter-annual (a) and smoothed inter-annual component (b) of the monthly mean temperature of three stations obtained by MRA (see in the text). Regression lines are also shown
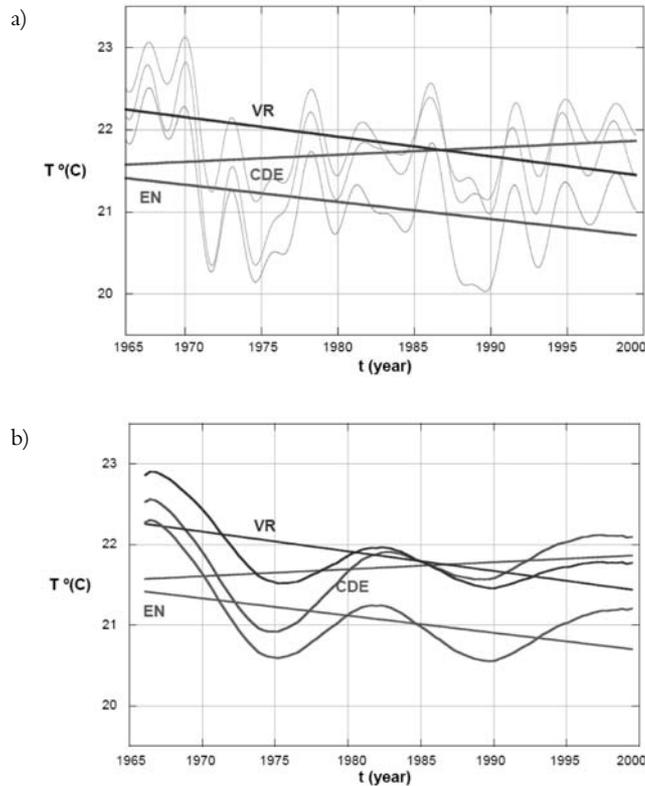
the influence of these episodes is mainly shown in precipitation data. In our series of temperature data, a minimum is observed around the year 1975 (see Figure 15b) coinciding with a very strong La Niña episode (water surface temperature in the Pacific below its normal values). The two subsequent maximums were located around 1982 and 1997, coinciding with episodes of El Niño (water temperature in the Pacific above its normal values).

As was commented at the beginning of this section, the mean temperature data has only been considered to illustrate the different types of analyses that can be applied to the data. It has already been observed how the MRA presents a significant advantage due to its capacity to split the original signal in two components: the intra-annual component, which is related to the seasonal variability of the data, and the inter-annual component, which may be related to long-term changes.

Next, in the following sections, the MRA is applied to maximum and minimum temperature, precipitation and relative humidity data. The trend detection is obtained via linear regression of the inter-annual components. As shown in Table 2, the trends can be obtained also from the smoothed inter-annual component. Therefore, this latter signal is also used since it presents less noise. Only the most relevant results obtained from the analysis are shown.

5.1   Study of the trends in the temperature data

The data available for maximum and minimum temperatures for all the stations are shown in Figure 16 (a, b, c). Except for the CM station (which, on the other hand, contains the shorter

Table 2. Linear regression parameters corresponding to Figure 15

15 (a)	SLOPE	INTERCEPT	R
CDE			0.14592
VR			0.43344
EN			0.33498
15 (b)	SLOPE	INTERCEPT	R
CDE			0.19368
VR			0.59800
EN			0.44320

data series), they show certain positive trends, which are more marked in the CDE and SDG stations (the closest to the dam).

Figure 17 shows the observed trends for the inter-annual component of the maximum temperatures for the six stations, as derived from the MRA.

As shown in Figure 17, all the stations present maximum temperatures increasing with time (positive slopes), with the SDG and CM stations standing out as those with the greatest growth. On the other hand, when considering the smoothed inter-annual component (Figure 18), the curves can be grouped into two groups: the first one (CDE, VR, EN stations) containing curves with many inflexion points and with dispersions around 5%, and the second group (CM, CON, SDG stations) containing flatter curves with even lesser dispersion (around 3%).

Figure 19 and Table 4 show similar results but in this case for the inter-annual component of the minimum temperature.

In the case of the minimum temperatures, positive slopes are also observed in all the stations except in the CM. The data series of the later station is incomplete and, therefore, it has to be considered with care, mainly when it presents discrepancies in its behaviour. Nevertheless, it is necessary to take also into account that it is situated in a zone of major changes in the land use and they could affect it. It should be noted that the two stations situated close to the dam (CDE and SDG) present a much greater slope (at least 4 times) than the others, which to a certain extent could be justified by the thermal regulation effect due to the reservoir water. Once again, two groups can be distinguished: the first (CDE, SDG and CON) with a flatter evolution throughout the time (dispersions between 3 and 8%) and the other (VR, EN and CM) more distant from the linear behaviour, with higher dispersions between 13 and 20%.

In Figure 20 and Table 5 results for the inter-annual and the smoothed inter-annual component of the thermal oscillation are shown.

In the case of daily thermal oscillation (difference between the maximum temperature and the minimum) only two stations show a negative slope: CDE and of SDG, i.e., the stations that border the dam development and which are subjected to the effect of the high thermal capacity of the water. It had been observed that, in general, the temperatures presented positive trends to increase for practically all the stations. However, the stations near the dam increase the minimum temperature much more than the maximum, thus decreasing the daily temperature oscillation. For the rest of the stations, the observed behaviour is just the opposite one.

In relation to the increase observed in temperature data, three factors could be mentioned that, at least a priori, can be acting: (i) the dam, (ii) the changes in the use of the land, and (iii) the possible effects of the global warming.

The effect of the dam is noticed, as mentioned before, in the increase of the minimum temperature recorded in the CDE and SDG stations as a consequence of the thermal regulation

Figure 16. Temporal evolution of the maximum temperature and minimum temperature of the six stations. The graphs also indicate the sign of the slopes resulting from the linear regression of the data
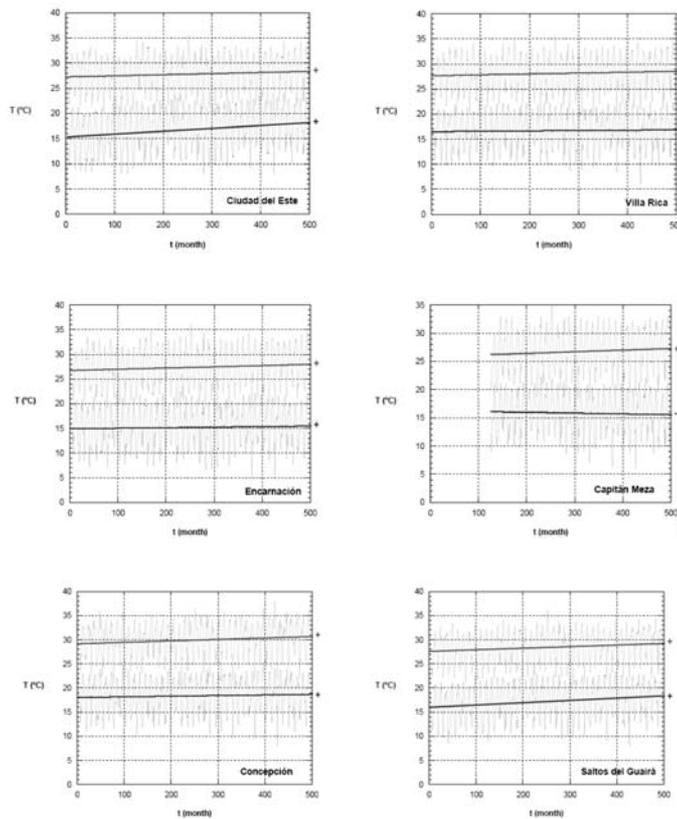

Figure 17. Inter-annual component of maximum temperatures as derived from the MRA and the regression lines for the six stations considered
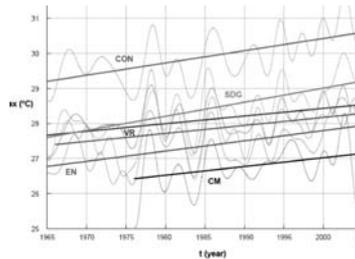

Table 3. Slopes of the regression lines corresponding to the inter-annual component of the maximum temperatures in each of the stations (see Figure 17)

STATION	SLOPE (value error)	Uncertainty (%)
Ciudad del Este (CDE)		9
Villa Rica (VR)		8
Encarnación (EN)		7
Capitán Meza (CM)		14
Concepción (CON)		6
Saltos de Guairá (SDG)		4

Figure 18. Smoothed inter-annual component of maximum temperatures as derived from the MRA and the regression lines for the six stations considered
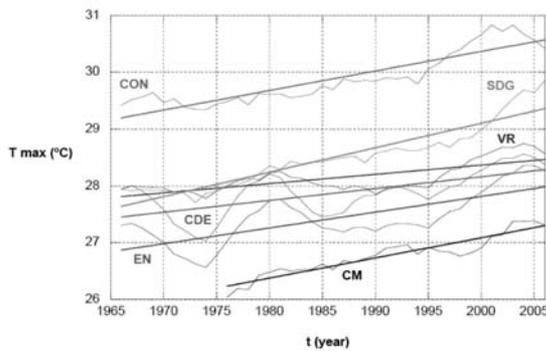
Figure 19. Inter-annual component of minimum temperatures as derived from the MRA and the regression lines for the six stations considered
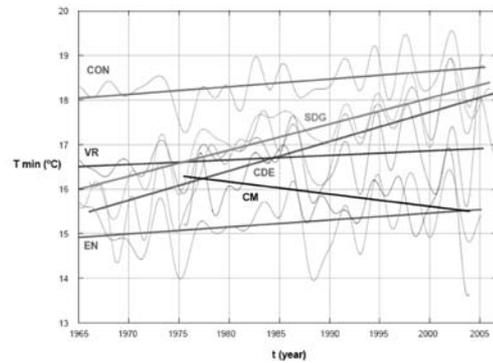
Table 4. Slopes of the regression lines corresponding to the inter-annual component of the minimum temperatures in each of the stations (see Figure 19)

STATION	SLOPE (value error)	Uncertainty (%)
Ciudad del Este (CDE)		3
Villa Rica (VR)		20
Encarnación (EN)		13
Capitán Meza (CM)		13
Concepción (CON)		8
Saltos de Guairá (SDG)		3

Figure 20. (a) Inter-annual and (b) smoothed inter-annual component of thermal oscillation as derived from the MRA and the regression lines for the six stations considered
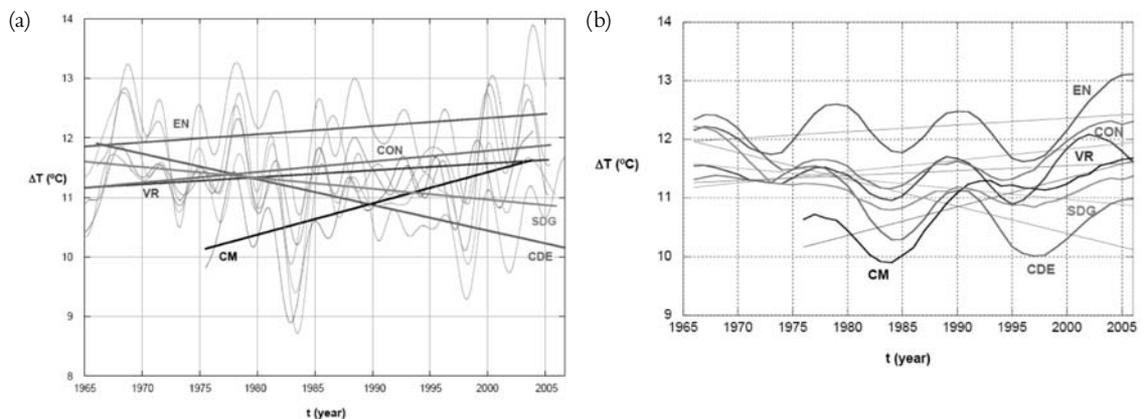
Table 5. Slopes of the regression lines corresponding to the inter-annual component of the thermal oscillation (maximum temperatures minus minimums) in each of the stations (see Figure 20a)

STATION	SLOPE (value error)	Uncertainty (%)
Ciudad del Este (CDE)		6
Villa Rica (VR)		18
Encarnación (EN)		19
Capitán Meza (CM)		7
Concepción (CON)		11
Saltos de Guairá (SDG)		12

Figure 21. Temporal evolution of the moving average of the monthly precipitation data for each month for CDE, EN and VR stations
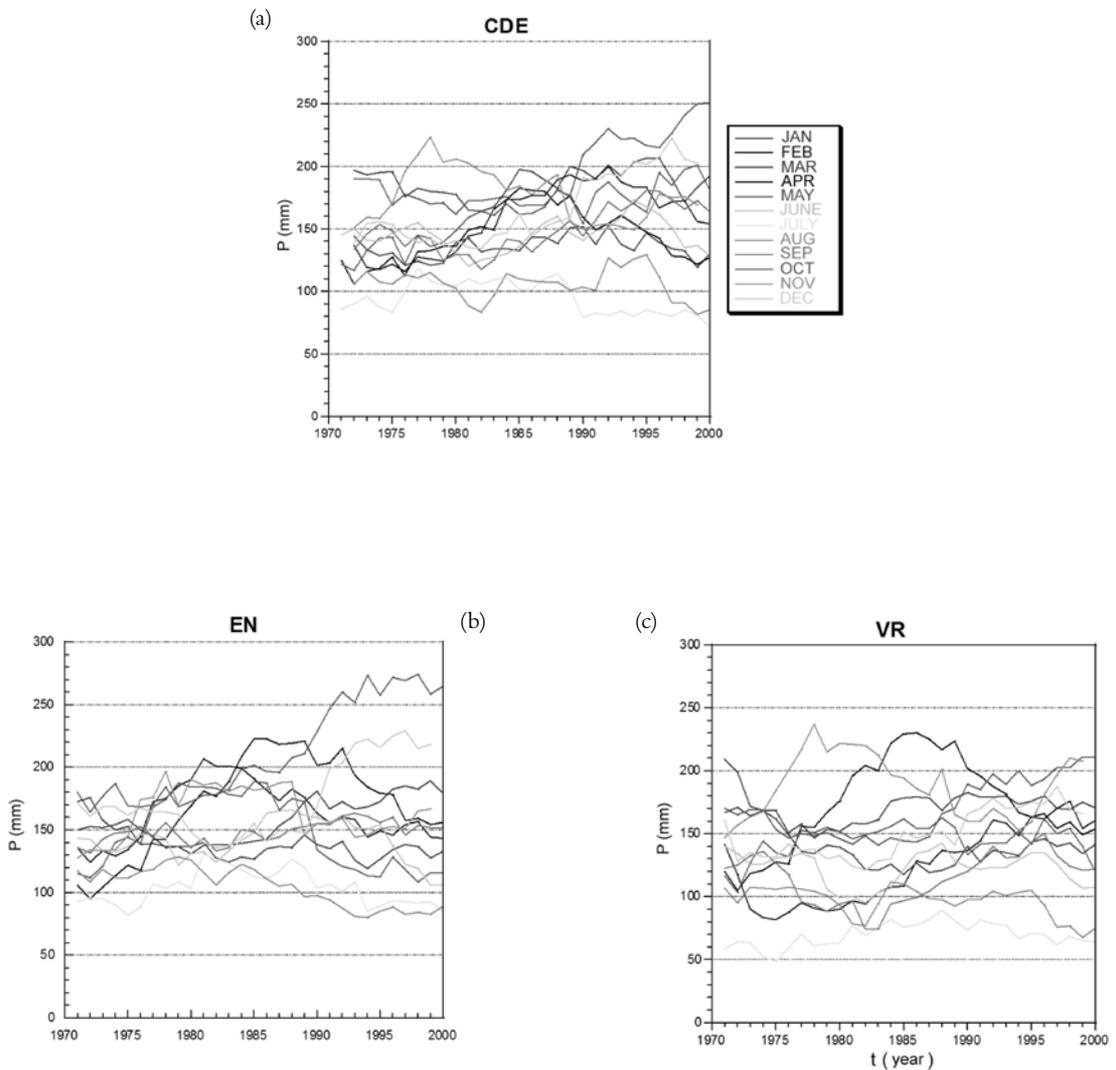
Figure 22. Evolution of the monthly precipitation data in the three stations (CDE, EN and VR) throughout the period studied
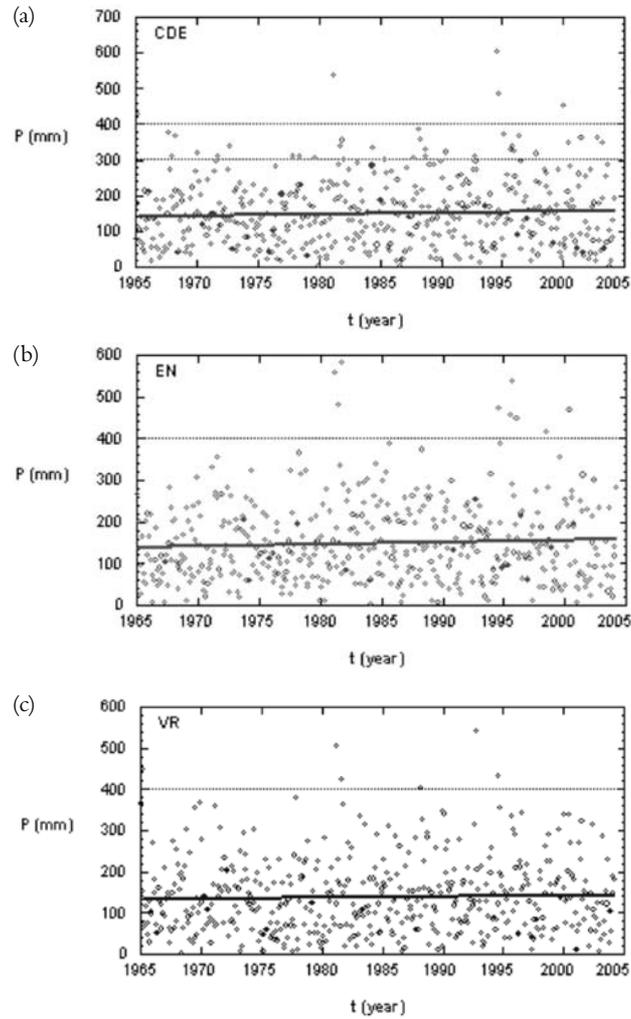
Figure 23. Evolution of the monthly relative humidity in the three stations throughout the period studied
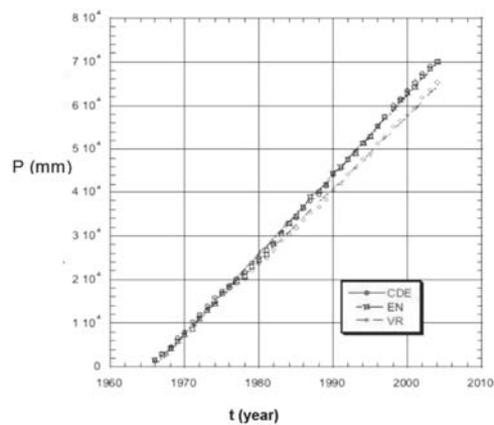
due to the water. For the same reason, a decrease in the maximum temperatures would have to be expected. But this decrease is not observed, which leads us to presume that there is another factor producing an increase in the temperatures and, then, masking the effect of the water.

On the other hand, the changes in the use of the land generally involve an increase in the maximums and a decrease in the minimums. This can be seen in the station most affected by them (CM), which is also the station with least data, with all the limitations that this entails. The zones surrounding the dam (stations CDE and SDG) also present deforestation; however, the trend observed here is different.

The remaining stations (EN, CON and VR) are distant from the area of influence of the dam and also present much lesser changes in the use of the land; their curves, however, continue presenting positive slopes.

Due to all of this, it seems that the study area is also being affected by an increase of temperature that may be related to a climatic change. Obviously, to verify this statement it would be necessary to study data from more stations situated throughout the country, and to check if the trend is maintained. This hypothesis is in agreement with the latest report of the IPCC (IPCC 2007).

5.2   Study of the trends in the precipitation data

The analyses of the precipitation data have been made following the guidelines set by the previously described methodology. Due to lack of time, the study of the precipitation (as also that of the relative humidity) has been carried out only considering the stations of CDE, EN and VR. The data corresponds to the monthly–accumulated precipitation, throughout the period of years studied from 1965 to 2006.

In a similar manner to the case of the temperatures, the monthly precipitation values also present a very high dispersion. The temporal evolution of the moving average (with a size window equal to 12), calculated for the monthly precipitation of all the months in the stations considered, is presented in Figure 21 for the stations CDE, EN and VR.

It can be observed that the CDE station presents an increase in the monthly precipitation during nine of the twelve months, whereas EN and VR stations present increases during seven and eight months respectively. In the set of stations considered it is possible to observe an increase in the monthly precipitation values within the period of analysis. This can also be observed in Figure 22 (a, b, c) in which all the monthly precipitation values appear. The slopes are all positive, but their linear fit presents high uncertainties (between 50 and 70%).

Figure 23 shows the accumulated precipitation data obtained for the three stations (CDE, EN and VR) during the all the period.

As shown in Figure 23, the three stations have a similar behaviour until dates approaching 1975 or, at least, no significant differences are found among them. From the year 1975, higher values for the accumulated precipitation are registered by Ciudad del Este and Encarnación station.

5.3   Study of the trends in the humidity data

In the data analyses for the relative humidity (H), each one of the previously described procedures has been followed for the stations CDE, EN and VR. All the procedures (study by months, study by moving average, adjustment of all the data throughout all the years) show the same result: a decrease in the humidity in Ciudad del Este and an increase in the other two stations. Thus, for example, Figure 24 (a, b, c) shows all the data, adjusted by means of a linear regression, and the table 6 shows the slope of the regression with the uncertainties.

A clear tendency to decrease in the Ciudad del Este station, and to increase in the other stations is observed. When analysing the data by using moving averages, sinusoidal adjustments and MRA, similar behaviours are observed. In particular, the results from the MRA are shown in Figure 25 (a, b) and Table 7.

Once again, the uncertainties are lesser when using the results from the MRA instead of the moving average. In particular, if the linear regression is applied to the smoothed inter-annual component, the uncertainties are reduced almost by a factor of ten. A decrease

Figure 24. Evolution of the accumulated monthly precipitation data of the three stations during the period studied
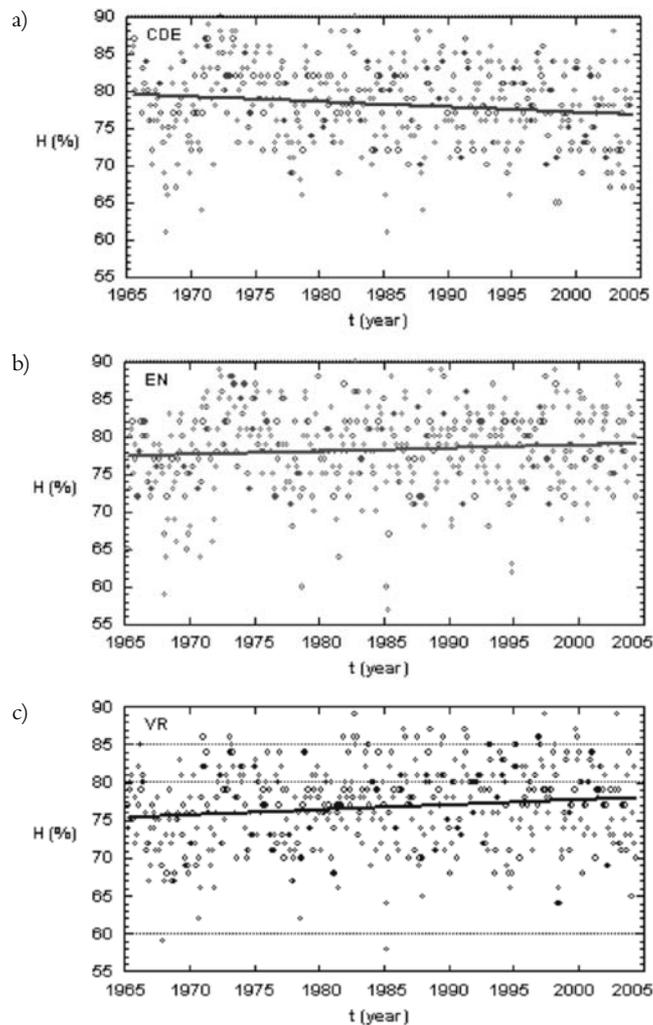
Table 6. Slopes of the regression lines shown in Figure 24 (a, b, c)

STATION	SLOPE (value error)	Uncertainty (%)
Ciudad del Este (CDE)		28
Encarnación (EN)		59
Villa Rica (VR)		35

Figure 25. Trends of the inter-annual (a) and of the smoothed inter-annual component (b) of the monthly relative humidity series obtained from the MRA for the CDE, EN and VR stations
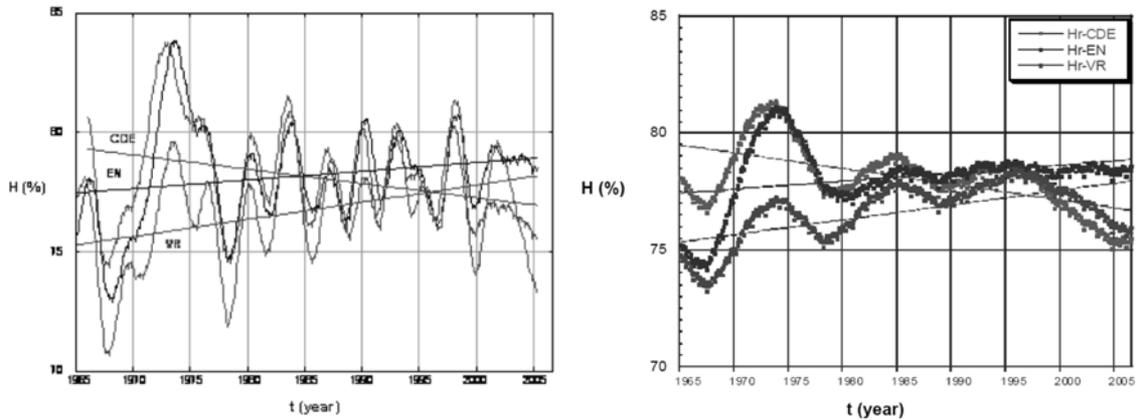
Table 7. Slopes of the linear regressions shown in figure 26 for the inter-annual (a) and the smoothed inter-annual component (b)

Fig. 26 (a)	SLOPE (value error)	Uncertainty (%)
Ciudad del Este (CDE)		14
Encarnación (EN)		23
Villa Rica (VR)		12
Fig. 26 (b)	SLOPE (value error)	Uncertainty (%)
Ciudad del Este (CDE)		5
Encarnación (EN)		14
Villa Rica (VR)		4

is observed in CDE humidity and an increase in the other stations. This behaviour could be a consequence of the anthropogenic activities occurring in the region of influence of the station (deforestation and urbanization) but a deeper analysis would be required to establish such a conclusion.

6. Conclusions

Several methodologies have been reviewed for the study of temporal series of data in order to identify trends, with special emphasis to the multi-resolution analysis (MRA) based on the wavelet transform. By means of this analysis, it has been shown that it is possible to isolate long-term positive or negative changes that can appear superimposed upon the seasonal variability that is inherent to these series.

The data analyzed correspond to monthly climatic records of temperature (mean, maximum and minimum), precipitation and atmospheric humidity throughout the last 40 years in a zone that is representative of the Eastern region of Paraguay. The study area presents a significant anthropogenic alteration (changes in the land use and the construction of the Itaipú dam). The values of the climatic variables of this zone are compared with those of other me-

teorological stations of the oriental region of the country, not so affected by the human influence and which, from the mesoscale point of view, present similar climatic characteristics.

The analysis of the observed trends in the data reveals some interesting behaviours. However, it is worth mentioning again that it would be necessary to take into account data from more stations in order to confirm them. Furthermore, a deeper analysis of the changes observed in the study area should be carried out (for example, to quantify the changes in the land use from remotely sensed data) to establish more comprehensive relationships between the observed trends and their causes.

With all these cautions, and as a result of the analysis, it is possible to observe the climatic mesoscale behaviour during the period between the years 1965 ad 2006 of the Eastern region of Paraguay, which shows that:

- when analyzing the temporal evolution of the maximum temperature, all the stations present positive trends, being the stations SDG and CM those with the greatest increase. Taking into account the shape of the curves, two groups are distinguished: a first one (CDE, VR, EN) with curves with many inflexion points and with dispersions around 5%, and a second group (CM, CON, SDG) with flatter curves presenting even lesser dispersion (around 3%).
- in the case of the minimum temperatures a positive slope can also be observed in all the stations, except in the CM, which, in addition, is lacking its complete series of data and, therefore, has to be taken with serious caution, mainly when it presents a discrepant behaviour. Nevertheless, it is necessary to also take into account that it is situated in the zone of greatest changes in the land use and might be showing their influence. It is worth noting that the two stations situated near the dam (CDE and SDG) present a much greater slope (at least 4 times greater) than the others, which would be justified by the thermal regulation effect due to the reservoir water. Again two groups can be identified: the first one (CDE, SDG and CON) with a flatter evolution over time (dispersions between 3 and 8%) and the second one (VR, EN and CM) very distant from the linear behaviour, with dispersions between 13 and 20%.
- In the case of the daily thermal oscillation (the difference between the maximum and the minimum temperature), as it was expected, only the stations CDE and SDG show a negative slope. These two are the stations situated near the dam and affected by the thermal effect of water. In general, the maximum temperatures present positive trends in practically all the stations but the stations close to the dam present a higher minimum temperature increase, leading a decrease in the daily thermal oscillation. For the rest of the stations, the opposite behaviour is found.
- The stations that are situated far away the dam and in an area with no land use changes (EN, CON and VR) an increase in temperature has been also observed that might be related to a climate change. This hypothesis agrees with the temperature trends shown by the IPCC (2007). However, it would be necessary to study the data from more stations, located all through the country, to check if the observed trend is maintained.
- In relation to the mean temperature, and lacking a more detailed analysis, the very acute minimum observed in the month 120 (year 1975) coincides with a very strong episode of La Niña (ocean surface temperature in the Pacific below its normal values) and that the two subsequent maximums are located around 1982 and 1997, coinciding with El Niño episodes (ocean surface temperature above its normal values).
- The precipitation increases slightly in the three stations studied (CDE, EN and VR). Since the year 1975 slight discrepancies in the behaviour of the accumulated precipitations of the CDE and EN stations with respect to the VR station are observed. In particular, the accumulated precipitation is higher in the CDE and EN than in VR.
- The relative humidity shows a decrease in Ciudad del Este and an increase in the other two stations (EN and VR). This behaviour could be related to the anthropogenic activities in the region around the station (deforestation and urbanization), but a further analysis would be useful to establish such a conclusion.

References

Abry P. (1997). *Ondelettes et turbulence. Multirésolutions, algorithmes de décomposition, invariance d'échelles.* Diderot Editeur, Paris.

Berri G.J. and Bertossa G. (2004). The influence of the tropical and subtropical Atlantic and Pacific oceans on precipitation variability over Southern Central South América on seasonal time scales. *International Journal of Climatology*, 24: 415-435.

Brunkow R., Andrade L. and Xavier C. (1987). Proceso de Estratificaçao térmica e de oxigenio dissolvido no reservatorio de Itaipú. Seminario da Itaipú Binacional sobre Meio Ambiente. Foz de Iguaçu.

Burke-Hubbard B. (1998). *The World According to Wavelets. The story of a Mathematical Technique in the Making.* 2nd ed., A.K Peters, Natick, Massachusetts.

Chow V., Maidlment D. and Mays L. (1994). *Hidrología aplicada*. Santa Fe de Bogotá, Colombia.

Cuadrat J.M., Pita M.F. (1997). *Climatología.* Cátedra, Madrid.

Daubechies I. (1992). Ten lectures on wavelets. CBMS-NSF Conference Series in Applied Mathematics, Society for Industrial and Applied Mathematics.

Fonseca L.M.G., Costa M.H.M., Manjunath B.S. and Kenney C. (1998). Automatic registration of satellite imagery. Image Registration Workshop (Greenbelt: NASA Goddard Space Flight Center): 13-27.

Furon A.C., Wagner-Riddle C., Smith C.R. and Warland J.S. (2008). Wavelet analysis of wintertime and spring thaw CO2 and N2O fluxes from agricultural fields. *Agricultural and Forest Meteorology*, 148: 1305-1317.

Galford G.L., Mustard J.F., Melillo J., Gendrin A., Cerri C.C. and Cerri C.E.P. (2008). Wavelet analysis of MODIS time series to detect expansion and intensification of row-crop agriculture in Brazil. *Remote Sensing of Environment*, 112: 576-587.

Gimeno J.F. (2003). *Estudio de la desertificación en la Península Ibérica mediante teledetección aplicando la transformada wavelet*. Trabajo Investigación. Departament de Termodinàmica, Facultat de Física, Universitat de València.

Grassi B. (2007). Reducing the impact of environmental emergencias through early warning and preparedness. The case of El Niño-Southern Oscillation (ENSO). <http://www.ccb.ucar.edu/un/paraguay.html>.

Horgan G. (1998). Wavelets for SAR image smoothing. *Photogrametric Engineering and Remote Sensing*, 64: 1171-1177.

Huang C., Kim S., Altstatt A., Townshend J.R.G., Davis P., Song K., Tucker C.J., Rodas O., Yanosky A., Clay R. and Musinsky J. (2007). Rapid loss of Paraguay's Atlantic forest and the status of protected areas − A Landsat assessment. *Remote Sensing of Environment*, 106: 460-466.

Hufty A. (1984). *Introducción a la climatología*. Ariel, Barcelona.

IPCC (2007). Climate Change 2007: The Physical Science Basis. Summary for Policymakers, Contribution of Working Group I to the 4th Assessment Report of the Intergovernmental Panel on Climate Change, WMO, UNEP, <http://www.ipcc.ch/>.

Itaipú (1973). Actos y Normas del Entidad Itaipú Binacional. Paraguay – Brasil.

Itaipú (2000). Plan Director de Gestión Ambiental, Entidad Itaipú Binacional. Paraguay – Brasil.

Lindsay R.W., Percival D.B and Rothrock D.A. (1996). The discrete wavelet transform and the scale analysis of the surface properties of sea ice. *IEEE Transactions on Geoscience and Remote Sensing*, 34(3): 771-787.

Mallat S. (1989). A theory of multiresolution signal decomposition: the wavelet representation, *IEEE Trans. Pattern Anal. Mchine Intell.*, 11, 674-693.

Mataix C. (1983). *Mecánica de fluidos y máquinas hidráulicas*. Segunda edición. Harper and Row Lainoamericana, México.

Meyer Y. (1993). *Wavelets: algorithms and applications*. Society for Industrial and Applied Mathematics.

Müller A. (1987). Plano Diretor da Área do Reservatório. Seminario da Itaipú Binacional Sobre Meio Ambiente. Foz do Iguaçu, Brasil.

Percival D.B. and Walden A.T. (2000). *Wavelet methods for time series analysis*. Cambridge University Press.

Percival D.B., Wang M. and Overland J.E. (2004). An introduction to wavelet analysis with application to vegetation monitoring. *Community Ecology*, 5: 19-30.

Sakamoto T., Yokozawa M., Toritani H., Shibayama M., Ishitsuka N. and Ohno H. (2005). A crop phenology detection method using time-series MODIS data. *Remote Sensing of Environment*, 96: 366-374.

Simhadri K.K., Iyengar S.S., Holyer R.J., Lybanon M. and Zachary J.M. (1998). Wavelet-based feature extraction from oceanographic images. *IEEE Transactions on Geoscience and Remote Sensing*, 36: 767-777.

Trenas M.A. (2000). Arquitecturas y aplicaciones de la transformada wavelet, Tesis Doctoral, Universidad de Málaga, Departamento de Arquitectura de Computadores.

UNEP (1972). Declaration of the United Nations Conference on the Human Environment, Stockholm, 5-16 June 1972.

WMO (1990). OMM – Nº 100, Guía de prácticas Climatológicas. Organización Meteorológica Mundial. Ginebra, Suiza.

WMO (2006). Scientific Assessment of Ozone Depletion: 2006. Global Ozone Research and Monitoring Project–Report No. 50. Geneva, Switzerland, World Meteorological Organization: 572.

WMO (2007). Position Paper. WMO's role in global climate change issues with a focuss on development and science based decision making. Revised september 2007, <http://www.wmo.ch/>.

Zhou J., Civco D.L. and Silander J.A. (1998). A wavelet transform method to merge Landsat TM and SPOT panchromatic data. *International Journal of Remote Sensing*, 19: 743-757.

Zhu C., and Yang X. (1998). Study of remote sensing image texture analysis and classification using wavelets. *International Journal of Remote Sensing*, 19: 3197-3203.

ESTIMATION OF FOREST CANOPY GAP FRACTION CHANGES THROUGH THE APPLICATION OF TERRESTRIAL LASER SCANNER AND HEMISPHERICAL PHOTO CAMERA

Carolina Giacosa
Facultad de Ingenieria, geoecología y medio Ambiente
Universidad Católica de Santa Fé
Argentina

Tutor: Prof. M. Danson
School of Environment and Life Sciences
University of Salford
United Kingdom

1. Introduction

Leaf area index (LAI) is a critical variable for understanding the biological and physical processes associated with vegetated land surfaces, and thus is a key input of climate and large-scale ecosystem models (Bonan, 1996). LAI is defined as one-sided green leaf area per unit ground area in broadleaf canopies and as the hemisurface needle leaf area in coniferous canopies (Chen and Black, 1992). Important processes such as canopy interception, evapotranspiration and net photosynthesis are directly proportional to LAI. Canopy gap fraction is defined as the probability of a ray of light passing through the canopy without encountering foliage or other plant elements. Canopy directional gap fraction describes the probability that a beam will not intercept a canopy element in a given direction. Weiss *et al.* review the methods to derive LAI from gap fraction measurements.

The main methodologies for estimating LAI employ either «direct» measures (involving destructive sampling, litterfall collection, or point contact sampling) or «indirect» methods (involving optical instruments and models) like hemispherical photographs and Terrestrial Laser Scanner data. Direct methods are the most accurate, but they have the disadvantage of being extremely time-consuming and a making large-scale implementation is feasible only marginally. Accuracy problems may, in this case, result from the definition of LAI, from the up-scaling method, or from accumulation error due to frequently repeated measurements. Because of its time-consuming and labour-intensive character and apart from other operational constraints, it can be said that the directly determination of LAI is not really compatible with the long-term monitoring of spatial and temporal dynamics of leaf area development (Chason 1991). However, the need for validation of indirect methods remains, so the direct techniques can be considered important as calibration methods. Indirect methods, in which leaf area is inferred from observations of other variables, are generally faster, amendable to automation, and thereby allow for a larger spatial sample to be obtained. For reasons of convenience, comparing to the directly methods, they are becoming more and more important.

Terrestrial laser scanners (TLS) are now capable of collecting 3d data clouds consisting of the x, y, z coordinates of laser hits, plus information on return intensity and, in some cases, target colour of several million data points in less than five minutes. TLS collect data at sub-centimetre resolution at a range of zenith view angles (Danson *et al.* 2006)

A laser scanner creates a model which is a representation of the 'real world'. The x y z coordinates relate the points, measured on 'real world' objects, to the origin of the scanner. The

ability of a laser scanner to capture large amounts of data in a short time, and with a fine resolution, means that the 'real world' can be accurately modelled.

At the present time, there is a considerable interest in the use of terrestrial laser scanner (TLS) data for 3D reconstruction and modelling within heritage recording and plant documentation fields.

On the other hand, the hemispherical photo is an indirect optical technique that has been widely used in the study of canopy structure and forest light transmission. Photographs, taken skywards from the forest basement with 180 degrees hemispherical (fisheye) lens, produce circular images that record the size, the shape, the density and the distribution of gaps within the forest (Baret, 2004). This technique is able to capture the species-, site-and age-related differences in canopy architecture, on the basis of light attenuation and contrast between features scanned by the photo (sky versus canopy). One of the main constraints of hemispherical photography for LAI assessment concerns with the selection of the optimal brightness threshold capable to distinguish leaf area from sky area, i.e. producing a binary image. A series of software packages for hemispherical image processing have been developed (e.g. GLA, Forest Renewal BC, Frazer S., 1999 and EYE-CAN Weiss, 2002). Previous research demonstrated that with a high resolution digital camera, the choice of the threshold level would be less critical, because the frequency of mixed pixels is reduced in comparison to the aggregation of pixels in cameras with a lower resolution (Blennow 1995).

The advantage of hemispherical photography over light interception measurements is that it provides a permanent two-dimensional record of canopy structure. Terrestrial laser scanners have the potential to provide a permanent 3d record of canopy structure and, with recent advances in scanner technology, to provide detailed information about forest canopy architecture.

The present work describes the results of a series of experiments where a TLS scanner was used to measure the three-dimensional structure of a broad-leaf deciduous woodland canopy at a range of dates with different leaf cover compared with hemispherical photographs

2. Project Aim and Objectives

In this research the above mentioned two techniques are compared in order to estimate Forest Canopy Gap Fraction changes through during different seasons and considering different experiments. The project aims at measuring the three-dimensional structure of a broad-leaf deciduous woodland canopy at a range of dates with different leaf cover. Some additional field work will be done inside the campus of the University. The devices used was the Terrestrial Laser Scanner (TLS) (Riegl 2006) and a hemispherical photo camera (Jonckheere *et al.* 2004). The laser data will be compared with near-simultaneous hemispherical photographs of the canopy shot from the same location.

The objectives of the proposed research are:

- collection of data in a site in the UK in different conditions using both TLS and hemispherical photos.
- data processing through different software
- multi-temporal variation computing of canopy leaf area index

3. Methodology

We worked in an area inside the campus of the University of Salford, England, in a period of time between October 2006 and March 2007 (see Figure 1). In this area, placed in front of

Figure 1. (a) Showing the Study Area and (b) The Study Area and TLS (source Google earth)

Latitude = 53.4876, Longitude = -2.2735
Lat = 53 degrees, 29.3 minutes North
Long = 2 degrees, 16.4 minutes West
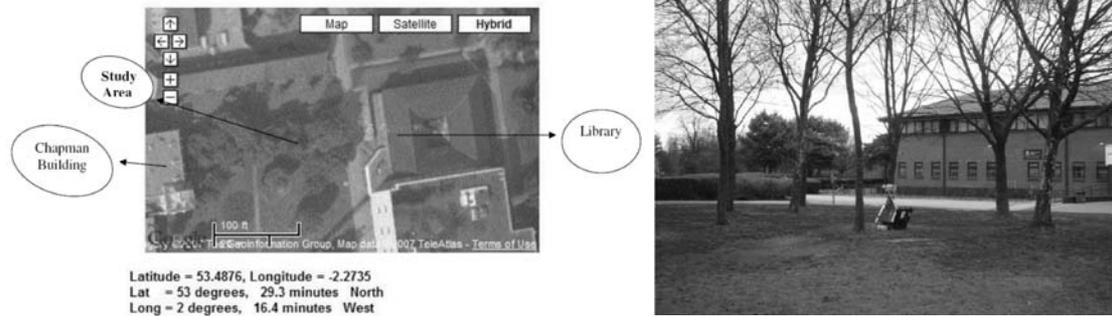
Figure 2. Show the two position of the TLS
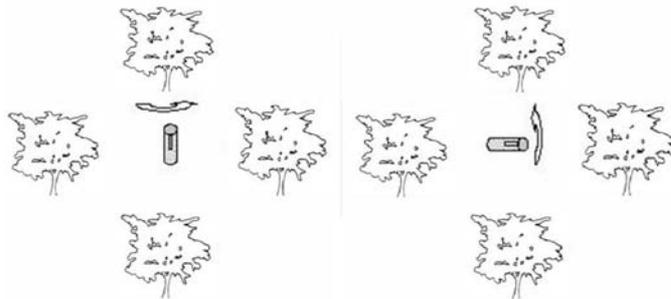
Figure 3. The Laser scanner and the camera at the same height

the university library where deciduous trees are planted, data are collected at a range of dates with different leaf cover. The deciduous trees, composed by birch and sycamore species, had an average height of 15 meters.

Spatially and temporally coincident, TLS data and digital hemispherical photographs were collected and then processed in order to compute multi-temporal variation in canopy leaf area index from gap fraction estimations.

The data were collected using a Riegl LMS Z210 terrestrial laser scanner and the field laser attached to a touch book computer was used. Survey control was facilitated by the RiScan-Pro survey software package, which is capable of visualizing point cloud data in the field. Scans were generally restricted to 180° in front of the scanner. The technical specifications of the scanner may be found in Hetherington *et al.* (2005). The TLS was mounted on the tripod at an inclination angle of 90° and a single scan was recorded with a line scan angle of approximately 80° and a frame scan angle of 180°. For each field work a new project was created. Then the TLS was rotated of 90° and a second orthogonal scan was recorded (Figure 2). The resolution was set at 0.108° in line. The laser scanner recorded the x, y, z position of all the laser hits, plus the intensity of return and colour information in an RGB file. Only the x, y, z position data are considered in this work.

With a calibrated hemispherical lens, a single hemispherical photograph was taken using an upward-looking Nikon Coolpix 4500. The hemispherical photographs were analyzed using the Gap Light Analyzer (GLA) software (Frazer 1999).

In order to record the data always from the same place, measurements placement within the area of study was physically marked through a stick. The TLS and the camera were mounted

on the tripod at a height of 1,30 metres from the ground. They were also levelled and then the data collected from two positions of the TLS and the camera (see Figure 2). These parameters were the same also for further field works (Figure 3).

3.1   Field surveys

The first field survey was carried out on 2nd November 2006 with the objective of practising with the use of TLS and the camera. Both of them were mounted on a tripod and oriented in order to measure canopy gap fraction over a near-complete hemisphere (see Figure 4).

After the first measurements, I started becoming familiar with specialized software to process hemispherical photographs, *Gap Light Analyzer* (Frazer *et al.* 1999) and the data acquired by the TLS (Riscan Pro, Riegl, 2006). Some experiments were carried out to calibrate the hemispherical photo camera, which included also processing phases.

The second field survey was carried out on 17th November 2006: two scans in different positions were performed, between 4 and 5 pm, the resolution was set at 0.108° and the last target data were recorded (see Figure 5). In this circumstance, we agreed the parameters that needed to be measured as better explained in the 'methodology' section of this report.

The last field survey was on 23rd, February, 2007. From the first position, five scans were created while from the second one four pictures, with different resolution (0.108° and 0.072°), were scanned. The first, the last and the first-last data were recorded (Figure 6).

The laser scanner was operated from the laptop with the software "*Riscan_Pro*" following this flow chart (see Figure 7):

The resolution that was generally used was 0.396 degrees. However, for the different scans the resolution and the target selection were changed depending on the objective of the project.

From the same positions and height, hemispherical photos were also taken, with the objective of comparing both techniques (see Figure 8). The camera was placed horizontally on the tripod and the photos were manually set. The photos were stored in the memory of the camera and then were downloaded into the computer in order to be manipulated with Gap Light Analyzer.

3.2   Data processing

The data were afterwards collected, observed and manipulated with the TLS, and finally exported from *Riscan_Pro*. The x, y, z and intensity data have been exported and a *.txt file created. This file were processed with *Matlab* software and run with a script called *lasergap.m* which was implemented just to calculate the hits values from the scan and the scan model. With this script, each datum was run with *lasergap* ('*scan1.txt*') where the word under brackets means the data that we wanted to calculate. Afterwards, further information, like the resolution in *theta* and *phi* angle − start and stop theta angle − had to be inserted into Matlab software in order to obtain the hits values of the scan model. Once the process ended, the obtained results consisted in 18 values of hits both for the scan and the scan model. The resulted data were copied into an Excel sheet in order to be further manipulated and finally the gap fraction achieved: the hits values of scan and scan model were kept separated and then the results of the gap fraction were represented in a chart.

The pictures collected by the camera were photos with 300 x 2000 of resolution. In order to process the photo with the grid of 90 degrees in the Gap Light Analyzer, first was processed with Paint Shop Pro software, then pasted in a big frame and finally enlarged to 4600 x 3600 square.

Figure 4. First field work with the laser scanner and Figure 5. The second field work in the afternoon
the camera

Figure 6. Measurements with the laser scanner in different positions

Figure 7. The steps to get a scan
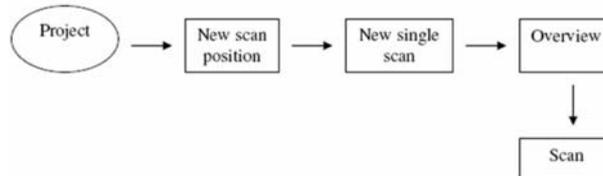
Figure 8. The camera at two different positions
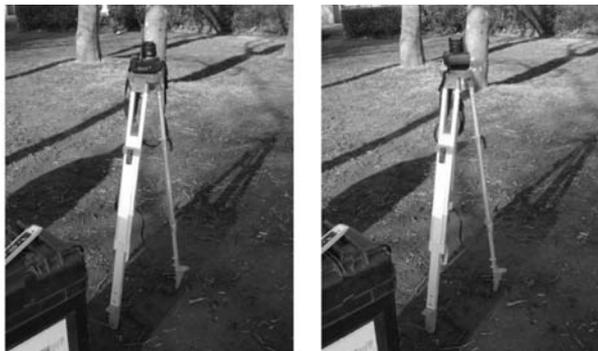
The first step was the image registration: the process by which the user identifies the geographic orientation and circular extent of the hemispherical image. In order to register an image, two control points on the image must be identified. The first point is located as initial point in GLA and it determines the geographic orientation of the image. The second point is located at an opposite azimuth (e.g. if the initial point is 0 degrees north, the second point will be 180 degrees south) and marks the circular extent of the image. When the registration is ended, the photo was cropped and two identical images were then created. The picture on the left was the registered image and the one on the right is the working image. Thanks to the overlay Sky-Region Grid, a vector grid can overlaid so that the hemispherical photo is split into discrete azimuth-by-zenith regions on the basis of equal-angular divisions of the sky.

Afterwards, the configuration containing the input data such as site location, was edited, saved or loaded. Over the white section of the photo, a mask was then created on the basis of the shape of the selected region and rectangle. This mask was then filled through the colour fill tool. After this procedure, the image classification was processed through the separation of pixels within the image array into sky and non-sky classes; for this purpose the Threshold function has been used.

The final step in the image analysis processing was the generation of output results. The function Plot Gap Fraction was used in the main menu Utilities and a graphic containing these data was automatically created (see Figure 9).

Figure 9. Showing the results of the threshold.
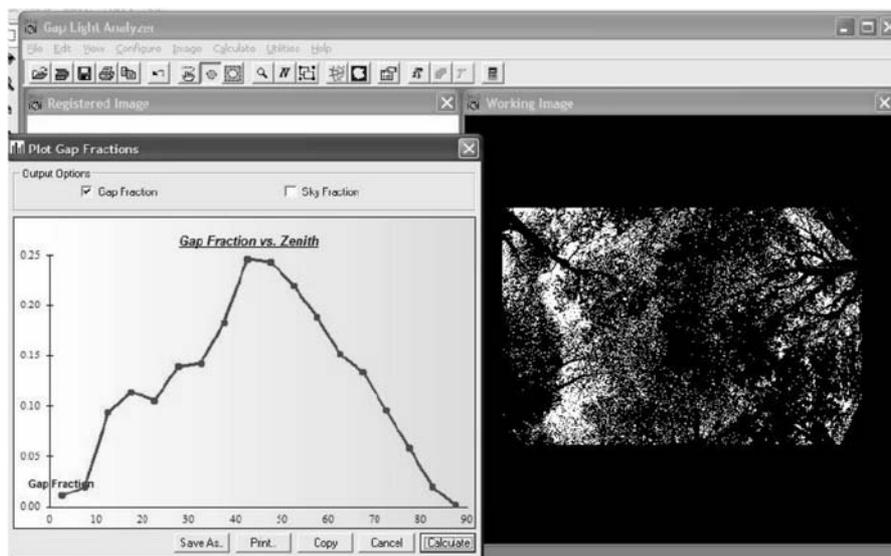
Table 1. GAP Fraction Tree_20061117 Project – 17th November, 2006

POSITION 1	POSITION 2
– OVERVIEW 1 Resolution 0.396 deg. – SCAN 1 Resolution 0.108 deg. Last Target	– OVERVIEW 1 Resolution 0.396 deg. – SCAN 1 Resolution 0.108 deg. Last Target

The following Figures, from the TLS and the hemispherical photos, are to compare: they are both taken on the same day, hour and position. Then the graphs may be seen with the average gap fraction data between the two positions using both techniques.

Figure 10. Position 1 Scan 1 – Tree_20061117 Project
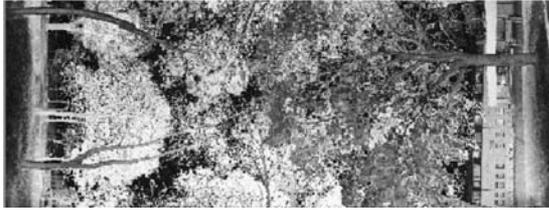
Figure 13. Position 2 Scan 2 – Tree_20061117 Project
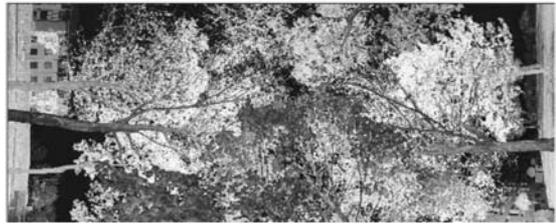
Figure 11. Position 1 Hemispherical photo 0098 – Tree_20061117 Project

Figure 14. Position 2 Photo hemispherical 0100 – Tree_20061117 Project

Figure 12. Gap Fraction from the TLS – Position 1 Scan 1 –Tree Project 17/11/2007
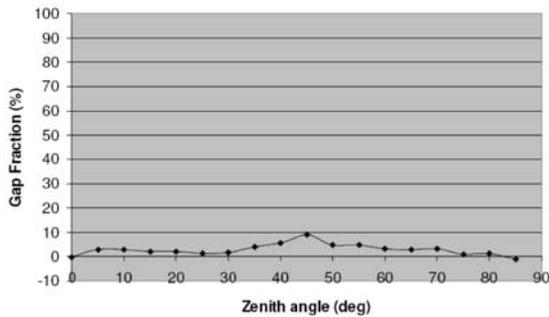
Figure 15. Gap Fraction from the TLS – Position 2 Scan 2 –Tree Project 17/11/2006
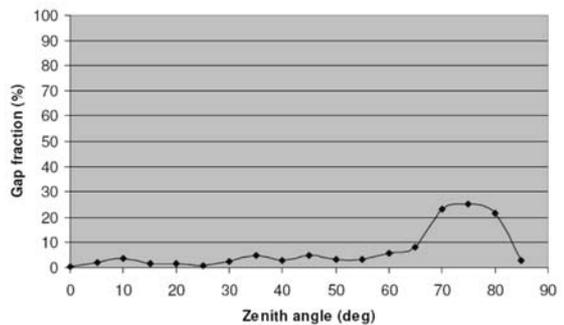
Figure 16. Average Gap Fraction from the TLS and the hemispherical photo – Position 1 and 2-Tree Project 17/11/2006
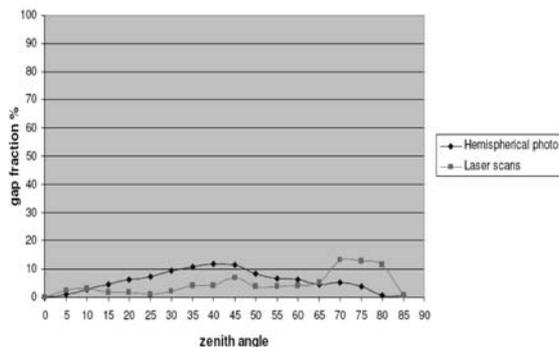
Table 2. GAP FRACTION – TREE_20070223 PROJECT – 23rd, February, 2007

POSITION 1	POSITION 2
–OVERVIEW 1: Resolution 0.396 deg. –SCAN 1: Resolution 0.108 deg. Last Target	–OVERVIEW 1: Resolution 0.396 deg. –SCAN 1: Resolution 0.072 deg. Last Target
–OVERVIEW 2: Resolution 0.396 deg. –SCAN 2: Resolution 0.108 deg. First Target	–OVERVIEW 2: Resolution 0.396 deg. –SCAN 2: Resolution 0.072 deg. Last Target
–OVERVIEW 3: Resolution 0.396 deg. –SCAN 3: Resolution 0.108 deg. First Last Target	–OVERVIEW 3: Resolution 0.396 deg. –SCAN 3: Resolution 0.072 deg. Last Target
–OVERVIEW 4: Resolution 0.396 deg. –SCAN 4: Resolution 0.072 deg. Last Target	–OVERVIEW 4: Resolution 0.396 deg. – SCAN 4: Resolution 0.108 deg. Last Target
–OVERVIEW 5: Resolution 0.396 deg. –SCAN 5: Resolution 0.072 deg. Last Target	

Figure 17. Position 1 Scan 1 Resolution 0.108 deg. Last target
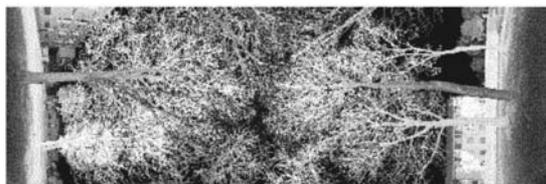
Figure 19. Position 1 Scan 2 Resolution 0.108 deg. First target
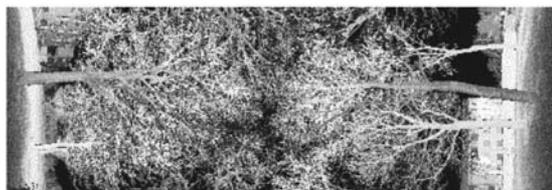
Figure 18. Graph corresponding to the Gap Fraction from the TLS – Position 1 Scan1 Tree Project 23/02/2007
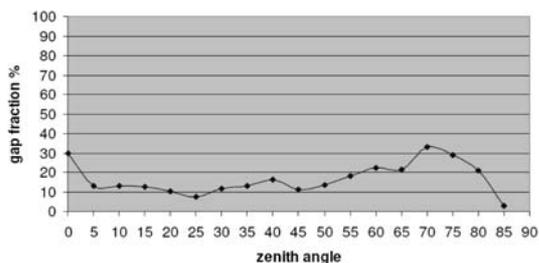
Figure 20. Graph corresponding to the Gap Fraction from the TLS – Position 1 Scan2 Tree Project 23/02/2007
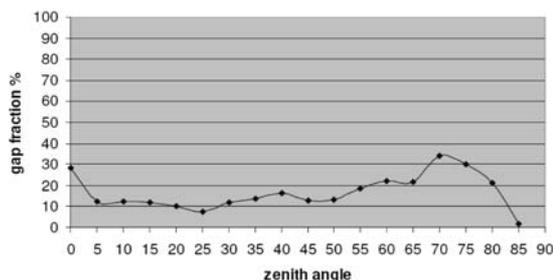
Figure 21. Position 1 Scan 3. Resolution 0.108 deg. First Last Target
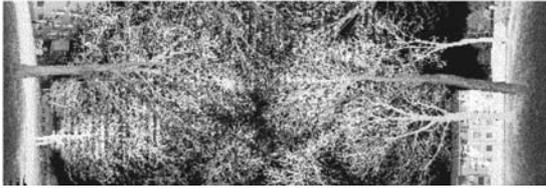
Figure 23. Position 1 Scan 4. Resolution 0.072 deg. Last target
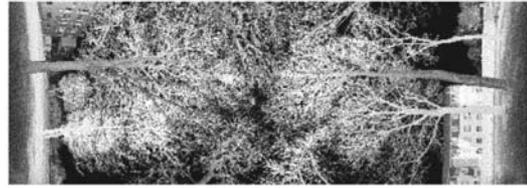
Figure 22. Graph corresponding to the Gap Fraction from the TLS – Position 1 Scan3 Tree Project 23/02/2007
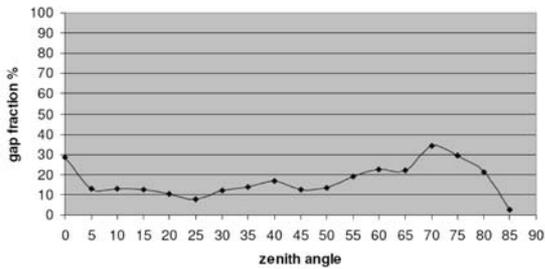
Figure 24. Graph corresponding to the Gap Fraction from the TLS – Position 1 Scan 4 Tree Project 23/02/2007
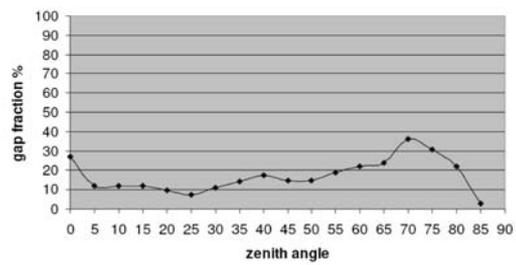

Figure 25. Position 1 Scan 5. Resolution 0.072 deg. Last target
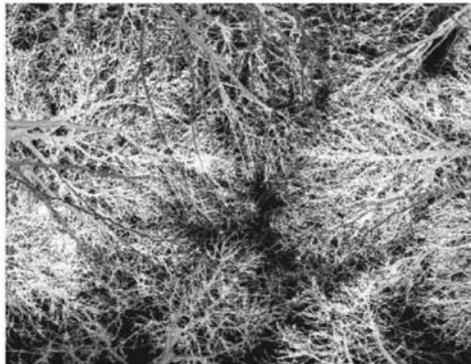
Figure 26. Graph corresponding to the Gap Fraction from the TLS – Position 1 Scan 5 Tree Project 23/02/2007
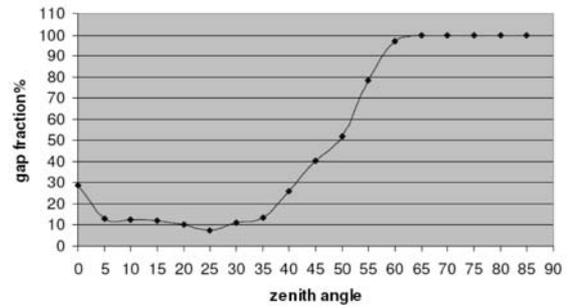
Figure 27. Position 1 Photo hemispherical 0507 – Tree_20060223 Project

Figure 28. Showing the results of the threshold
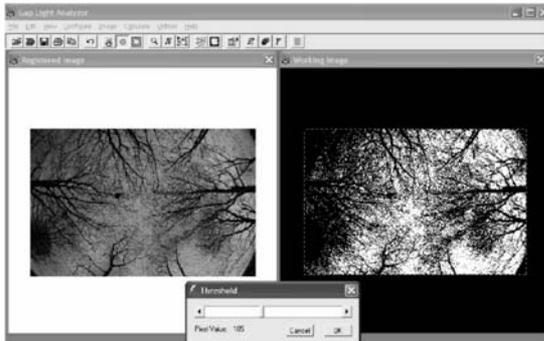
Figure 29. Graphs with the results of the gap fraction vs. zenith angle
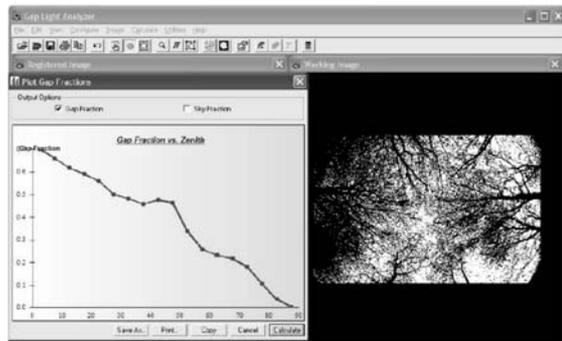
Figure 30. Position 2 Scan 1. Resolution 0.072 deg. Last target
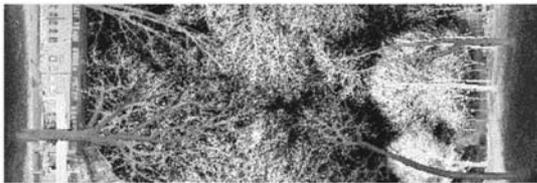
Figure 32. Position 2 Scan 2 Resolution 0.072 deg. Last target
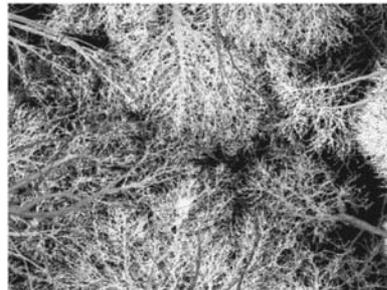
Figure 31 − Graph corresponding to the Gap Fraction from the TLS − Position 2 Scan 1 Tree Project 23/02/2007
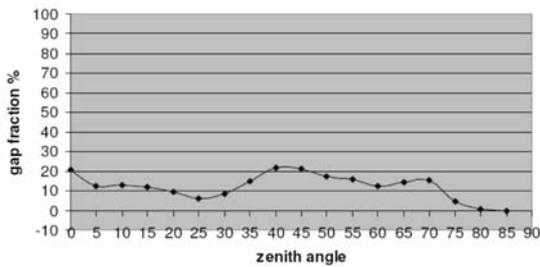
Figure 33. Graph corresponding to the Gap Fraction from the TLS − Position 2 Scan 2 Tree Project 23/02/2007
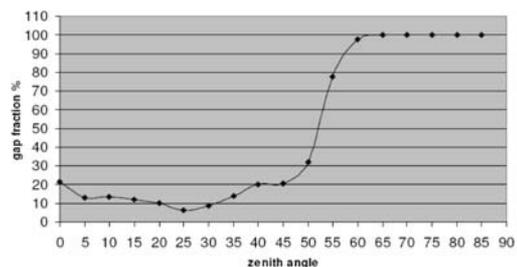
Figure 34. Position 2 Photo hemispherical 0510 − Tree_20060223 Project

Figure 35. Position 2 Scan 3 Resolution 0.072 deg. Last target
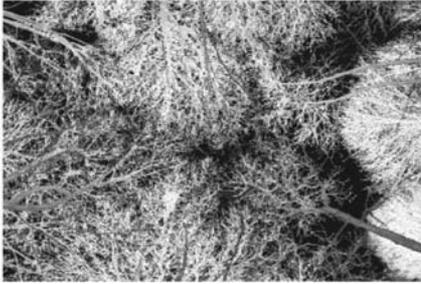
Figure 37. Position Scan 4 Resolution 0.108 deg. Last target
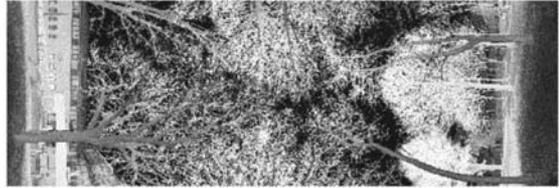
Figure 36. Graph corresponding to the Gap Fraction from the TLS – Position 2 Scan 3 Tree Project 23/02/2007
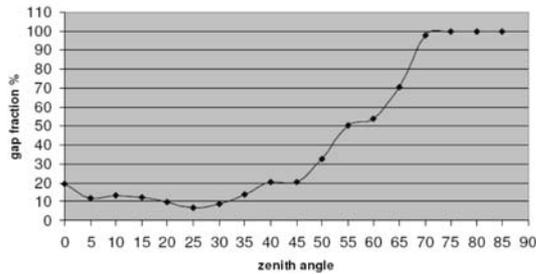
Figure 38. Graph corresponding to the Gap raction from the TLS – Position 2 Scan 4 Tree Project 23/02/2007
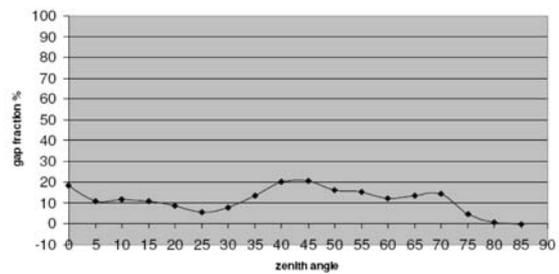

Figure 39. Showing the results of the threshold
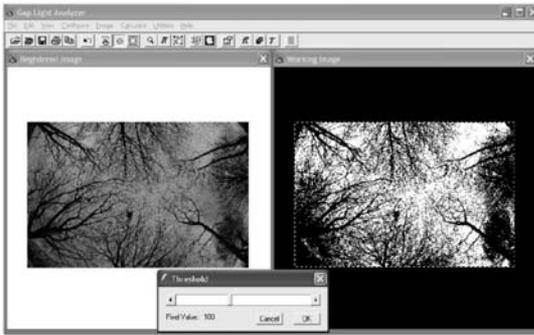
Figure 40. Graphs with the results of the gap fraction vs. zenith angle
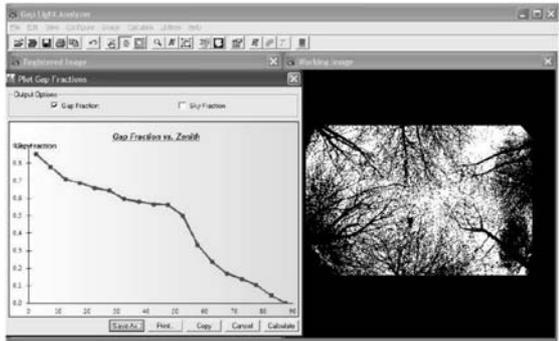

Figure 41. Average Gap Fraction from the 0TLS and the hemispherical photo – Position 1 and 2– Tree_20070223 Project
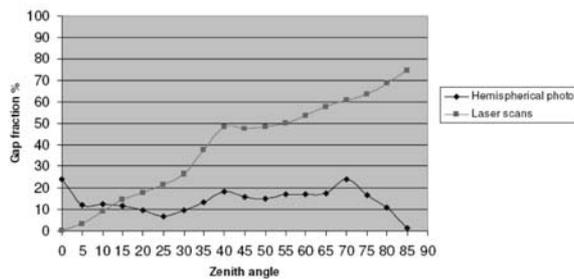
4. Conclusion

The results of this experiment highlight the potential of TLS for measuring the 3d structure of forest canopies. The comparison of the results between the gap fractions, determined from the hemispherical photography and from the laser scanner, showed some differences. The graphics showed that the hemispherical photography indicates a gap fraction percentage higher than the laser scanner and the difference can be also noticed looking at the figure from the laser scanner and the hemispherical photo. These differences may be due to the high resolution in the photograph, or errors related to the manual threshold of the digital image. Some errors might occur in the laser scanner data registration due to an underestimation of vegetation cover: probably for the fine structure of the tree or the low resolution of the image. Moreover, differences in tree height, canopy cover and laser scanner characteristics may also explain these results. On the other hand, the results of TLS data, taken with different target selection: first last, first and last return data, were similar. Referring to this, we can assess that TLS underestimated gap fraction can be compared to hemispherical photography. However, we keep on working in this project in order to achieve more details concerning with the effectiveness and accuracy of these tree canopy parameters measurement techniques.

5. Other Parallel Works

5.1 Calibration of fisheye lens

The calibration of the fisheye lens referred to the document «A simple method to calibrate hemispherical photographs» (Baret undated). All the steps, in this paper further explained were followed up.

First, the optical centre was characterized and therefore three small holes were drilled in the cap of the fisheye lens and also photographs were taken from twelve different positions (see Figure 42).

The code automatically computed the coordinates of the actual optical centre (see Figure 43).

The second step was the characterization of the projection function. In order to get the expected results, within a 50x50 cm frame, a 30x30 cm square was cut on the centre of several photographs. The problem at this stage was that, at the first attempts, the angle calculated by the code did not reach 90 degrees of value. The experiment was carried out taking into account different variables. In order to obtain the correct figure with the 90 degrees angle, the code was run with various data of photographs taken at different distances and ways. The variations were carried out as follows:

First, the photos were taken in a straight way at two distances (see Figure 44), although not all the centimetres could be seen in the photo. When the codes were run with the data coming from these photos, the figures could not show all the 90 degrees angle, (only from 65 to 70 degrees – Figure 45).

In order to get the 90 degrees of angle, the square was moved so that the photos could be taken at two distances. Again all the centimetres could not be seen in the photos and the obtained results were not as expected (Figure 46 and 47).

Finally, the photos were taken with the rotate camera in the two directions (Figure 48 and 49) and all the centimetres of the ruler could be seen.

Then the photos have been the rotated of 33.6196 degrees and then data and entered into the code. Consistently, the photo was 3613x3331 pixels bigger than the original one and the optical centre had to be changed in order to run the new code (1806, 1665) (see Figure 50 and 51).

Although new data were entered in the code, the 90 degrees angle still was not obtained. To solve this problem the code was filled with all the centimetres that could be seen in the in-

Figure 42. Twelve photos showing different positions of the three holes drilled on the cap of the fisheye lens
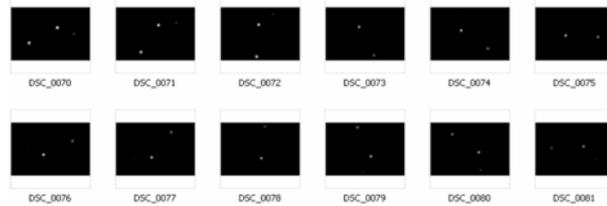

Figure 43. Output of the code 'hemis_centre.m' showing the adjustment of the circles to the holes positions in the case of three holes. The actual optical centre is shown by the cross and the mean coordinates are indicated in the lower left corner
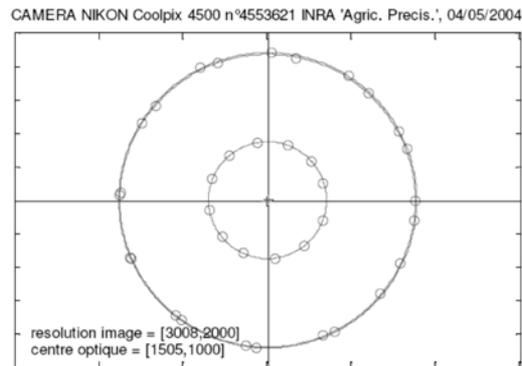

Figure 44. The nearest photo taken in a straight way   Figure 45. The farthest photo taken in a straight way
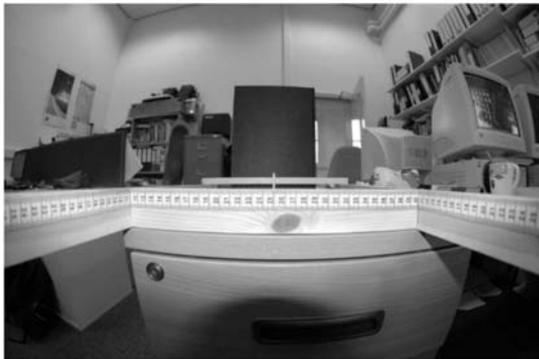
clined photo instead of the eight centimetres as suggested by the referred paper. Fortunately, when the two new codes were run, one corresponding to the nearest photo and the other to the farthest one, figures with the 85 degrees were obtained (Figure 52 and 53)

In order to fulfil the requirements of the code all these parameter were measured: the optical centre, a fixed direction on the left lateral ruler, on the right lateral ruler and the perpendicular ruler. Firstly, these values were measured for the nearest photo; the x values and the centimetres values were taken for each fixed direction. Then the farthest photo was examined to determine in which centimetre the x values were located respecting to the nearest photo. Secondly, the x values were measured in relation to each centimetre of the perpendicular ruler,

Figure 46. The nearest photo taken with the inclination square
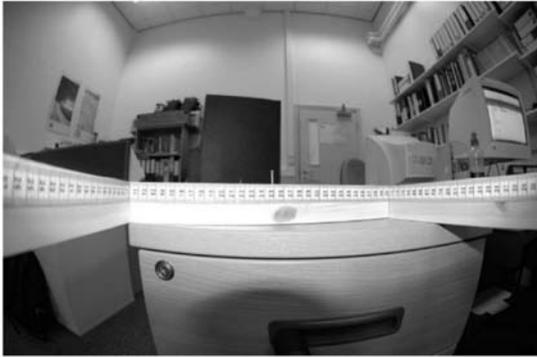
Figure 47. The farthest photo taken with the inclination square

Figure 48. The nearest photo taken with rotate camera

Figure 49. The farther photo taken with rotate camera

Figure 50. The nearest photo rotate in an angle of 33.6196 degrees
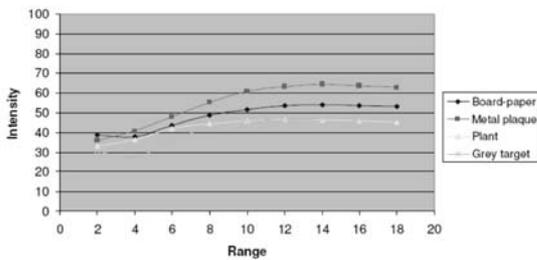
Figure 51. The farthest photo rotate in an angle of 33.6196 degrees

Figure 52. Showing the projection function with the angle of 85 degrees for the nearest photo
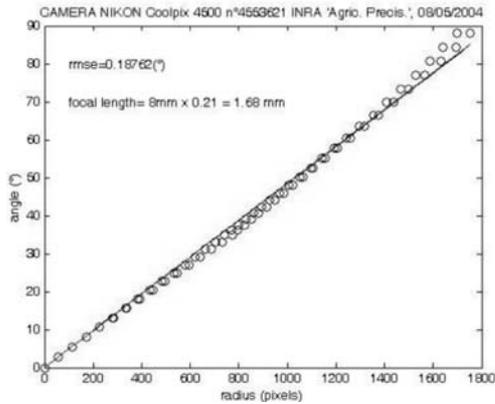
Figure 53. Showing the projection function with the angle of 85 degrees for the farther photo
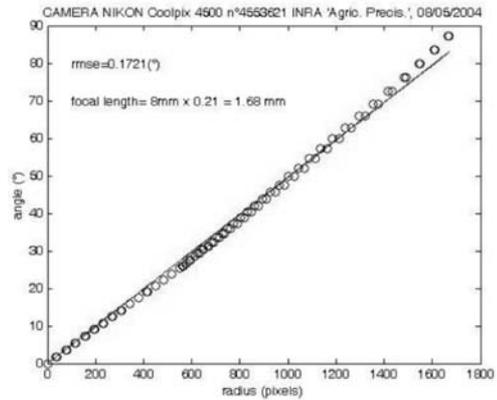
Figure 54. The TLS in front of the grey target

the left lateral ruler and the right lateral ruler. Finally, the two codes were run with the data that were taken, one for the nearest photo and the second for the farthest one.

Another variation was to measure the distance between the nail and the optical centre of the camera with a ruler. The optical centre of the fisheye lens was considered on the gold line that surrounded it. Then this distance (H) was inserted into the Matlab code. Then, both the code results, the measured distance and the distance that the Matlab assessed were compared. It was possible to observe that good results were obtained with both the two alternatives. Although Baret's work indicated only the single eight centimetres, I inserted into the code all the x values deriving from the centimetres that could be observed in the photo.

After several alternatives, we could state that in order to obtain reliable results in the calibration of fisheye lens, it is necessary to rotate the camera when the photo is taken. Only in this case the 90 degrees angle, required to fulfil, together with the x values, all the visible centimetres, can be achieved.

5.2. Intensity

The first experiment concerning with the intensity was carried out on 10th, January, 2007 and was named «Peel corridor» project. A grey target with known reflectance was put on a table in the Peel Corridor.

In front of the laser scanner, the grey target was scanned at different distances and then moved each two meters for sixteen meters. Eight scans were then done from the end of the corridor:

–OVERVIEW 1 (two meters)	–OVERVIEW 5 (ten meters)
–SCAN 1	–SCAN 5
–OVERVIEW 2 (four meters)	–OVERVIEW 6 (twelve meters)
–SCAN 2	–SCAN 6
–OVERVIEW 3 (six meters)	–OVERVIEW 7 (fourteen meters)
–SCAN 3	–SCAN 7
–OVERVIEW 4 (eight meters)	–OVERVIEW 8 (eighteen meters)
–SCAN 4	–SCAN 8

The overview resolution was 0.396 degrees and the scan resolution was in Theta angle 0.072 deg. and in Phi angle 0.018 deg. With respect to target selection, it was the measurement of the Last Target.

The next step was the calculation of the intensity of the grey target and the background wall of the corridor. This computation was made with Riscan_Pro v 1.4.1, a 2D view was created and a frame over the grey target was made. Then, the cursor was placed on the frame, clicked the right bottom and clicked again in 'Calc StdDev of selection rectangle', and a table like the one shown in Figure 55 came up.

The step before was done for each scan and the data were copied and pasted into Excel in order to process chart showing the trend of the intensity percentage. (see Figure 56)

The same calculation was done with the background wall of the corridor and the data achieved have been added into the same chart for a comparing analysis of the trends (see Figure 57).

The second experiment on the intensity was done on 9th, February, 2007 and the project was named «Peel corridor_09-02-07». In this experiment, a board, a metal plaque and a plant were put at the end of the corridor and the laser scanner was moved each two meters (see Figure 58).

Ten scans had been done until the laser scanner was at a distance of two metres from the three objects:

–OVERVIEW 1 (20 meters)	–OVERVIEW 6 (10 meters)
–SCAN 1	–SCAN 6
–OVERVIEW 2 (18 meters)	–OVERVIEW 7 (8 meters)
–SCAN 2	–SCAN 7
–OVERVIEW 3 (16 meters)	–OVERVIEW 8 (6 meters)
–SCAN 3	–SCAN 8
–OVERVIEW 4 (14 meters)	–OVERVIEW 9 (4 meters)
–SCAN 4	–SCAN 9
–OVERVIEW 5 (12 meters)	–OVERVIEW 10 (2 meters)
–SCAN 5	–SCAN 10

The resolution of the overviews was 0.396 degrees and the resolution of the scans was 0.072 degrees, the highest one. Then the reflectivity of these objects was measured with a radiometer (Figure 59).

The following graphics show the intensity of the three objects in this experiment and the grey target from the previous experiment was added in order to compare the results (Figure 60).

The results that we achieved were not the ones we expected. In theory, the intensity values should decrease with the range.

However, we can assess that no return of data occurred since the distance of measurements between the laser scanner and the objects was too short, as explained in the figure 61:

Figure 55. The table with different data
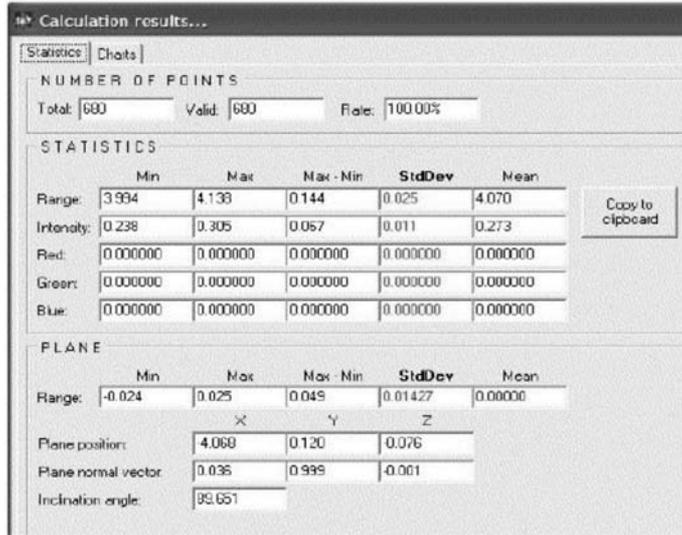
Figure 56. Intensity of the grey target
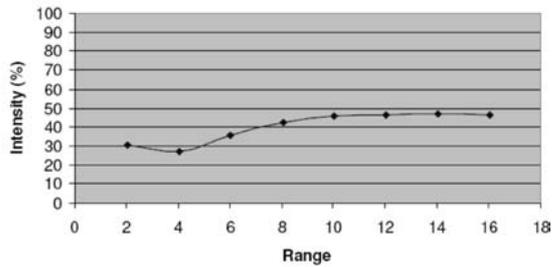
Figure 57. Comparison between the grey target and the background wall intensity.
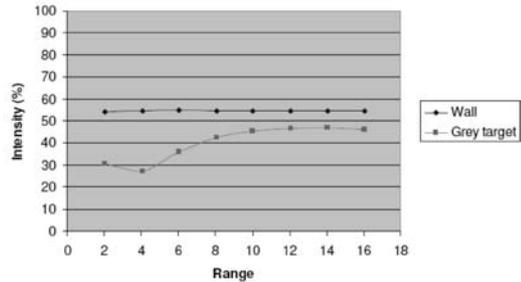

Figure 58. The TLS in front of three different target

Figure 59. Showing the radiometer

Figure 60. The intensity from both experiments
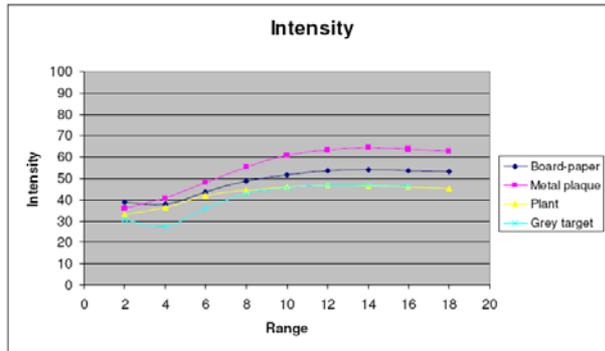
Figure 61. Distance measurements between laser scanner and objects.
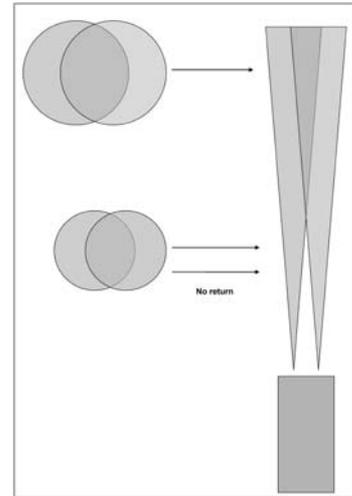
References

Baret F. (undated). A simple method to calibrate hemispherical photographs. INRA-CSE, Site Agroparc, 84914 Avignon, Cedex 09, France, baret@avignon.inra.fr

Baret F., Weiss M. (2004). CAN_EYE, Processing digital photographs for canopy structure characterization. Tutorial. Avignon.

Blennow K. (1995) Sky view factors from high resolution scanned ®sh–eye lens photographic negatives. *J Atmos Oceanic Technol*, 12: 1357-1362.

Bonan G.B. (1996). A Land Surface Model (LSM version 1.0) for ecological, hydrological, and atmospheric studies: Technical Description and user Vs guide, NCAR/TN-417 +STR, pp. 88-102.

Chason J.W., Baldocchi D.D. and Huston M.A. (1991). Comparison of direct and indirect methods for estimating conifer forest canopy leaf area. *Agric. For. Meteorol.* 57: 107–128.

Chen J.M. and Black T.A. (1992). Defining leaf area index for non–flat leaves. *Plant, Cell and Environment*, 15: 421-429.

Danson F.M., Hetherington D., Morsdorf F., Koetz B. and Allogower B. (2006). *Forest Canopy Gap Fraction from Terrestrial Laser Scanning*. Centre for Environmental Systems Research, University of Salford, Manchester and Department of Geography, University of Zurich, Switzerland.

Frazer G.W., Canham C.D. and Lertzman K.P. (1999). *Gap Light Analyzer (GLA), Version 2.0: Imaging software to extract canopy structure and gap light transmission indices from true-colour fisheye photographs, users manual and program documentation*. Simon Fraser University, Burnaby, British Columbia, Canada, and the Institute of Ecosystem Studies, Millbrook, New York.

Hetherington D., Heritage G.L., Milan D.J. (2005). Reach scale sub-bar dynamics elucidated through oblique lidar survey. In: *International Association of Hydrological Scientists Red Book Publication*. IAHS Publication 291: 278–284.

Jonckheere I., Fleck S., Nackaerts K., Muys B., Coppin P., Weiss M. and Baret F., (2004). Review of methods for in situ leaf area index determination –Part I. Theories, sensors and hemispherical photography. *Agricultural and Forest Meteorology*, 121: 19-5.

RIEGL, Laser measurement systems, technical documentation and users instructions, Austria, 2006. <http://www.riegl.com/>.

Weiss M., Baret F., Smith G.J., Jonckheere I. and Coppin P., (2004) Review of methods for in situ leaf area index (LAI) determination Part II. Estimation of LAI, errors and sampling. *Agricultural and Forest Meteorology*, 121: 37-53.

IMPACTS OF CLIMATE CHANGE ON SOIL EROSION WITHIN A SPECIFIC AREA INVESTIGATED BY THE CIOMTA PROJECT

Ludmilla Grasso
Facultad de Ingenieria, geoecología y medio Ambiente
Universidad Católica de Santa Fè
Argentina

Tutors: Prof. M. Bindi and Dr. M. Moriondo
Department of Agronomy and Land Management
Università degli Studi di Firenze
Italy

1. Introduction

Climate changes are a serious issue. They have always succeeded throughout history but now the alarm concerns with the rate of the changes.

Climate changes cause many impacts all over the planet subsystems. Some of them can be seen nowadays, for example formerly dry areas are now becoming wetter and more arid, and temperature is increasing all around the world. These events have their consequence in land use changes and population settlements. Animals and plants need to adapt themselves to the new environment situation; otherwise they are domed to extinction. For that reason, it is important to study the impacts of climate changes in order to minimize their negative effects.

This research attempts to analyze the impact of such changes on soil erosion. Soil is an important system because it sustains ecosystem biodiversity.

Soil erosion is a serious threat since can cause both economic and environmental damage as consequences. The causes of this phenomenon are various: unsustainable use of land and protective layer reduction due to crop harvesting and climate change.

The agricultural activity developed on Argentine soils is increasing at large scale, and in many areas the use of the land is changing. Unfortunately, in most of these areas the use of the land is often no sustainable. The quali–quantitative soil erosion evaluation, both in the present and in the future, is necessary for land planning. By these means, it is possible to become aware of the soil importance and then adopt the right conservative measures.

Through USLE model application we tried to determine the soil loss in the present time and its variations according to climate changes in various future scenarios. We worked with different hypotheses of land use in order to assess erosion values changes. The study was carried out within a CIOMTA (Centro de Investigación, Observación y Monitoreo Territorial y Ambiental; Santa Fe, Argentina) testing area.

2. Materials and method

The study area is located in the northern of Argentina, where two different zones can be distinguished: an eastern and western one. The necessary ancillary data were provided by the CIOMTA centre.

The eastern zone is almost 4 million hectares wide and includes the whole province of Misiones and the north-eastern part of Corrientes Province. The height above sea level varies from 50 m AMSL in Corrientes province to 800 m AMSL in the north of Misiones. The

land morphology is characterised by moderate slopes (which vary from 0° to 10° in isolated plots) all over the area.

The Western zone (17 million hectares) includes part of the following provinces: western of Santiago del Estero, eastern of Catamarca, almost all Tucumán, central Salta and southern of Jujuy. The height above sea level varies from 90 m AMSL in the eastern to 4600 m AMSL in the western, while land slope oscillates from 0 to 45 degrees.

In order to evaluate the soil water erosion in the study area, the USLE (Universal Soil Loss Equation) model was applied. Other information levels were integrated using the Geographic Information System software ESRI ArcView 3.2.

The USLE is a quantitative empiric model which can predict soil loss, such as the annual soil erosion (only surface and gully one) during long periods and considering various variables. The negative aspects of this model consist both in the extremely generalization of the problem within soil erosion assessment and in the lack of sediment deposition data within the algorithm. According to USLE, soil erosion is determined by environmental characteristics (precipitation erosivity, soil erodibility, slope, etc.), and human activities (management and land use, conservation practices, etc).

The geo-topographic base was obtained using the 830 x 830 meters grid of resolution Digital Elevation Model (DEM) (see Figure 1).

2.1   USLE Model Application

The same model was applied both to the eastern and western study areas. The general formula that has been applied is the following: A = R K L S C P

Where:

A = soil loss per area unit and time.

R = Precipitation and run off erosivity factor.

K = Erodibility soil factor, which reflects the soil loss per each R unit, and which corresponds to the soil susceptibility or resistance to erosion. This datum is measured within a standard land of 22,13 m wide, with 9% of land slope, and is applied slope-wise and during fallow periods.

L = Length factor: relationship between soil loss and length of the study area within a standard land of 22.13 m wide.

S = Slope factor, relationship between soil loss and land slope of the study area with a 9% of slope.

C = Crop management factor: relationship between crop and management study land with another one. It is applied in fallow periods and in land without vegetation.

P = Conservation practices factor: relationship between soil loss within a specific land portion and a cropped and tilled land portion without any conservation practices (plowed slope-wise)

2.1.1 Calculation of the Factors

2.1.1.1 R factor

The erosivity factor can be calculated applying the Erosion Index (EI30). This index is the product of the sum of each storm (E) kinetic energy (expressed in J/m2), and the maximum amount of precipitation registered in 30 minutes (I30), expressed in mm/h. The R factor can be calculated monthly, yearly or over a mean of more than a year.

In order to obtain this factor, the synthetic data series, representing the present climatic scenario and two hypothetic future scenarios made by the CIOMTA, were used. To obtain such data series, the CIOMTA applied particular change indexes to each statistical character-

Figure 1 – DEM of the Study area – Source: CIOMTA. Map performed with topographic level curves, which corresponds to a 1:250.000 scale in cartography, and belongs to the SIG250 of the IGM (Instituto Geográfico Militar)
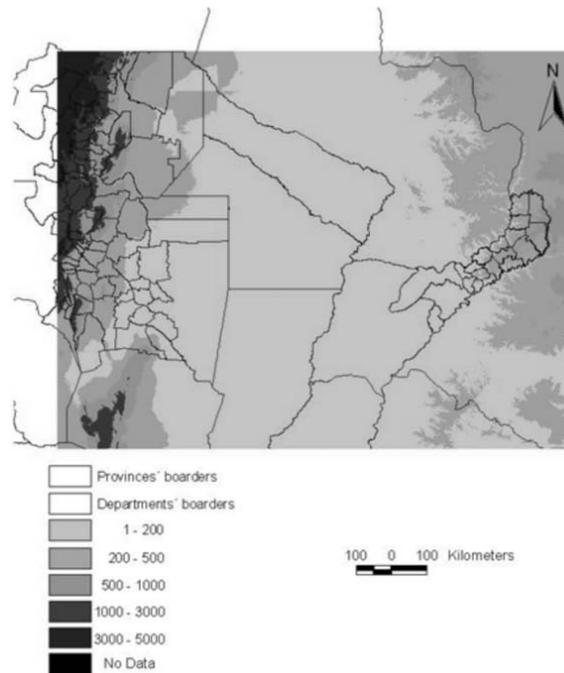
istic of measured points (obtained from meteorological stations). Such indexes were gathered from experimental data with a HADCM3 (developed by the Hadley Centre and the UK Meteorology Office) general circulation model.

In order to achieve this 'regionalization', the CIOMTA applied a daily-scale stochastic weather generator (LARS-WG). Through this program it is possible to obtain a statistical parameter file for each station (from actual series), and to print changes in mean values and variability. Such change indexes were also obtained by using LARS but with the global model data, whose grid matches each particular station.

Finally, the CIOMTA used LARS to generate the synthetic series by using each site's statistical parameters, which were affected by the changes projected by the global model.

Two scenarios (A2 and B2) were used and a range of 30 years was taken into account for both of them.

Actual Synthetic data-set:
Present Period: (1971-2000)
Scenario A2:
    A2_2: (2030-2059)
    A2_3: (2070-2099)
Scenario B2:
    B2_2: (2030-2059)
    B2_3: (2070-2099)

Each scenario considered different aspects such as world population growth, global economy increase, technology development, limits within the use of energetic resources of fossil fuels, agricultural development: all of these factors produce various greenhouse gases in the atmosphere.

The families of 'A' scenario enjoyed a high economic increase while the group of 'B' had a low economic development. According to the sample, in year 2100, the CO2 global concentration will be 120% higher than the present for the group of scenario 'A', and 100% higher for the 'B' one.

Due to the lack of hour per hour data, it was necessary to apply a substitutive formula to calculate R (Arnoldus 1980):

R = 4.17x(p2/P) − 152

Where:
p: monthly precipitation
P: annual precipitation

The p and P values were derived from meteorological stations of the National Meteorological System (SMN) and National Institute of Agricultural Technology (INTA).

For the eastern zone, four stations were available: Cerro Azul (INTA), Paso de los Libres (SMN), Iguazú Aero (SMN) y Posadas Aero (SMN).

For the western zone, there were ten: Córdoba Aero (SMN), Río Cuarto Aero (SMN), Tucumán Aero (SMN), Manfredi (INTA), Salta Aero (SMN), Villa Dolores (SMN), Faimalla (INTA), Santiago del Estero (SMN), Villa María (SMN), Pilar Obs (SMN) (see Figure 2).

Figure 2. Meterological stations of Western and Eastern areas
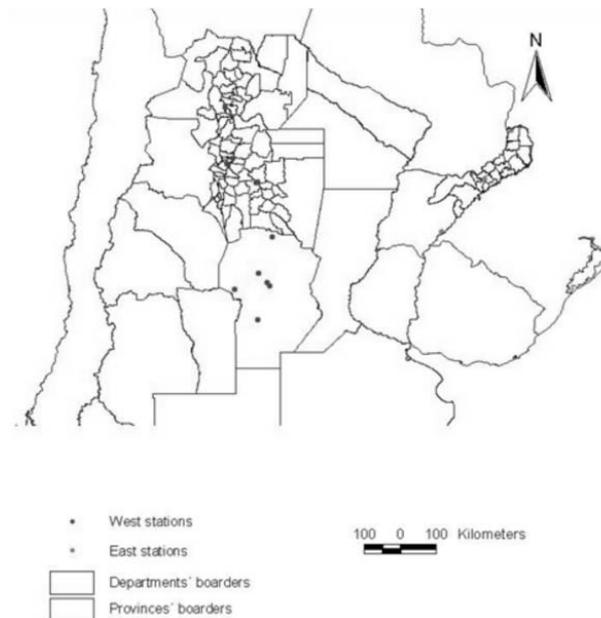
The R value of each station was interpolated for the whole area by calculating the inverse of the distance weight (IDW). With this method pondered weights can be interpolated. The result form is a linear combination of weights which are multiplied with the distances from the interpolated point. Furthermore, while the distance from the sample points to the interpolated point increases, it's weighting importance decreases. Data weights assignment is done using a distance power, which controls the weight factors level of decrease in combination with the increasing of the distance from the nodes (sampling plots).

By this means, five maps with the R value were produces: one for each scenario. If we compare all the scenarios, we can state that R values increase in the future scenarios compared to the present. It is worth mentioning that it is not possible to generalize an increase prevalence between the scenario families, since some departments showed, for the same time period, a higher R value increase in the A family, whereas some others in the B one.

2.1.1.2 K Factor

Soil erodibility (i.e. the susceptibility of soil particles to detach through rainfall and runoff events) was evaluated taking in account the CIOMTA soil map (see Figure 3). Based on the US Agricultural Research Service classification, K was an assigned value according to soil texture type, being the organic matter content of 2%.

2.1.1.3 L Factor

This factor takes into account the land length which is expressed as the distance between the point where runoff event starts and the point where sediments are deposited, due to slope decrease.

In this research the length parameter was considered as a constant of 200 meters and the formula (Giordani and Zanchi 1995) was applied to obtain L factor. According to this, soil loss per unit area increases proportionally with the land length increment, raised up through an 'm' exponent, which varies with the slope.

$$L = (l/22,13)^m$$

Figure 3. Soil map CIOMTA
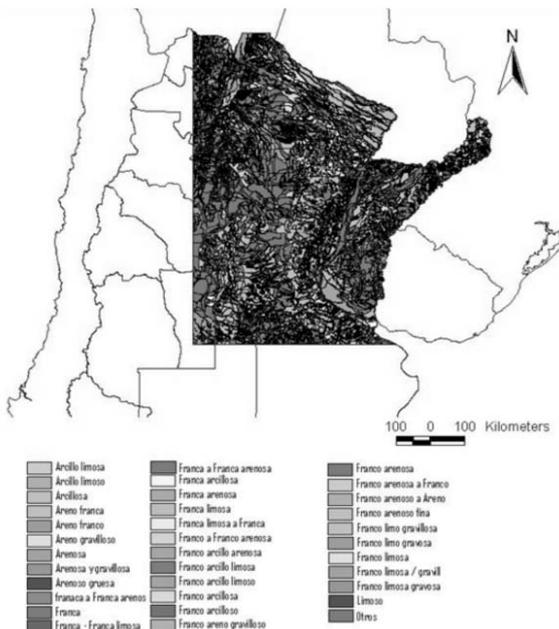
Where:

l: land length
m: coefficient which varies with the slope: 0.5 with slope of 5% or higher; 0.4 with slope be-
tween 3 and 5%; 0.3 with slope between 1 and 3%; 0.2 with slope lower than 1%.

2.1.1.4 S Factor

Slope factor. Soil loss increases with the slope because rain drops gain a higher speed with
a slope degree increment. The slope map derives form the DEM (see Figure 4) and the S value
was calculated trough the following equation (Giordani and Zanchi 1995):

$$S = 65,41 \; sen^2(a) + 4,56 \; sen(a) + 0,065$$

2.1.1.5 C Factor

The C factor considers the effects of vegetation land cover on soil erosion, and takes into
account different types of flora species, crop succession, agriculture practises and waste man-
agement which occur over the land.
This factor derives from the CIOMTA land use map, according to the classification (with
some changes) used by the CORINE program in the European Community (see Figure 5).
Then, these land uses were re-classified and different C factor values were assigned referring
to table 1 (Giordani and Zanchi 1995).
Besides, we made different hypothesis of soil use:

Figure 4 .Soil map of the study areas
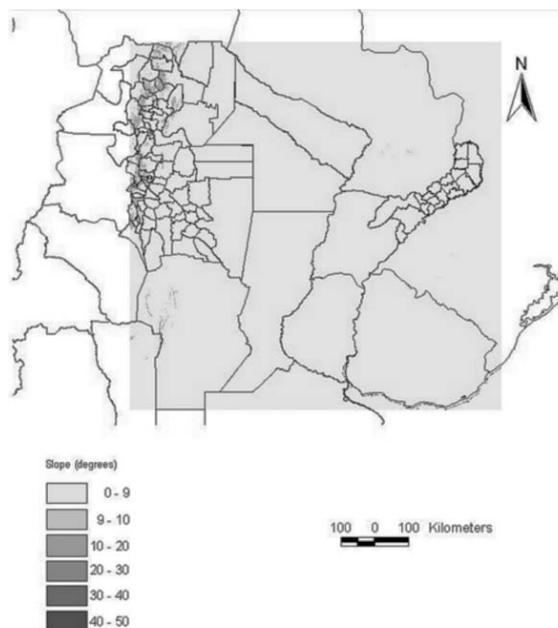
- Lands covered with high productivity of legumes and grasses (> 7 t/ha). C = 0.004
- Lands covered with moderate productivity of legumes and grasses. C = 0.01
- Lands covered with alfalfa and trefoil. C = 0.02
- Lands covered with undisturbed forest. C = 0.001

Figure 5. Land use map, CMIOTA
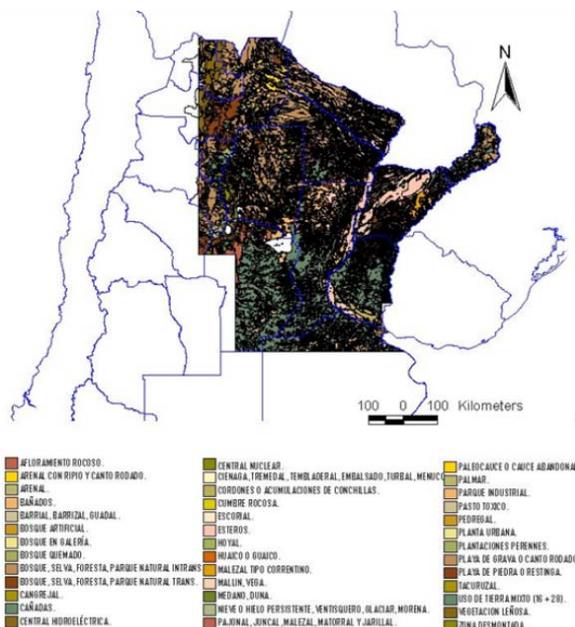
Source: CIOMTA. Land use map based on the CORINE Program classification of the European Community.

Table 1. Land cover type and factor C values assigned

		DESCRIPTION	C FACTOR VALUES
1. Natural vegetation	1. Forest	Land covered with different perennial tree species, no more than 3 or 4 meters high.	0.003
		Lands covered with different perennial tree species ,more than 3 or 4 meters high	0.003
		Arboreal and shrub-like natural vegetation on river and stream levees.	0.003
	2. Herbaceous	Low land marsh, of elongate shape, with or without water stream, and covered with wet-land typical vegetation.	0.11
		Fertile, wet and low soil, with natural herbaceous vegetation.	0.11
		Land covered with different vegetation types like pajones (Danthonia dominguensis), totoras (Thypa domininguensis), rushes, which generally grow in wet lands.	0.11
2. Agrarian vegetation	1. Herbaceous	Land covered with different crops like cereals, ranges and forestry alternated.	0.004
		Weeds growing in cracked lands constituted by clayey quagmires.	0.004
	2. Arboreal	Lands covered with artificially-planted trees, of any destination or industrial classification (fruit, yerba mate, for shade, for timber, etc.)	0.007
		Lands covered with persistent vegetation systematic plantations such as trees, yerba mate, coffee, tea and fruit, etc.	0.007

	DESCRIPTION	C FACTOR VALUES
	Lands covered with palm trees.	0.007
	Any species vegetation (tola, llareta, and so on) which allows to make fire.	0.007
3. With no erosion	Forest areas partially or totally reduced by human or natural causes	0.07
	It comprises forest areas which have been partially or totally destroyed by fire, where there are standing or fallen burnt trunks.	0.07
	Rocky composition resulting from mineral associations of different nature and hardness, as a consequence of a given geological process.	0
	Surface manifestation of strata, veins or mass of any rock type which protrudes from the land surface and which can affect relatively large areas.	0
	Sand accumulation, not always close and at sea level, due to a translation movement caused by wind action.	0
	When the sands also contain decomposition, accumulation, quarry, etc. materials.	0
	Wet and low lands which are little resistant, swampy, peaty, covered by grass, and which break down easily.	0
	Soil constituted by loose sand, whose transport conditions are enhanced with rain.	0
	Low, flat and generally wet land covered with mud, which in drought periods turns into an almost impalpable powder.	0
	Old riverbed zone semi o totally deactivated, which may have water or not under some climatic conditions, and which may be transformed into flooded and swamp areas.	0
	Water logged land whose ground is swampy, impassable and with a regular amount of water.	0
	Surface covered with natural or artificial water which comprises a large portion of land. This definition includes double-margin rivers.	0
	Water logged land which contains water all year and whose ground is generally muddy, swampy or marshy and covered with shallow waters coming from overflowed rivers, lakes or streams, or the sea.	0
	Zone built for urban purposes and destined to human activities.	0
	Coastal ranges formed by accumulation of shells as a consequence of the littoral currents.	0
	Relatively deep and large fissure produced by levigation and solar radiation.	0
	Land covered with loose rocks (of different size and composition), whose origin may vary.	0
	Persistent ice mass produced by snowdrift.	0

The difficulties met with the necessity of applying R and K factors were solved: R factor was calculated by using the empiric formula (Arnoldus 1980) validated for USA and Africa, while K factor was defined using CIOMTA soil map texture values as near as possible to the table of the texture classes, applied by the US Agricultural Research Service (1975).

3. Results

We applied the same methodology both to the eastern and western zones. First of all we made different maps for each scenario using ton per hectare annual erosion values (see Figure 6). We then decided to work at department level calculating the annual mean erosion for each one.

Figure 6. Annual erosion (tn/ha) − Western zone. Present scenario. Current soil
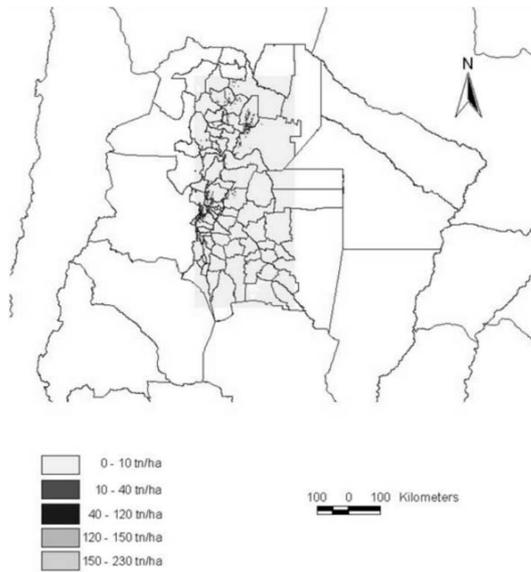
Figure 7. Average erosion for each department − Present scenario − Current soil
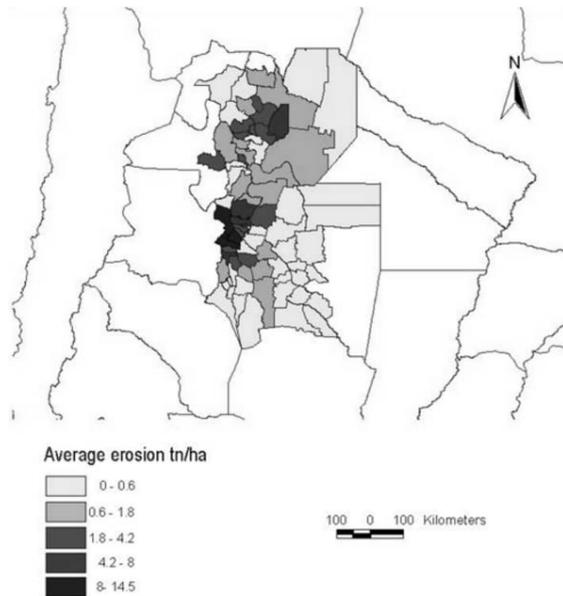
The eastern zone comprehends partially or completely 21 departments, whereas the western zone comprehends 76 ones.

3.1   Western zone

We calculated the mean annual erosion for each department for the present period (see Figure 7). The average erosion values varied from 0 to 15 tn/ha. The highest values of the departments are located in the western area where are the highest slopes. Only three departments presented values of around 15 tn/ha, and most of them showed a soil loss of less than 2 tn/ha.

In order to calculate the future soil loss with the climate change and with the same land use, the erosion percentage variation in the next (A22 and B22) and far (A23 and B23) future scenarios with respect to the present time was calculated.

Soil erosion tended to increase with time although land use conditions were the same. According to this, in the next future (2030-2059) most of the departments presented a higher soil erosion increase for 'B' scenario, whereas in the far future more pessimistic values were foreseen for the 'A' scenario.

The processed maps showed that in the near future of 'B' scenario (see Figure 8), the soil erosion will increase of the 10% in most of the departments with respect to the present, reaching up a 17% in the western and centre of the departments (Tucuman province). Meanwhile the 'A' scenario (see Figure 9), was less pessimistic, since soil erosion decreased up to 12% only in two central areas of the departments, while in the south−eastern zone it increased up to 22%, and in the other areas an increment between 5 and 15% occurs.

In the far future (2070-2099) soil erosion tends to increase even more. The 'A' scenario (see Figure 10) was more critical. The southern areas of the departments presented a soil loss variation of up to 55%, while most of the northern ones presented an increment of 20 to 30%. On

Figure 8. Average soil erosion − Percentage variation scenario B22 − current soil
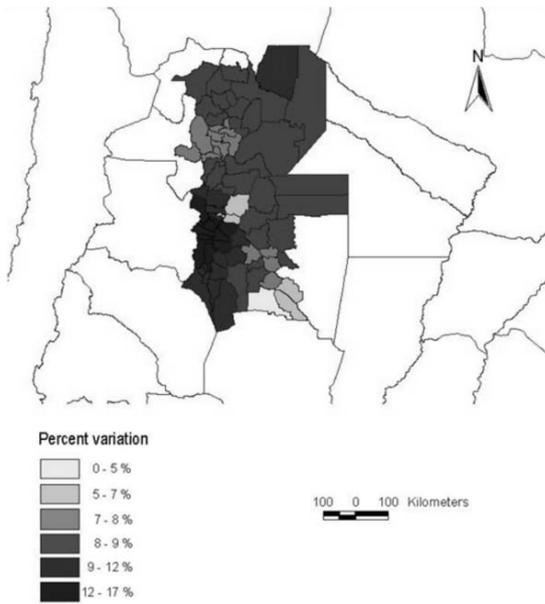
Figure 9. Average soil erosion − Percentage variation scenario A22 − current soil
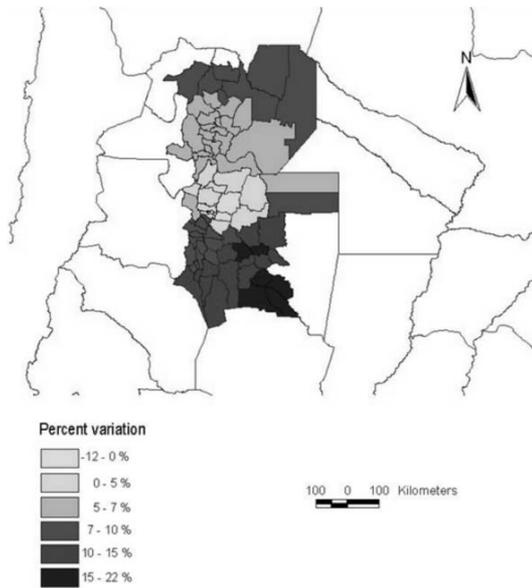
Figure 10. Average soil erosion − Percentage variation scenario A23 − Current soil
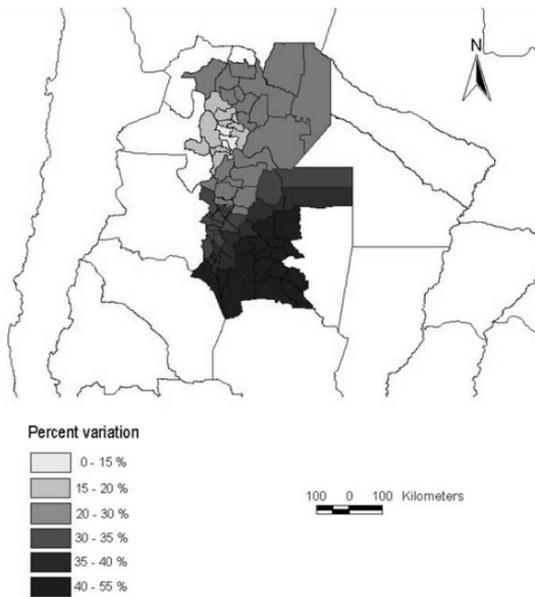
Figure 11. Average soil erosion − Percentage variation scenario B23 − Current soil
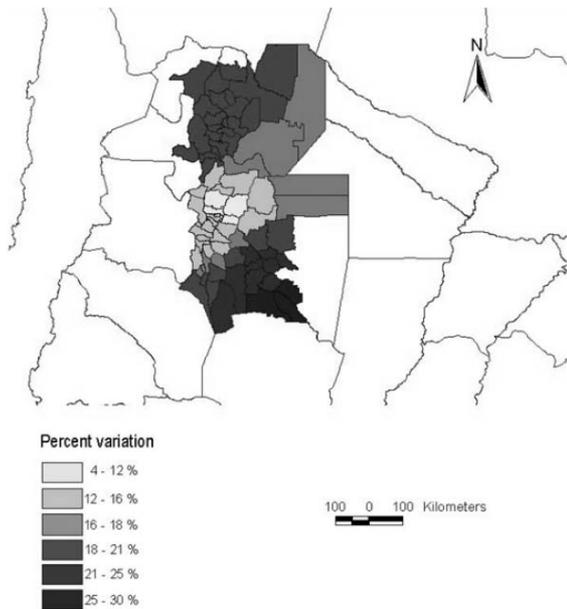
the opposite, the 'B' scenario (see Figure 11) presented values varying from 16 to 21% for the northern area of the departments, less than 15% for the centre ones, and a maximum increase of values of 30% for the southern ones.

The same percentage of variation, according to the present, was calculated taking into account the following land uses: lands covered with high productivity of legumes and grasses (> 7 t/ha), lands covered with moderate productivity of legumes and grasses, lands covered with alfalfa and trefoil, and lands covered with undisturbed forest.

According to the maps, soil erosion in forest lands tended to decrease to a large scale for all the scenarios (see Figures 12, 13, 14 and 15), while in planted with alfalfa or trefoil lands an increment of soil erosion has been observed within the whole area (see Figures 16, 17, 18 and 19).

In lands with high cropping productivity, soil erosion decreased in most of the departments and increased in only in few of them (see Figures 20, 21, 22 and 23). However, if the productivity was moderate, soil erosion increased in most of the departments and decreased in only a few ones (see Figures 20, 21, 22 and 23).

3.2   Eastern zone

Similarly to the western zone, the mean annual erosion per department was calculated for the present scenario also for the eastern zone (see Figure 24). This zone presented less soil erosion than the western one because is characterized by lower slopes. The maximum mean erosion value obtained was 1.7 tn/ha.

In order to analyse the variance with climate change, it was then calculated the erosion percentage variance for the next (A22 and B22) future scenarios and for the far (A23 and B23) future scenarios with respect to the present scenario.

Soil erosion tended to increase with time if the soil keeps the same conditions of the present. Most departments showed a high erosion increment in the next future (2030-2059) in 'B' scenario, while in the far future the highest increase was observed in 'A' scenario.

According to the resulted maps, in the far future the maximum erosion variation reached 21% in 'B' scenario, but most of the area increased between 12 and 15% (see Figure 25). The scenario 'A' is less pessimistic since the maximum variation reached a maximum of 12% in the southern and central areas, while the northern ones presented values from 5 to 8% (see Figure 26).

For the second future period (2070-2099) soil erosion tends to increase even more. The scenario 'A' presented variations from 21 to 27% in all the departments as regards to the present (see Figure 27). On the other side, 'B' scenario presented a variance from 21 to 26% in the southern and central areas of the departments, and an increment only from 9 to 15% (see Figure 28) in the northern ones.

Considering the present scenario, the same percentage of variation was calculated taking into account the following land use changes: lands covered with high productivity (more than 7 t/ha) of legumes and grasses; lands covered with moderate productivity of legumes and grasses; lands covered with alfalfa and trefoil; and lands covered with undisturbed forest.

According to the maps, we can state that:

- considering the type of scenario, if land use doesn't change, soil erosion tends to increase up to 25%.
- if high productivity cropping occurs, soil loss tends to decrease (see Figures 29, 30, 31 and 32).
- if moderate productivity cropping occurs, soil erosion increases (see Figures 33, 34, 35 and 36), since agriculture practices are not very sustainable.
- if trefoil and alfalfa are cropped as in the Eastern zone, soil erosion increases more (see Figures 37, 38, 39 and 40), an opposite trend occurs if the forest remains undisturbed (see Figures 41, 42, 43 and 44).

Figure 12. Average soil erosion − Percentage variation scenario A22 − Soil under forest undisturbed
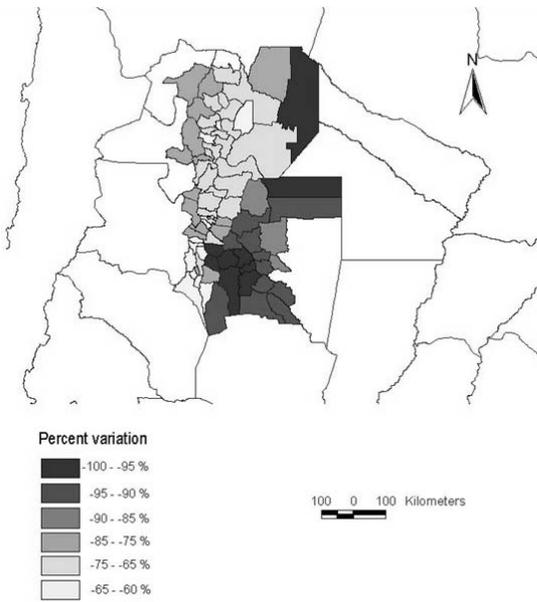

Figure 13. Average soil erosion − Percentage variation scenario A23 − Soil under forest undisturbed
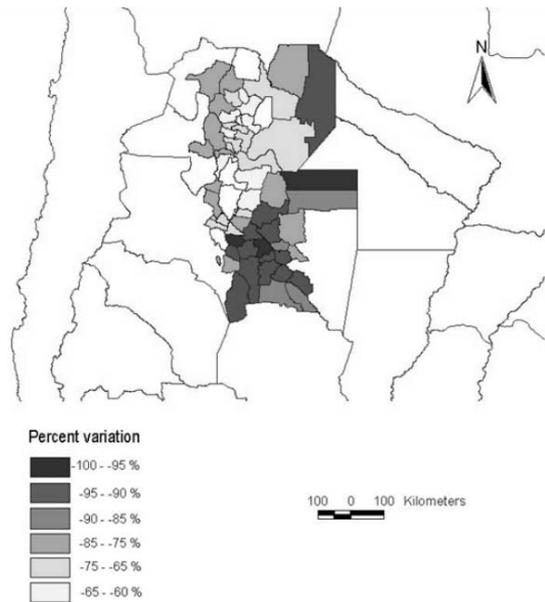

Figure 14. Average soil erosion − Percentage variation scenario B22 − Soil under forest undisturbed
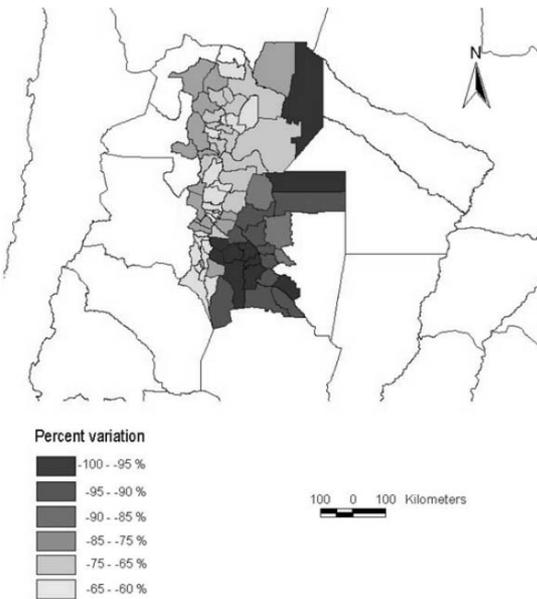

Figure 15. Average soil erosion − Percentage variation scenario B23 − Soil under forest undisturbed
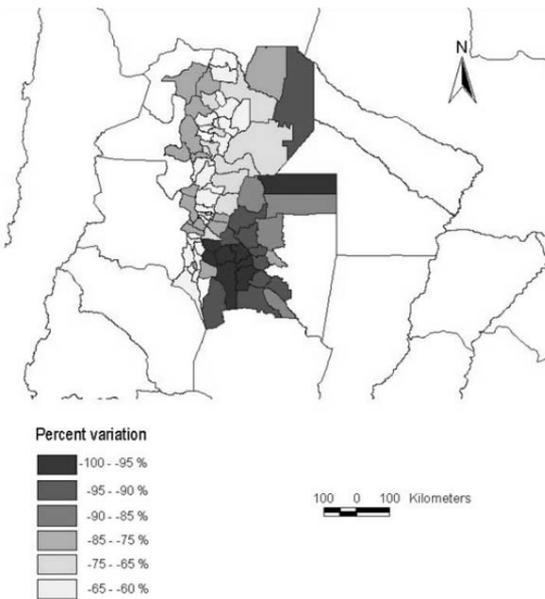
Figure 16. Average soil erosion − Percentage variation scenario A22 − Soil under trefoil, alfalfa
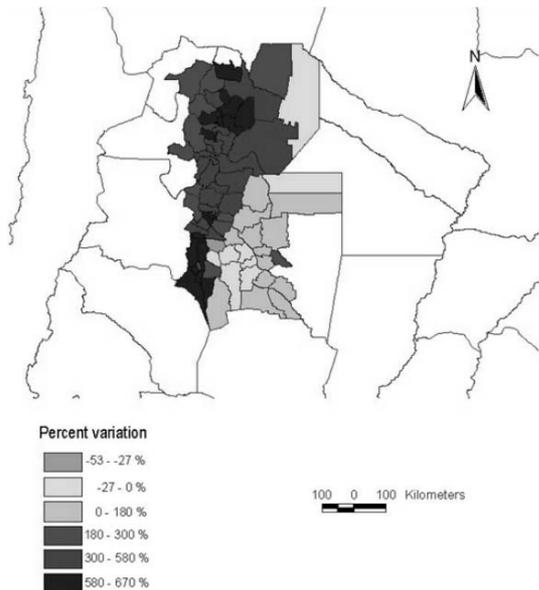
Figure 17. Average soil erosion − Percentage variation scenario A23 − Soil under trefoil, alfalfa
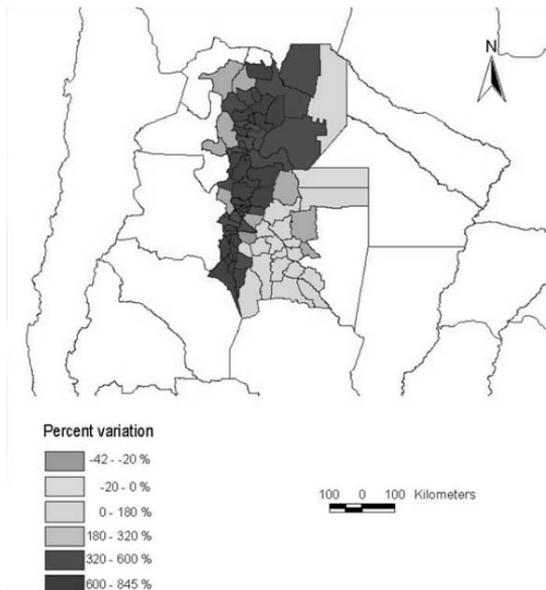
Figure 18. Average soil erosion − Percentage variation scenario B23 − Soil under trefoil, alfalfa
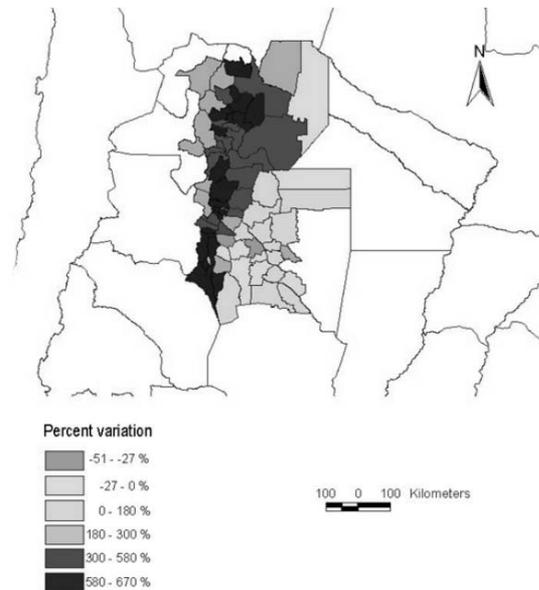

Figure 19. Average soil erosion − Percentage variation scenario B22 − Soil under trefoil, alfalfa
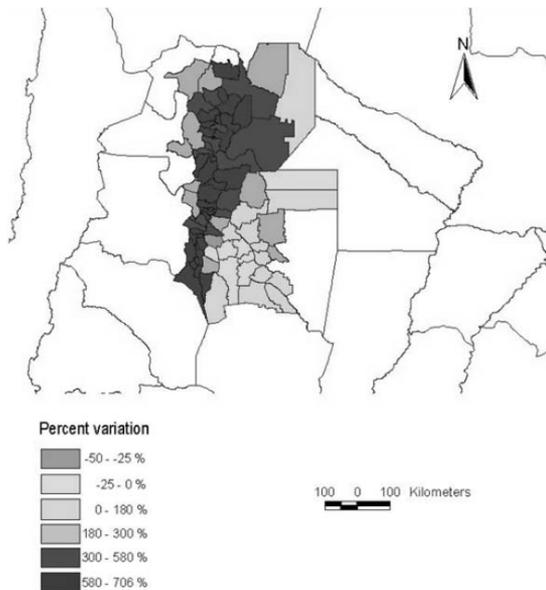
Figure 20. Average soil erosion − Percentage variation scenario A22 − Moderate productivity soil
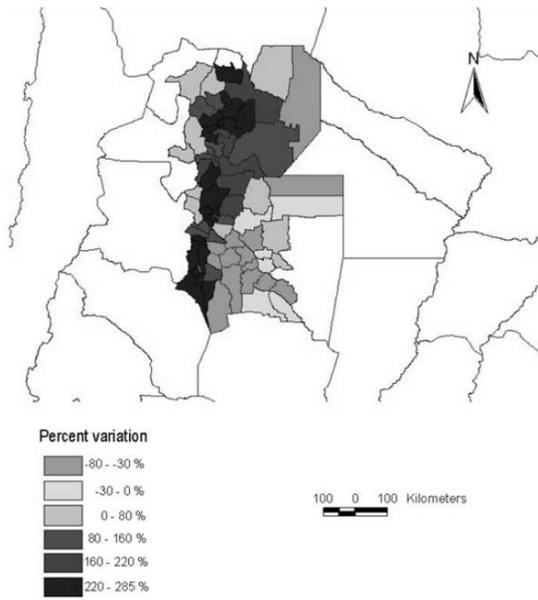
Figure 21. Average soil erosion − Percentage variation scenario A23 − Moderate productivity soil
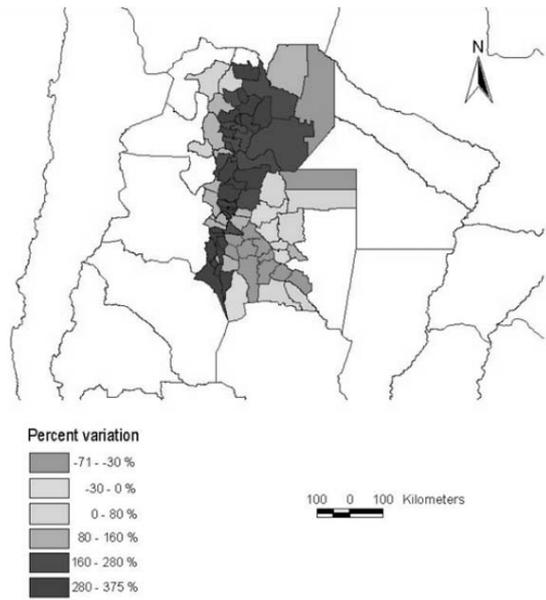
Figure 22. Average soil erosion − Percentage variation scenario B22 − Moderate productivity soil
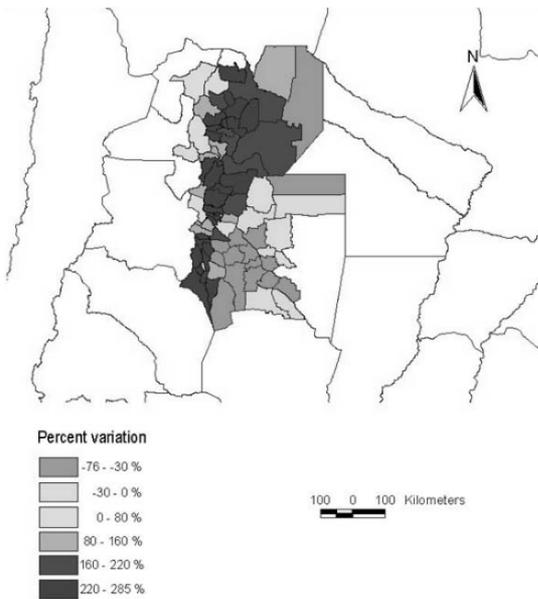
Figure 23. Average soil erosion − Percentage variation scenario B23 − Moderate productivity soil
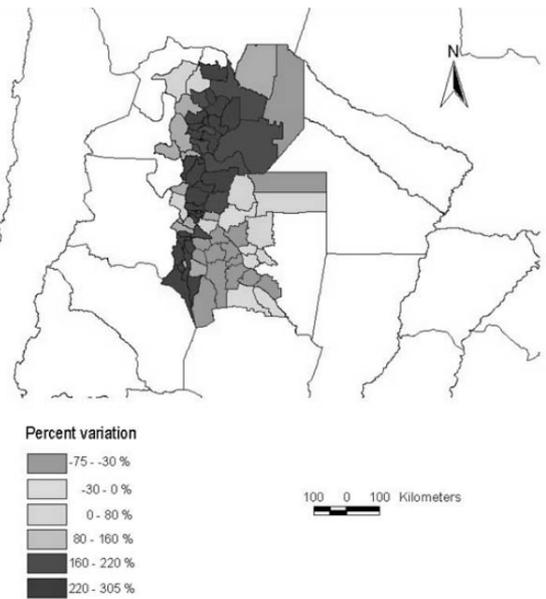
Figure 24. Average erosion for each department – Present scenario – Current soil
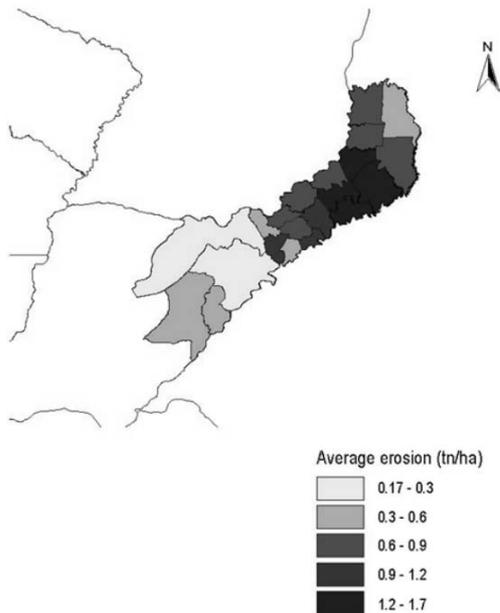
Figure 25. Average soil erosion – Percentage variation scenario B22 – Current soil

Average erosion (tn/ha)
0.17 - 0.3
0.3 - 0.6
0.6 - 0.9
0.9 - 1.2
1.2 - 1.7

Percent variation
6 - 9
9 - 12
12 - 15
15 - 18
18 - 21
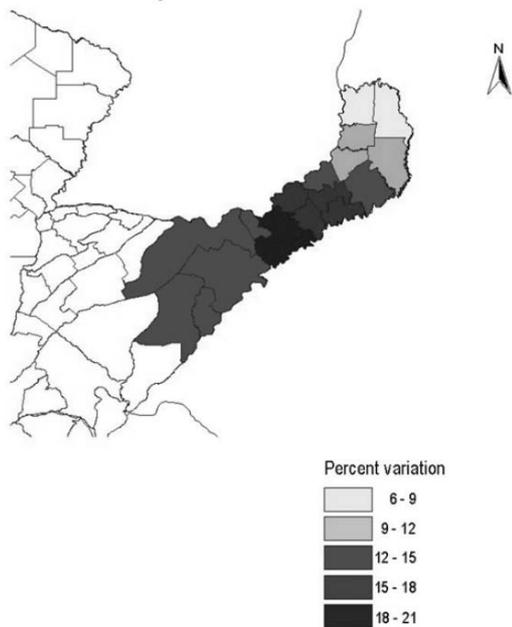
Figure 26. Average soil erosion – Percentage variation scenario A22 – Current soil
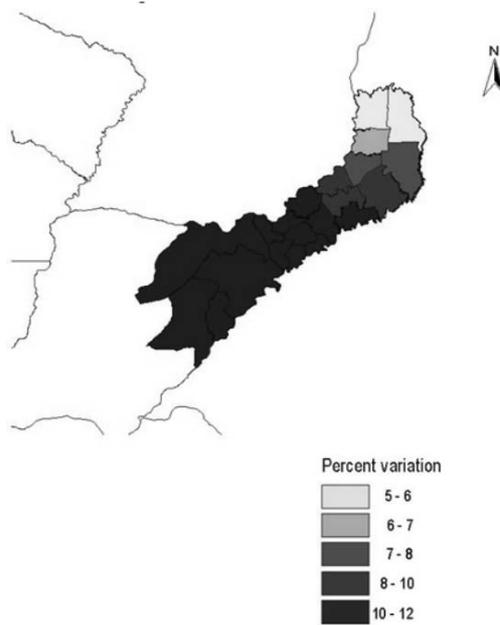
Figure 27. Average soil erosion – Percentage variation scenario A23 – Current soil

Percent variation
5 - 6
6 - 7
7 - 8
8 - 10
10 - 12

Percent variation
21 - 23
23 - 24
24 - 25
25 - 26
26 - 27
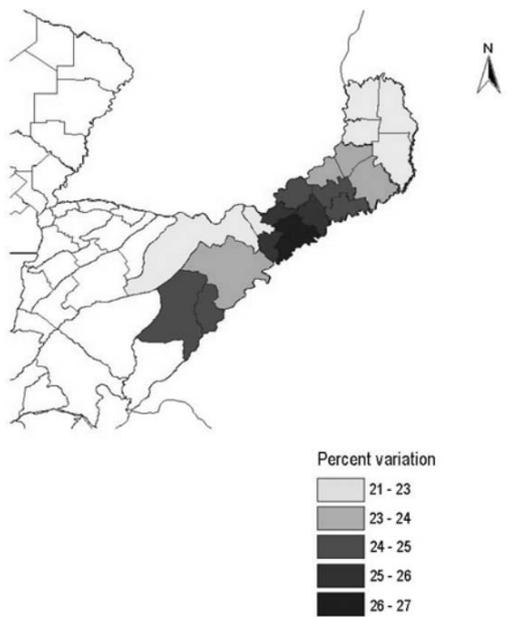
Figure 28. Average soil erosion − Percentage variation scenario B23 − Current soil
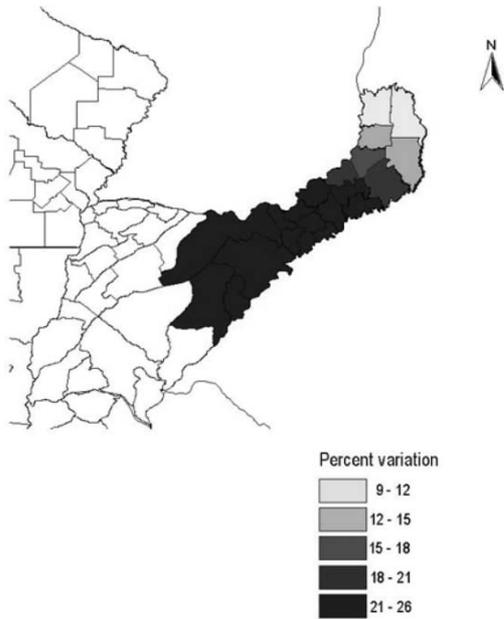
Figure 29. Average soil erosion − Percentage variation scenario A22 − High productivity soil
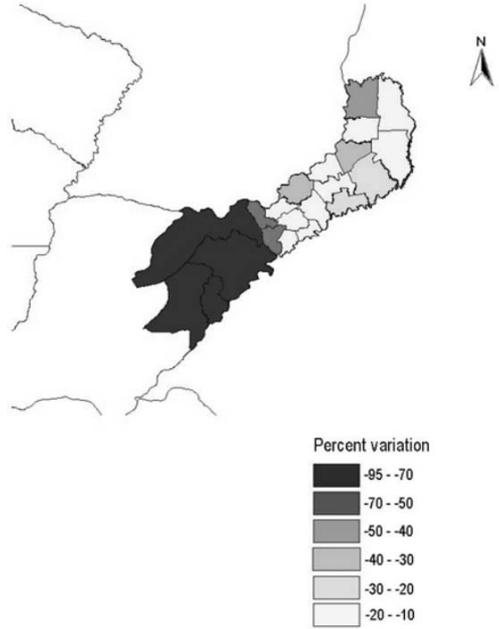
Figure 30. Average soil erosion − Percentage variation scenario A23 − High productivity soil
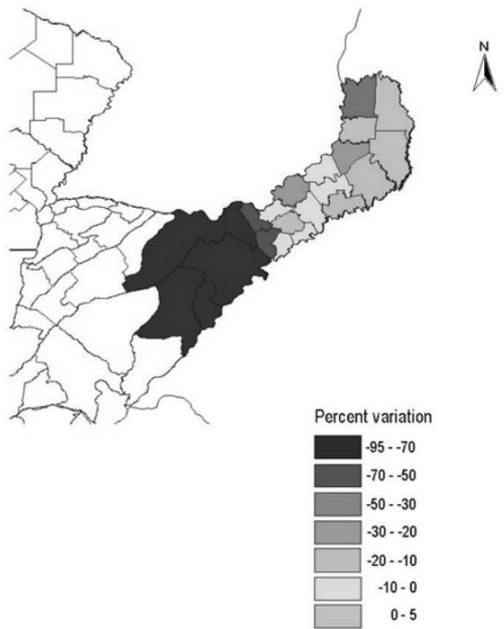
Figure 31. Average soil erosion − Percentage variation scenario B22 − High productivity soil
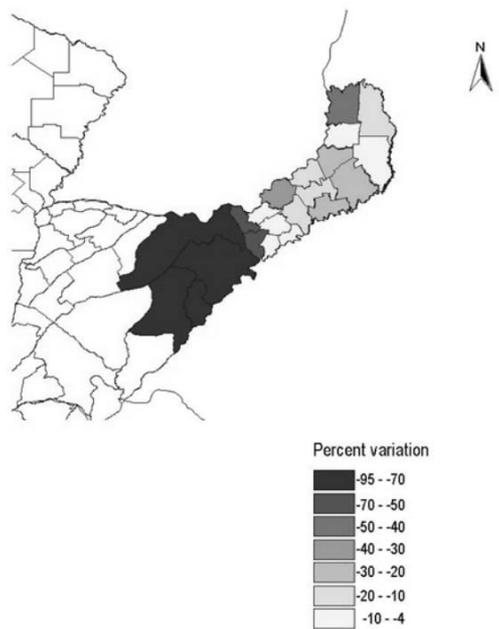
Figure 32. Average soil erosion − Percentage variation scenario B23 − High productivity soil
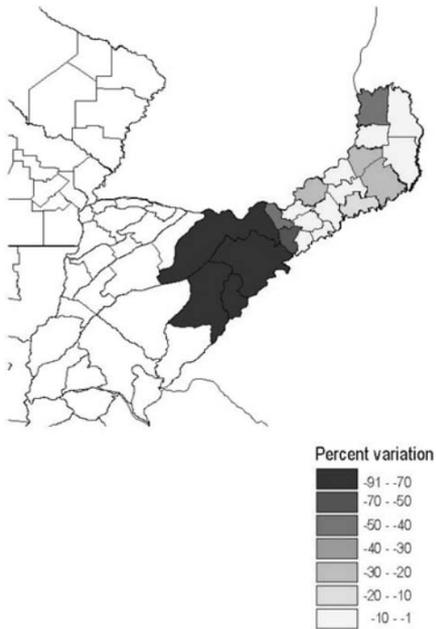
Figure 33. Average soil erosion − Percentage variation scenario A22 − Moderate productivity soil
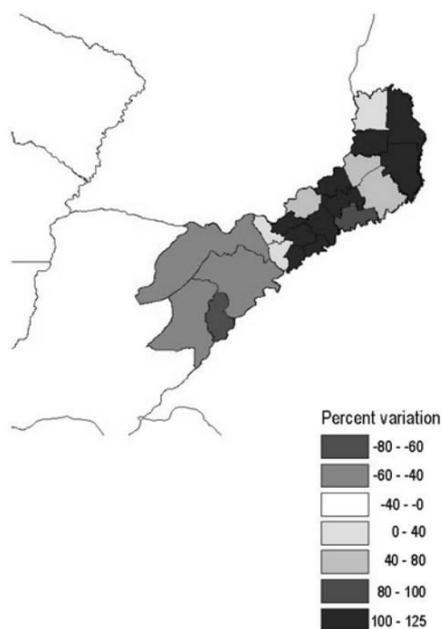

Figure 34. Average soil erosion − Percentage variation scenario A23 − Moderate productivity soil
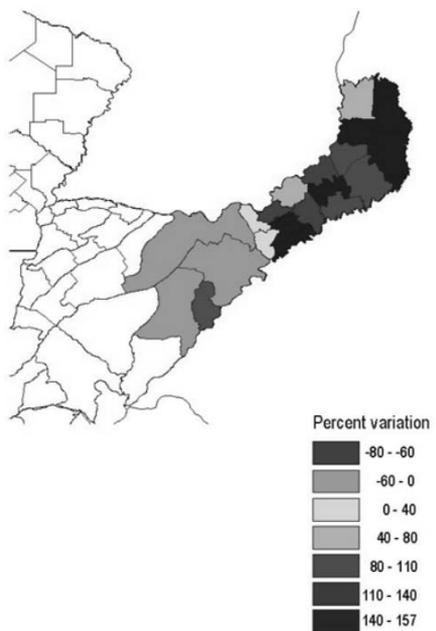

Figure 35. Average soil erosion − Percentage variation scenario B22 − Moderate productivity soil
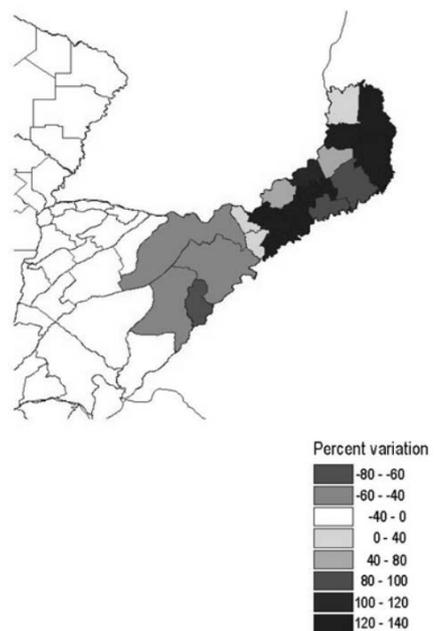
Figure 36. Average soil erosion − Percentage variation scenario B23 − Moderate productivity soil
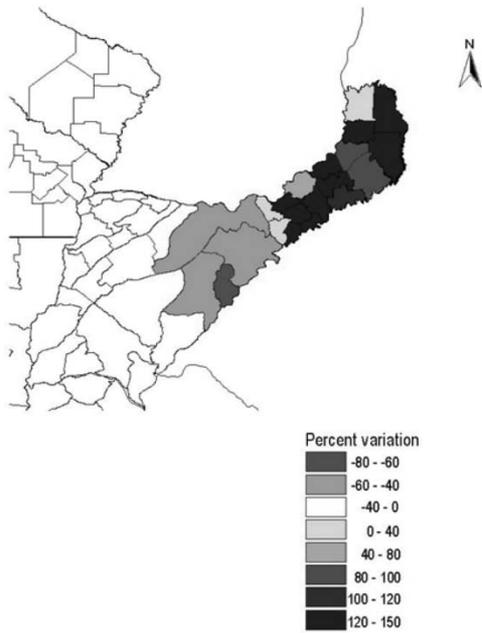
Figure 37. Average soil erosion − Percentage variation scenario A22 − Soil under trefoil, alfalfa
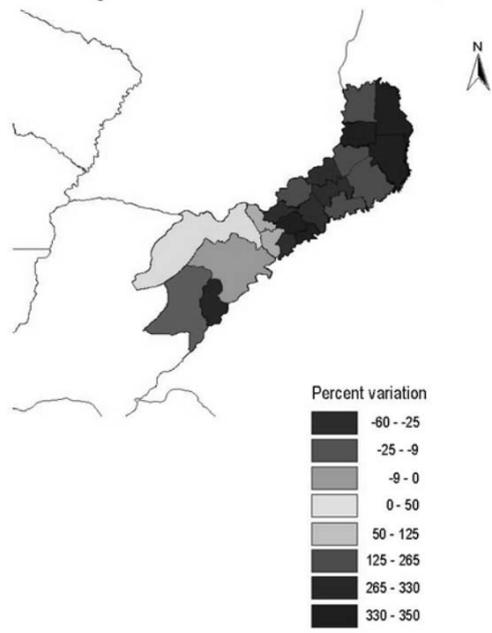
Figure 38. Average soil erosion − Percentage variation scenario A23 − Soil under trefoil, alfalfa
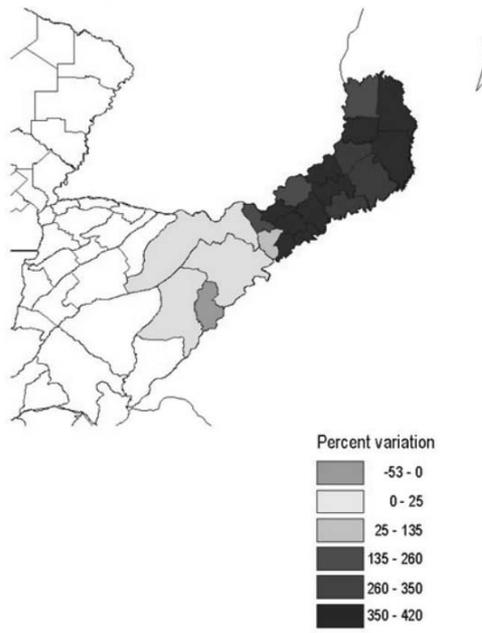
Figure 39. Average soil erosion − Percentage variation scenario B22 − Soil under trefoil, alfalfa
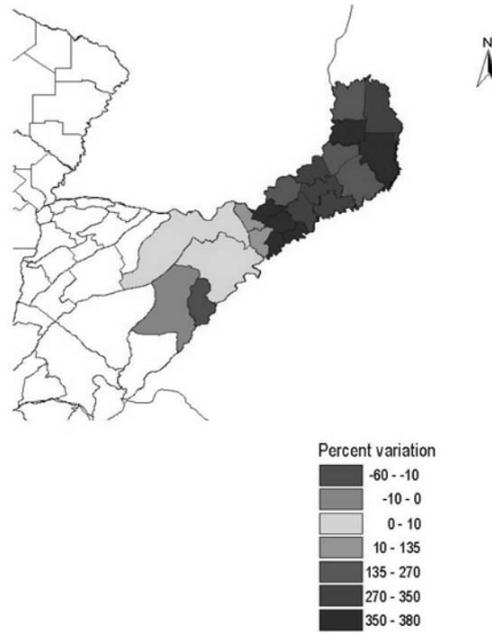
Figure 40. Average soil erosion − Percentage variation scenario B23 − Soil under trefoil, alfalfa

Percent variation

-55 - 0
0 - 20
20 - 160
160 - 270
270 - 350
350 - 395
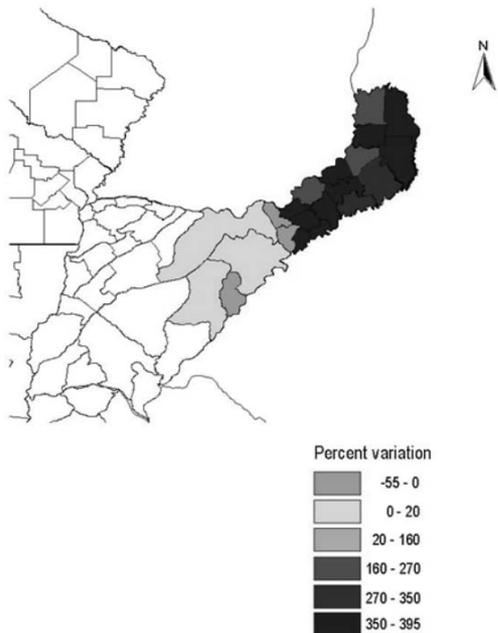
Figure 41. Average soil erosion − Percentage variation scenario A22 − Soil under forest undisturbed

Percent variation

-100 - -95
-95 - -90
-90 - -85
-85 - -80
-80 - -75
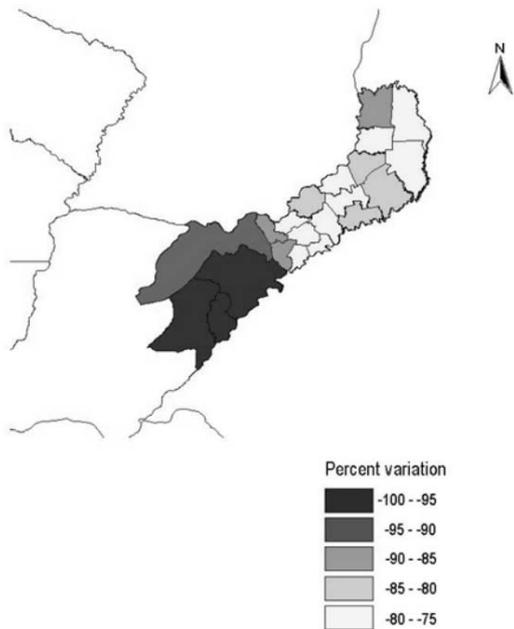
Figure 42. Average soil erosion − Percentage variation scenario A23 − Soil under forest undisturbed

Percent variation

-100 - -95
-95 - -90
-90 - -85
-85 - -80
-80 - -74
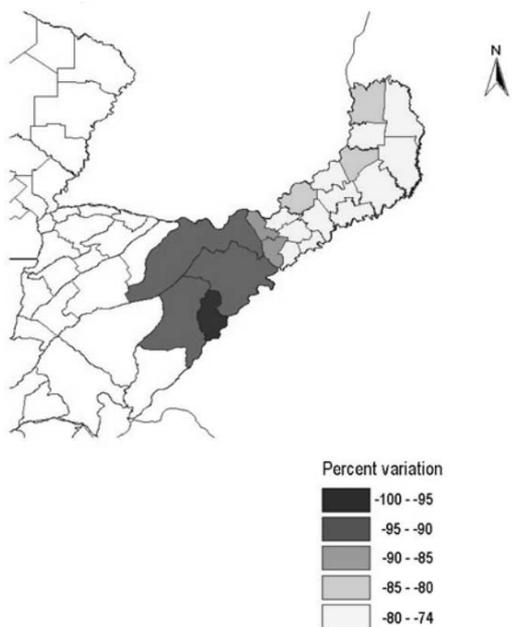
Figure 43. Average soil erosion − Percentage variation scenario B22 − Soil under forest undisturbed

Percent variation

-100 - -95
-95 - -90
-90 - -85
-85 - -80
-80 - -75
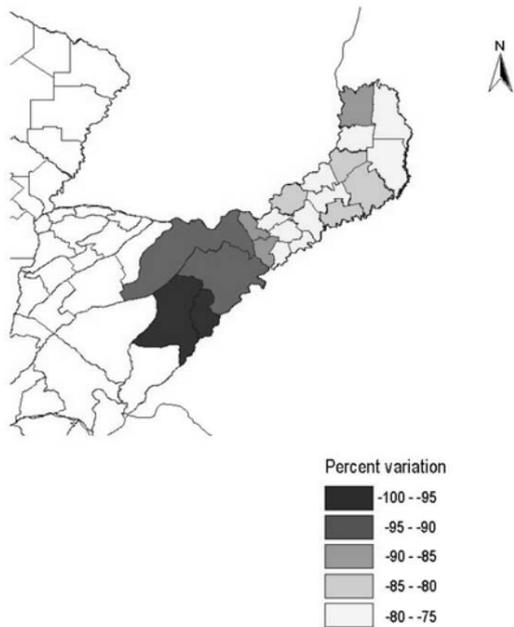
Figure 44. Average soil erosion − Percentage variation scenario B23 − Soil under forest undisturbed

Percent variation
- -100 - -95
- -95 - -90
- -90 - -85
- -85 - -80
- -80 - -75
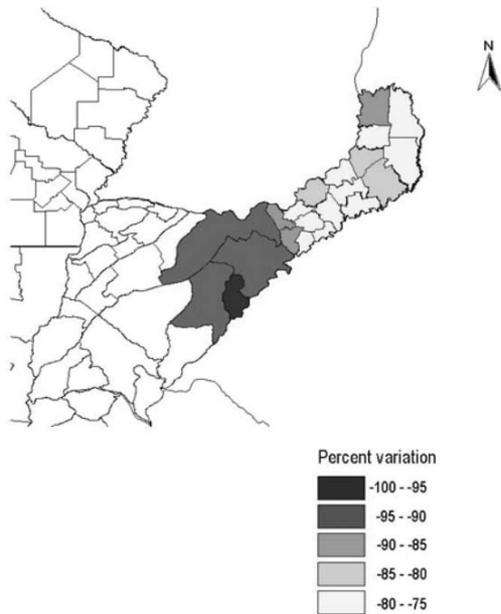
It seems obvious that these various hypotheses of land use are not likely to occur since it is not possible that in all the areas the forest cover is present or that high productivity cropping can be practiced, etc. The different maps are only useful for having an idea of how erosion varies in combination with land use changes.

4. Conclusion

Through this research we were able to assess how climate variation impacted on soil erosion. The obtained results showed that if the land use doesn't change, soil erosion increases, and it decreases when higher productivity cropping is practiced. However, if productivity is moderate, erosion increases as much as in case of range cropping. It seems obvious that soil erosion will decrease mostly in case of forest cover lands, since trees conserve rainwater, and reduce water runoff events and sediment deposition after storms.

It is worth mentioning that high crop productivity and, consequently, less water erosion, does not only mean more input uses in the agricultural production: the application of an integral production system which combines agriculture practises (i.e. adequate crop rotation and varieties) with proper use of cultivation inputs (fertilizers, pesticides, irrigation, etc.) and guarantees a sustainable and efficient use of the natural resources, the agronomic potential of the soil is maximized also in a long term period of reference.

Comparing soil erosion values of both studied zones, we can observe that the Western zone is the one that has the highest values − up to 15 ton/ha mean annual erosion, while the Eastern reaches a maximum of 1.7 ton/ha. It is possible that these differences in values are mainly due to the different slopes and heights of the lands, rather than due to the rainfall amount.

5. Recommendations

In order to correctly validate the data achieved − especially those ones related to the R factor calculation − it would be necessary to count on field all the data.

References

Arnoldus H.M.J., (1980). An approximation of the rainfall factor in the Universal Soil Loss Equation. In: *Assessment of erosion*. De Boodt & Gabriels, eds., Wiley & Sons: 127-132.
Giordani C., Zanchi C. (1995). *Elementi di Conservazione del Suolo.* Patron, Bologna.

A PRELIMINARY EVALUATION OF THE CROPSYST MODEL FOR SUGARCANE IN THE SOUTHEAST OF BRAZIL

Jônatan Dupont Tatsch
Department of Atmospheric Sciences
Universidade de São Paulo
Brasil

Tutors: Prof. M. Bindi and Dr. M. Moriondo
Department of Agronomy and Land Management
Università degli Studi di Firenze
Italy

1. Introduction

Sugarcane is cultivated in more than 20 million hectares in tropical and subtropical regions of the world and has served as a source of sugar, accounting for almost two thirds of the world's production (Menossi *et al.* 2007). Brazil is the main producer of sugarcane in the world (FAO, 2006). The actual estimated area (2006/2007), where sugarcane is cultivated, is 6.2 million hectares wide producing about 475 million tonnes of cane, approximately 77 tonnes per hect–are (CONAB 2007). The largest and most efficient sugarcane growing areas of Brasil are located in the central–southern region: only the State of Sao Paulo accounts the 70% of overall cultivated crop.

About the 55% of Brazilian sugarcane is transformed into ethanol and the 45% in sugar. Brazilian ethanol is attracting considerable interest within international trade market due to the environmental benefits if used as fuel and energy supplier (e.g. De Oliveira *et al* 2005). Between 2000 and 2005 years, the world sugarcane production has grown at a rate of 13% per year. In 2004/2005, Brazil was the world's largest producer of sugarcane, sugar, and ethanol with respectively 34%, 19%, and 37% of the world overall production (Martines-Filho *et al.* 2006). All cars in Brazil are fuelled by mixed alcohol. The Government has ruled the propor–tion of the gasoline which must include a 20–26% of ethanol. Of the ~20 million vehicles in Brazil, 15 million of them drive by a mixture of ethanol and gasoline, and about 2,2 million are pure ethanol fuelled.

The major areas of sugarcane cultivation are in Brazil's central–southern and northeastern regions, where two harvest seasonal times occur. The production therefore is constant during the whole year. Depending on when it is planted, the sugarcane cultivation needs around one year and a half to be ready for harvesting and processing for the first time of its timelife. Rat–ton crops regrow from underground stalk which still remain from the previous harvest, but significant investments need to be applied in order to maintain its productivity. After three or four rattons, the crop needs to be ploughed out and then replanted.

The possibility of using simulation models to study the dynamics of various crop and soil variables within agro–system ecosystems has aroused big interest (e.g. Stockle 1989; Wallach 2006). Considering the growing expansion of the sugarcane areas, the application of cropping simulation models is an efficient research tools which can provide a technical support within system analisys, for a better planning, management and monitoring of the crop. This study evaluates the performance of CropSyst simulation model which has been applied in order to assess the above ground biomass of sugarcane crop located in the southeastern region of Brazil.

2. Materials and Methods

2.1   Simulation Model

The CropSyst (Stockle *et al.* 1994; 2003; Stockle and Nelson 1999) is a process–based, multi–year, multi–crop, daily time step cropping simulation model, implemented in order to be used as an analytical tool to study the effect of cropping system management on crop productivity and environment. The model has been written in C++ and uses an object oriented programming approach in order to improve its user interface (Stockle *et al.* 2003). A suite of programs co–operatively works in CropSyst, whose main components are: CropSyst parameter editor, a weather generator (ClimGen), a GIS–CropSyst simulation (ArcCS), a watershed analysis tool (CropSyst Watershed), and several other utility programs. This feature makes CropSyst a suitable model to analyse the growth and yield of single crops or crop rotations at various temporal and spatial scales.

CropSyst has been applied to several crops (maize, wheat, barley, soybean, sorghum, sugarbeet, lupins, potato, bean, tea, sunflower, wine grape, flooded rice) in several regions (Western US, Southern France, Northern and Southern Italy, Northern Syria, Northern Espain, Western Australia, Russia and Africa) generally with good results (Stockle *et al.* 1994; Pala *et al.* 1996; Stockle and Debaeke 1997; Donatelli *et al.* 1996, 1997; Francaviglia and Bartolini, 1997; Rinaldi and Ventrella 1997; Stockle *et al.* 1997; Giardini *et al.* 1998; Pannkuk *et al.* 1998; Ferrer–Alegre *et al.* 1999a, b; Francaviglia and Marchetti 1999; Francaviglia *et al.* 1999a, b; Richter *et al.* 1999; Bechini *et al.* 2000; Bellocchi *et al.* 2000; Donatelli and Stockle 2000; Donatelli *et al.* 2000, Confalonieri and Bocchi 2005). Nevertheless, at the moment any result concerning the application of this model within sugarcane cultivation and its performance have been published yet, while simulations of perennial crops have already been tested in the northern region of Italy (Confalonieri and Bechini 2004). Another application of CropSyst consists in the study of the potential effects of climate change on agricultural production and in the evaluation of the main adaptation strategies (changes in variety, sowing date, fertilisation and irrigation levels, etc.) in order to cope with these impacts. Future scenarios derived from General Circulation Models (GCMs), considering different levels of the atmospheric carbon dioxide increasing rate, in several regions of Europe have been applied for this purpose (Bindi *et al.* 1999; Tubiello *et al.* 2000; Donatelli *et al.* 2002b; Crisci *et al.* 2001; Giannakopoulos *et al.* 2005).

CropSyst model simulates the soil water budget, the soil–plant nitrogen budget, crop canopy and root growth, crop phenology, dry matter production, yield residue production and decomposition, soil erosion and pesticide fate. In the model, precipitation, irrigation, runoff, interception, water infiltration, water redistribution in the soil profile, deep percolation, crop transpiration, and evaporation are included with water budget. Potential evapotranspiration can be estimated by Penman–Monteith or Priestley-Taylor methods. Crop evapotranspiration is determined at full canopy and ground coverage through a crop coefficient which uses the canopy leaf area index. Soil water dynamics are handled by both a simple cascading approach or by Richards' equation, the latter method solved numerically using finite difference technique.

The nitrogen budget includes soil N transformations (mineralisation, nitrification, denitrification, volatilisation), ammonium sorption, symbiotic N fixation, crop N demand and crop N uptake. Both water and nitrogen budgets interact with each other in order to produce a simulation of N transport within the soil. Chemical budgets (pesticides, salinity) are also kept and they interact with water balance.

Crop growth is simulated for the whole canopy by calculating unstressed biomass growth and is based on potential transpiration and on crop intercepted photosynthetically active radiation. This daily potential growth, expressed as biomass increment per unit area, is corrected by four limiting factors: light, temperature, water, and Nitrogen. According to the harvest index (HI = harvestable yield/aboveground biomass), both crop production and translocation

factor are calculated. The Root depth is simulated as a function of leaf area development, and reaches its maximum in flowering times. The length time of phenological phases is calculated taking into account the heat units, which can be eventually modulated by photoperiod and vernalisation. The thermal time may be accelerated by water stress.

Most important model inputs are: daily weather data, properties and initial conditions of soil profile (such as soil texture, thickness, field capacity, wilting point, bulk density, crop residues, water content, mineral nitrogen and organic matter), cultivar genetic coefficients (such as photoperiodic sensitivity, duration of grain filling, maximum LAI, etc.), dates and amounts of products applied for each fertilisation and irrigation event, sowing date, tillage operations and residue management. Main daily model outputs are above-ground biomass (AGB), leaf area index (LAI), root depth, potential and actual evapotranspiration, soil water and nitrogen balance. Details on the technical aspects and use of the CropSyst model are reported in Stockle *et al.* 1994 or in Stockle and Nelson 1999).

2.2   Site Description

The experimental data used in this study were collected over a 351 ha sugarcane areas (Saccharum spp.) belonging to Santa Rita Mill and located in the São José do Pulador Farm (Farm nº 27) at Luiz Antônio city, São Paulo state, Brazil.

On the experimental site, in early February 2005 over a ratton sugarcane crop (variety SP83-2847) a micrometeorological tower was installed,. The crop was planted with a spacing distance of 1.5 m and attained a height of 3m at harvest. The crop harvesting occurred on 10th May 2006 (3rd cut or 2nd ratton) and 28th May 2007 (4th cut or 3rd ratton). The Mill yield (fresh weight of stalks) estimated in the 2005/06 (2006/07) crop season was 102,4 t ha–1 (63 t ha–1) and that one which was obtained by sample of biomass reached the 118 ± 23 t ha–1 (85± 14 t ha–1) (Cabral et al 2006, 2007).

The soil type is red–yellow latossoil and has a sandy texture. The granulometry analysis for each layer of soil profile until 2 m of depth (see Figure 1) showed a mean composition of 22% of clay, 3% of silt and 74% of sand.

The regional climate is typically warm and wet in the summer, and mild and dry in winter time (see Figure 2). Both temperature and precipitation show a marked annual cycle. The mean monthly temperature varies between 19 °C in June and 24 °C in February. The mean annual temperature is 22 °C. The mean monthly rainfall is about 50 mm in the dry season and reaches more than 200 mm during wet season. The total dry season precipitation amount represents less than 15% of long term average of annual precipitation (1500 mm, with interannual variation of ± 312 mm). Details about seasonal variability of meteorological and biophysical variables over the sugarcane site in the 2005-2006 period have been found in Tatsch (2006).

The meteorological data set required by CropSyst were measured by an automatic weather station. The data were sampled every 10s and registered as 10 min averages in a datalogger (CR10X, Campbell Systems). From these data, the daily mean (or summed) values were calculated. Daily meteorological data include: rainfall (mm dia–1), maximum and minimum air temperatures (°C), global solar radiation (MJ m-2 dia-1), maximum and minimum relative humidity (%) and wind speed (m s-1).

AGB was taken as summed dry biomass of the stalks, trash, green leaves and senesced leaves. It was determined by collecting ten random samples of 1m each (corresponding to 1.4 m2) in different planting rows. Sub-samples from each component were weighted and stored in an oven at 60 °C until constant weight to determine the dry matter weight. The sampled biomass components were collected every 25 days during the period of April 2005 and June 2007, including two crop seasons. AGB in 2006–2007 crop season showed a strong decrease: about 40% in comparison to 2005–2006 crop season. This last variable was used for model calibration (see figures 3-4).

Figure 1. Soil profile of experimental area located at Luis Antônio city, SP
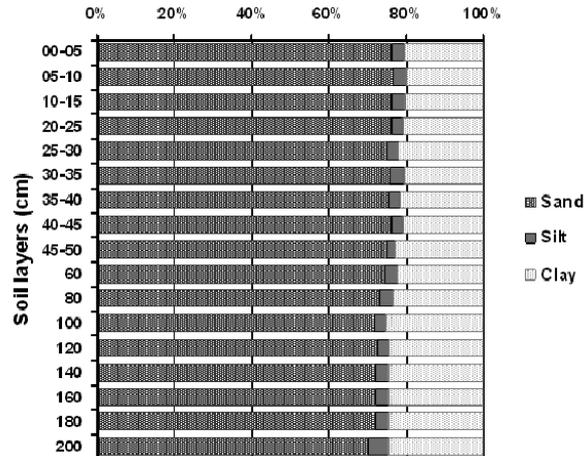
Figure 2. Distribution of mean monthly air temperature for Luis Antônio, SP. (b) Distribution of mean monthly precipitation of 6 stations located in the region around Luis Antonio city. The boxplot represents the maximum, third quartile, median, first quartile and minimum values of monthly mean time series. The horizontal solid line connected box–whisker is the long term mean
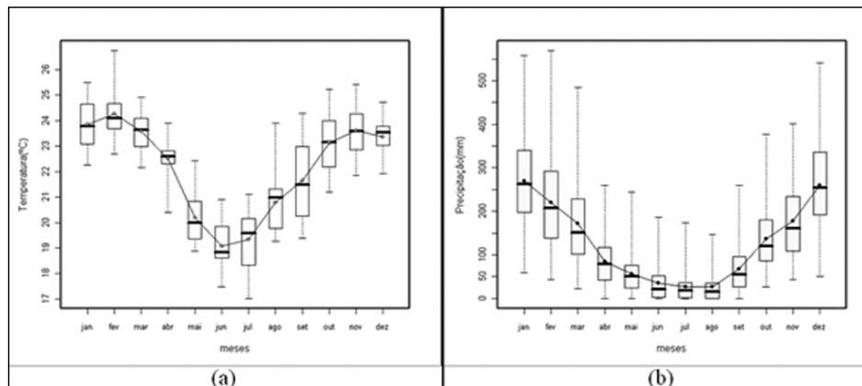
2.3   Model Calibration

The 3.04.01 CropSyst release (February 9, 2004) was used. The simulations were performed with the Penman-Monteith evapotranspiration model. This option requires: daily maximum and minimum air temperatures, global solar radiation, maximum and minimum relative humidity and wind speed. Soil water redistribuition was simulated with the finite difference approach. The Erosion and Nitrogen sub-models was off. Table 1 indicates the period used for the simulations. The C4 photosynthetic pathway and perennial option (cultivations cutting down in agreement of the crop dates) were also set in the model.

The parameters values used in order to characterize the sugarcane are described in Table 1. Most of these values were compulsory based on observations or suggested by the CropSyst manual (C4 plants), by literature or by local experience. For some parameters it was necessary to carry out a calibration procedure. A sensitivity analysis was performed mainly within growth and morphology module parameters calculation (wilting leaf water potential, leaf

Figure 3. Time series of daily meteorological data observed in the experimental site during two crop seasons (from February 2005 to June 2007). From top to bottom are: maximum and minimum relative humidity (respectively, Rhmax and Rhmin, %) maximum and minimum air temperatures (respectively, Tmax and Tmin, °C), Global solar radiation (Srad, MJ m-2 day-1), precipitation (Prec, mm day-1); mean wind speed (Wind, m s-1)
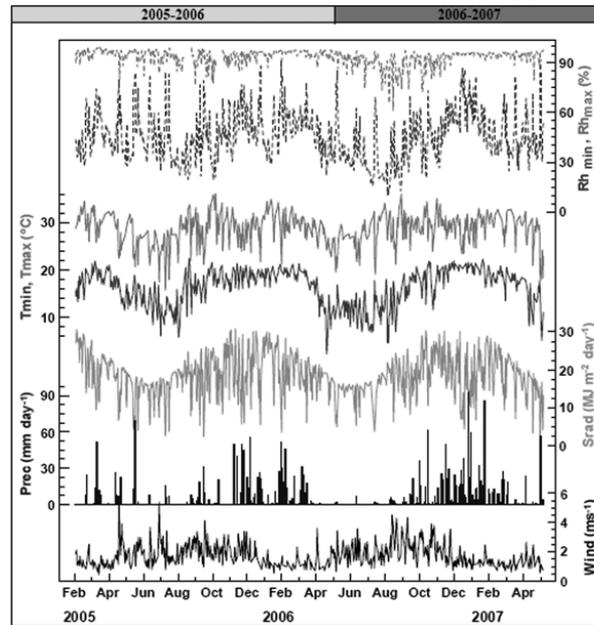
Figure 4. Measured sugarcane biomass (dry matter) in the two crop seasons. The shaded area indicates one standard deviation of the above ground biomass to roughly indicate the magnitude of sampling variation
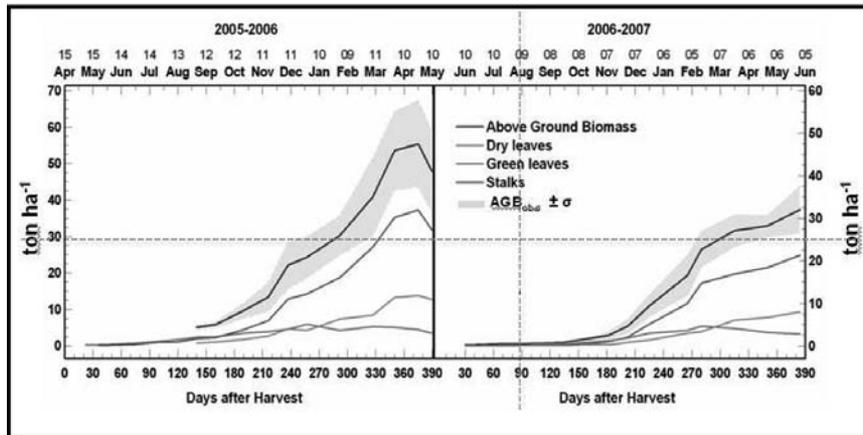
Table 1. Time sets of simulation in the CropSyst model

Crop season	Beginning (day of year)	Harvest (day of year)
3rd cut (4th ratoon)	15/04/2005 (105)	10/05/2006 (130)
4th cut (5th ratoon)	11/05/2006 (131)	29/05/2007 (149)

water potential at the onset of stomatal closure, from actual to potential transpiration ratio that limits leaf area and root growth, specific leaf area, stem/leaf partition coefficient, optimum mean daily temperature for growth)., Some specific parameters of other modules still need to be tested due to the lack of references to some parameters of sugarcane for Brazilian climate conditions. The CropSyst model was developed to estimate the growth and development occurring in optimal conditions. Thus, the values of the parameters that describe both morphological and physiological processes refer to optimal conditions for growth. Therefore, the answer to stress conditions should be used to define the parameters that quantify the effect of stress on crop growth.

The agreement between observed and simulated values was expressed by using the following statistical indices: the parameters of the linear regression equation between observed and predicted values (coefficient of determination – R2, and slope), the modelling efficiency (EF; $-\infty$ to $+\infty$, optimum = 1, if positive, indicates that the model is a better predictor than the average of measured values, if negative, the model cannot be recommended), the relative root mean square error as an indicator of the relative magnitude of the error (RMSE/observed mean, minimum and optimum = 0%), the Willmott's index of agreement (d=0, poor model and d=1, perfect model) (Table 2).

Table 2. Crop input parameters used for simulation of sugarcane crop (Saccharum spp.) in Luis Antônio, São Paulo, Brazil. ★The values between parenthesis are the altered parameters in the second crop season

Parameter	Value	Unit
Morphology		
Maximum rooting depth	1	M
Maximum expected leaf area index (LAI)	3.1	m2 m–2
Specific leaf area (SLA)	14	m2 kg –1
Stem/leaf partition coefficient (SLP)	2	–
Leaf duration sensitivity to water stress	1	–
Fraction of max. LAI at physiological maturity	0.8	–
Extinction coefficient for solar radiation (k)	0.5	–
Evapotranspiration crop coefficient at full canopy	1	–
Growth		
Above ground biomass-transpiration coefficient	10 (9)★	kPa kg m-3
Light to above ground biomass conversion	4 (3.5)★	g MJ-1
Maximum water uptake	5.2	mm dia-1
Wilting leaf water potential	–500	J kg-1
Leaf water potential at the onset of stomatal closure	–1300	J kg-1
Optimum mean daily temperature for growth	22	° C
Actual to potential transpiration ratio that limits leaf area growth	0.96	–
Actual to potential transpiration ratio that limits root growth	0.8	–
Fenology		
Base temperature	13	° C
Cutoff temperature	34	° C
Degree-days at emergence	150	°C day
Degree-days at Peak LAI	1020	°C day
Degree-days at Physiological maturity	2000	°C day
Phenological sensitivity to water stress	0	–

Figure 5. (a) Observed (dots) and Simulated (line) AGB values in tonnes per hectare for the period from 15 april 2005 to 29 may (2007).The shaded area indicate one standard deviation of the above ground biomass measure to indicate the magnitude of sampling variation. (b) Scatter plot for simulated versus observed AGB
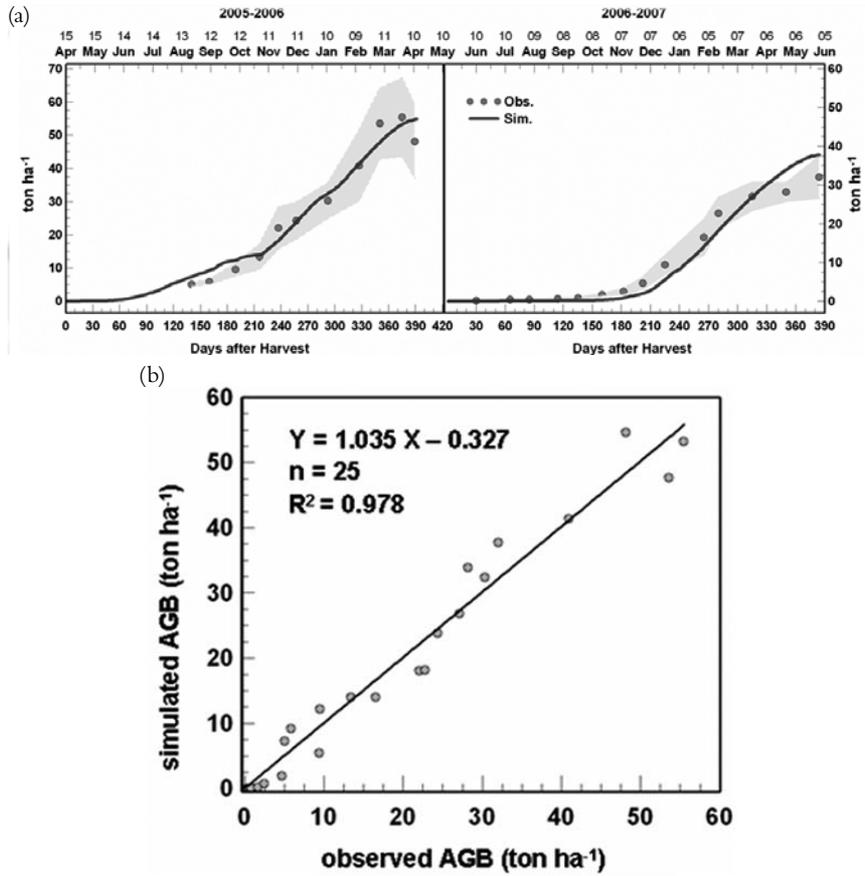
3. Results and Conclusion

The agreement between observed and simulated AGB values is shown in Fig. 4 and in Table 3. In general, the trend over time of simulated AGB was consistent with the observed values, and fell within the sampling error of the measured AGB throughout most of all crop seasons (Fig. 5a). Slight over and under estimation of AGB occurred at the beginning of the growth season in the first and second case, respectively. Particularly in the 2006–2007 crop season, the model overestimated the final AGB. The regression between the simulated and observed values presented a coefficient of determination of around 0.98 and the slope was close to 1 (not statistically different from 1, at 95% confidence).

Table 3. Statistical summary comparing observed data with simulated values using the CropSyst model

Obs. Mean (ton ha–1)	Sim. Mean (ton ha–1)	RMSE (ton ha–1)	RRMSE (%)	d (0–1)	EF (– ∞< EF < 1)
18.22 ± 17.60	18.14 ± 18.09	3.15	0.17	0.99	0.96

A statistical analysis of the obtained results is reported in Table 3. The observed and simulated mean AGB for the 25 data points were very close, with RMSE representing 0.17% of the observed mean (3.15 ton ha-1), while d and EF were close to 1. The values of indices confirm the good performance of the model.

In this study, the CropSyst simulation of sugarcane AGB provided satisfactory estimates. Following these preliminary results, further investigation is required over long-term cultivation. The set crop parameters used in this evaluation have to be considered as an initial adaptation of the model to this particular environment and may be improved with future data. Next steps are:

• detailed information inclusion concerning fertilization and management practices, in order to activate also the Nitrogen module;
• comparison between observed and simulated evapotranspiration and Soil Water content data;
• model validation using data from others field studies conducted in sugarcane areas (e.g. Cabral *et al*. 2003).

References

Bechini L., De Palma R., Romani M., Bocchi S. (2000). Calibration and validation of the simulation model CropSyst for the growth of Italian rye grass (Lolium multiflorum Lam.). 3rd International Crop Science Conference, 36. Hamburg, Germany, 17-22 August.

Bellocchi G., Ashman M., Shevtsova L., Donatelli M., Smith P., Romanenkov V., Smith J., Dailey G. (2000). Using CropSyst and SUNDIAL to simulate soil organic matter dynamics at two sites in Eastern Europe. 3rd International Crop Science Conference, 44. Hamburg, Germany, 17-22 August.

Bindi M., Donatelli M., Fibbi L., Stöckle C.O. (1999). Estimating the effect of climate change on cropping systems at four European sites. Proceedings First International Symposium Modelling Cropping Systems, Lleida, Spain, 21–23 June, pp. 147-148.

Cabral, O.M.R., Rocha, H.R., Ligo, M.A.V., Brunini, O., Silva Dias, M.A.F., 2003: Turbulent fluxes of sensible heat, water vapour and CO2 over a sugarcane (Saccharum sp.) plantation (*Saccharum sp.*) in Sertãozinho, SP. *Brazilian Journal of meteororlogy*, 18 (1): 61-70 (in Portuguese).

Cabral O.M.R., Ligo M.A.V., Rocha H.R., Freitas H.C., Tatsch J.D., Gomes E. (2006). Micrometeorological measurements over a sugarcane plantation at Luis Antônio-SP. 1° Research report presented to Santa Rita Mill (in Portuguese).

CONAB (2007). National Supply Company, Ministry of Agriculture. Acompanhamento da Safra Brasileira Cana-de–Açúcar – Safra 2007/2008, 3° levantamento. Brasília, novembro/2007. Available at <http://www.conab.gov.br/conabweb/> (accessed in december 2007).

Confalonieri R., Bechini L. (2004). A preliminary evaluation of the simulation model CropSyst for alfalfa. *European Journal of Agronomy*, 21: 223-237.

Confalonieri R., Bocchi S. (2005). Evaluation of CropSyst for simulating the yield of flooded rice in northern Italy. *European Journal of Agronomy*, 23: 315–326.

Crisci A., Moonen C., Ercoli L., Bindi M. (2001). Study of the impact of climate change on wheat using an historical weather dataset and a crop simulation model. Proceedings Second International Symposium Modelling Cropping Systems, 18 July, pp. 119-120, Florence, Italy, 16.

Dias De Oliveira M.E., Vaughan B.E., Rykiel E.J. jr. (2005). Ethanol as Fuel: Energy, Carbon Dioxide Balances, and Ecological Footprint. *BioScience*, (55) 7: 593–602.

Donatelli M., Stöckle C.O. (2000). Simulation-based rules to schedule nitrogen fertilization of field crops. 3rd International Crop Science Conference, 187. Hamburg, Germany, 17-22 August.

Donatelli M., Spallacci P., Marchetti R., Papini R. (1996). Evaluation of CropSyst simulations of growth of maize and of water balance and soil nitrate content following organic and mineral fertilization applied to maize. 4th European Society for Agronomy Congress, 342-343. Veldhoven-Wageningen, The Netherlands, 7–11 July.

Donatelli M., Stöckle C.O., Ceotto E., Rinaldi M. (1997). Evaluation of CropSyst for cropping systems at two locations of northern and southern Italy. *European Journal of Agrononomy*, (6): 35–45.

Donatelli M., Peruch U., Poggiolini S., Barbanti L., Amaducci S. (2000). Approaching modelling of sugar beet quality. 3rd International Crop Science Conference, 187. Hamburg, Germany, 17-22 August.

Donatelli M., Acutis M., Fila G., Bellocchi G. (2002b). A method to quantify time mismatch of model estimates. Seventh Congress of the European Society for Agronomy, 15-18, pp. 269-270. Cordoba, Spain, July 15.

Ferrer-Alegre F., Villar J.M., Carrasco I., Stöckle C.O. (1999a). Developing management decision tools from yield experiments with the aid of a simulation model: a first example with N fertilization in corn. Proceedings of 1st Modelling Cropping System International Symposium, 179-180. Lleida, Spain, 21-23 June.

Ferrer-Alegre F., Villar J.M., Castellvì F., Ballesta A., Stöckle C.O. (1999b). Contribution of simulation techniques to the evaluation of alternative cropping systems in Andorra. Proceedings of 1st Modelling Cropping System International Symposium, 179-180. Lleida, Spain, 21-23 June.

FAO (2006). Food and Agricultural commodities production. Available at <http://www.fao.org/es/ess/top/commodity.html;jsessionid=051B3E79C2FD549C004A9235380DEEC?lang=enanditem=156andyear=2004> (accessed March 26, 2006).

Francaviglia R., Bartolini D. (1997a). Calibrazione del modello CropSyst su una rotazione mais da granella-frumento tenero nella bassa Pianura Padana. *Agricoltura Ricerca*, (171): 73-80.

Francaviglia R., Marchetti D. (1999b). Comparison of cropping systems models in the simulation of crop biomass and green leaf area index development. Procedings of 1st Modelling Cropping System International Symposium, 181-182. Lleida, Spain, 21-23 June.

Giardini L., Berti A., Morari F. (1998). Simulation of two cropping systems with EPIC and CropSyst models. *Italian Journal of Agronomy*, (1): 29-38.

Giannakopoulos C., Bindi M., Moriondo M., Tin T. (2005). Climate change impacts in the Mediterranean from a 2°C global temperature raise. A report for WWF. July(2005). Available at <http://assets.panda.org/downloads/medreportfinal8july05.pdf>.

Martines-Filho J., Burnquist H.L., Vian C.E.F. (2006). Bioenergy and the Rise of Sugarcane-Based Ethanol in Brazil. *Choices*, 2nd Quarter, 21(2).

Marris E. (2006). Business Feature. Drink the best and drive the rest. *Nature* (444), 7 December.

Menossi M., Silva-Filho M.C., Vincentz M., Van-Sluys M.-A., Souza G.M.. (2007). Sugarcane Functional Genomics: Gene Discovery for Agronomic Trait Development. *International Journal of Plant Genomics*, doi:10.1155/2008/458732.

Pala M., Stöckle C.O., Harris H.C. (1996). Simulation of durum wheat (Triticum durum) growth under differential water and nitrogen. *Agricultural Systems*, 51: 147-163.

Pannkuk C.D., Stöckle C.O., Papendick R.I. (1998). Validation of CropSyst for winter and spring wheat under different tillage and residue management practices in a wheat-fallow region. *Agricultural Systems*, 57: 121-134.

Rinaldi M., Ventrella D. (1997). Uso dei modelli EPIC e CropSyst in sistemi colturali del Sud Italia. *Agricoltura Ricerca*, (171): 47-58.

Richter G.M., Agostini F., Donatelli M., Smith P., Smith J. (1999). Modelling the N-dynamics of a wheat-sugarbeet rotation at different complexity. Proceedings of 1st International Symposium Modelling Cropping Systems, Lleida, Spain, 21-23 June, 239-240.

São Paulo Sugarcane Agroindustry Union (UNICA) (2006). Sugarcane Agroindustry – Sugarcane's high competitiveness in São Paulo. Available at <http://www.unica.com.br/i_pages/agroin-dustria_alta.asp> (accessed February 21, 2006).

Stöckle C.O. (1989). Simulation models in agriculture: from cellular to field scale. Proc. 1989 Summer Computer Simulation Conference, Austin, Texas, USA.

Stöckle C.O., Martin S.A., Campbell G.S. (1994). CropSyst, a Cropping systems simulation model: water/nitrogen budgets and crop yield. *Agricultural Systems*, 46 (3): 335–359.

Stöckle, C.O., Donatelli, M., nelson, R. (2003).CropSyst, a cropping systems simulation model. *European Journal of Agronomy*, 18 (3/4): 289–307 (Second special issue «2nd International Symposium on Modelling Cropping Systems, Florence, Italy»).

Stöckle, C.O., Nelson R.L. (1999).CropSyst User's Manual. Biological Systems Engineering Department, Washington State University, Pullman, WA, USA. Available at <http://www.bsyse.wsu.edu/cropsyst/>.

Stöckle C.O., Debaeke P. (1997). Modelling crop nitrogen requirements: a critical analysis. *European Journal of Agronomy*, (7): 161–169.

Stöckle C.O., Cabelguenne M., Debaeke P. (1997). Comparison of CropSyst performance for water management in southwestern France using submodels of different levels of complexity. *European Journal of Agronomy*, (7): 89–98.

Tatsch J.D.(2006). An analysis of Microclimate and surface fluxes over savanna, sugarcane and eucalyptus: implications for regional climate changes. Master Thesis of Institute of Astronomy, Geophysics and Atmospheric Sciences. Department of Atmospheric Sciences. University of São Paulo (in Portuguese).

Tubiello F., Donatelli M., Rozenweig C., Stöckle, C.O. (2000). Effects of climate change and elevated CO2 on cropping systems: model predictions at two Italian locations. *European Journal of Agronomy*, (2–3): 179–189.

Wallach D. (2006). Evaluating crop models. In: Wallach D., Makowski D., Jones J.W (eds). *Working with dynamic crop models: evaluation, analysis and applications.*

ESTIMATION OF SOIL MOISTURE FOR THE VALENCIA ANCHOR STATION REGION (VAS) BY THE USING OF TEMPERATURE–VEGETATION DRYNESS INDEX (TVDI) OBTAINED FROM MODIS SATELLITE IMAGES

Ricardo Acosta
Department of Atmospheric Sciences
Universidade de São Paulo
Brasil

Tutors: Prof. M.A. Gilabert Navarro and Dr. Ernesto Lopez Baeza
Departament de Física de la Terra i Termodinàmica
Universidad de València
Dr. Moliner, 50. 46100–Burjassot (Spain)

1. Introduction

Soil moisture is a key parameter for a large number of environmental studies. Its knowledge is valuable to a wide range of governmental agencies and private companies which concerns with weather and climate, potential runoff and flood control, soil erosion, reservoir management and water quality.

Compared to other components of the hydrologic cycle, the volume of soil moisture is small; nonetheless, it is of fundamental importance to many hydrological, biological and biogeochemical processes, as well as in many applications such as hydrological modelling, weather and climate (Gillies *et al.* 1997)

Soil moisture has a major relevance in numerous problems derived from the lack of rain (Ruiz-Calaforra 2005). Thus, suffering from prolonged droughts, soil moisture may cause changes in ecosystems, land use and desertification in the long term.

It is important to emphasize that the soil water content is a parameter of difficult measurement since it presents a great spatial and temporal variability.

The application of remote sensing techniques within agroforestry systems is increasing. The Temperature Vegetation Dryness Index (TVDI) uses other two indexes Land Surface Temperature (LST) and Normalized Difference Vegetation Index (NDVI) to evaluate the dryness of the soil. Both the indexes are obtained by means of remote sensing techniques. The combination of LST and NDVI can be used as an indicator of drought, desertification monitoring, validation of hydrological models and the evaluation of the state of surface water and evapotranspiration (Sandholt and Pedersen 2004).

TVDI, also called «the index of dryness», can be very useful for monitoring and forecasting droughts. Due to droughts occurring in very broad areas, it is very difficult to monitor this phenomenon using only conventional methods. It is, therefore, a type of data set of great interest derived from Earth Observing Systems (EOS).

This study is being carried out within the framework of the Soil Moisture and Ocean Salinity (SMOS) Mission of the European Space Agency (ESA) which aims at observing soil moisture content from L band brightness temperatures (passive microwaves). The SMOS mission is developed jointly by France and Spain in order to determine, in a comprehensive manner, the content in soil moisture and ocean salinity; two parameters that the numerical weather prediction and simulation environmental models can not control so far and nevertheless have a definite importance on the reliability of their predictions.

The application to the Valencia Anchor Station (VAS) area is made as a preparation for the future validation of the soil moisture estimates retrieved from SMOS. This station has been chosen by the SMOS Mission as one of the primary validation sites for the Mission Commissioning Phase.

For the acronyms, see Table 1.

Table 1. Acronyms

a.s.l.	Above sea level
AWC	Absolute Soil Water Content
Cal/Val	Calibration/Validation
DOY	Day of year
ESDT	Earth Science Data Type
ESA	European Space Agency
EOS	Earth Observing System
IR	Infrared
LAI	Leaf Area Index
LST	Land Surface Temperature
MELBEX-I	Mediterranean Ecosystem L–Band characterisation Experiment (shrubs, matorral)
MELBEX-II	Mediterranean Ecosystem L–Band characterisation Experiment (vineyards)
MOD11A2	MODIS/Terra Land Surface Temperature/Emissivity 8-Day L3 Global 1km SIN Grid
MOD13A2	MODIS/Terra Vegetation Indices 16-Day L3 Global 1km SIN Grid
MODIS	Moderate Resolution Imaging Spectroradiometer
NASA	National Aero-Spatial Agency – United States
NDVI	Normalized Difference Vegetation Index
RWC	Relative Soil Water Content
SDS	Science Data Sets
SMOS	Soil Moisture and Ocean Salinity Mission
SM	Soil Moisture Content
SVAT	Soil-Vegetation–Atmosphere Transfer
TVDI	Temperature -Vegetation Dryness Index
VI	Vegetation Index
VAS	Valencia Anchor Station
VWC	Vegetation Water Content

2. Objective

The aim of this study is to use satellite imagery, by the creation of TVDI maps, in order to estimate soil moisture content in the whole region of study. The obtained remotely sensing data from MODIS sensor are then compared with soil moisture measurements obtained from Valencia Anchor Station. Afterwards, we should be able to estimate soil moisture for the whole region through an empirical relation that has still to be calculated.

3. Theoretical Background

3.1 The vegetation index – RVI, NDVI

The vegetation index (VI), defined as the arithmetic processing/combination of one or more spectral bands (related to different features of the vegetation), characterises the state or

type of vegetation. It is widely used for phenological monitoring purposes, morphological parameters assessment, vegetation classification, thinning/burning vegetation detection and any agriculture support.

Several are the types of VIs implemented, although RVI (Ration Vegetation Index) and NDVI (Normalized Difference Vegetation Index) indexes are the most used.

RVI is a first ratio–based vegetation and its formula is (Pearson and Miller 1972):

$$RVI = \frac{NIR}{RED} \tag{1},$$

where NIR is the reflectance in the near-infrared band and RED is the reflectance in the red band of the electromagnetic spectrum.

The RVI varies from zero to infinity while NDVI values may range between –1 (water stress) and 1 (exuberant vegetation with total coverage). The Normalized Difference Vegetation Index (NDVI) is the most often used and operational, global–based vegetation index, partly because its «ratio» properties can good cancel out the noise due to changing sun angles, topography, clouds or shadows, and atmospheric conditions (Huete and Justice 1999). Hence, both RVI and NDVI are functionally equivalent and can be related to each other by the following equation:

$$NDVI = \frac{NIR - RED}{NIR + RED} = \frac{RVI - 1}{RVI + 1} \tag{2},$$

NDVI calculation derives from two reflectance bands, one in the RED and the other in the NIR; in fact in these two bands, the vegetation has two specific answers. These data are collected by radiometer sensors installed on satellites or on any other platform placed near the target of interest.

The sequence of pictures below (Figure 1) shows images of leaves and respectively their reflectance at RED and NIR spectral bands and (1c) the corresponding NDVI values. In all figures we have 3 leaves, 2 green (active chlorophyll) and one yellow (dry, inactive chlorophyll). The images derived from the reflected radiance that reaches the sensor, resampled in scales of grey. Grey scale images range from 0 to 255 values, where 0 means black (no radiation reflected coming to the sensor) and 255 means white (maximum reflection from the target).

Figure 1. All figures have 3 leafs: 2 greens and 1 yellow – a) reflectance RED – b) reflectance NIR – c) NDVI

a   b   c
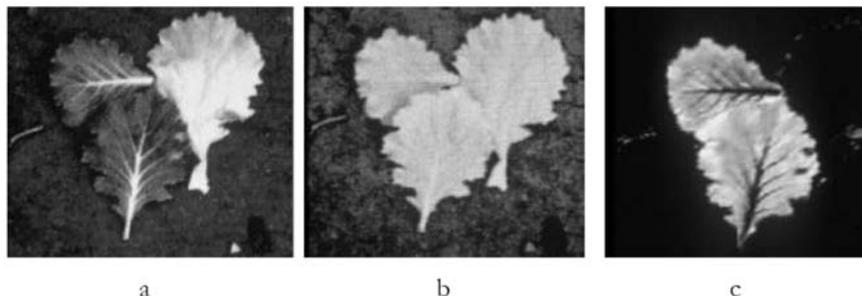
Figure 1.a) shows the RED reflectance of the leaves. In this range of wavelength, green leaves absorb most of the incident radiation, therefore the reflected radiation that reaches the sensor is very low (around 0). On the opposite, the yellow leave, due to its lack of chlorophyll, reflects almost all the radiation of the sun and the sensor registers high values of radi-

ance (around 255). As regards to NIR reflectance (Figure 1.b), all the three leaves show a high reflection, since, within this range of the spectrum, they have a low energy absorption. Thus, regardless of the amount of chlorophyll present in the leaf, all of them show a high value of radiation absorbed by the sensor.

In the last picture (Figure 1.c) NDVI values are shown. Since NDVI values come from the difference between the NIR and RED values, the yellow leaf is completely dark and hardly appears in the image. This is due to the high values of reflectance in both channels and because the difference between them is close to zero. The opposite occurs with the green leaves, where the difference between NIR and RED gives a higher value. It can be seen that the index is not perfect, since some interference appear in the picture.

Some considerations are needed: in despite of the response given by the vegetation in these bands, not everything reflected is due to vegetation response. Also bare soil or soil with some patches of vegetation show low values of NDVI, but although positive values. Except from water, is not expected to get negative values of NDVI, since RED reflectance is much higher than the NIR one. In confirmation of this, NDVI value may change a lot within a same region if the land is irrigated.

Another important factor is that clouds reflect in a similar way in the band of the visible and near infrared, so the expected values of the pixel are close to zero. Thus it is possible to create a mask for the clouds. A possible cause of uncertainties in the values of the index is the fact that small clouds, smaller than the size of the pixel, can not be detected by masking, reducing therefore the real value of NDVI. This happens for example in the Amazon region, where the presence of cloudiness is almost constant.

The vegetation index has been successfully used for studies concerning with biophysical parameters of the vegetation, such as biomass (Prince 1991), leaf area index (Clevers 1989); photosynthetically active radiation absorption (Asrar *et al.* 1984; Hatfield *et al.* 1984; Sellers 1985); agricultural productivity (Asrar *et al.* 1985); accurate soil moisture assessment.

3.2   *Temperature–vegetation dryness index (TVDI)*

This index is based on the physical interpretation of scatter plots that are created by the brightness temperatures versus NDVI. If the entire range of the fraction of vegetation cover and moisture content are represented in the data, the result has a triangular shape. The triangular shape of the scatter diagram is indicative of the physical limits on the distribution of soil moisture content and of the amount of vegetation cover (Gillies *et al.* 1997).

The edge of the point cloud created by the brightness temperatures versus NDVI represents the range of variation in brightness temperature. The upper boundary (dry edge) represents soils without available moisture; the lower boundary (wet edge) represents wet soils (Ruiz-Calaforra 2005).

NDVI is a rather conservative indicator of water stress, because vegetation remains green also after an initial water stress process. In contrast, the surface temperature can rapidly rise as a consequence of water stress (Goetz 1997). However, the amount of vegetation is an important factor for surface temperature estimation.

One of the alternative proposals, based on a simple empirical approximation and capable of representing all parameters involved in the process is the TVDI index (Sandholt *et al.* 2001). The simplification takes into account the air temperature, radiation balance, and atmospheric forcing variance by the empirical estimation of the LST/NDVI space. The method is conceptually and computationally straightforward and only satellite-derived information are used. With a direct observation of the limits of the triangular shape and during the analysis of LST versus NDVI, it is possible to obtain estimates of water stress in the soil. It is important to

Figure 2. Schematic diagram of the LST/NDVI space (Sandholt *et al.* 2002)
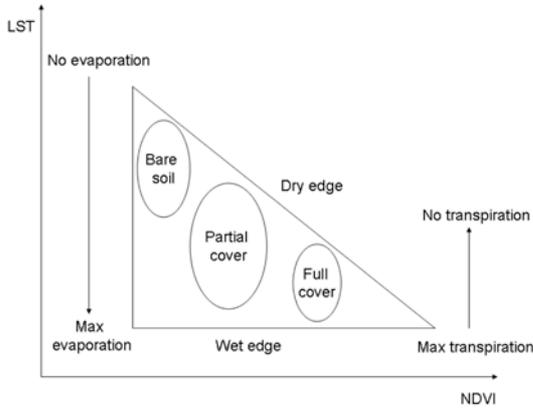
Figure 3. Scatter plot for example de ratio A/B. Adapted of Sandholt *et al.* 2002

$$TVDI = \frac{A}{B}$$
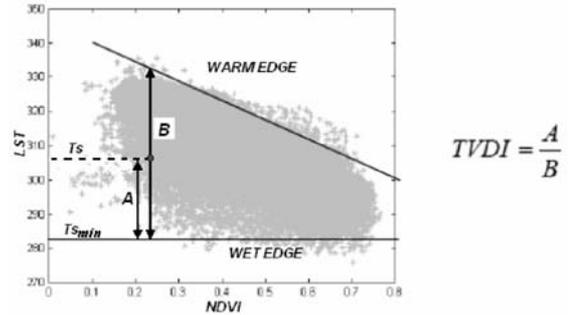
emphasize that, in order to ensure the correct representation of the limits of the triangle; the method requires a large amount of data.

The TVDI is an index that measures the dryness of the soil surface, based on empirical parameters (indirect method) of the relationship between LST and NDVI, since the index is related to soil moisture (Sandholt *et al.* 2002). The advantage of this method is that it can be used with all types of soil and is valid also for both dense vegetation cover and bare soil (Figure 2) (Andersen *et al.* 2002).

The index is defined by the ratio between the distance of a point on axis wet and wheelbase for a given value of NDVI.

The TVDI for a given pixel (NDVI, Ts) is the result of the ratio of lengths of the lines A and B (Figure 3).

The index TVDI relates to LST and NDVI through the equation,

$$TVDI = \frac{LST - LST_{MIN}}{LST_{MAX} - LST_{MIN}} \tag{3},$$

where LST and NDVI are the observed values for a given pixel. LST_{MIN} is the minimum surface temperature that we found in the study area.

Figure 4 shows the triangle defined by the point cloud formed by placing values of LST (y axis) versus the values of NDVI (x axis) for each value (pixel) of the study area. The coefficients «a» and «b» are constants and define the upper edge of the triangle (dry). Both the coefficient are obtained from the regression line formula,

$$LST_{MAX} = a + b.NDVI \tag{4},$$

This regression line corresponds to one formed from the maximum temperature of the soil surface (LSTMAX) that is achieved for each of the values of NDVI of the study area. This line defines the dry edge for each image. The maximum values of LST for a given NDVI, are represented by the dry edge (TVDI = 1), e.g. when water availability is limited. Whereas, the minimum values are limited by the wet edge (TVDI = 0) where evapotranspiration is high and therefore unlimited access to water.

Figure 4. Definition of the triangle and boundary dry. Adapted of Sandholt *et al.* 2002
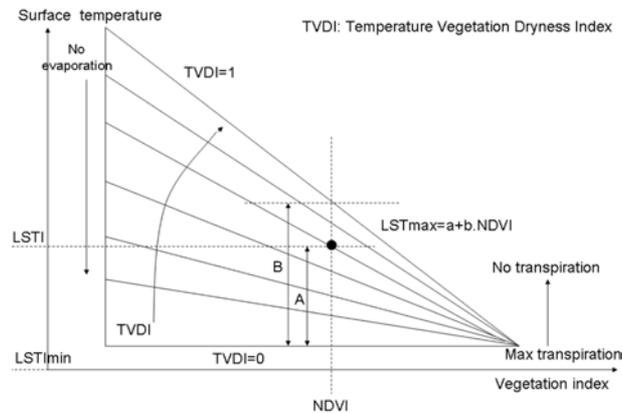
4. Methods, Data Sets and Study area

4.1. Study area

The study area (see Figures 5 and 6a,b), the natural region of La Plana de Utiel–Requena is located on the western area of Valencia, Spain. The region represents ~2000 km2 and is characterized by a dry continental climate, with frequent frosts and some snow events in winter, and even during spring, and cool nights in the short summer (Ruiz–Calaforra 2005).

The predominant soils are Haplic Calcisols, Petric Calcisols and Calcaric Cambrisols. The Calcaric soils and Haplic Calcisols are deep soils with accumulation of carbonates and low organic matter content. In general, there are clearly two layers, the first of 20–25 cm in dark yellowish brown moist texture with moderate fine-granular. The second layer is a solid and hard conglomerate with a crust of calcium carbonate (cite missing, 2004).

The relief is characterized by generally plain (slope <2%) and slightly undulated regions (8%-15%), by quaternary sediments and is surrounded by mountainous regions on the North and East, and by the Cabriel River basin on the western and southern boundaries of the plateau.

In spite of the relatively flat topography of the area, the small altitude variations of the region clearly influence climate, which oscillates between semiarid in the areas of the towns of Utiel and Caudete de las Fuentes and dry − sub–humid towards Villagordo del Cabriel. The altitudinal difference between both climate types, correspond to $800 − 850$ m of height on sea level. Annual mean temperatures oscillate between 12°C of Villagordo del Cabriel and 14.2°C of Caudete de las Fuentes. Annual precipitation values vary between 396 mm in Utiel and 451 mm of Caudete de las Fuentes and Villagordo del Cabriel. The periods without frost are the same for all the three town areas, from May to November. Maximum precipitation values occur in spring and autumn. The spring month of maximum precipitation occurrences is generally May, whereas the autumnal month is variable: October for the areas of Caudete de las Fuentes and Utiel, and November for Villagordo del Cabriel (Figure 7).

The Utiel meteorological station of INM collected a complete data set of monthly precipitation, days of precipitation and days of precipitation above or equal to 1 mm, 10 mm and 30 mm from 1971-2006 without any data failure. The significant data are shown in the following graphs. October, in autumn, and May and April in spring are the months where the most significant precipitation events occurred (Figure 8).

Figure 5. Location of the area of study and types of land use
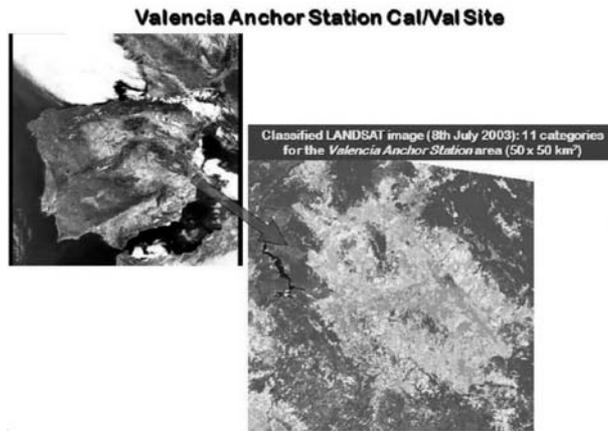

Figure 6. a) The region of study, demarcated by the small square; b) Map with type of use of the land area

   (a)   (b)
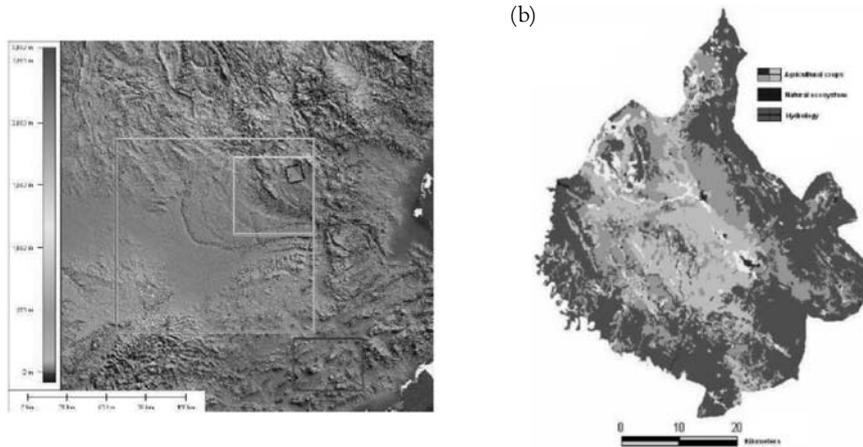
Figure 7. Monthly mean precipitation in different towns of the area, namely, Requena, Caudete de las Fuentes, Utiel and Villagordo del Cabriel
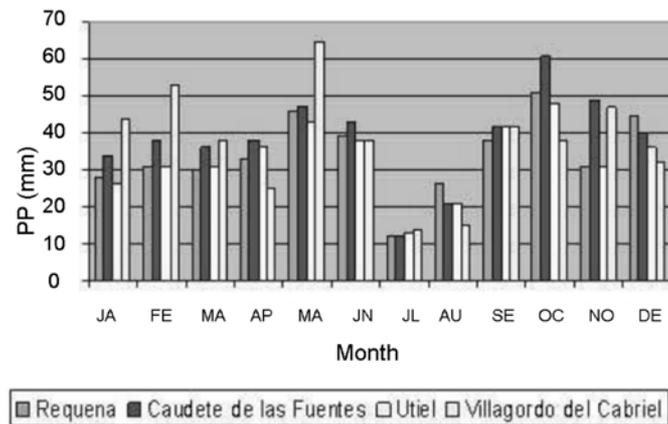
Figure 8. a) Annual precipitation at Utiel; b) Monthly mean precipitation at Utiel for different annual periods
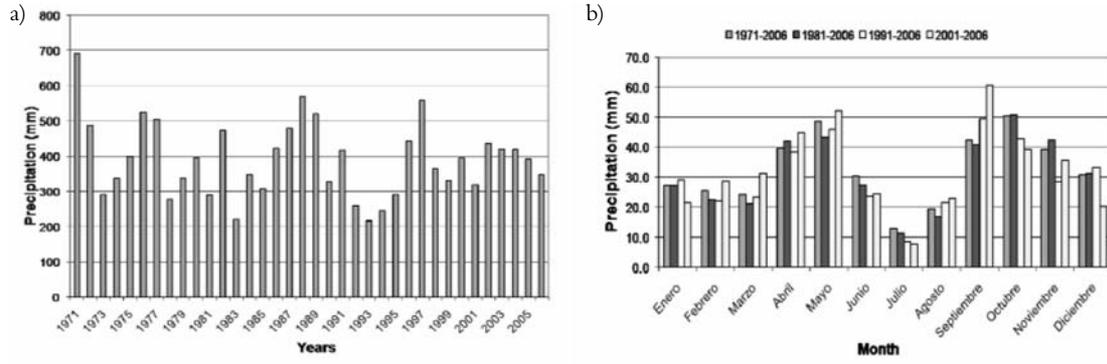

Figure 9. a) Theta Pobre sonde used in obtaining the soil moisture; b,c) Probe installed in the vineyard
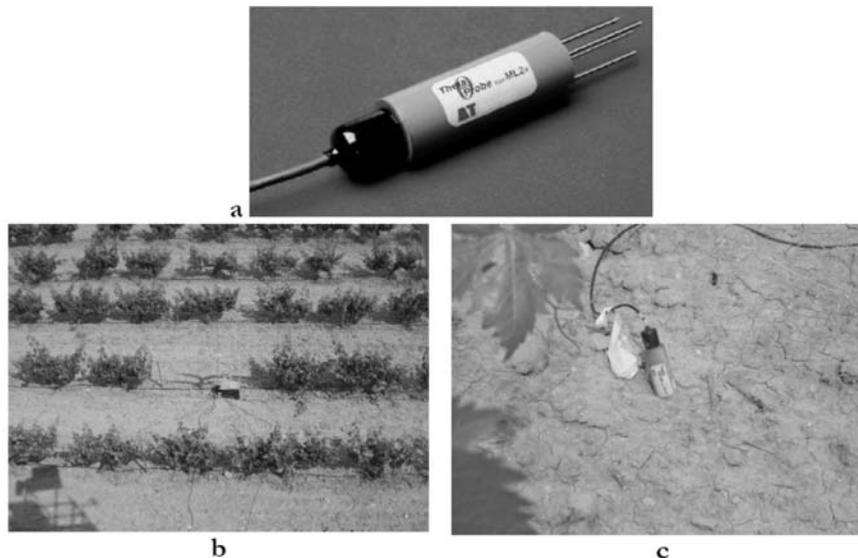
4.2   Data sets

4.2.1 Soil moisture

The Theta Probe (Figure 9) sonde was used to measure the water content in soil. Through changes in dielectric constant values in soil moisture, which are proportional to moisture contents, the absolute water content can be measured.

The probe is an impermeable device that contains board electronic and 4 sensors and can be fixed in the soil. When running, it generates a signal of 100MHz which can be attenuated by means of two components: a dielectric apparent constant and an ionic conductivity.

It was installed under the vineyards (Figure 9 b,c) of the region VAS, and started to collecting the information every 10 minutes beginning from the 1st of April, 2007 until December 31, 2007.

4.2.2 LST and NDVI – MODIS Satellite

MOD11 and MOD13 products have been used to obtain the TVDI index in order to respectively calculate land surface temperature and NDVI vegetation index. The sub-products we have chosen are MOD11A2 and MOD13A2, version 004, of validated data. Table 2 presents the characteristics of the data obtained.

Table 2. Characteristics of MODIS products used

	MOD11A2	MOD13A2
ESDT	MODIS/Terra – Land Surface Temperatura Emissivity 8-Day L3 Global 1 km SIN Grid	MODIS/Terra – Vegetation Indices 16-Day L3 Global 1 km SIN Grid
Área	~1100 x 1100 km	~1100 x 1100 km
Size of file	24MB	32 MB
Spacial Resolution	1 km	1 km
Projection	Sinusoidal	Sinusoidal
Data type	16-bits entero sin signo	16-bits entero sin signo
Data format	HDF-EOS	HDF-EOS
SDSs	12	11

MOD11A2 obtains images and information of LST, averaging eight days with a resolution of 1 km, while MOD13A2 are NDVI global images obtained by averaging every 16 days, also 1km resolution.

The images refer to the period between January 1, 2007 and 31 December, 2007. During that period we used the existing images every 16 days, e.g. 24 images for each MOD13A2. All images were used in pairs, at the same time.

4.3   Methods

In order to generate a TVDI image, the values of surface temperature and NDVI for each pixel of MODIS data, placed on board of the NASA EOS Terra and Aqua satellites, were extracted. The achieved triangular LST/NDVI relationship was modelled by linear adjustment procedures. In order to calculate the coefficients of the linear regression model, scatter plots were created and the information extracted. LSTMAX in each NDVI class was used to model the dry region and LSTMIN was used for the wet region. The following step will be the application of the equation to generate the TVDI image for the Valencia Anchor Station that is the primary validation area for SMOS. It is expected to get, in a short future, the empirical relationship between the index TVDI and soil moisture for the pixel of the VAS. It is also expected to find high correlations that will allow us to build a map of soil moisture for the study region.

5.   Results and discussions

Referring to the year 2007, the region of study, located within Valencia Anchor Station area, presents a rainfall regime characterized from two predominant periods (the upper diagram of Figure 10). The first maximum, characteristic of spring (see Figure 7), occurred in the first half of the month of April, reaching values of 71.8 mm accumulated in a period of 16 days. The measurements of soil moisture started up precisely in this period, and it is observed that

Figure 10. In the table above, the accumulated precipitation in 15-day and absolute soil moisture in the VAS. Below, the temperature and humidity of the air and observed Land Surface Temperature obtained by MODIS satellite
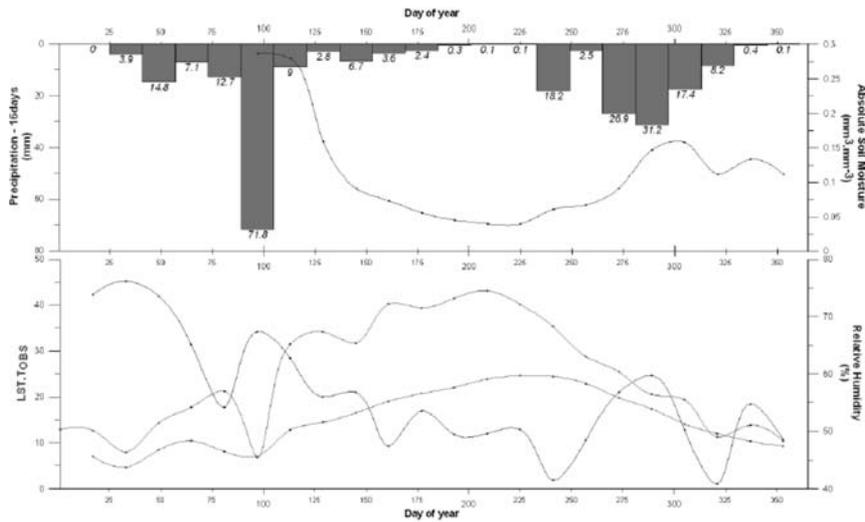
for the period of study the highest values of soil moisture occurred in this 15-day, with values of 0.28 and 0.29 m³, fortnights for the DOY 097 and 113, respectively.

The period of drought was unexpectedly four months long. This is obvious if both rainfall and soil moisture values are measured at the VAS (see Figure 10). In August, the rain events returned, therefore a positive trend in soil moisture occurred, reaching its second annual maximum during the month of November. It is important to note that there is a lag of 15 days, between the maximum of rain and maximum moisture in the soil.

The variables of temperature and humidity have the expected behaviour according to the seasonality. The values of minimum and maximum temperature respectively occurred in January (4.69°C) and August (24.66°C). The same figure also contains the plot of LST obtained by satellite, and, as expected, it follows the curve of air temperature. There is a greater decay of LST than half of Tair on DOY 097. This will be discussed below.

Figure 11 shows the daily accumulated precipitation in the VAS and the TVDI index calculated for the same point through satellite images processing. As mentioned above, TVDI index is a good indicator of water stressed soil. It appears that together with rainy periods decreasing values of TVDI also occur, due to a more presence of water. For the first maximum value of rain in April, the index quickly responded with efficiency to the changes of rainfall and temperature observed.

However, there is a shift during the rainy season of autumn. The TVDI reaches its maximum value before the peak of soil moisture observed (see Figure 10). One possible explanation is based on the curve of infiltration of water into the soil. During the first rain observation, in April, the rainfall was so intense that still presents a condition of greater wetting (rain in February and March).

For the station of autumn, the ground is at a disadvantage, with a high water deficit.

For this reason, the process of wetting the soil, is located in another phase of the curve of infiltration, and it depends on water processes distribution in the vertical column, therefore the process is much slower. The TVDI takes into account only two variables, LST and NDVI, in its form may not be able to represent this process.

Figure 12a diagram shows the result for DOY 273. As for any analysis (except DOY 017 and 033), a triangular distribution of points is obtained. Since various types of vegetation cover

Figure 11. The daily accumulated precipitation and the index calculated TVDI and RWC
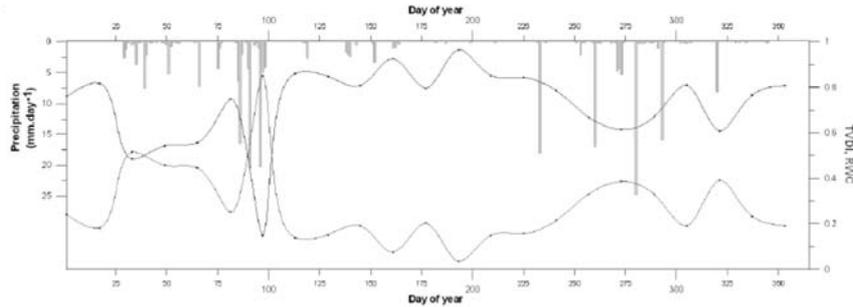
Figure 12. a) Scatterplot LST versus NDVI in DOY 273, b) the edge dry, or line LSTMAX
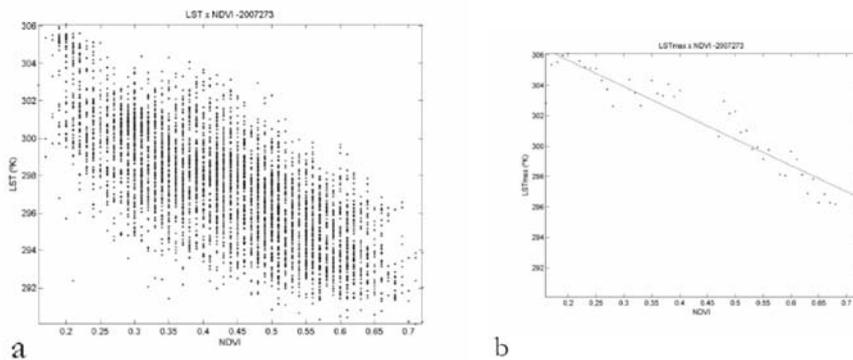
(forest, bush, vineyards) and of bare soil are present in the study region, we can confirm that, improving a look more reliable, all surface conditions can be answered by the calculation of TVDI. Figure 12b exemplifies the dry limit obtained in figure 12a. All figures for the studied period are presented in Appendix II.

The Figure 13 shows the map of TVDI, LST and NDVI obtained for the period leading up to fifteen days the DOY 273. Note that the values of NDVI are low and the average values are below 0.7. Three main areas with distinct vegetation are characterized by the highest values of NDVI: the central region, the southern, which is manly vineyards cultivated, and the region that circumvents the central region. This identification is presented according to the map of land use as is shown in Figure 6b. In the Vineyard lands the NDVI assumes values between 0.22 and 0.35 both in winter and in summer, while in forest lands, reaches minimum values of 0.5 and maximum of 0.8.

In order to obtain the images of LST, it may happen to have the presence of many pixels with very low values. This problem is due to the interference of high cloudiness during that period. We found this kind of problem for DOY 097. The fifteen days later on this date (DOY 097) heavy rains occurred (Figure 11), on average, below the expected values for many pixels in the region of study.

The index TVDI was both spatially and temporally very satisfactory to explain the water stress condition suffered by the soil. There was a relationship between the period of rain and low index TVDI. While we can not obtain quantitative measures (due to the low consistency of the dataset) of the correlation between the index TVDI and soil moisture observed. There is a linear dependence between the two variables. Garcia *et al.* (2006) in his work suggested a

Figure 13. a) TVDI estimated for DOY 273, images obtained b) NDVI; c) LST
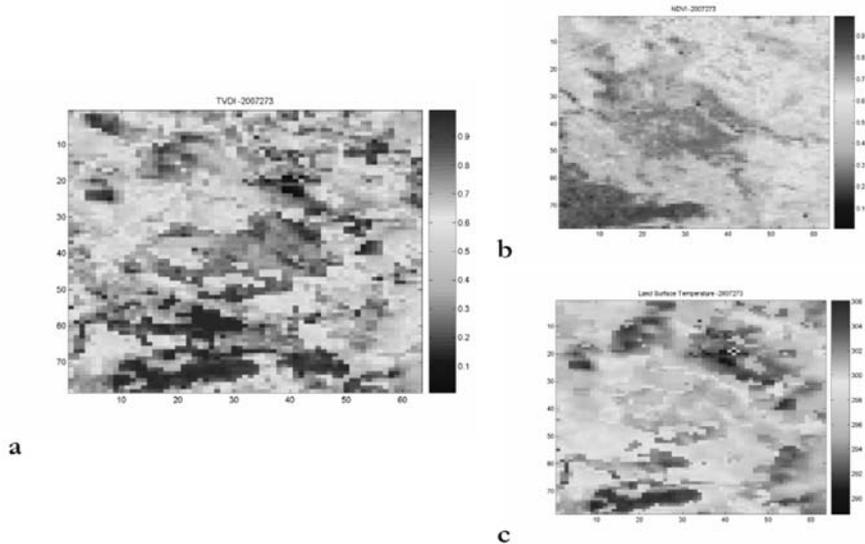

Figure 14. Relative Water Content, Image for DOY 273
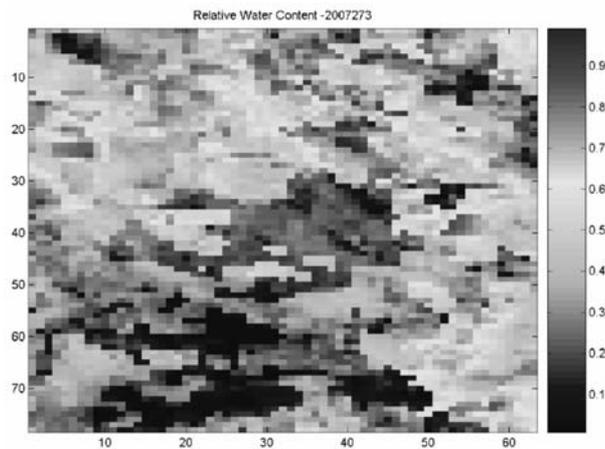
direct proportionality between the TVDI and potential evaporation. Drawing up the same concepts, an approach for RWC (Relative soil Water Content) may be suggested by the equation:

$$RWC = 1 - TVDI \qquad\qquad\qquad (5)$$

The Figure 14 exemplifies a future product to be achieved through the analysis of TVDI. The AWC (Absolute soil Water Content) can also in future be measured. In order to obtain the calculation of daily TVDI in scale, as the mean of 15 days, a greater range of data is required so then patterns of temperature and rainfall in the region can be mixed. Important empirical models, that are obtained for each type of vegetation (Agricultural crops, Natural Ecosystem), will be applied for construction of maps of soil moisture absolute.

6. Conclusions

The index TVDI was able to represent the spatial and temporal patterns of the conditions of water stress soil in the region of Valencia Anchor Station. This is closely related to the variability of rainfall, although the review was only qualitative, since the rainy periods are followed by decreasing of the index TVDI.

Through the index, it is possible to estimate two variables of the state of the soil: (i) the relative soil moisture, through the application of a procedure based on the correlation between the index and saturated soil moisture and (ii) the absolute soil moisture, through applying an empirical model in order to correlate the index with soil moisture in situ measurements.

For future studies, in order to obtain the index TVDI, it is suggested the use of daily data. If the data results are then overlaid with land use map, an estimation of the actual content of water in the soil can also assessed. All these information opportunely calibrated and validated, can be further applied also to wider areas.

Acknowledgments

References

Andersen J., Sandholt I., Jensen K.H., Refsgaard J.C.Y., Gupta H. (2002). Perspectives in using a remotely sensed dryness index in distributed hydrological models at the river basin scale. *Hydrological Processes*, 16: 2973-2987.

Asrar G., Fuchs M., Kanemasu E.T., Hatfield J.L. (1984). Estimating absorbed photosynthetic radiation and leaf area index from spectral reflectance in wheat. *Agronomy Journal*, v. 76, n. 2: 300-6.

Asrar G., Kanemasu E.T., Jackson R.D., Pinter P.J. (1985). Estimation of total above ground phytomass production using remote sensed data. *Remote Sensing of Environment*, v. 17, n. 3: 211–20.

Clevers J.G.P.W. (1989) The application of a weighted infrared–red vegetation index for estimating leaf area index by correcting for soil moisture. *Remote Sensing of Environment*, v. 29, n. 1: 25-37.

Garcia M., Palacios-Orueta A., Puigdefábregas J., Contreras S., Barrio G.D., Fernández F.J., Moreno M.T. (2006). Estimating evapotranspiration from TVDI: Towards a land degradation indicator for regional analysis. The 2nd International Symposium in quantitative remote sensing, 2006. Torrent, Spain.

Gillies R.R., Carlson T.N., Gui J., Kustas W.P., Humes K.S. (1997). A verification of the 'triangle' for obtaining surface soil water content and energy fluxes from remote measurements of the Normalized Difference Vegetation Index (NDVI) and surface radiant temperature. *International Journal of remote sensing*, 18 (15): 3145-3166.

Goetz S.J. (1997). Multi–sensor analysis of NDVI, surface temperature and biophysical variables at a mixed grassland site. *International Journal of Remote Sensing*, 18: 71-94.

Hatfield D.L., Asrar G., Kanemasu E.T. (1984). Intercepted photosynthetically active radiation estimated by spectral reflectance. *Remote Sensing of Environment*, v. 14, n. 1-3: 65-75.

Huete A.R., Justice C. Modis (1999). Vegetation index (MOD13) algorithm theoretical basis document. Ver. 3.

Pearson R.L., Miller L.D. (1972). Remote mapping of standing crop biomass for estimation of the productivity of the short-grass. 8th International Symposium on Remote Sensing of Environment, MI, p. 1357-1381,

Prince S.D. (1991) A model of regional primary production for use with coarse-resolution satelitte data. *International Journal of Remote Sensing*, v. 12, n. 6: 1313-30.

Ruiz-Calaforra C. (2005). Verificación y aplicación del índice de sequedad del suelo temperatura-vegetation diference index con datos de teledetección del sensor MODIS, en la comarca de la Plana de Utiel-Requena. Trabajo de fin de carrera. Universidad de Valencia. Noviembre, 2005.

Sandholt I., Rasmussen K., Andersen J. (2001). Derivation of a dryness index from NOAAAVHRR data for use in large-scale htdological modelling. Remote sensing and Hydrology 2000 (Proceedings of a symposium held at Santa Fe, New Mexico, USA, April 2000). IAHS Red Books, 267.

Sandholt I. *et al.* (2002). A simple interpretation of the surface temperature-vegetation index space for assessment of surface moisture status. *Remote Sensing of the Environment*, 79: 213-224.

Sandholt I.Y Pedersen M.W. (2004). Relation between field measurements of soil moisture and information derived from satellite observations of vegetation and surface temperature. *Geophysical Research Abstracts*, 6: 05490.

Sellers P. (1985). Canopy reflectance, photosynthesis and transpiration. *Int. J. Remote Sens*, 8: 1335-1372

Appendix I

Figure 15. Images obtained for DOY 001. a) TVDI; b) NDVI; c) LST
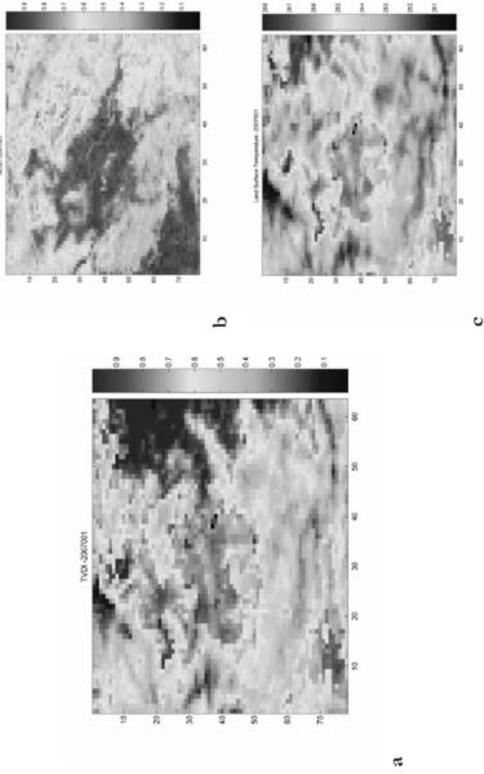
Figure 16. Images obtained for DOY 017. a) TVDI; b) NDVI; c) LST
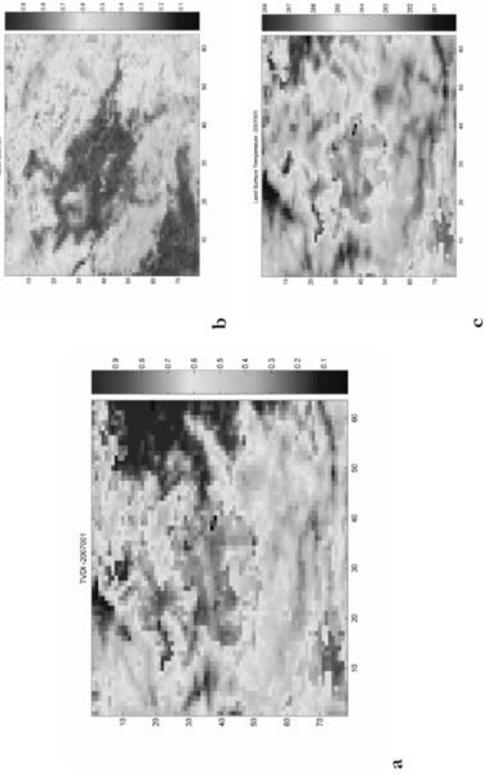
Figure 17. Images obtained for DOY 033. a) TVDI; b) NDVI; c) LST
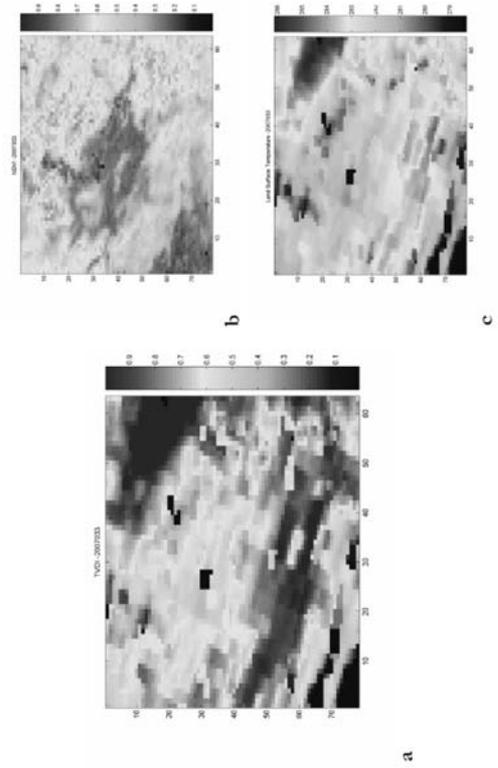
Figure 18. Images obtained for DOY 049. a) TVDI; b) NDVI; c) LST
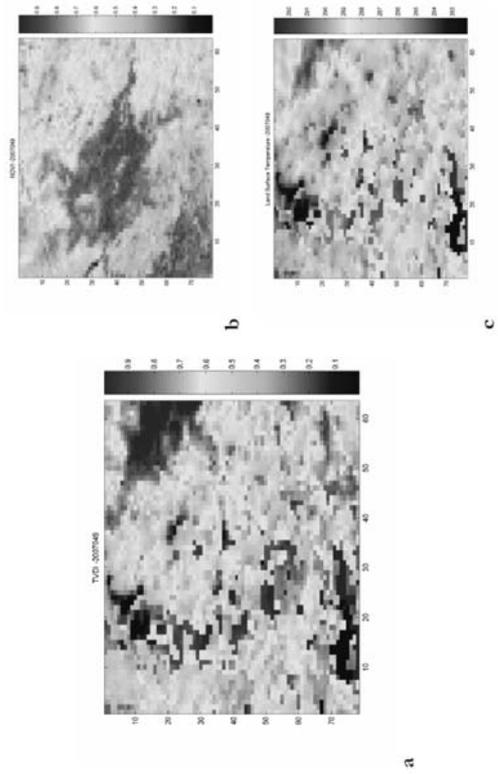
Figure 19. Images obtained for DOY 065. a) TVDI; b) NDVI; c) LST
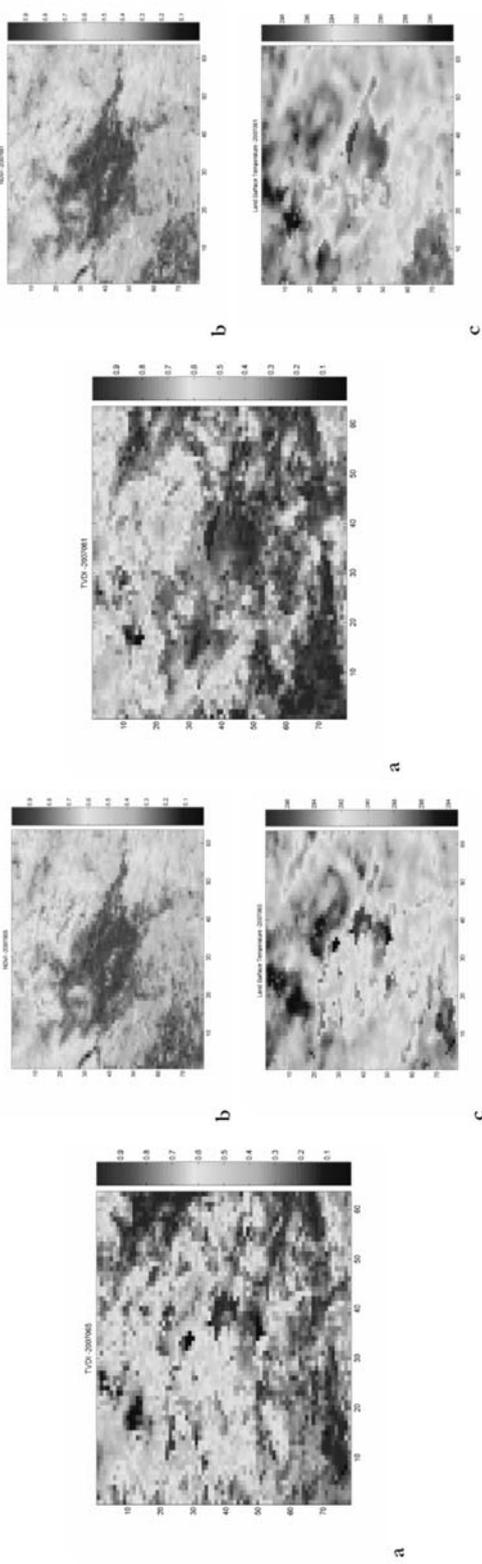
Figure 20. Images obtained for DOY 081. a) TVDI; b) NDVI; c) LST
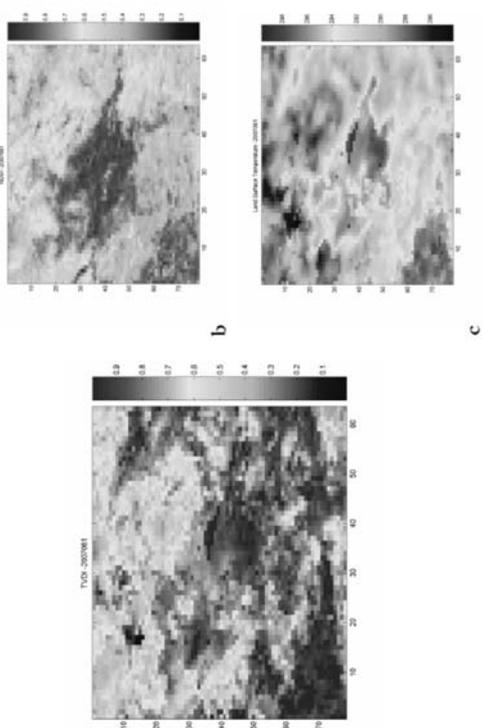
Figure 21. Images obtained for DOY 097. a) TVDI; b) NDVI; c) LST
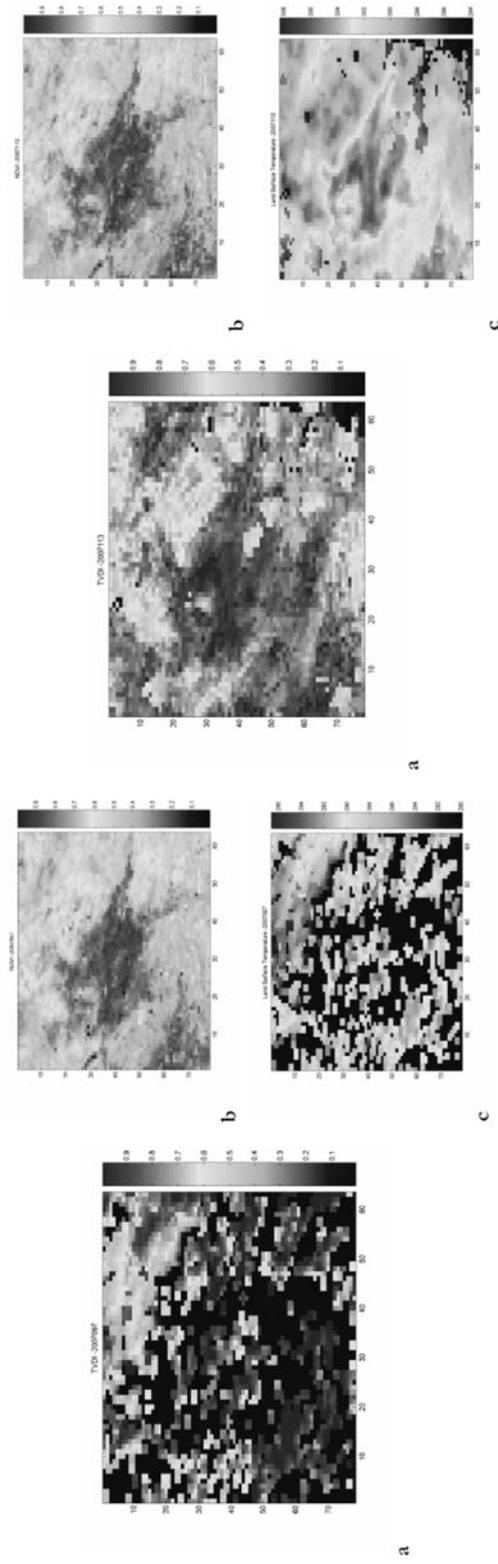
Figure 22. Images obtained for DOY 113. a) TVDI; b) NDVI; c) LST
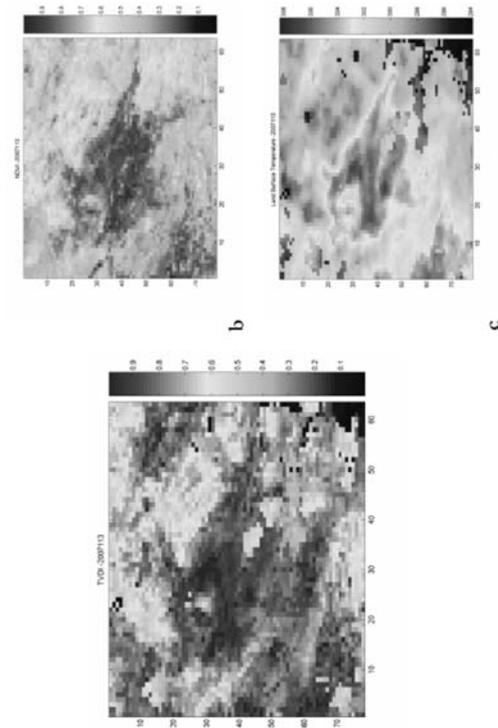
Figure 23. Images obtained for DOY 129. a) TVDI; b) NDVI; c) LST
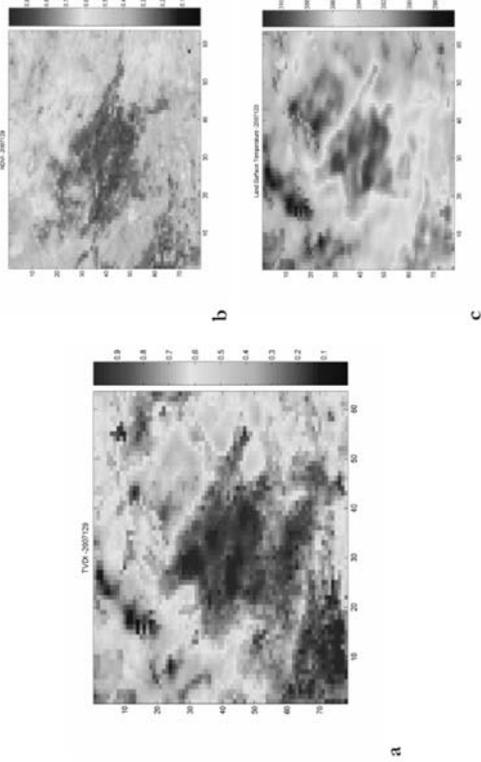
Figure 24. Images obtained for DOY 145. a) TVDI; b) NDVI; c) LST
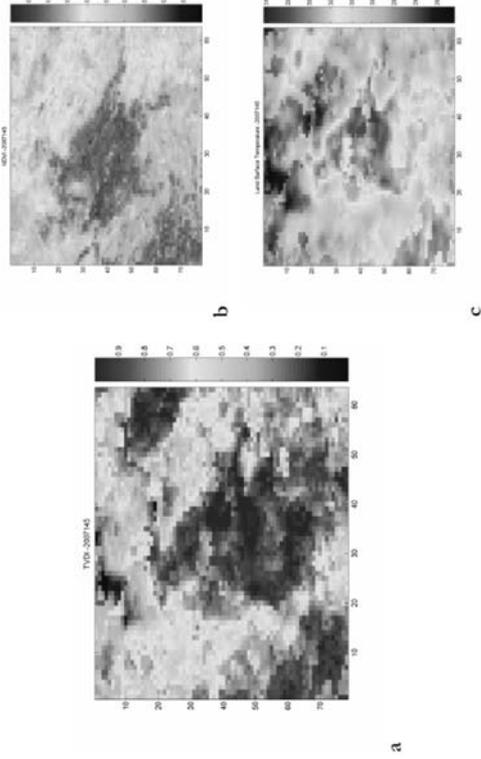
Figure 25. Images obtained for DOY 161. a) TVDI; b) NDVI; c) LST
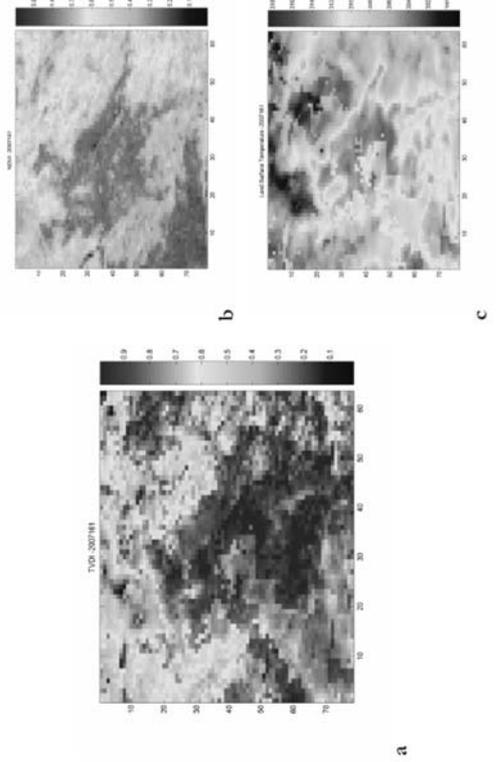
Figure 26. Images obtained for DOY 177. a) TVDI; b) NDVI; c) LST
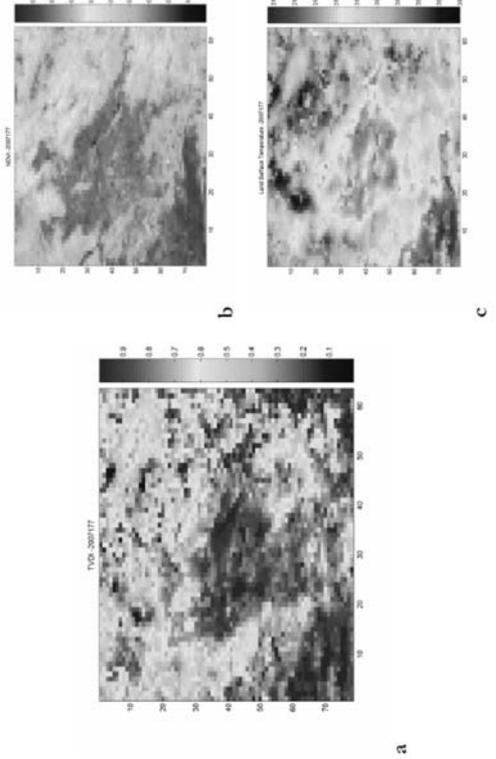
Figure 27. Images obtained for DOY 193. a) TVDI; b) NDVI; c) LST
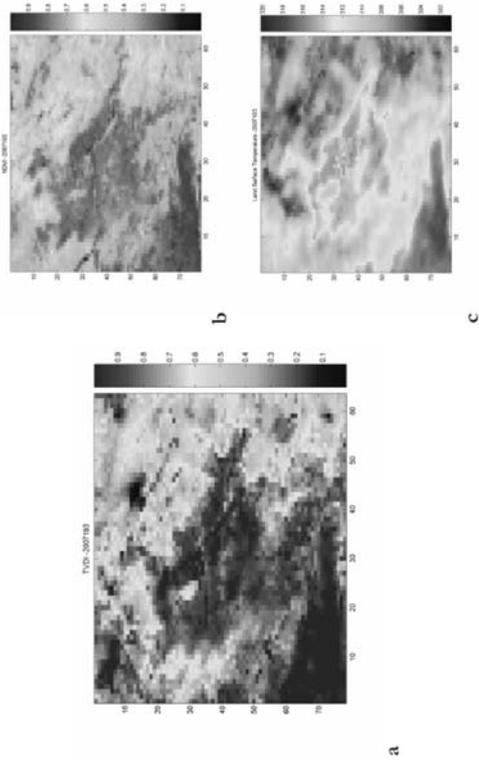
Figure 28. Images obtained for DOY 209. a) TVDI; b) NDVI; c) LST
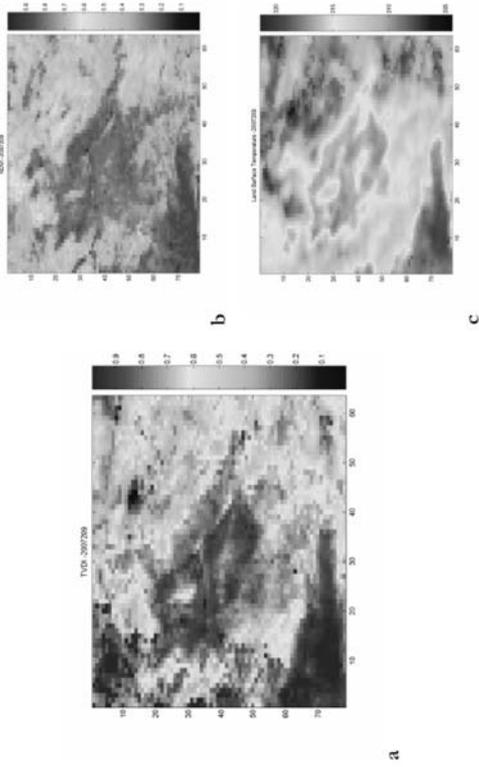
Figure 29– Images obtained for DOY 225. a) TVDI; b) NDVI; c) LST
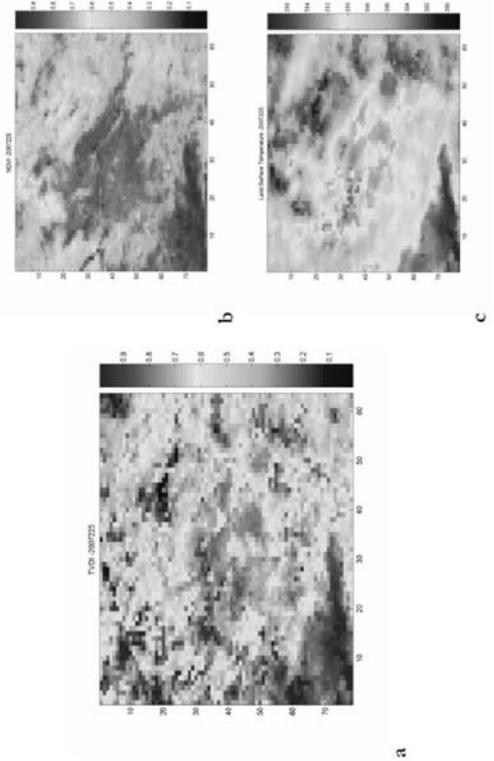
Figure 30. Images obtained for DOY 241. a) TVDI; b) NDVI; c) LST
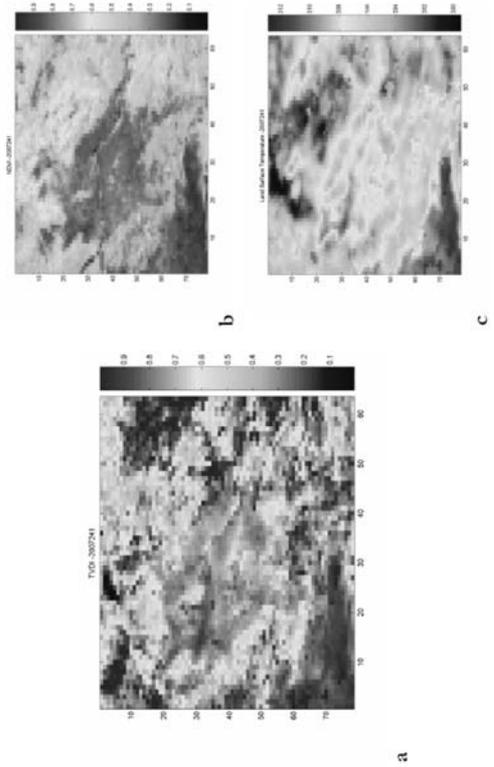
Figure 31. Images obtained for DOY 257. a) TVDI; b) NDVI; c) LST
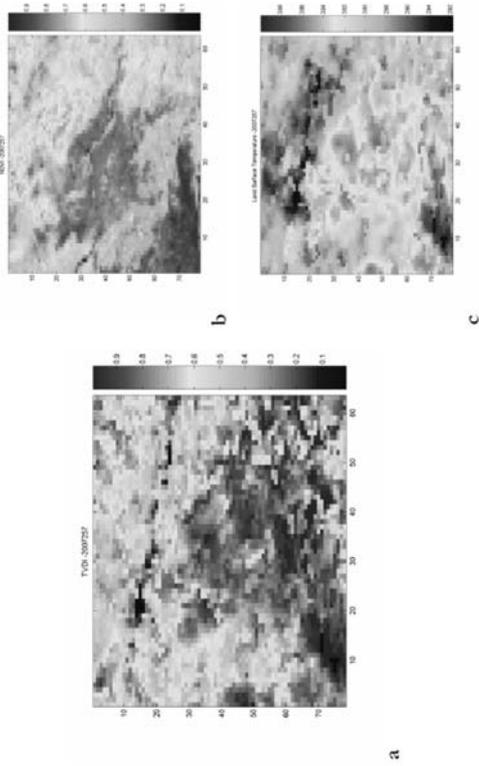
Figure 32. Images obtained for DOY 273. a) TVDI; b) NDVI; c) LST
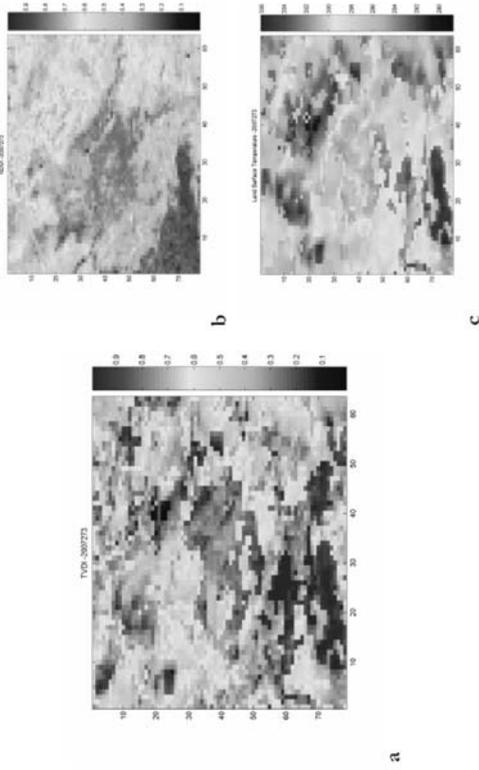
Figure 33. Images obtained for DOY 269. a) TVDI; b) NDVI; c) LST
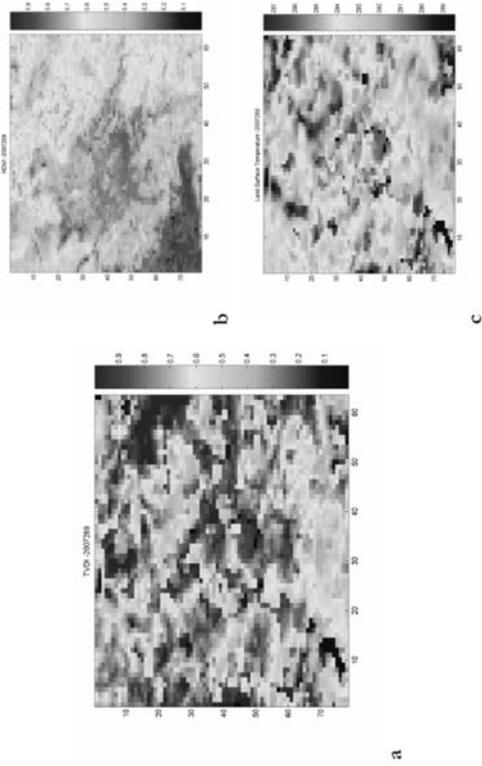
Figure 34. Images obtained for DOY 305. a) TVDI; b) NDVI; c) LST
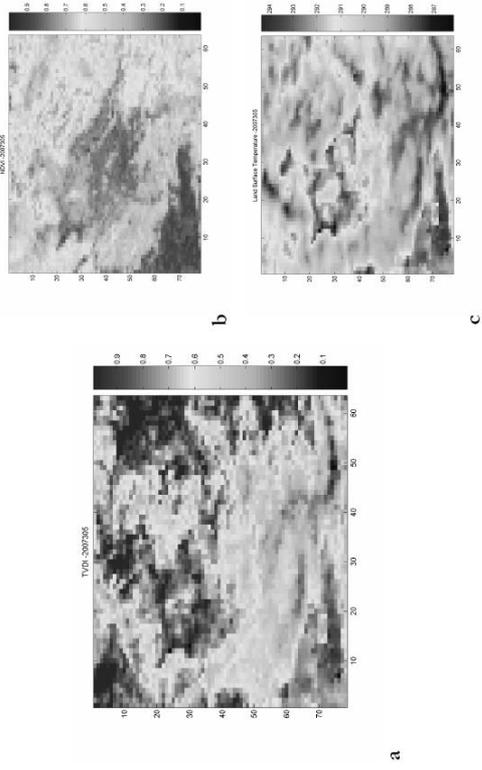
Figure 35. Images obtained for DOY 321. a) TVDI; b) NDVI; c) LST
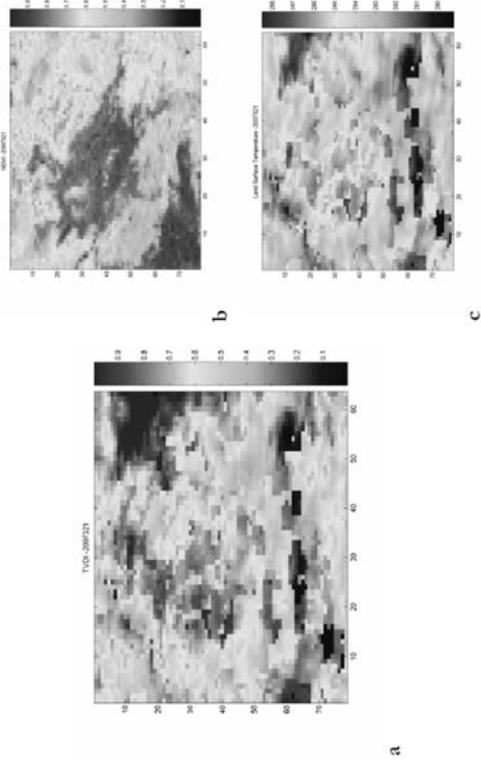
Figure 36. Images obtained for DOY 337. a) TVDI; b) NDVI; c) LST
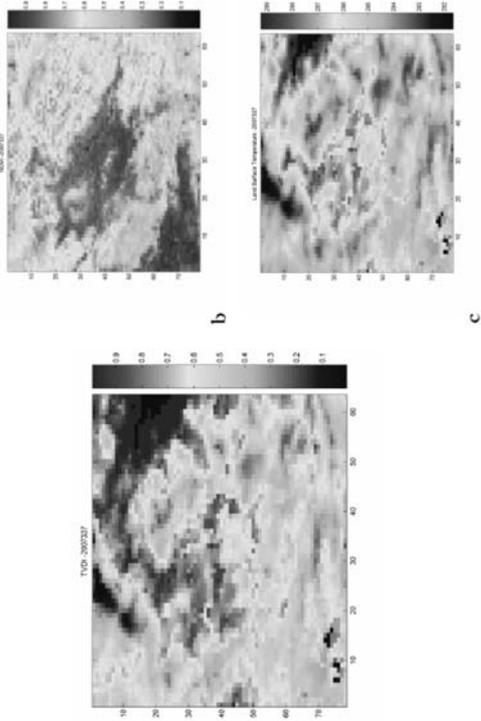
Figure 37. Images obtained for DOY 345. a) TVDI; b) NDVI; c) LST
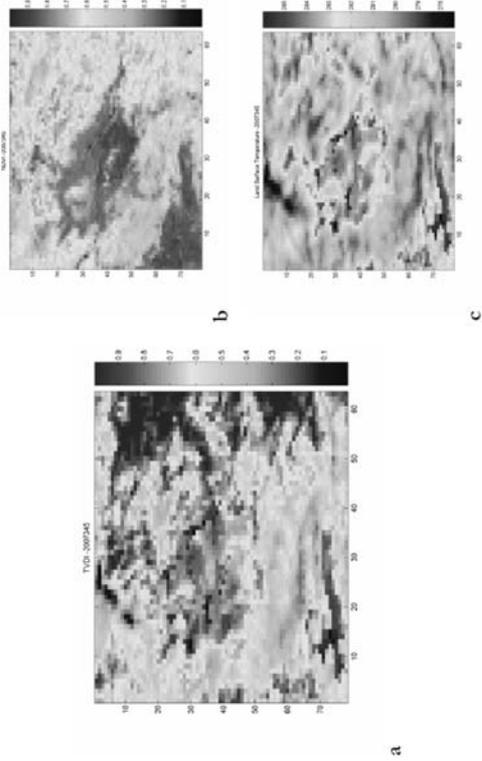
Figure 38. Images obtained for DOY 353. a) TVDI; b) NDVI; c) LST
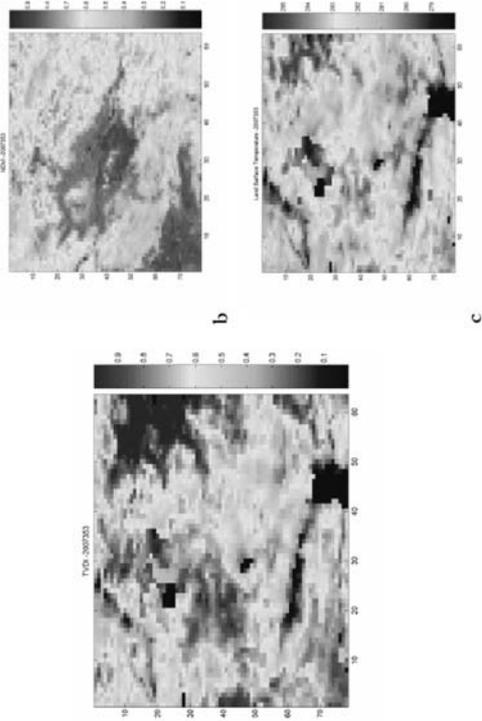
Appendix II

Figure 39. a) Scatterplot LST versus NDVI in DOY 001, b) the edge dry, or line LSTMAX
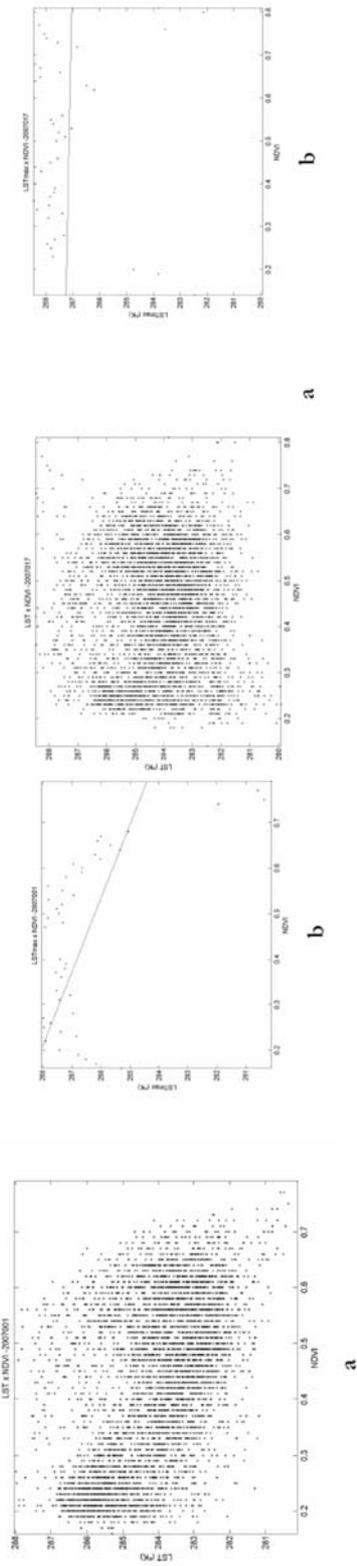
Figure 40. a) Scatterplot LST versus NDVI in DOY 017, b) the edge dry, or line LSTMAX
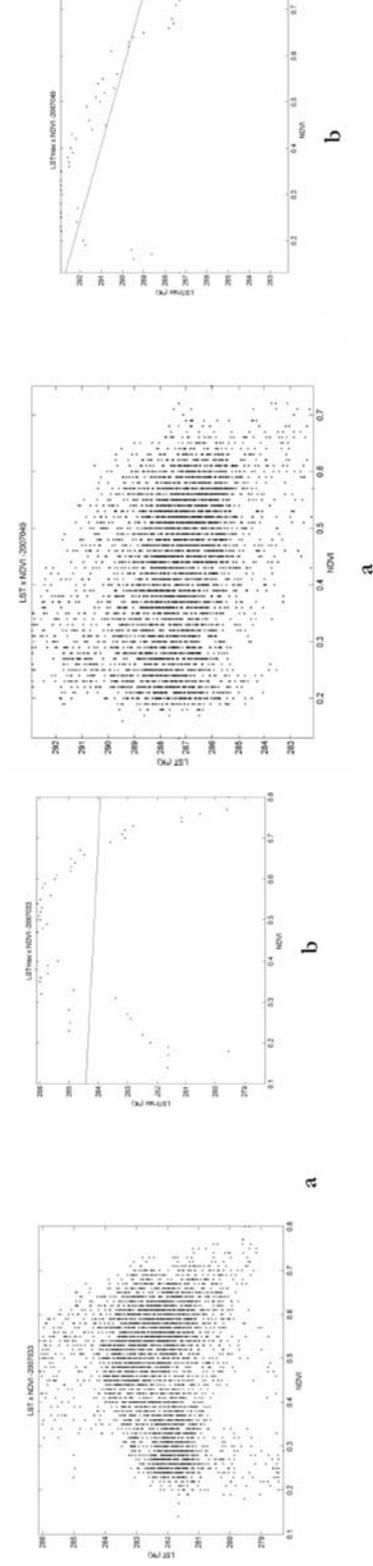
Figure 41. a) Scatterplot LST versus NDVI in DOY 033, b) the edge dry, or line LSTMAX
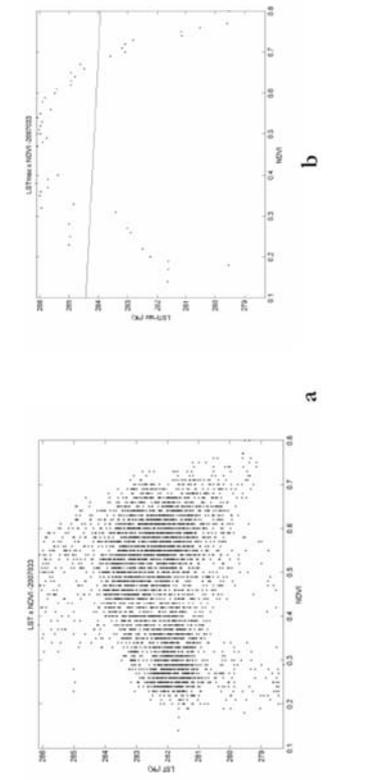
Figure 42. a) Scatterplot LST versus NDVI in DOY 049, b) the edge dry, or line LSTMAX
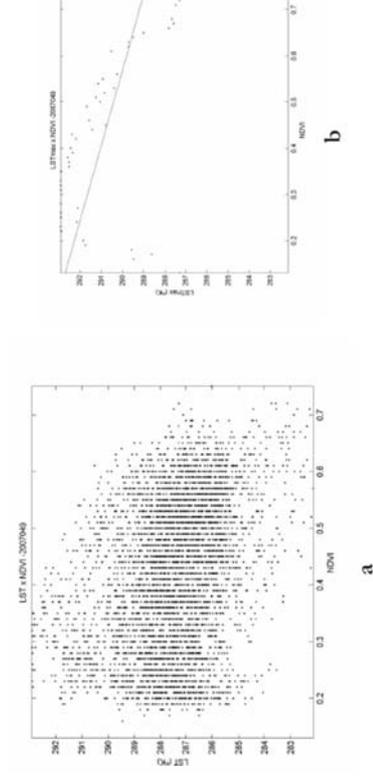
Figure 43. a) Scatterplot LST versus NDVI in DOY 065, b) the edge dry, or line LSTMAX
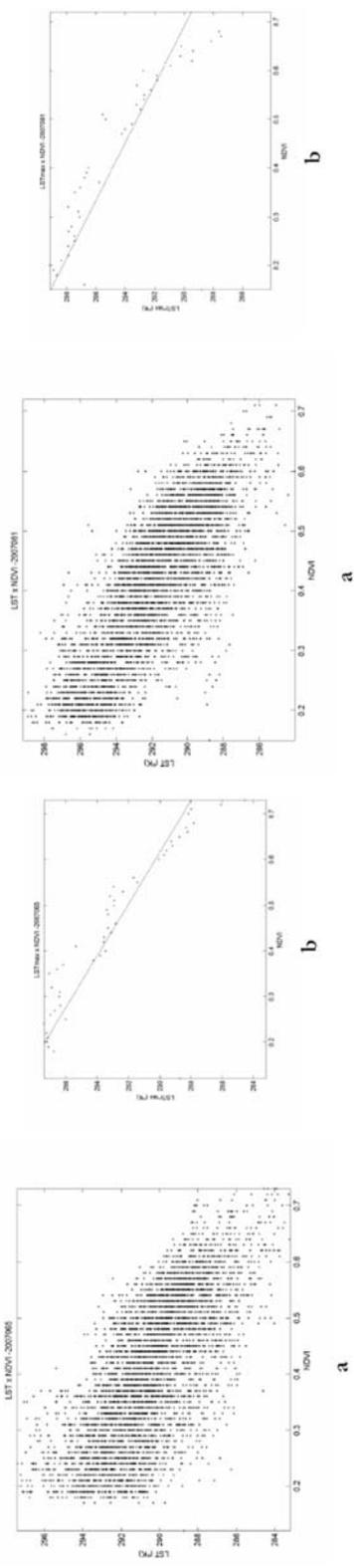
Figure 44. a) Scatterplot LST versus NDVI in DOY 081, b) the edge dry, or line LSTMAX
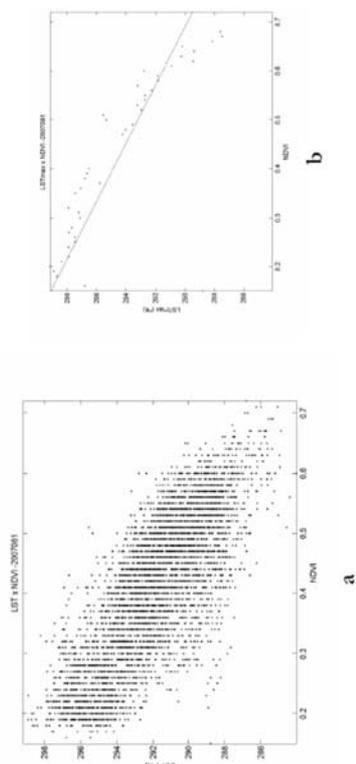
Figure 45. a) Scatterplot LST versus NDVI in DOY 097, b) the edge dry, or line LSTMAX
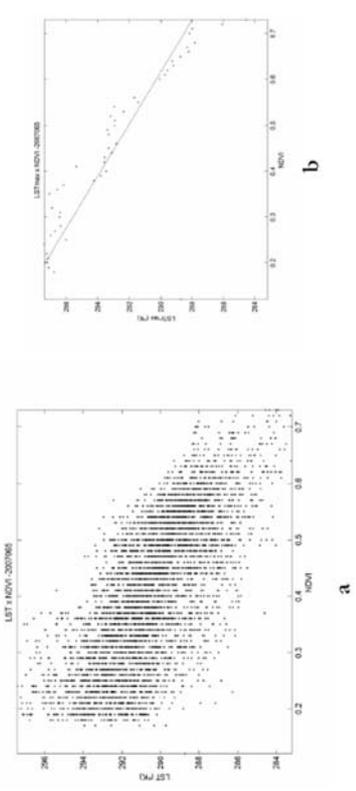
Figure 46. a) Scatterplot LST versus NDVI in DOY 113, b) the edge dry, or line LSTMAX
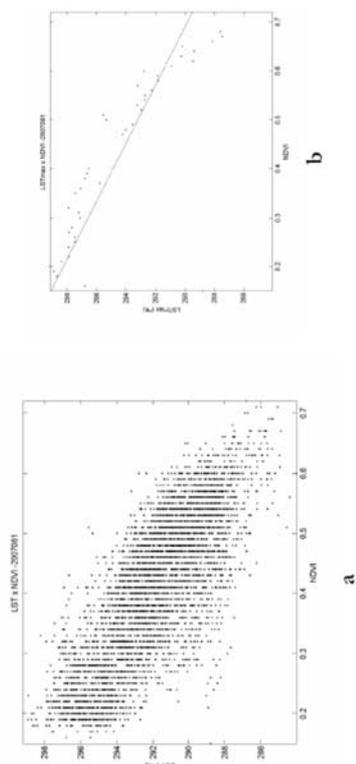
Figure 47. a) Scatterplot LST versus NDVI in DOY 129, b) the edge dry, or line LSTMAX
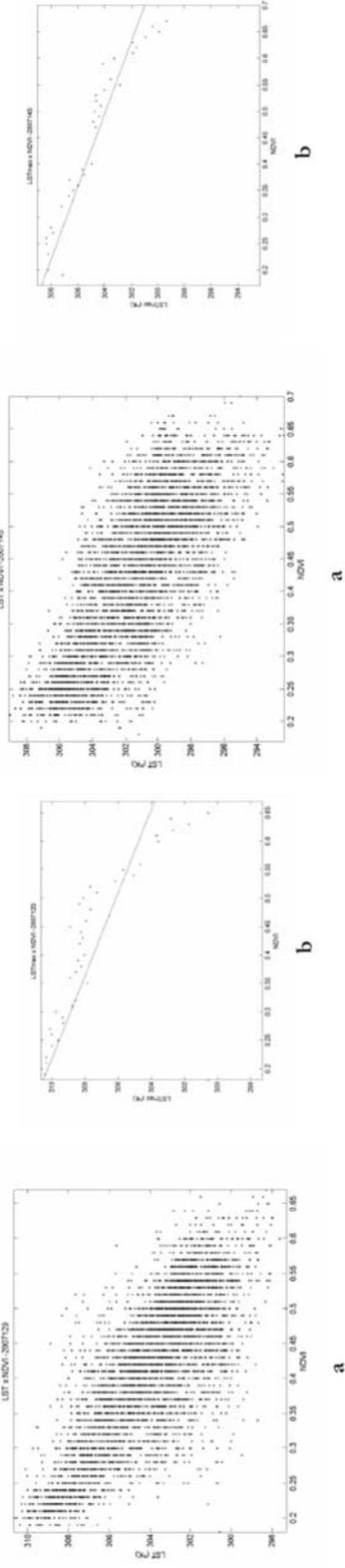
Figure 48. a) Scatterplot LST versus NDVI in DOY 145, b) the edge dry, or line LSTMAX
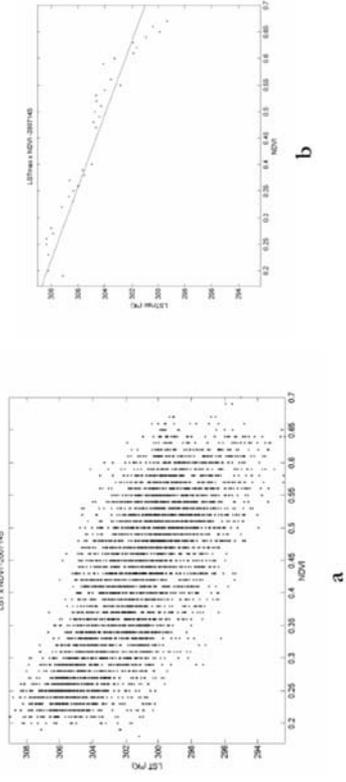
Figure 49. a) Scatterplot LST versus NDVI in DOY 161, b) the edge dry, or line LSTMAX
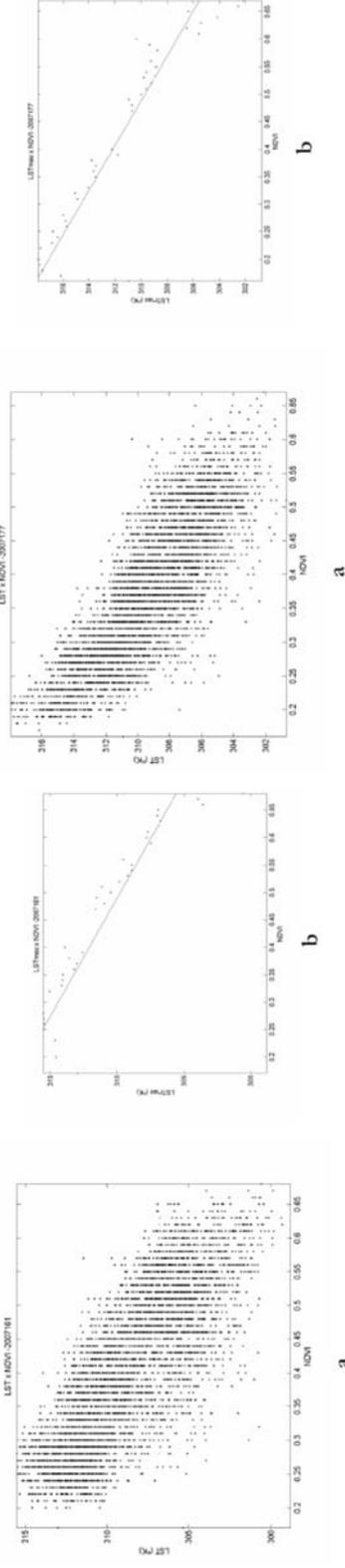
Figure 50. a) Scatterplot LST versus NDVI in DOY 177, b) the edge dry, or line LSTMAX
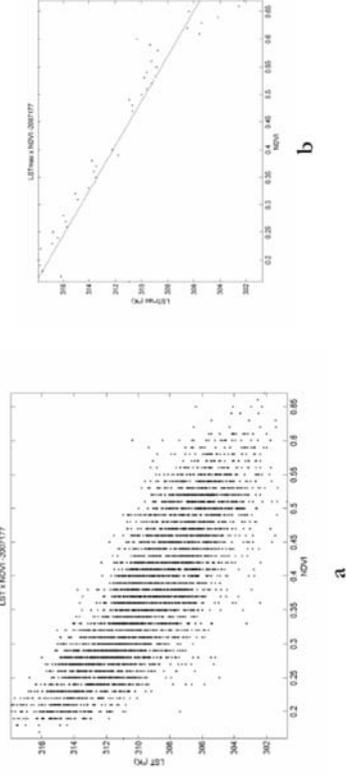
Figure 51. a) Scatterplot LST versus NDVI in DOY 193, b) the edge dry, or line LSTMAX
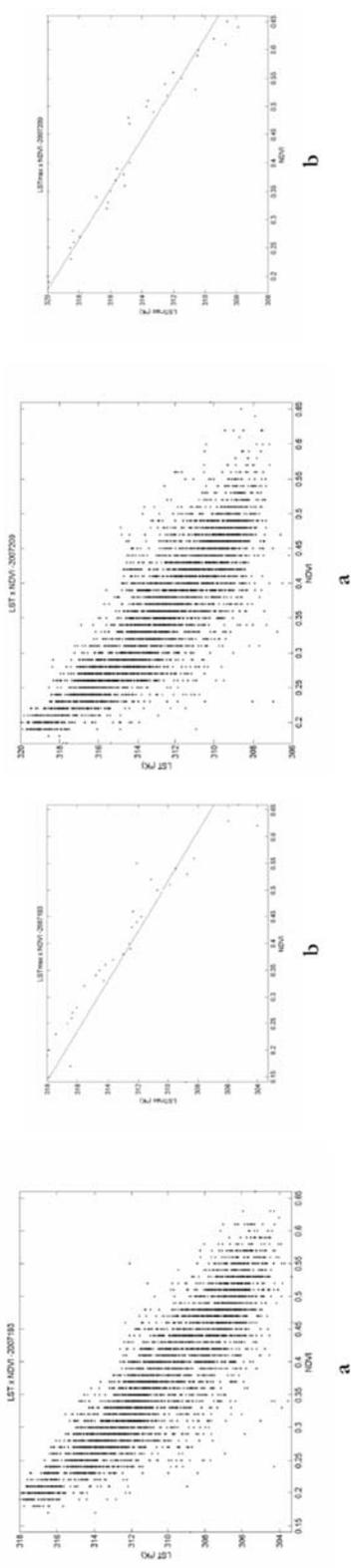
Figure 52. a) Scatterplot LST versus NDVI in DOY 209, b) the edge dry, or line LSTMAX
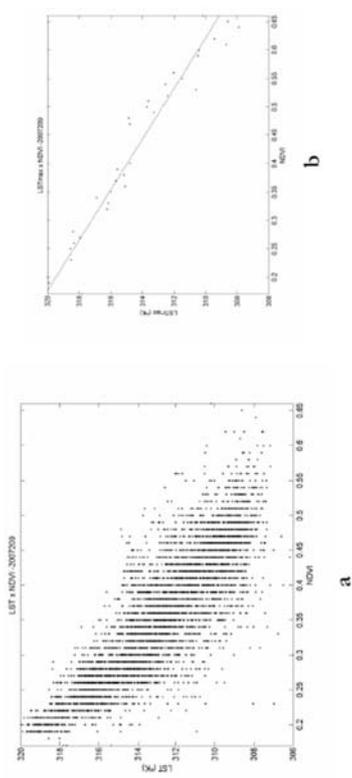
Figure 53. a) Scatterplot LST versus NDVI in DOY 225, b) the edge dry, or line LSTMAX
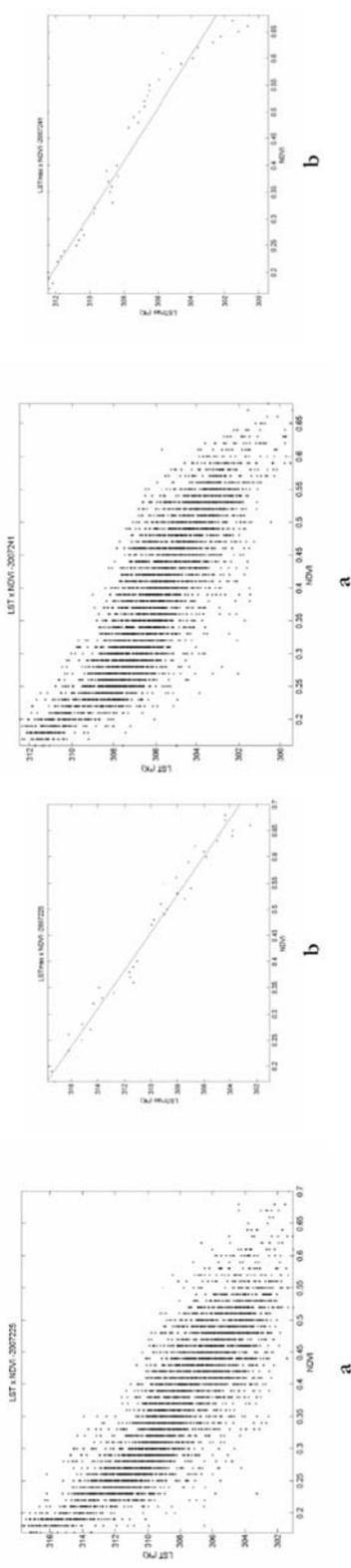
Figure 54. a) Scatterplot LST versus NDVI in DOY 241, b) the edge dry, or line LSTMAX
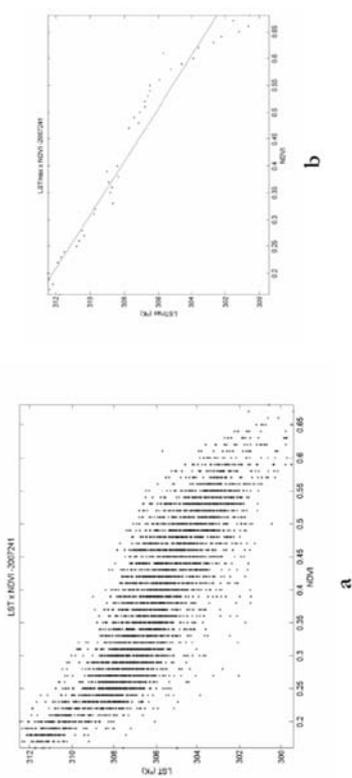
Figure 55. a) Scatterplot LST versus NDVI in DOY 257, b) the edge dry, or line LSTMAX
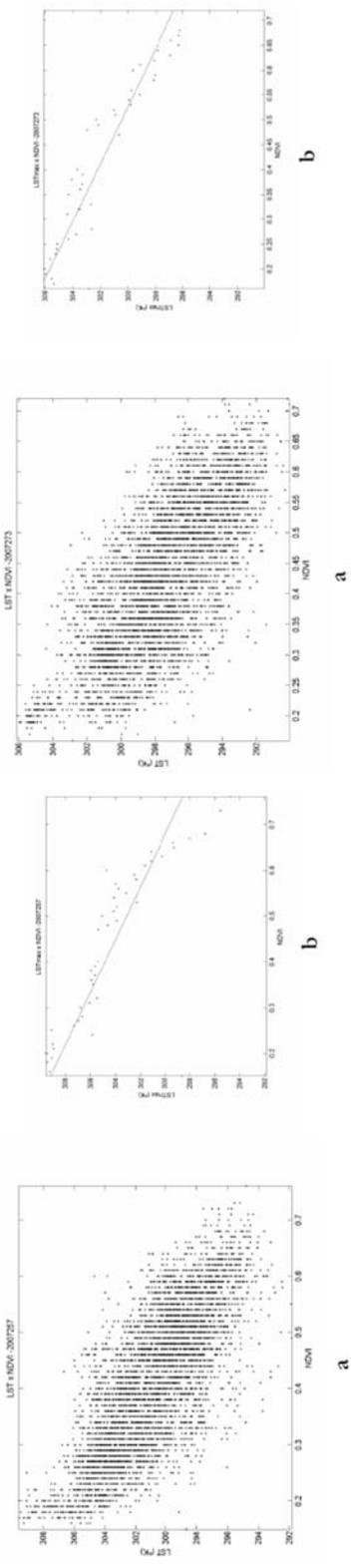
Figure 56. a) Scatterplot LST versus NDVI in DOY 273, b) the edge dry, or line LSTMAX
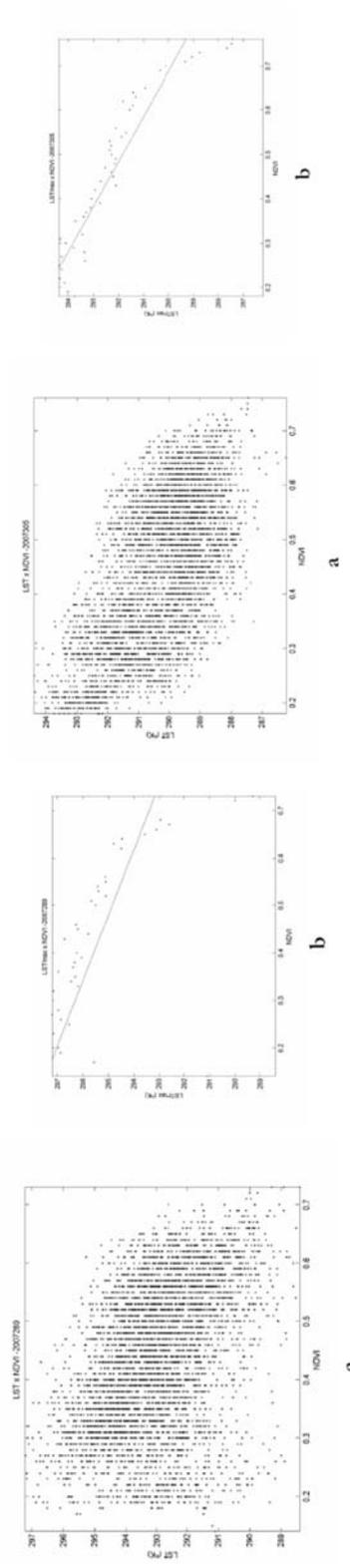
Figure 57. a) Scatterplot LST versus NDVI in DOY 289, b) the edge dry, or line LSTMAX
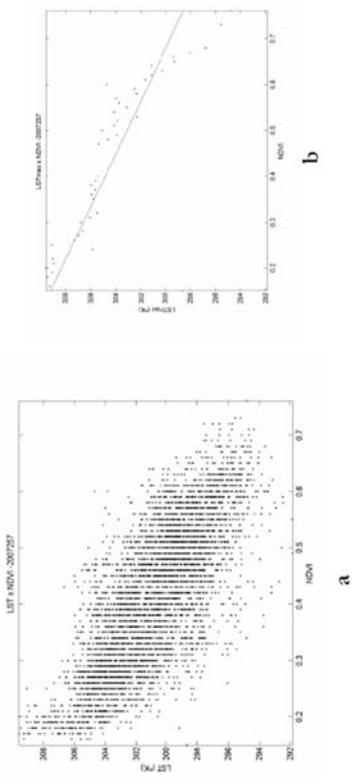
Figure 58. a) Scatterplot LST versus NDVI in DOY 305, b) the edge dry, or line LSTMAX
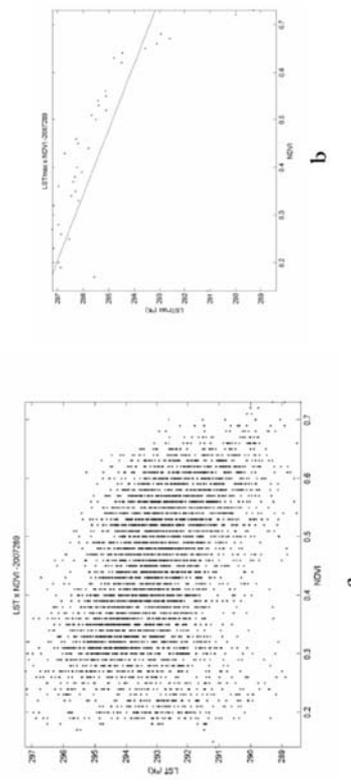
Figure 59. a) Scatterplot LST versus NDVI in DOY 321, b) the edge dry, or line LSTMAX
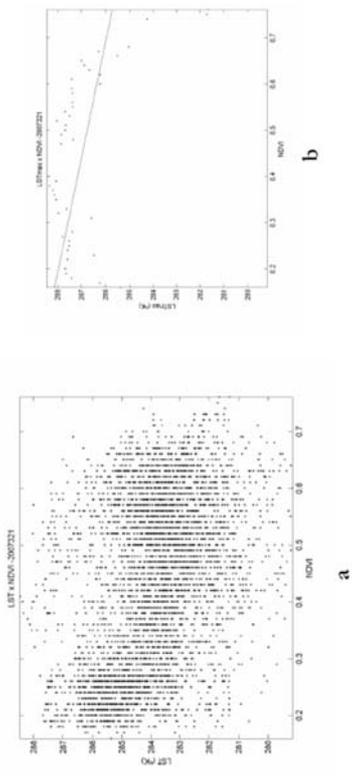
Figure 60. a) Scatterplot LST versus NDVI in DOY 337, b) the edge dry, or line LSTMAX
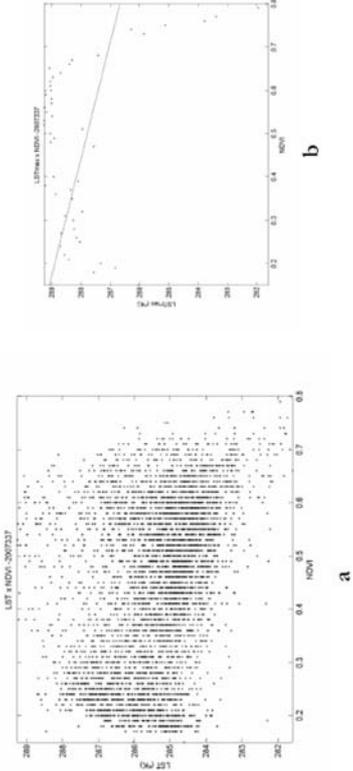
Figure 61. a) Scatterplot LST versus NDVI in DOY 353, b) the edge dry, or line LSTMAX
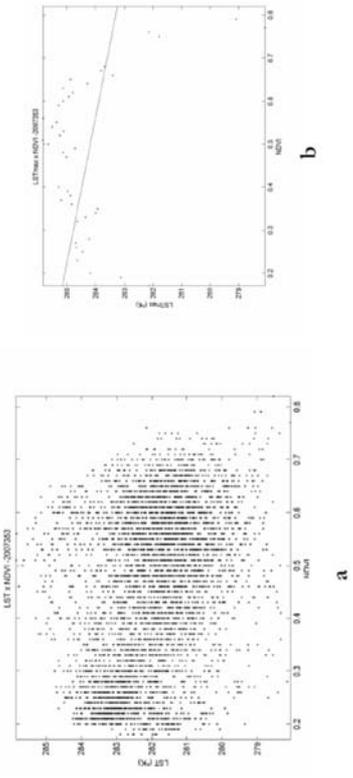
CO2 MEASUREMENT AND DATA PROCESSING IN ORDER TO ASSESS THE EFFECT OF CLIMATE CHANGE ON NATURAL ECOSYSTEMS

Lorenzo Vita
Department of Agronomy and Land Management
University of Florence
Italy

Tutors: Prof. T.F. Gutierrez and Dr. Susana Vanlesberg
Facultad de Ingenieria, geoecología y medio Ambiente
Universidad Católica de Santa Fé
Argentina

1. Introduction

Climate change, characterized during the last decades by the warming up of atmosphere, is a complex topic concerning different aspects of the relationships among atmosphere, troposphere, earth and solar radiation.

Generally speaking climate can be considered as the effect of the energetic equilibrium between the total flux of absorbed energy, basically incoming solar radiation, and the total flux of emitted energy, constituted by the sum of the radiation reflected by atmosphere, soil and clouds more the radiation emitted by the earth. Whatever, alteration of such equilibrium can lead to climate change.

Global climate system is a consequence and a link between atmosphere, biosphere and geosphere. Such components continuously interact exchanging energy and matter fluxes. Interactions among components can depend by some important cycles, like Carbon cycle. Only by consideration of the climate system in these terms, it is possible to understand the flows and the cycle of energy and matter in the atmosphere, an understanding, which is required to investigate the causes (and the effects) of climate change (IPCC).

To simplify the analysis of climate change at a regional scale is possible to describe climate elements using 5 main variables: air temperature, air humidity, wind speed, solar radiation and precipitation. Put it simply, regional climate change depends on how much, where, how often, these variables can change over a limited area (Da Rocha 2002).

A land use change (i.e. deforestation) can lead to a decreasing of evaporation at regional scale and consequently to a decreasing of precipitation unless masses of humid air are brought into the area from other regions by large scale convergence of humidity. Even the response of land surface to income radiation can change in terms of heating and water evaporation, due to land use change. Measurements of soil temperature and precipitation, carried out in the Brazilian Amazon during the last 20 years highlight how deforested areas show an higher soil temperature and a decreasing of precipitation compared with those in which forest still exists (Da Rocha 2002).

Such phenomena depend on the fact that, with deforestation, a larger amount of solar radiation is spent to warm up air and soil, instead of producing evaporation. The energetic equilibrium changes, as well as climate.

These mechanisms at regional scale are substantially important in the tropical region, where the regime of convection, dominated by heating and availability of humidity, prevails. Instead,

at middle and high latitudes, where the action of cold front is intense, changes in precipitation are mainly due to the large scale convergence of moist air masses.

Indeed, the deep changes in land use and land cover that have taken place mainly during the last 2 centuries can partly explain climate change, but they are not the only reasons.

Being climate the result of the system earth–atmosphere energetic balance, reasons of climate change at global scale can be either external to the system (exogenous) or internal to the system (endogenous).

External causes are those ones due to some astronomical phenomena influencing the incident angle of the incoming solar radiation: changes in terrestrial orbit eccentricity and obliquity. Eccentricity depends on the shape of terrestrial orbit that changes about every 100.000 years; obliquity depends on rotation axis inclination that changes every 20.000 years. These phenomena are responsible of glacial and interglacial (warm) periods long term alternation.

Speaking about endogenous mechanisms influencing climate behavior it is possible to identify some natural phenomena leading to changes in atmospheric composition like natural fire and volcanism. But even human activity, mainly during the last 2 centuries, have increased the emission into the atmosphere of greenhouse gases, especially CO_2, altering the response of the atmosphere to solar radiation.

Deforestation, urbanization and industrialization affect the 2 main cycles related to energetic dynamics: the cycle of water and the cycle of CO_2.

To impoverish green areas means decreasing drastically the sink of Carbon represented by vegetation, as well as the ecosystem capability of water storage. Emissions of gases by urban area and factories enlarge the amount of CO_2 in the atmosphere.

Solar radiation reaches the earth like visible light with a certain wavelength; its energy is split basically in 2 main processes: the warming of air masses (that generates convection) and the evaporation of water. When the water storage decreases, a larger amount of energy is going to produce heating. At the same time a greater CO_2 concentration avoid the reflected radiation (having a shorter wavelength than the incoming one) to get out of the atmosphere and the entrapped energy is again turned into heat.

It is impossible to certainly state that the temperature rising during the last century is due exclusively to the human behavior (world is currently on an interglacial period), but indeed the anthropological impact had got a heating effect on the environment. Since industrial revolution, in fact, fuel combustion and deforestation have leaded to a dramatic increasing of CO_2 concentration in the atmosphere, altering CO_2 natural cycle, and consequently, the energetic equilibrium of the planet.

In such a scenario it is evident that a deep investigation of Carbon dynamics is compulsory to better understand climate change, especially at present time, and consequently to elaborate new land use planning strategy aiming to reduce the CO_2 concentration in the atmosphere and to mitigate the greenhouse effect.

Vegetation, throughout photosynthetic process, is able to convert atmospheric CO_2 into those substances (i.e. cellulose) composing its structure. It means that vegetation can represent a long term sink of Carbon, more than good storage of moisture.

To evaluate the ecosystem carbon sink capability and, more generally, to investigate about carbon exchange above the troposphere, an important device, adopted widely since 1990, is the so called Flux Tower that, joined with the Eddy covariance technique, allows to estimate the flux of water vapor and CO_2 above the vegetation canopy. A lot of projects, all over the world (Euro flux, Ameriflux, etc), have been developed in the last years using the implementation of flux tower in different ecosystems in order to get information about the contribution of each one of them in subtracting CO_2 from the atmosphere. The main objective is to aid policy maker in their land use planning for mitigation of global warming, especially in those countries that had complied with the Kyoto Protocol.

The Universidad Católica de Santa Fe (UCSF) is owner of two Flux towers, one of them was set up in 2003 by the CIOMTA Institute and has stored data until the year 2005, when it stopped to work properly due to calibration problems. Tower location was a natural pasture in wet lands and will be described later.

The purpose of the present work is to process and analyze the available data collected in the year 2005 by the tower, aiming at: establishing if the ecosystem surrounding the tower could be considered a sink for Carbon; evaluating if relationships between CO2 flux and other meteorological variables do exist; examining how incoming radiation behaves in such ecosystem. Gross primary production will be also extrapolated on the basis of temperature and net ecosystem carbon exchange, following the work developed by Law in 2002.

Unfortunately the set of available data is pretty poor and sometimes incomplete due to technical problems that have affected towers during the last years, but it could be considered a first step toward the exploitation of the important investigation resource represented by flux towers in Argentina.

2. The Study Area

Flux tower has been set up in the meteorological station called La Cigueña in the Santa Fe province of Argentina. Coordinates of the site are 29°16'32'' south and 61°02'28'' west, located within a large (about 2 million of hectares) alluvial depression generated by the near Parana river.

Alluvial plain is often flooded during the rain season while is relatively dry during the summer (January and February), when natural fire is a common phenomenon, and very dry in winter (June and July). From a topographical point of view, the landscape is extremely homogeneous; the dominant vegetation is constituted by grass and shrubs and trees are very rare (Figure 1). The ecosystem can be defined subtropical grassland, characterized by native pasture, the more represented specie is Spartina Argentinensis, belonging to the Poacea family also known as Gramineae, with typical radial formations, reaching the height of about 1.5 m. This endemic plant can reproduce either in sexual or asexual way and has the property of regeneration with higher photosynthetic power after burning. While during the dry season, under water stress condition, Spartina has a lower photosynthetic rates respect to all the other plants of the area.

The major constraints of the soil for cultivation are the difficult drainage (especially during flooding) and the salinity that characterize the dry season.

Figure 1. Native pasture of La Cigueña

The plain is subjected to the continuous action of the wind, typical of the region, that doesn't find any obstacle.

The distribution of precipitation shows two peaks, one at the end of summer (March–April) and the other one in spring; winter is commonly very dry. Temperatures are generally pretty high, with a low peak during the winter months (June, July and August) in which, however, they are never less than 10°C (data refer to the near station of Reconquista, being no available those of La Cigueña).

3. Materials and Methods

Flux tower. It is constituted by a sonic anemometer, an open path infrared gas analyzer, a box for the flux control unit containing a PCU for store data coming from the anemometer, a Tacos unit for data transmission and a memory to store data.

Three axis sonic anemometer Metek is a device capable to measure, at high frequency mainly, the three components of wind speed and the sound speed useful to calculate the sonic temperature according to the equation (Kaimal and Gaylor, 1991 in Moncrieff, 1997):

$T_{son} = C_s^2 / 403$, where T_{son} is the sonic temperature and C_s is the speed of sound

Once obtained the sonic temperature, it is possible to calculate the air temperature using other parameters like vapor pressure of the water in the air e and the absolute atmospheric pressure p, in accordance with the equation (Stull,1988 in Moncieff, 1997):

$T_{son} = T_{air}(1 + 0.38 \, e/p)$

Anemometer is capable to take measurement 20 times per second (20Hz) and send data to the control unit like digital signal.

Gas Analyzer LICOR 7500 uses infrared beam to measure concentration of different gases, in this case CO_2 and water vapor. It transmits data to the Metek through analogic signal, Metek turns all data into digital format and sends them to the Flux control unit at the same frequency of its own data (Figure 2 shows the Metek sonic anemometer and the Gas Analyzer Licor 7500 set up jointly on the top of the tower).

Data arrive to the PCU where a software called Eddylog stores them as ASCII files each one containing one hour of data. They can also be transmitted by the Tacos unit.

Solar panels (Figure 3) supply power to a set of 12 V batteries, anemometer and gas analyzer are placed jointly on the top of a 3 meters support.

3.1 Eddy Covariance Technique

It is a technique developed theoretically since 1951 by Swinbank, but grown in importance recently, when technological progress has allowed the collection of data at high frequency as occurs with flux tower. It consists in sampling atmospheric eddies for their vertical speed and concentration of scalar of interest, averaging the fluctuation of the scalar concentration over a 30 minutes period it is possible to calculate the net amount of scalar being transported along the vertical above the surface. It can be defined as a micrometeorological technique allowing measurements of matter and energy fluxes between biosphere and atmosphere, using high frequency data collection of wind speed and one or more scalar concentration.

Theory started from the conservation equation of a scalar:

Figure 2. Metek sonic anemometer and the Gas Analyzer   Figure 3. Solar panels for energy supply
Licor 7500 set up jointly on the top of the tower
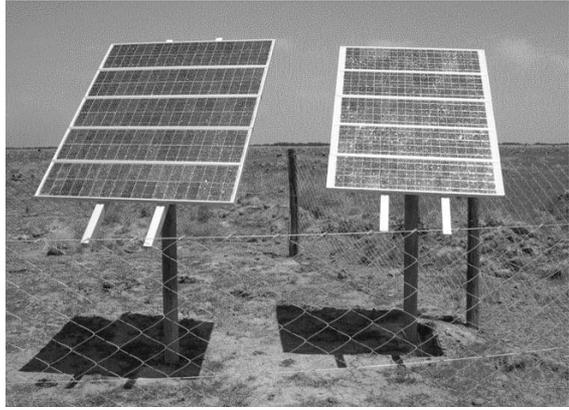
$$\frac{\partial \rho_s}{\partial t} + u\frac{\partial \rho_s}{\partial x} + v\frac{\partial \rho_s}{\partial y} + w\frac{\partial \rho_s}{\partial z} = S + D$$

where is the scalar density, u, v, and w are the wind velocity components, respectively, in the direction of the mean wind (x), the lateral wind (y) and normal to the surface (z). S is the source/sink term and D is the molecular diffusion. Two assumptions are now necessary: firstly that lateral gradient and molecular diffusion can be neglected and second that over a suitable interval of time there is no air mass movement in the vertical direction (w = 0) (Moncrieff 1997).

Applying the Reynold decomposition:

$$u = \bar{u} + u', v = \bar{v} + v', w = \bar{w} + w', \rho_s = \overline{\rho_s} + \rho_s'$$

where the overbars characterize time averages and the primes fluctuations around the average, integration along z and assumption of no horizontal eddy flux divergence, equation above becomes:

$$\int_0^{h_m} S dz = \overline{w'\rho_s'} + \int_0^{h_m} \frac{\partial \overline{\rho_s}}{\partial t} dz + \int_0^{h_m} \bar{u}\frac{\partial \overline{\rho_s}}{\partial x} dz + \int_0^{h_m} \bar{w}\frac{\partial \overline{\rho_s}}{\partial z} dz$$
$$\quad I \qquad II \qquad\qquad III \qquad\quad IV \qquad\qquad V$$

Where the term I represents the scalar sink/source, II the eddy flux (measured with the Eddy covariance system), III the scalar concentration under the measurement high (in case of carbon dioxide this term was found to be notable in forest ecosystems but it can be ignored in this case, dealing with grass land) (Grace *et al.* 1996; Goulden *et al.* 1996), IV and V respectively horizontal and vertical advection that are insignificant in flat areas (the first) and in low crops (the second).

In the case of the present research it is clearly possible to avoid III, IV and V terms, thus simplifying, assuming CO2 as scalar of interest, the equation become:

$N_e = Fc$ [$Fc = wp + w'p'$ (Reynold decomposition) (assumption $w = 0$) => $Fc = w'p'$]

Where N_ℓ is the net ecosystem exchange of carbon dioxide, coincident with Fc that is the eddy flux.

At elevated wind speeds mechanism can calculate an overflux (that is a constrain of the technique), in this case a correction (Webb) should be apply.

Eddy covariance technique is typically used to calculate (from flux tower data): the sensible heat flux (H, in W/m^2), that represents the heat warming air masses, responsible of convection movements, the latent heat flux (Le, in W/m^2), that represents the energy spent for water evaporation (at 25°C 2450 Jg^{-1}), the fluxes of CO_2 and water vapor (in $\mu mol / m^2 s$).

Let's now illustrate how the whole principle works. Over a land terrestrial vegetated ecosystem, the exchange of carbon is mostly due to CO_2, and several processes are defined in the CO_2 flux. Plants uptake carbon by photosynthesis (called Gross Primary Productivity, GPP), and loose carbon by respiration. The difference between the two is called Net Primary Production, NPP. At the same time, carbon is continuously emitted by heterotrophic respiration, mostly in the soil, resulted from the activity of microorganisms decomposing organic matter. The subtraction of NPP minus the heterotrophic respiration results in the Net Ecosystem Exchange, NEE. It means that during day time, when photosynthesis takes place, the air parcels immediately above the vegetation will be poor in CO_2, due to the plants subtraction, while the upper parcels will be relatively rich in CO_2. Assuming turbulence exists, if carbon uptake exists too, rich parcels should go down and the poor ones should go up. Being the flux defined as the covariance between vertical wind speed (w) and CO_2 concentration (p), Fc = w'p', there are four possibilities about the turbulent term: w' > 0 (ascending movements), w' < 0 (descending movements), p' > 0 (rich parcel) and p'< 0 (poor parcel). If w' and p' are both positive (rich parcels go up) or both negative (poor parcels go down) there is emission of CO_2 by the ecosystem and the net flux is conventionally assumed positive. In the other two cases, when poor parcels go up (w' > 0 and p' < 0) or rich parcels go down (w' < 0 and p' > 0) there is sinking of CO_2 and the net flux is negative (da Rocha).

When there is no turbulence another term should be taken into account: the non turbulent flux, but it use to happen by in forest environment (especially by night) and can be ignored for the present research.

3.2 Data processing

To obtain flux data starting from flux tower measurements the implementation of software for calculation is compulsory. In the present work processing have been performed using two software, Eddy_post.exe, created by the Ibimet Institute of Florence, and Edire, downloaded for free from the site of the Edinburgh University, where it has been developed.

Eddy_post.exe is needed to clean files.dat downloaded by the tower, thus make them ready to be read by the software Edire that otherwise cannot work properly.

Edire can process several files (remember that each file correspond to 1 hour of data taken at 20 Hz) contemporary, averaging measurements on half an hourly bases in order to calculate for each 30 minutes CO_2, sensible and latent heat fluxes, temperature, wind speed and other environmental variables. Edire has to be provided with information about procedure it has to follow and the format of raw data files. The software is even responsible of the Webb correction application and is able to build preliminary graphics of F (uncorrected flux).

3.3 Carbon Flux behavior

Once that data have been processed by Edire, the Fc measurements are plotted on daily basis and than averaged to build a yearly graphic showing the level of CO_2 of each month. As

previously said, Fc for grassland is very close to the Net Ecosystem Exchange, so it is possible to understand if the ecosystem of interest can be considered or not a sink for carbon. Behavior of carbon flux during the day have been even described in order to better understand CO2 dynamics on the earth surface. In those analysis the sink of carbon is considered with positive sign, opposite to the convention explained before; in the present work positive values of Fc mean carbon storage by ecosystem.

Fc have been plotted and analyzed jointly to other environmental variables of interest and qualitative relationships among them have been discussed. Variables analyzed have been air temperature (both on monthly and daily basis).

3.4   *Energy balance*

Atmosphere energetic balance plays a key role in understanding climate change and its relationships with carbon flux; it describes how available energy is shared to carry out different processes within the ecosystem. Energy reaches earth surface as electromagnetic radiation; incoming solar radiation is the main component and arrives like short waves radiation (Ki), part of that is reflected by earth at shorter wavelength (Kr), the ratio between Kr and Ki is called albedo and is about 25% (Da Rocha) but can vary among different ecosystems. At the same time earth emits, like every black body, long wave radiation toward atmosphere (Lwe), in opposite direction long wave radiation is moving even from air masses to the earth (Lwi). The net radiation on the surface (Rn) is therefore the algebraic sum of the four components:

$$Rn = (\ Kr - Ki) + (Lwe - Lwi)$$

Net radiation represents the available energy at the earth surface level. Such available energy is distributed into several processes. First of all a part of it, called Sensible Heat Flux (H, W/m^2), is represented by energy spent to warm up the air above the surface, the 'sensible' effect is the temperature increasing of air masses. Second but not least, there is the energy needed for water evaporation; in every ecosystem there is surface water available, as well as plants transpiration, and the water phase changing consumes a certain amount of energy that does not produce temperature increasing. This energy is called Latent Heat Flux (LE, W/m^2). There are even other energy fluxes in which net radiation is utilized, like for instance the soil heat flux or photosynthetic flux that represent the fraction of Rn producing the warming of deeper soil layers (that someone called C) and the part of Rn utilized for photosynthetic reaction, respectively (A). But according with Da Rocha (2001) in an ecosystem entirely covered by vegetation, the main components in which Rn is shared are Sensible and Latent heat fluxes, that joined together cover about the 90% of net radiation. Therefore it is possible to simplify the energy balance closure:

$$Rn = H + LE$$ neglecting the other components for the purposes of this research.

So keeping constant Rn it is possible to state that the higher is H, the lower is LE and vice versa; it means that the larger is the water presence within the ecosystem, the lower is the warming up.

The ratio H / LE is called Bowen ratio (B) and can describe the healthy and the phenological status of the ecosystem. B is about 0.1 over green forests or dense green crops, while arises up to 10 over agricultural bare soil. It usually ranges from 0.2 to 2 over agricultural crops according to the health and the vegetative cycle.

In the present work the energy balance closure over native pasture has been analyzed as well as the Bowen ratio along the year.

3.5   Ecosystem respiration

According with Law (2002) it is possible to estimate the total ecosystem respiration basing on night NEE measured by flux tower. Supposing that at night, when photosynthesis does not occur, Fc is almost totally due to respiration (and measured emissions of CO2 confirm that), once measured night carbon flux, with an Arrhenius regression equation developed by Lloyd and Taylor in 1994, is possible to estimate daily ecosystem respiration basing on soil temperature.

The Arrhenius equation is:

$$R_{enight} = R_{eTref} e^{(E_a/R(1/T_K))}$$

where R_{enight} is the CO2 flux measured at night time, R_{eTref} the ecosystem respiration at reference temperature (assumed being 283,16 K, Law 2002), Ea the activation energy in J / mol, R the gas constant (8,134 J /Kgmol) and Tk the soil temperature.

R_{eTref} and E_a are the fitted parameters of the regression.
The steps followed in the regression of half an hourly data have been:
–applying ln to both terms of the previous equation:
–assuming ln R_{enigth} as y, 1 / Tk as x, ln R_{eTref} as a and Ea / R as b is possible to apply the regression linear equation:

y = *a* + *b*x

Once obtained the *a* and *b* parameters it becomes easy to estimate R_{eTref} (inverse of ln a) and Ea (b★R).
Then is possible to apply such parameters to all flux measurements and obtain daily ecosystem respiration.
In case that the adjusted equation of Law does fit well with environmental characteristics of our study area, it is even possible to calculate the gross ecosystem productivity (GEP) by subtraction of Respiration from the NEE.
Being not available the half-hourly measurements of soil temperature, it has been estimated from air temperature basing on the work of the Granada University Edafic department in which soil temperature is assumed to be approximately 1°C higher than the air one.
In the present research data of March 2005 (one of the more complete month in terms of data set) have been used for the regression, with the purpose of using the values of Ea and Re-Tref for the yearly estimation.

4. Results

4.1   Carbon Flux behavior

Behavior shown by CO2 dynamics during the day is quite similar to what it was theoretically expected. Carbon sink (that in this case as already said is indicated by positive sign) starts with the sunrise and becomes higher until reaching its maximum between 12 and 14 hour, when photosynthetic activity is larger; while during night time emissions of CO2 prevail due to ecosystem respiration. The graphs below (1 and 2) represent some examples of Fc daily behavior.
For each month, when data was available, the half-hourly Fc have been averaged in order to built a 'typical' day behavior. The 'typical' day of each month has been used to compare

Fc with temperature data, averaged in the same way. Some results are shown in Figure 4, evidencing a similar daily trend between the two variables.

Figure 4. Example of daily Carbon flux relative to 11th of January 2005
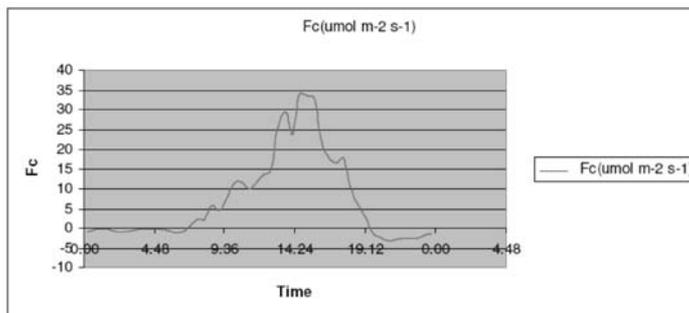
The average of each day has also been calculated to build monthly graphs of carbon level (Figures 7, 8, 9, 10 and 11). It appears very clear how the studied ecosystem can be considered a sink of carbon for almost the whole year. Unfortunately the set of data does not include the months of September and October due to technical problems, and other monthly data are incomplete (February, April, June, August and December).

Fc and Temperature have similar trend even on monthly basis as shown in Figures 12 and 13, relative to the month of March.

4.2   Energy Balance

Due maybe to some errors in tower calibration, data about sensible and latent heat fluxes (H and LE) do not comply with predictions and this made impossible the elaboration of such a data. Bowman index has been found to be larger then 10 for the most of the year; being 10 the value of bare soil, some mistakes in data collection are easily assessing.

4.3   Ecosystem respiration

Application of regression on the set of data correspondent to the month of March allows to calculate Ea (activation Energy) in order to estimate consequently the ecosystem respiration.

To obtain the value of Ea it is only necessary to multiply the variable X found with the regression (10495,38) by the gas constant R (8,134 J / Kgmol).

$$Ea = X \ R = 85369,42 \ J$$

Unfortunately the correlation coefficient (r=0,35) is too low to confirm the reliability of the relationship (Table 1). As a matter of fact the value found for Ea is really high.

The equation utilized by Law does not fit well with the study case, although the coefficients of the same one are significant according to the levels of obtained probability type I of the analysis. In order to obtain better results in the calculations of ecosystem respiration and consequently GPP (gross primary production) for the examined study area, possibly, it is necessary to perform another equation. For such a purpose it is compulsory to collect real field data of GPP but this did not comply with time and possibility of the research.

Figure 5. Example of daily Carbon flux relative to 17th of March 2005
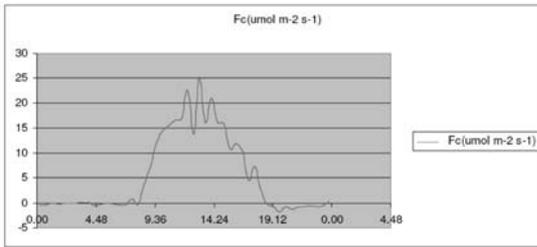
Figure 6. 'Typical' January day
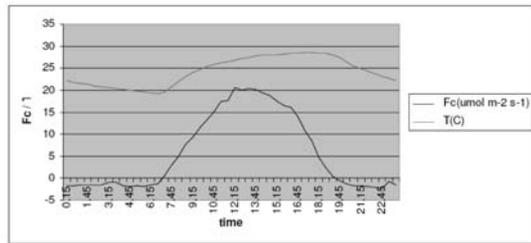
Figure 7. Carbon absorption of January 2005
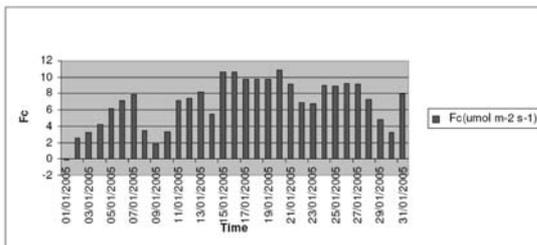
Figure 8. Carbon absorption of March 2005
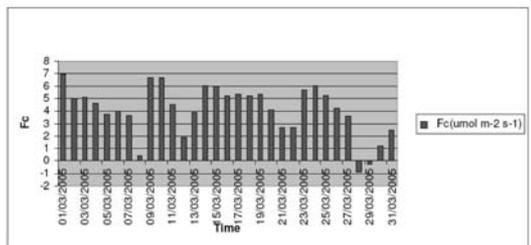
Figure 9. Carbon absorption of May 2005
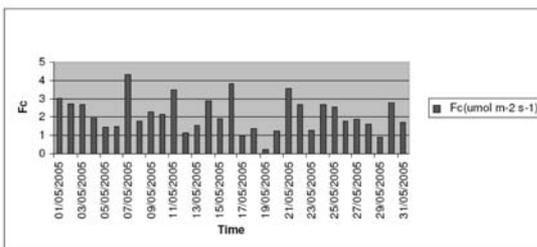
Figure 10. Carbon absorption of July 2005
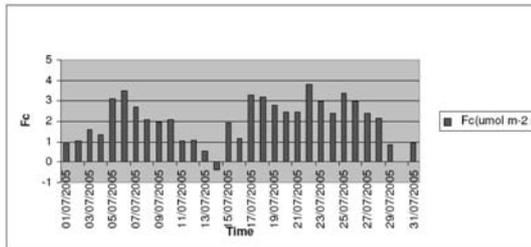
Figure 11. Carbon absorption of November 2005
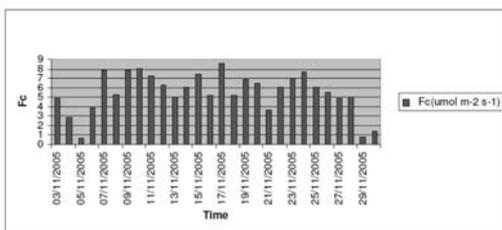
Figure 12. Temperature and Fc of March 2005
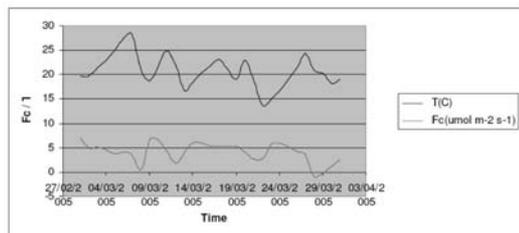
5. Conclusions

Due to the poor set of available data and also to the uncertainty related to the flux tower conditions, it is only possible to state that the studied ecosystem can be considered reasonably to have good properties of carbon storage.

Figure 13. Trend lines of Temperature and Fc (March 2005)
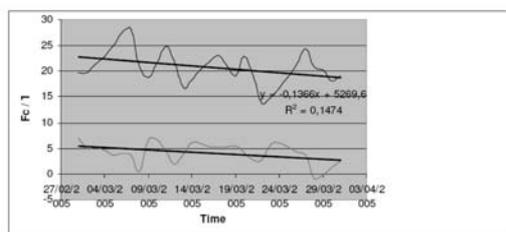
Table 1. Regression Summary

Resume	
Regression Statistics	
Multiple correlation coefficient	0,352498422
Determination Coefficient R^2	0,124255137
R^2 adjusted	0,123074888
Typical error	1,268447173
Observations	744

Variance Analysis

	Degrees of freedom	Sum of squares	Mean of squares	F
Regression	1	169,3890882	169,3890882	105,2787357
Residuals	742	1193,847007	1,60895823	
Total	743	1363,236095		

	Coefficients	Typical Error	T Statistical	Probability
Intercept	–1,610528144	0,127007887	–12,6805365	1,71669E–33
Variable X 1	10495,38409	1022,887818	10,26054266	3,44748E–23

For almost the whole year 2005, in fact, ecosystem behaves as a sink for carbon and further investigations became necessary to better understand the magnitude of its contribution in subtracting CO_2 from atmosphere.

Natural ecosystems like this might represent a great richness for Argentina in which green natural areas are very abundant and a deep knowledge of carbon dynamics related to them is the only way to a full exploitation of such a resource.

The hope is that the flux towers owned by the CIOMTA institute of the UCSF can work properly in the future, with the correct supervision and maintenance, in order to get data that can be meaningful even under quantitative aspects.

Flux towers should even be set up (at least for the beginning) in place where other meteorological station are working on, in order to check better the measurements and to familiarize such a new device.

Unfortunately problems highlighted previously did not allowed a good estimation of energy balance, that is a very important topic related to climate change and warming up of the

atmosphere. So questions about how the ecosystem can mitigate the income solar radiation still stays on and new researches have to be done in this area, with a better aid furnished by new instruments.

As said before the only concept that can be surely assessed is that the ecosystem of study can subtract CO_2 from atmosphere, in a larger proportion than the one emitted by respiration, and this is enough to mitigate the greenhouse effect.

This is the reason for which encouraging project aiming green areas preservation could represent a good economic income for Argentina in accordance with the assumption of Kyoto Protocol and with the international banks politics that are going to assign a price (carbon tax) to CO_2 adsorption.

References

Da Rocha U.R. (2002). Using Flux Tower to Investigate Climate Variability and the Role of Ecosystem. II Seminàrio Internacional de Cambio Climatico y Sumideros de Carbono (Santa Fè, Argentina).
Goulden M. L. *et al.* (1996). Diel and Seasonal Patterns of Tropical Forest CO_2 Exchange.
Grace J. *et al.* (1996). Kluwer Academic – An Introduction to Boundary Layer Meteorology.
Kaimal J.C. and Gaylor J.E. (1991), Another look at sonic thermometry. *Boundary-Layer Meteorology*, 56: 401–410.
Law B.E. *et al.* (2002). Agricultural and Forest Meteorology 113 – Environmental Control over Carbon Dioxide and Water Vapor Exchange of Terrestrial Vegetation.
Moncrieff J.B. *et al.* (1997). Journal of Hydrology 188-189 – A System to Measure Surface Fluxes of Momentum, Sensible Heat, Water Vapor and Carbon Dioxide.

Internet references

<http://www.asiaflux.net/>.
<http://www.unitus.it/dipartimenti/disafri/progetti/eflux/euro.html>.
<http://www.fluxnet–canada.ca>.
<http://public.ornl.gov/ameriflux/>.
<http://www.daac.ornl.gov/FLUXNET/>.

INCREASING THE QUALITY OF DATA SETS FOR STUDIES OF CLIMATE CHANGE IN SOUTH AMERICA

Eder Paulo Vendrasco
Department of Atmospheric Sciences
Universidade de São Paulo
Brasil

Tutors: Prof. J. Baez, Prof. L. Lugo and Prof. H. Ribeiro da Rocha
Facultad de Ciencias y Tecnología
Universidad Católica Nuestra Señora de la Asunción
Paraguay

1. Introduction

The use of climate change scenarios, derived from general circulation models (GCM) data, are applied for studies of impact on agriculture, energy and surface climate. The data, which often are downloadable on the web, are often not appropriate, and may lead to an increasing uncertainty of the projections and of the vulnerability scenarios. Usually such type of data have a coarse-resolution (an average of 150 to 300 km x km horizontal scale), which is not sufficient to cover all spatial heterogeneity of the studied area, e.g. land-use changes (urbanization, vegetation cover, and topographic variations). In other words, most of the GCM grid cells have an average area cell dimension, which do not solve the sub-grid of cell variability. Therefore, they may not be representative of the scale at which the model is skilled, and consequently they can not characterize some phenomena of regional atmospheric circulation, (such as breezes, mountain-valley circulations, convective systems) with enough accuracy. These constraints also limit the comparisons of climate projections with land surface weather stations.

The aim of this work was to prepare physically sounded climate change prediction scenarios, which derived from the outputs of general circulation models, to be implemented over key regions in Paraguay, Brazil and Argentina. The dataset of climate scenarios with also hydroclimatological and surface maps (vegetation, soil, others) were efficiently organized and distributed to the final users through proper techniques.

The emissions of greenhouse gases (GHG) resulting from certain activities are the main causes of the unusual heating of the planet during the last 150 years. This ongoing process is known as Anthropogenic Climatic Change. Actually, it is a global warming of the planet that also involves an important climatic change not only in temperature but also in the other climate variables such as precipitation, winds and humidity.

The 90's decade was characterized by the hottest air temperatures ever recorded from the first measurements, made in the XIX century (see Figure 1).

The increasing temperature is mainly due to the use of a huge amount of fossil fuel. During the 1760-1960 time period (Industrial Revolution) the atmospheric CO_2 concentration increased from 277 to 317 ppm, an increment of 40 ppm. On the other hand, during the 1960–2001 period (only 4 decades), the atmospheric CO_2 concentration increased from 317 to 371 ppm, an increment of 54 ppm (Marengo 2006). The GHG gases absorb part of the solar energy reflected by the Earth surface and re-distribute it through the atmospheric and ocean circulations.

Some evident consequences of these phenomena are the glacier smelting in the poles and the increase of ten centimetres in the sea level in just a century. The dynamics of the climatic

Figure 1. Global temperature anomaly (based on the 1961-1990 period). The line shows the moving average of 10 years (Source: Climate Research Unit 2006)
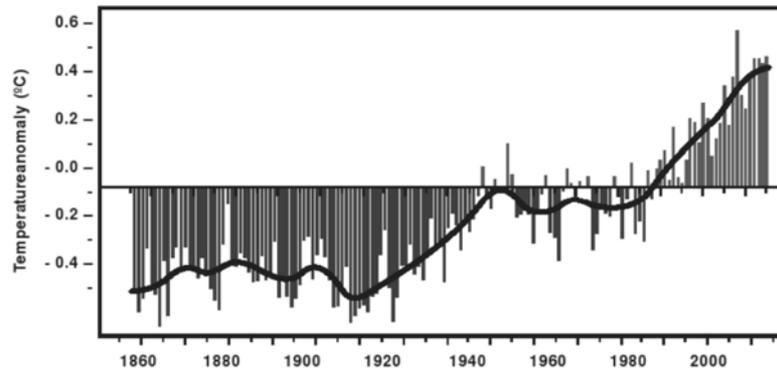
Figure 2. Air global temperature anomaly based on 1850-1920 period (observations), and an ensemble of oceanic-atmospheric accomplished model simulations forced with: (a) only solar and volcanic; (b) anthropogenic (with tropospheric and stratospheric gases, greenhouse etc, change in the tropospheric ozone concentration and the direct and indirect sulfate aerosols etc; and (c) a combination of all forcing (naturals and anthropogenic). The lines show the observations and the results of 4 climatic models. Source: Intergovernmental Panel on Climate Change (2001)
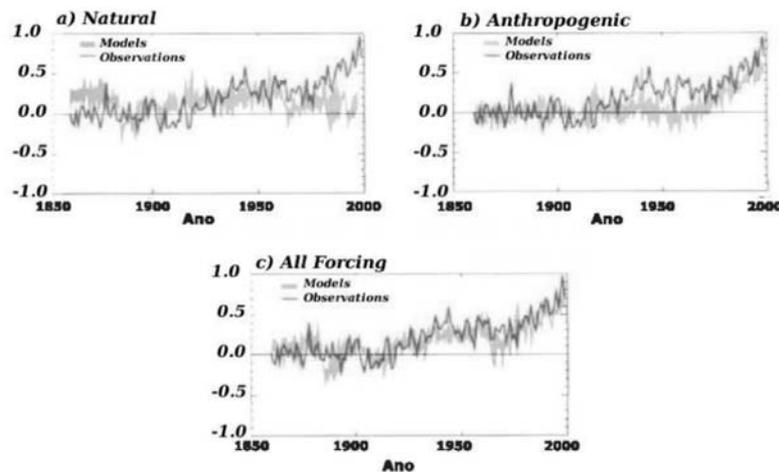
system, such as any other complex systems, consist in the alteration of the equilibrium statistical conditions without any forced external cause. This phenomenon is called «internal variability».

Using global climate models, it is possible to discard with great probability, the internal variability which generated the global observed trend. Since in climate simulations referred to thousands of years, these models do not reproduce trends of the global temperature of 100 years as pronounced as the current trend of the last century (Barros *et al.* 2006). The Figure 2 shows how the model cannot reproduce the observed increase of temperature if only natural forcing are considered, however, when anthropogenic forcing are included, the model fits much better the observations.

In the next future, the evolution of the emission of GHG gases will depend on numerous factors whose prediction is quite complex such as: the economic and demographic growth, the technological changes and even the development towards a society with more or less equity. Finally, but not less important, it will depend on the collective answers of the humanity to reduce

or at least to diminish the rate of growth of the emissions. Since all these factors are very difficult to be foreseen, the only possibility is to build probable socioeconomic scenarios of the future.

It is possible to develop as many emission scenarios as they arise from the combinations of the driven factors of the level of economic activity and of its characteristics, without certainty which of them will really occur.

The climate effects of GHG gasses concentrations have been studied with the help of global climate models that simulate the climatic system in almost all its complexity. These models represent the physical processes of the sea, the atmosphere, the soil and the cryosphere, and simulate their evolution using advanced software. The different GCM models produce various values of the global temperature, still under the same socio-economic scenarios. Nevertheless, they all give the same qualitative response: important warming throughout the twenty first century for any of the socioeconomic scenarios. The GCM are a reliable methodology to assess climate changes at global scale, but they still have a limited capacity to simulate the changes at a regional scale. At the moment, this is an important limiting factor in order to evaluate the impacts of the climate change.

Since the outputs provided by GCMs in general do not have enough spatial resolution to be applied at regional climatic change impacts evaluations, several methods have been developed in order to generate regional scenarios based on GCMs but with a higher resolution. This procedure is called downscaling.

The term downscaling refers to the use of either fine spatial–scale numerical atmospheric models (*dynamical downscaling*), or statistical relationship (*statistical downscaling*) in order to achieve detailed regional and local atmospheric data. The starting up point for the downscaling procedure is typically a larger-scale atmospheric or coupled oceanic–atmospheric model, which runs globally. The downscaled high resolution data can then be inserted into other types of numerical simulation tools such as hydrological, agricultural, and ecological models (Castro *et al.* 2005).

2. Methodology

In order to prepare projection scenarios of climate change at regional scale physically sounded for the key regions in Paraguay, Brazil and Argentina, a dynamic downscaling was performed and the Brazilian Regional Atmospheric Modeling System (BRAMS 4.0 –<http://www.cptec.inpe.br/brans/>) was used. BRAMS was originally developed to facilitate research within predominately mesoscale and cloud-scale atmospheric phenomena, but has been extended to larger scales over the last decade (Cotton *et al.* 2002). This model is fully three-dimensional, non hydrostatic, includes telescoping, interactive nested grid capabilities, supports various turbulence closure, short and long wave radiation, initialization, and boundary condition schemes (Pielke *et al.* 1992). BRAMS model application was the major stage in this project, but before the model running, several other procedures were performed. These procedures are the following:

1. It was built the cluster (see more details in Appendix A).
2. It was installed and configured all the software required, including the BRAMS model (see more details in Appendix B).
3. It was acquired the Global Hadley Centre data from the Brazilian Center for Weather Forecasting and Climate Studies (CPTEC) (the Table 1 gives details concerning these data). The data were used as initial and boundary conditions in the BRAMS model.
4. It was developed some software in Fortran language, Shell Script and Grads Script for reading the global data and converting the files into the BRAMS input data format.
5. It was performed some simulations in order to verify the procedure applied. The aim of this step was to find some probably spurious errors and fix them.

Table 1. Data available for this project obtained from Hadley Centre global model (HadCM3)

Type	Members	Available Period
Present Time	Member 1	1960 – 1985
	Member 2	1960 – 1990
Future Time (Scenario A2)	Member 1	2069 – 2082
	Member 6	2069 – 2099

6. It was chosen the best grid model size and resolution that could fit not only the objectives of this project, but also the available time to perform it.

    After having completed all the required procedures, BRAMS model was run in two phases:

- It was run the model for the present time (1960-1985 period, member 1). This procedure was done in order to compare the present data with future scenarios and in order to explore changes between the present and the future.
- It was run the model for future time (2070-2085 period, member 1).

2.1 Selected region for downscaling

The region chosen for downscaling is shown in the Figure 3.

Although, the spatial resolution was different, both the present time period and the scenario A2 period were downscaled for the same area. For the first one, the model ran with 80km of spatial resolution, for the second it was used a grid with 40km of resolution. The vertical resolution for both periods was the same.

The main reason because this area was selected is because it is located in a very important region, where the biggest hydroelectric power plant in the world is placed, and three of South American countries involved in this project are placed. In addition, the grid includes the whole Sao Paulo state which provides data also for other ICONE on going projects.

2.2 BRAMS setup

The Table 2 shows the main setup of the BRAMS model for both the two runs.

Figure 3. Region where the downscaling was performed
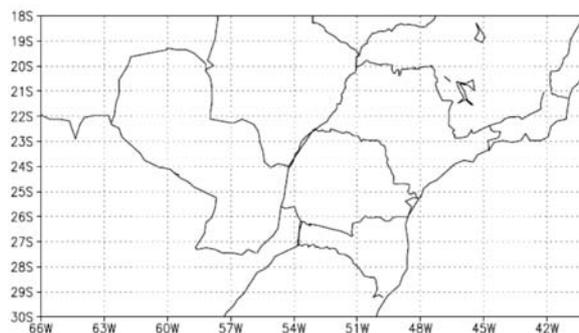
Table 2. Main characteristics of the numerical simulations

	BRAMS setup	
Simulation	Present Time	Scenario A2
Integration time (years)	20	10
Number of grids	1	1
Spatial resolution (horizontal)	80 km	40 km
Spatial resolution (vertical) Δz rate	100 km 1.2 until 1000m and constant above	100m same
Number of points for lateral boundary nudging	5	5
Nudging time for lateral boundary	1800	1800
Nudging time for top domani	10800	10800
Laterla boundary scheme	Klemp e Willhelmson (1978)	Same
SW and LW radiation	Chen and Cotton (1983)	Same
Cumulus parameterization	Grell (1993)	Same
Turbulence parameterization	Anisotropic deformation (Smagorinky 1963) based on modifications of Hill (1974) and Lilly (1962)	Same

3. Results

The Figure 4 shows a time series of diurnal mean temperature for seven different regions (see Figure 4). It is clear that the spatial distribution of temperature is very similar to the expected distribution: it is hotter over the Paraguayan Chaco (region 2) and cooler over Santa Catarina (region 7). A similar figure was produced also for the precipitation (Figure 6). As it was expected, the region with largest amount of precipitation was the region number 7 (Santa Catarina), due to the front systems from the Southern Brazil (which is frequent in that area), and the driest region was the Paraguayan Chaco. However, in both the cases the model under–estimate the volume of overall precipitation, as it is shown in detail in the forward figures.

It was performed an average of temperature and accumulated precipitation over a time period of 20 years for each month (see Figures 7 and 8). In order to estimate the bias of the model, the same average with observed data from Climatic Research Unit (CRU) is also reported. Additionally, it was calculated the time correlation between them.

Figure 4. Map indicating some key regions
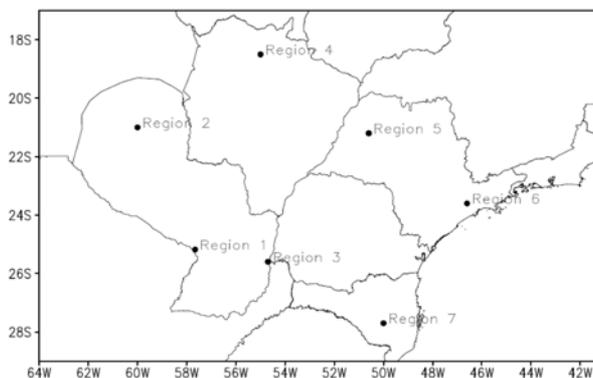
Figure 5. Daily mean temperature [Celcius degree] for all regions (see map in Figure 4). The mean was calculated using tmed=((tmin + tmax)/2), where tmin is the minimal temperature of the day and tmax is the maximum. The red line is the mean over all period (1960–80)
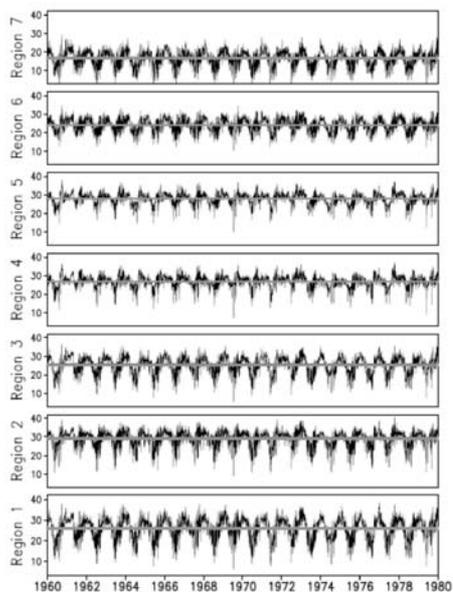
Figure 6. Daily accumulated precipitation [mm/day] for all regions (see map in Figure 4)
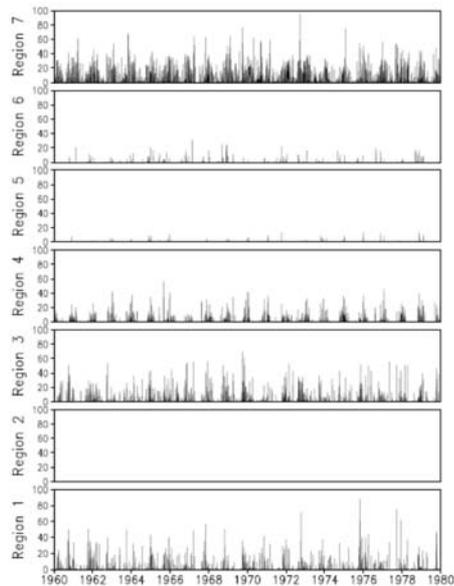
Figure 7. Monthly mean temperature [Celsius degree] for all regions (see map in Figure 4). The mean was retrieved using the arithmetic mean over the data from Figure 5. The flat line is the mean over all months. The lines represent the observations and the model. It is also shown the correlation between them. Observations from Climatic Research Unit (CRU)
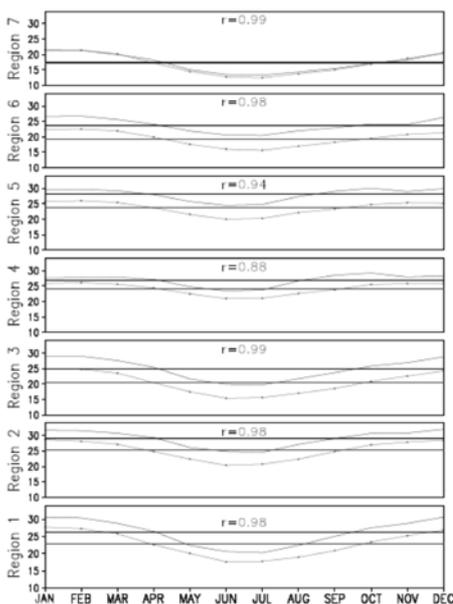
Figure 8. Monthly accumulated precipitation [mm/month] for all regions (see map in Figure 4). The red line represents the observations and the black bar is the model. It is also shown the correlation between them. Observations from Climatic Research Unit (CRU)
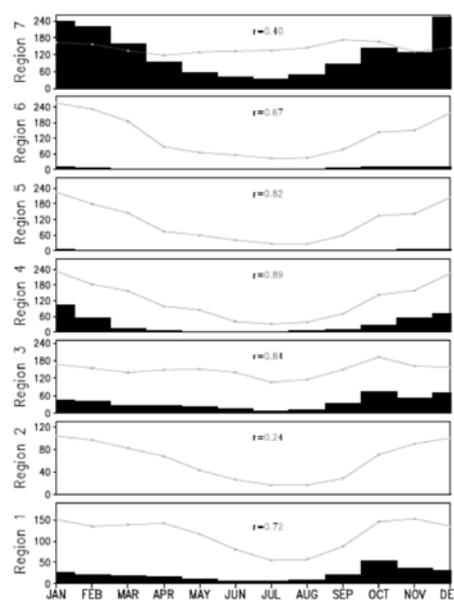
The model temperature shows values much higher than the observed data for almost all the regions, except from region 7 which are very close. On the other hand, the time correlation between model and observation data is very high (almost 1 in some cases). Despite of the observed data, precipitation values are much higher than the model output, the time correlation is good, reaching 0.89 in region 4.

All the Figures from 9 to 16 show the fields of seasonal averages of temperature and monthly accumulated precipitation (model output and observation). It is shown that the model temperature/precipitation distribution is very close to observation, however, the absolute values are not so close, particularly the precipitation data. The Table 3 shows that only in one case the spatial correlation was <50%. In Spring and Winter time the correlation between modelled and observed temperatures is above 90%.

Table 3. Spatial correlation between BRAMS output and CRU data for each season

r	Summer	Autumn	Winter	Spring
Temperature	0.87	0.85	0.90	0.93
Precipitation	– 0.11	0.55	0.87	0.56

Figure 9. Seasonal mean of temperature In Summer time in Southern Hemisphere, (a) model and (b) observation – [C]

(a)   (b)
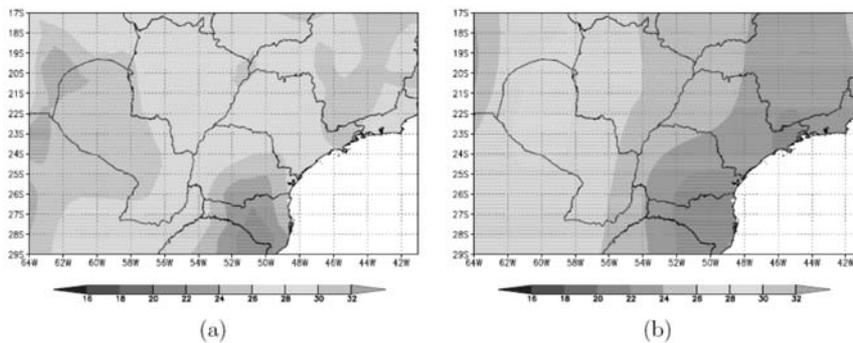
Figure 10. Seasonal mean of temperature in Autumn time in Southern Hemisphere, (a) model and (b) observation – [C]

(a)   (b)
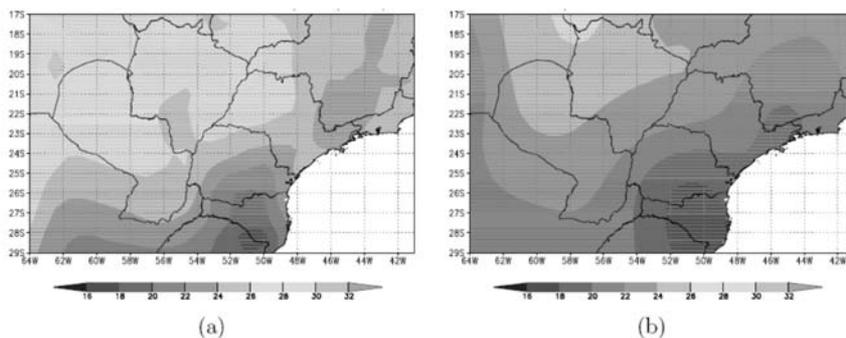
Figure 11. Seasonal mean of temperature in Winter time in Southern Hemisphere, (a) model and (b) observation – [C]
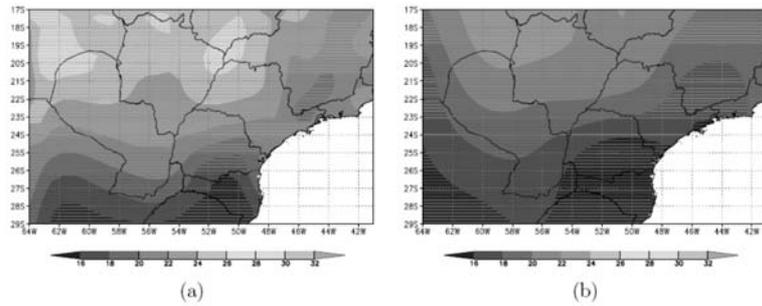
Figure 12. Seasonal mean of temperature in Spring time in Southern Hemisphere, (a) model and (b) observation – [C]
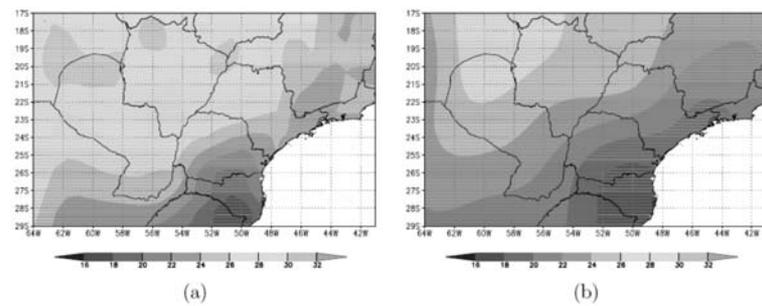
Figure 13. Seasonal mean of month accumulated precipitation in Summer time in Southern Hemisphere, (a) model and (b) observation – [mm/month]
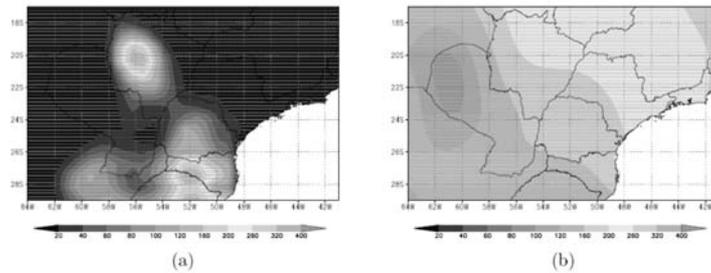
Figure 14. Seasonal mean of month accumulated precipitation in Autumn time in Southern Hemisphere, (a) model and (b) observation – [mm/month]
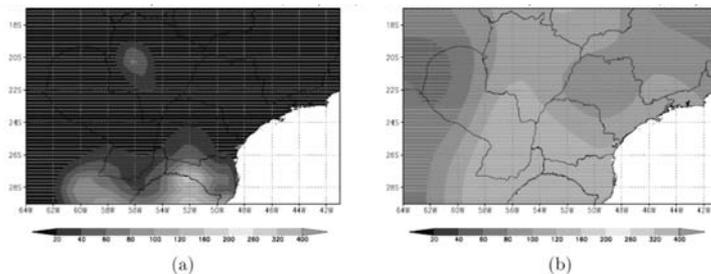
Figure 15. Seasonal mean of month accumulated precipitation in Winter time in Southern Hemi-sphere, (a) model and (b) observation – [mm/month].
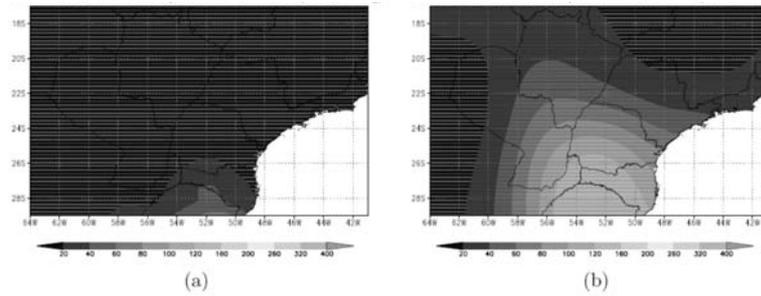
Figure 16. Seasonal mean of month accumulated precipitation in Spring time in Southern Hemi-sphere, (a) model and (b) observation – [mm/month]
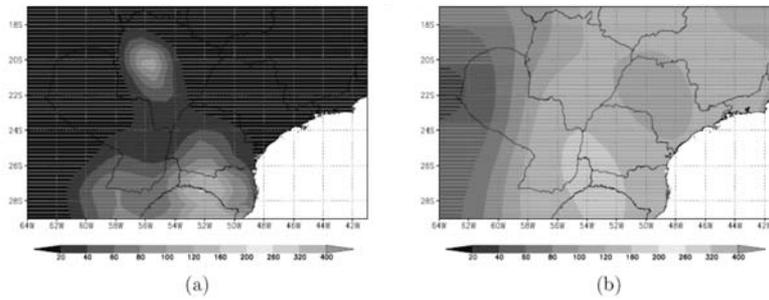
Figure 17. Difference between seasonal mean temperature from «future time» (2070/80) and «present time» (1960/80) downscaled data. (a) Summer and (b) Autumn – [C]
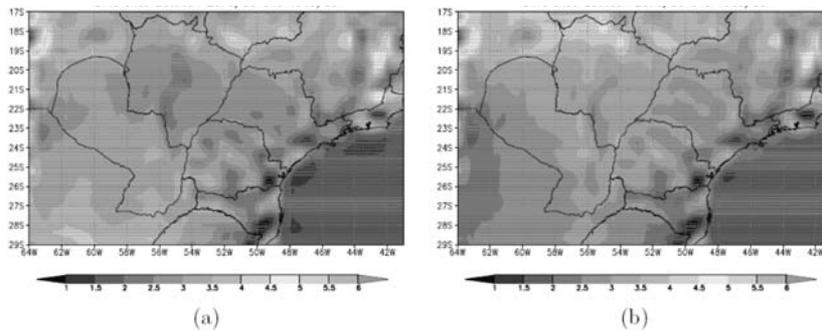
Figure 18. Difference between seasonal mean temperature from «future time» (2070/80) and «present time» (1960/80) downscaled data. (a) Winter and (b) Spring – [C]
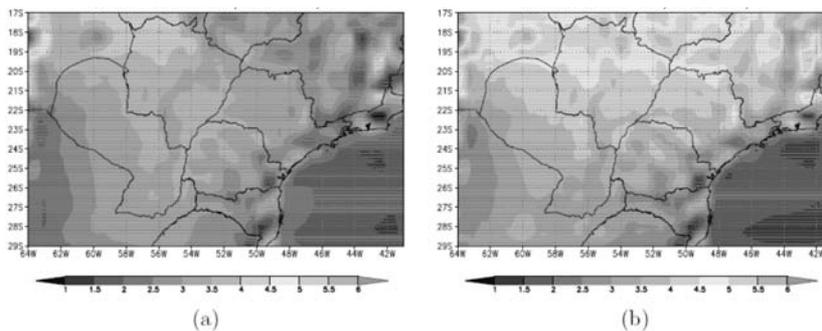
Figure 19. Difference between accumulated mean precipitation from «future time» (2070/80) and «present time» (1960/80) downscaled data. (a) Summer and (b) Autumn – [mm/month]

(a)   (b)
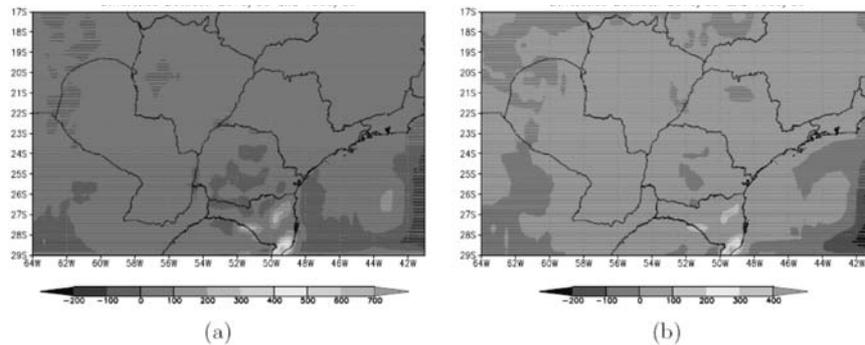
Figure 20. Difference between seasonal accumulated mean precipitation from «future time» (2070/80) and «present time» (1960/80) downscaled data. (a) Winter and (b) Spring – [mm/month]

(a)   (b)
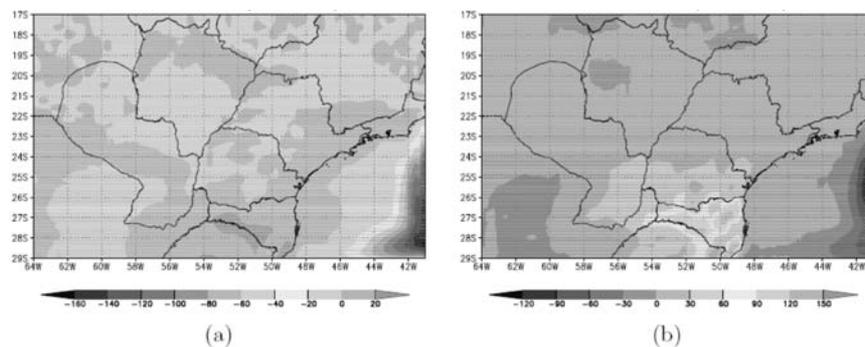
The results show that the model performance, used to represent the spatial distribution of both temperature and precipitation, is very good, although the absolute value is quite low. In addition, the region 7 was identified as the most reliable area for further analysis (climate scenarios). Figures 17 and 18 show the difference between the seasonal mean temperature of future time run and that one of present time (see Tables 1 and 2).

As was seen on the previous figures, the model is not well accurate for absolute values, except for region 7, therefore the values showed in Figures 17 and 18 can be biased. On the other hand, all figures agree with a heating of the air in all modelled area. The most reliable area, region 7, shows a heating of 2-3 degrees. Regarding the precipitation, Figures 19 and 20, the results do not show any specific trend (positive or negative): the values have a great variation.

4. Conclusions

In general, this project has provided several positive outputs. The first concerns with the exchanging of experiences and technologies opportunities, thanks to them a very useful tool was implemented for all kinds of modelling works, manly for the atmospheric one. In addition, this project gave the chance to two universities, the UCA and USP, to get in touch and to cooperate working together. This is very important because in South America much work should be done within climate changes topics, especially in Paraguay, where data and investigation in this subject are still lacking. Therefore, the cooperation between the two research

groups may enhance the knowledge of climate change effects and their management in specific areas of interest.

The professional experience got by the grant holder was very positive, since he had the chance to learn more about climatic data treatment, and about the model strengths and weaknesses. Besides, it was very attractive to work with other climate change experts.

Finally, the model is little biased from the observations, although any thorough model calibration was applied due to the short time left for the project accomplishment. Thus, according to what experienced with BRAMS model, enhanced results can be achieved if a thorough calibration is performed. In addition, the spatial distribution of both temperature and precipitation was relatively good considering that it is a climate simulation.

Appendix A. The cluster building and its hardware and software

This project required a strong computational capability, thus, with support of the Catholic University of Asunciòn (UCA) and the big help of Prof. Pedro Silva Dias and Pedro Pais Lopes from University of Sao Paulo, it was build a cluster with 8 processors and a gigabit network connection among the CPU's.

Many problems occurred during the cluster building, mainly with respect of the gigabit network board. It was not compatible with the first kernel version installed in the cluster. Initially, it was installed the *Debian Sarge* Operational System with the Kernel version 2.6.6 but it gave several problems. Therefore, a *Sarge Debian* release placed in order to test the Debian version (Etch) which has the 2.6.18 Kernel version.

With installation of *Sarge Debian* version, the cluster worked very well. Finally, it was made the communication among the nodes and the server with the VARAL software developed at University of Sao Paulo – Brazil. The Table 4 shows the mainly characteristics of the cluster:

Table 4. Cluster characteristics

Number of CPU's	4
Number of Processors	8 (Dual Core)
Processor	Pentium D 3.4 Ghz
RAM Memory	1Gb
Hard Disk	950Gb
Network Board	2 (1Gbit and 1 10/100)
Switch	8 port gigabit

Appendix B. Necessary software for running the BRAMS model

A number of software was installed in order to properly run the BRAMS model. The list below shows these software and explains their functionality:

- C and Fortran compilers – Since the BRAMS model source code is written in Fortran and C languages, it was necessary to install also two language compilers: the GCC and GFORTRAN, both GNU GPL software.
- HDF Library – Some BRAMS input data are storaged in HDF format.
- MPI Library – Responsible for the parallelism.
- Grib2dp and NC-GRA2dp – It was necessary to convert GRIB, NC or GRA data format into RALPH2 data format (BRAMS input data format).

- RAMSPOST – Necessary for pos-processing BRAMS's output. This software generates binary files that can be read and manipulate with Grads.
- Grads – An easy visualization tool.
  http://www.atmet.com/html/docs/data/ralph2.pdf 1

Appendix C. Complementary activities

Considering the big amount of data, their manipulation was very difficult, and all processes requested a lot of time for running. For this reason, other complementary activities were carried out while the data processing was applied:

- A2 times a day forecasting with a grid centred in the triple-boundary between Brazil, Argentina and Paraguay was implemented. The forecasting runs automatically and generates graphics of temperature, relative humidity, wind direction and velocity, sea level pressure and precipitation. All these outputs will be available on the CTA web page (see Figure 21)

Figure 21. Meteogram
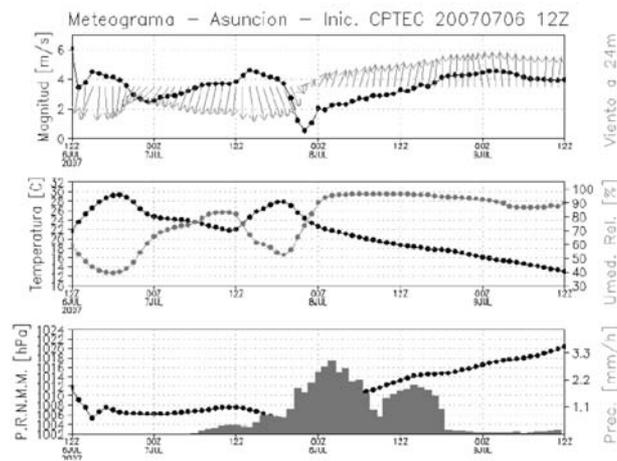
Figure 22. Precipitation diagram

(a)   (b)
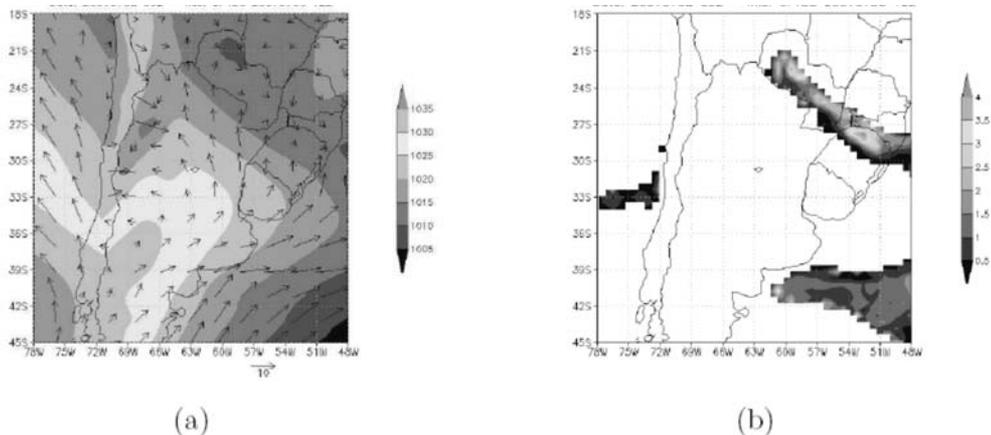
- A seminar entitled "The Use of Numerical Modeling as a Meteorological Tool" was carried out in CTA. The aim of the event was to explain the students, professors and everyone interested in the numerical modelling and climate change issues, the ICONE project (Figure 22).
- A student lesson course was also carried out in order to explain the function of the cluster and the model, besides an explanation of the basic tools and software required to process all the data before the running process was also provided. This course aimed at training experts within cluster and model management in order to keep on working at the study began by the grant holder.

References

Barros V., Robin C., Silva Dias P.L. (2006*). Climate Change in the La Plata Basin*. Consejo Nacional de Investigaciones Cientificas y Tecnicas. CONICET, Buenos Aires, Argentina.

Castro C.L., Pielke R.A. sr., Leoncini G. (2005). Dynamical downscaling: Assessment of value retained and added using the Regional Atmospheric Modeling System (RAMS). *J. Geophys. Res.*, 110 (D05108), doi:10.1029/2004JD004721.

Chen C., Cotton W.R. (1983). A one-dimensional simulation of the stratocumulus-capped mixed layer. *Boundary-Layer Meteorol.*, 25: 289-321.

Cotton W.R., Pielke R.A., Walko R.L., Liston G.E., Tremback C.J., Jiang H., Mcanelly R.L., Harrington J.Y., Nicholls M.E., Carrio G.G., Mcfadden J.P. (2002). RAMS 2001: Current status and future directions. *Meteorol. Atmos. Phys.*, 82: 5-29.

Grell G.A. (1993). Prognostic evaluation of assumptions used by cumulus parametrization. *Mon. Wea. Rev.*: 121: 764-87.

Hill G.E. (1974). Factor controlling the size and spacing of cumulus clouds as revealed by numerical experiments. *J. Atmos. Sci.*, 31: 646-673.

Intergovernmental Panel on Climate Change, 2001: Climate Change (2001). The Scientific Basis . Working Group I, http://www.grida.no/climate/ipcc tar/.

Klemp J.B., Wilhelmson R.B. (1978). The simulation of three-dimensional convective storm dynamics. *J. Atmos. Sci.*, 35: 1070-1096.

Lilly D.K. (1962). On the numerical simulation of buoyant convection. *Tellus*, 2: 148-172.

Marengo J.A. (2006). Mudanças climáticas globais e seus efeitos sobre a biodiversidade: caracterização do clima atual e definição das alterações climáticas para o território brasileiro ao longo do século XXI. Instituto Brasileiro do Meio ambiente e dos Recursos Renovaveis, Brasil.

Pielke R.A., Cotton W.R., Walko R.L., Tremback C.J., Lyons W.A., Grasso L.D., Moran M.E.N.M.D., Wesley D.A., Lee T.J., Copeland J.H. (1992). A comprehensive meteorological modeling system – RAMS. *Meteorol. Atmos. Phys.*, 49: 69-91.

Smagorinsky J. (1963). General circulation experiments with the primitive equations: 1. the basic experiment. *Mon. Wea. Rev.*, 91: 99-164.

THE STUDY OF CLIMATE CHANGE ON THE HYDROLOGY OF THE ITAIPU HYDROPOWER BASIN

Jose Miguel Rivarola Sosa
Facultad de Ciencias y Tecnología
Universidad Católica Nuestra Señora de la Asunción
Paraguay

Tutors: Prof. M. Bindi and Dr. M. Moriondo
Department of Agronomy and Land Management
Università degli Studi di Firenze
Italy

1. Introduction

The hydrologic basin of the Itaipu Hydroelectric Power Plant is formed by the Paraná River, which begins in the east and southeast of Brazil and then includes the eastern part of Paraguay, with 820,000 km² of drainage area. The Paraná River is the most important river of the Plata Basin, which is the second largest basin of South America after the Amazon, and the fifth largest in the world. It includes parts of southern Brazil, eastern Bolivia, all Paraguay, western Uruguay and north–eastern Argentina. The Plata Basin is the most developed region of South America producing most of the economic goods of the continent. Its water resources are essential for agriculture activities of Paranà and for hydropower of all the countries which share the basin. Therefore, it is important to know how climate change may affect its rivers and, consequently, how it may affect hydropower potential and extreme events which can occur (maximum and minimum).

Thus, in order to attempt the uncertain future prediction, the use of 'Scenarios' is recommended. These future scenarios may frequently be just a few contrasting hypotheses by which the uncertainty of future consequences can be investigated. Regardless of this, many of the climate change scenarios used in this study were developed by using only one CGCM model. Further studies need to be developed using other scenarios in order to appreciate their impacts on agriculture and hydropower.

The main objective of this study was the use of climate change scenarios in the region around the Itaipu Hydroelectric Power Plant in order to verify their impact on water availability within the studied basin. The changes in climate and their impacts in terms of changes in runoff mean and variability are of particular interest, especially with regard to the changes in runoff volumes (mean), seasonal changes and extreme events change (maximum and minimum).

2. Study area

The Itaipu Hydroelectric Power Plant is located on Paraná River, on the stretch of the frontier between Brazil and Paraguay.

The northern part of the basin is strongly regulated by other reservoirs. The basin from Porto Primavera Dam and Rosana Dam to the Itaipu Dam is an unregulated basin covering over 20% of the entire basin (see Figure 1). This basin is called "Itaipu incremental basin" and has a drainage area of 147,000 km² wide.

The study area is the «Itaipu incremental basin», where the two most important rivers are the Ivai and Piquiri, on the left side of Paraná River. The runoff on the right side is small.

Figure 1. Location of the Itapu Hydropower plan and study area ("Itapu incremental basin") indicated by the oval

3. Background

Recent literature concerning climate change impacts on hydrologic basins has described several methods of joining climate model with hydrologic models.

Table 1 shows a summary of several researches carried out in USA, Canada, England and Sweden. The several methods used in order to transfer the climate alarms signed by climate change models to those ones of hydrologic basins, are described below. These methods range from high resolution dynamical downscaling, down to simple delta change approach, or to statistical-stochastical based techniques.

4. Methodology and Data

4.1 Methodology summary

This study was developed following the steps listed below:

- Collection and check up of daily meteorological data within the study area.
- Selection of the period baseline scenario, through available observed data. Selection of climate change scenarios period.
- Generation of daily spatial mean precipitation for each sub-basin.
- Analysis of hydrologic model performance.
- Generation of daily synthetic spatial mean precipitation for the baseline scenario using LARS-WG model (through it statistical characteristic of observed data can be achieved and synthetic precipitation for each sub–basin can be generated).
- Generation of daily synthetic spatial mean precipitation for all climate change scenarios.
- Selection of the socioeconomic IPCC scenarios and CGCM's output achievement.
- Generation of statistical characteristic of CGCM as output.
- Generation of change parameters.

Table 1. Background about study of Climate Change (CC) on Hydrology about this research

Study	Authors	GCM(s) chosen	Hydrologic Model	Transfer method of CC signal
Exploring the range of uncertainty in climate change impacts on run-off and hydropower for the Lulealven River	Swedish Meteorological and Hydrological Institute – Bengt Carlsson et al. 2005	HadAM3H, ECHAM4; Downscaling: RCM	HBV hydrdogical	a) Delta change at observed data b) Direct methods (ensemble)
Potential implication of PCM Climate. Change Scenarios for Sacramento –San Joaquin River Basin Hydrology and Water Resources	Department of Civil and Environmental Engineering, University of Washington –Nathan T. Van Rheenen et al. 2004	DOE/NCAR PCM-statistically downscaling	VIC(Distributed Model) and the Central Valley Model	ensemble
Evaluation of Potential Impacts on Great Lakes Water Resources Based on Climate Scenarios of Two GCMs	NOAA/Great Lakes Environmental Research Laboratory – Brent M. Lofgren et al. 2002	CGCM1, HadCM2	Croley Model (1983;	Delta change at observed data
California Climate Change. Hydrologic Response, and Flood Forecasting	Earth Sciences Division. California, USA - Norman L Miller et al. 2003	HadCM2 PCM	Sacramento Model	Temperature difference and precipitation ratio
Water Management & Climate Change in the Okanagan Basin	University of British Columbia– Roxanne Brewer et al. 2001	CGCM1	HBV-EC model	Statistics temporal analogue, and Process modeling(about observed data)
Exploring impacts of climate change on the hydrology of The Okanagan basin	University of British Columbia – Wendy S. Merritt et al. 2001	CGCM2/statistical downscaling	UBC Watershed Model	LARS-WG/ WGEN/GEM/SDMS
Hydrologic impact of climate change in the Saguenay watershed	Department of Civil Engineering and School of Geography and Geology-Canada-YB. Dibike at al.	Three method of downscaling	HBE-96 WATFLOOD	Regression based(SDSM) – LARS-WG – Neural Networks (TLFN)
Downscaling global climate model outputs to study the hydrologic impact of climate Change	Department of Civil Engineering arid School of Geography and Geology-Canada– Paulin Coulibalv et al. 2005	CGCM1	IHMS HBV-96 mode	Regression based (SDSM), LARS-WG, Neural networks (TLFN)
Regional Probabilities of climatic change for Decision Making	NCAR, USA– Linda Mearns, Claudia Tebaldi et al. 2005	21 GCMs of IPCC	Sacramento Model	Statistical approach (Probability curve)

- Generation of synthetic spatial mean precipitation for each sub–basin using LARS–WG model.
- Delta change of daily observed evaporation data for each scenario.
- Use of synthetic series and for all scenarios foreseen, daily hydrological model running and Runoff achievement.
- Monthly change Runoff achievement.

The Figure 2 shows the conceptual schema of the study.

4.2   Data description

Through the data sets provided by Itaipu Binational, DINAC (Paraguay), Simepar (Brazil), IAPAR (Brazil) and ANA(Brazil), 51 rain gauges were used.

Forty rain gauges, which belonged to Itaipu operation network, were used. However, in order to improve the spatial distribution, further 11 rain gauges with good precipitation da–ta availability were also added. Therefore, 55 rain gauges were finally used during this study (see Figure 3).

Figure 2. Conceptual schema
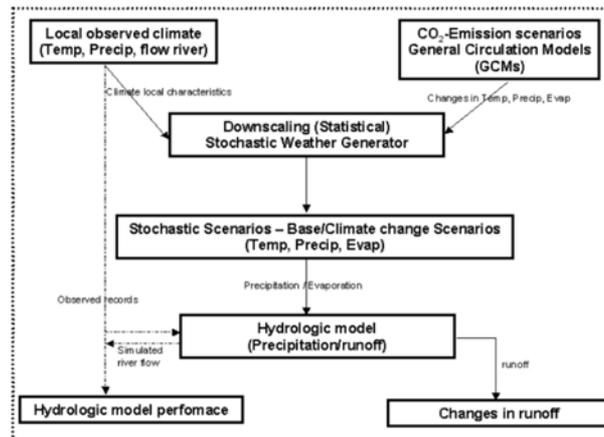
Figure 3. Location of the rain gauges (51 stations with daily precipitation available)
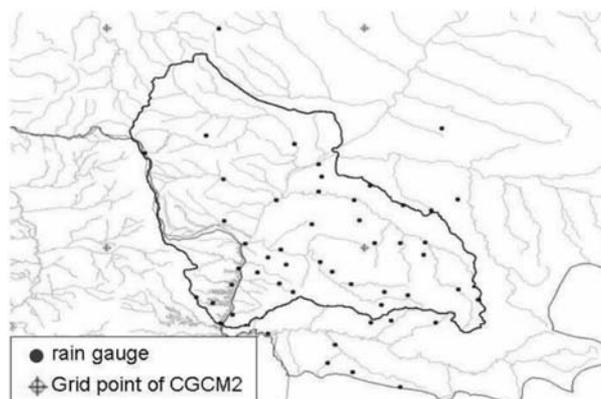
A basic consistency was developed. Wrong data have been deleted from visual inspection when P > 'maximum value' was found (250 mm, 200 mm and 150 mm as reference data were used). All negative values were also deleted.

Gap-filling was developed in 6 rain gauges using the data of the nearby stations: Dourados, Ponta Pora, Cantagalo, Cascavel, Marquinhos and Santa Maria.

In addition, a fast process of non-stationary analysis was also developed with daily spatial mean precipitation series (for each sub-basin). Trends found which were very low, are not included in this report.

4.3   Climate model

There are several global climate models (GCMs) that may be used for this study: Hadley Centre for Climate Prediction and Research (HadCM3), Australia's Commonwealth Scientific and Industrial Research Organization, CSIRO-mk2, Max Planck Institute fur Meteorologie, ECHAM4, National Centre for Atmospheric Research, NCAR–PCM, Canadian Centre for Climate Modelling and Analysis, CGCMs.

The model used in the present study was the Coupled global Climate Model, CGCM2, of the Canadian Centre for Climate Modelling and Analysis, which has a daily output of meteorological data with the provisional IPCC SRES 'A2' GHG and aerosol forcing scenario. The simulations of this model begin from 1990 with daily data availability of 1961–2100 time periods.

The data are referred to a 97x48 Gaussian grid (approximately 3.75° lat x 3.75° long). The data downloaded were: Screen (2m) Temperature (°C), daily maximum and minimum screen temperature, precipitation rate (mm/day), evaporation (mm/day).

There are three grid points nearby our study area: over Mato Grosso (Brazil), eastern region (Paraguay) and Paraná state (Brazil). All of them were used in this study and named as 'MG', 'PY' and 'PR'.

With the purpose of knowing the main characteristics of the study area, the Figure 4 shows the CGCM topography in South America and Figures 5a, b, c climate mean characteristics of the used grid points MG, PY and PR.

Figure 4. CGCM Topography in South America
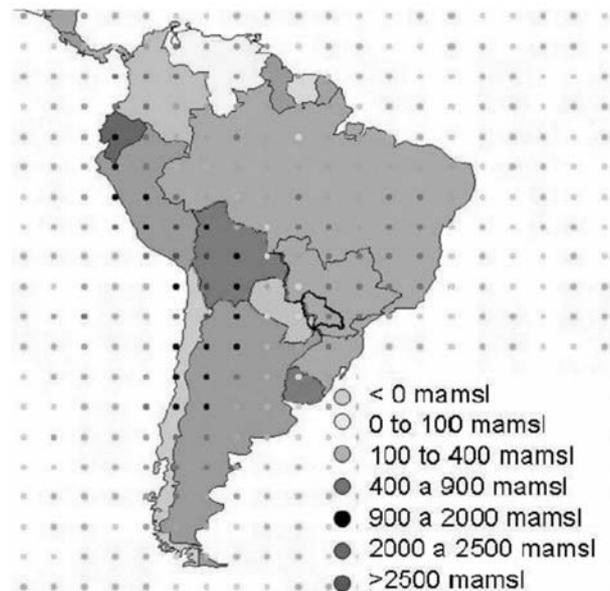
Figure 5a. Overview about climate model grid point 'PY'
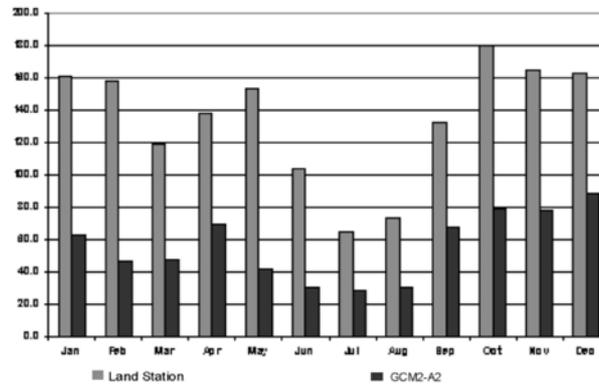
Figure 5b. Overview about climate model grid point 'PR'
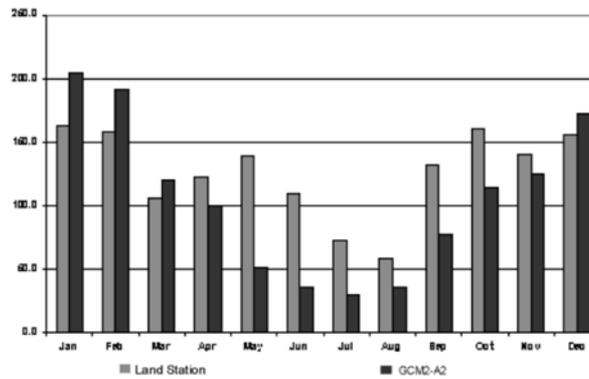
Figure 5c. Overview about climate model grid point 'MG'
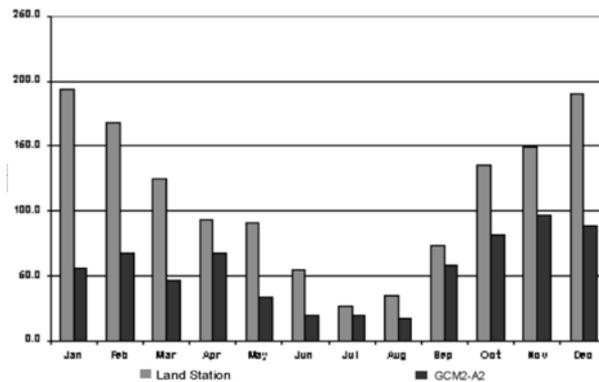
In 'PY' and 'PR' points the observed monthly precipitation present a slight increase in autumn and spring, instead in "MG" presents two seasons: wet and dry. The same trend can be seen in CGCM2 and 'PY' grid point.

We must take into account that grid box values are not directly comparable to station data. Climate models attempt to represent the full climate system from first principles on large scales and their outputs may be used to study the impacts of climate variability and climate change.

4.4 *Downscaling techniques and overview of downscaling methods*

It is necessary to transfer climate change signals from the global scale of the GCMs to the local or regional ones, which are required as inputs by hydrological models. Thus, it is important to know the downscaling techniques which are frequently used.

Downscaling methods could be used for assessing the potential impacts of climate change and variability upon the hydrological regime. In general, among these downscaling procedures two broad categories currently exist: dynamical downscaling (DD) and statistical downscaling (SD) techniques. The first ones (DD) consist in the extraction of regional scale information from large-scale circulation data based on the modelling of regional climate dynamical processes. The latter procedures (SD) relied on the empirical relationships between large-scale atmospheric variables and surface environment parameters (Nguyen V.T.V. 2005).

The SD techniques present several positive factors due to their practical technique application and computational resources. Statistical downscaling (SD) methodologies may be: regression methods; stochastic weather generators and others (e.g.: weather typing approaches).

The regression-based downscaling methods (SD) mainly rely upon the empirical statistical relationships between large-scale predictors and local-scale parameters. Different approaches in this empirical downscaling category can be identified according to the choice of the mathematical function to describe the predictor-predicting relationship, the computational technique used, or the selection of the predictor variables which can be considered (Wilby *et al.* 2002a) (e.g.: SDSM, TLFN-Neural networks). In general, the main advantage in the use of the regression downscaling procedures is that these methods are simple and less computationally demanding, compared to other downscaling methods. However, the application of regression-based procedures is limited to the locations where good predictor-predicting relationships could be found. The regression-based techniques assume the validity of the estimated model parameters under future climate conditions (Nguyen V.T.V. 2005).

The stochastic weather generators have been extensively used in the planning, design, and management phases of water resources systems. Stochastic weather generator methods are based mainly on stochastic weather generator models such as WGEN (Richardson 1981) and LARS-WG (Semenov and Barrow 2002). These models typically involve the modelling of the daily rainfall occurrences, the description of the distribution of rainfall amount on a wet day, and other weather variables conditioning (such as temperature, radiation, etc.) on the wet/dry status of the day. Climate change scenarios are then stochastically generated and based on the link between stochastic model parameters and correspondent variable changes in the GCM. In general, both generators have a similar structure: the observed data at a determined site were used to assess the probability distributions parameters of daily climate variables (minimum and maximum temperatures, precipitation, and solar radiation). In addition, both models analyze dry and wet days separately and thus include a mechanism of precipitation status selection for each day. The generators differ mainly in the choice of the probability distributions which can be used. WGEN generator uses standard distributions (e.g., two-parameter Gamma), whereas LARS-WG generator employed semi-empirical distributions. One advantage of using a standard distribution is that it has a smoothing effect on the empirical frequency of observed data and requires only few parameters estimation (Nguyen V.T.V. 2005).

However, such distributions may fit very well with observed data. A semi-empirical distribution, with a larger number of parameters, is much more flexible and able to describe accurately any type of empirical frequency distribution. The performance of both WGEN and LARS-WG has been tested using data from a range of various climate types (Semenov *et al.* 1998). LARS-WG generator seemed to be able to better describe the observed weather characteristics than WGEN.

In general, the main advantage of stochastic weather generator procedures consists in the chance of reproducing many observed statistical characteristics of daily weather variables for a

specific site. In addition, the stochastic weather generators can generate a large number of different climate scenarios for risk assessment studies. However, the main disadvantage of these procedures is related to the arbitrary manner of determining the model parameters for future climate conditions (Wilby *et al.* 2002b).

The SDSM is best model since is a hybrid between stochastic weather generator and regression–based methods. The model permits the spatial downscaling of daily predictor–predictand relationships using multi-linear regression techniques and generates 'synthetic predictand' that represents the generated local weather. Further details of SDSM are provided by Wilby *et al.* (2002a).

The comparison between some selected statistics of observed weather data and statistics of weather data generated by the two models, indicates that the LARS-WG model can provide daily precipitation statistics more comparable to observed data ones than SDSM model. However, both models were unable to reproduce accurately these observed statistics. (Nguyen V.T.V. 2005)

The SDSM and LARS-WG models seemed to be able to adequately describe the daily temperature extremes observed statistics, while SDSM was somewhat more accurate than the LARS-WG. In terms of practical applications, the calibration of the LARS-WG model is much easier than SDSM's one.

In order to successfully establish good relationships between large-scale predictor variables and surface weather variables at a local site, the calibration of the SDSM requires a complex procedure. (Nguyen V.T.V. 2005)

4.5   Stochastic Weather Generator – LARS-WG

The LARS-WG model (Semenov and Barrow 2002) is a stochastic weather generator which can be used for the simulation of weather data at a single site, under both present and climate change conditions. These data are daily time series of precipitation (mm), maximum and minimum temperature (°C) and solar radiation (MJm-2day-1). In order to determine the parameters of specifying probability weather variables distributions, LARS-WG model uses data input which are daily weather observed for a given site. The generation procedure produces synthetic weather data that are then based on selecting values from the appropriate distributions using a pseudo-random number generator.

LARS-WG is not a predictive tool that can be used in weather forecasting, but is simply an algorithm for generating time-series of synthetic weather which is statistically 'identical' to the observations.

At the moment, the output from global climate models (GCMs) has insufficient spatial and temporal resolution and reliability to be used directly on impact models. Therefore, a stochastic weather generator can used as a tool to produce multiple-year climate change scenarios at daily time scale which incorporate changes in both average climate and in climate variability.

The main focus of this model was to overcome the limitations of the Markov chain model of precipitation occurrence which considers two precipitation states, wet and dry and condition on the previous day only. This model is not always able to correctly simulate the maximum dry spell length, which is crucial for a realistic assessment of agricultural production and water resources. The LARS-WG model develops a new approach of 'series', in which the simulation of dry and wet spell length is the first step in the weather generation process.

LARS-WG model is based on the series weather generator described in Racsko *et al.* (1991). It utilises semi-empirical distributions of lengths of wet and dry day series, daily precipitation and daily solar radiation. Random values from the semi-empirical distributions are chosen first selecting one of the intervals (using the proportion of events in each interval as the selection probability) and afterwards through the selection of a value within that interval from the consistent distribution.

Such a distribution is flexible and can round up a wide variety of shapes by adjusting the intervals. The cost of this flexibility is that the distribution requires 21 parameters (11 denoting the interval bounds and 10 values indicating the number of events within each interval) have to be specified.

The simulation of precipitation occurrence is modelled as alternate wet and dry series, where as wet day is meant a day with precipitation height higher than 0.0 mm. The length of each series is chosen randomly from the monthly wet or dry semi–empirical distribution from which the series starts. In order to determine the distribution, observed series are also monthly allocated. For a wet day, the precipitation value is generated from the semi–empirical precipitation distribution for the certain month independently from the length of wet series or from precipitation amount on previous days.

Daily minimum and maximum temperatures are considered as stochastic processes with daily means and daily standard deviations and are conditioned on the wet or dry status of the day. The technique used to simulate the process is very similar to that one described in Racsko *et al.* (1991). The seasonal cycles of mean and standard deviations are modelled by finite Fourier series of third order and the residuals are approximated by a normal distribution. The Fourier series for the mean are fitted to the observed mean values for each month. Before fitting the standard deviation Fourier series, the observed standard deviations for each month are adjusted in order to give an estimated daily average standard deviation removing the estimated effect of the changes in the mean within the month. This adjustment is calculated using the fitted Fourier series calculated before for the mean.

The distribution of solar radiation also varies significantly on wet and dry days. Therefore, separate semi–empirical distributions were used to describe solar radiation on wet and dry days. An autocorrelation coefficient was also calculated for solar radiation and was assumed to be constant throughout the year. Solar radiation is modelled regardless of temperature.

The Long Ashton Research Station Weather Generator was named as LARS–WG in memory of the location where was developed for climate change scenarios implementation.

The principal advantage of LARS–WG model application within this study is the ability to simulate changes in variability. While, the principal shortcoming in LARS–WG model use within this study (in hydrologic basins) consists in the independence of stochastic time series generation for each sub- basin, therefore the model doesn't have any spatial correlation at a daily scale.

The process developed during this study (using the spatial mean precipitation for each sub-basin with LARS–WG model application) was:

- Calibration process: observed statistical characteristics calculation.
- Validation: any statistically–significant differences within observed and synthetic data analysis.
- Generation of synthetic data: generation of daily synthetic data for a baseline scenario and two climate change scenarios. For the baseline scenario, daily synthetic data are generated using the same statistical characteristics which are obtained from observed data. For climate change scenario, daily synthetic data are generated using the perturbed statistical characteristics. Statistical characteristic change parameters are obtained from the statistical characteristic of CGCM precipitation output, by grid points. Each sub–basin data series is perturbed using the neighbouring CGCM grid points ('PY', 'PR' or 'MG').

4.6   Hydrologic model

4.6.1 Formulation - Rainfall-runoff modelling

In this study the hydrological 'Sacramento' model was used to interpret hydrological change by several climate scenarios.

The Sacramento model is a deterministic conceptual and semi–distributed hydrologic spa–tial model of soil water balance (Peck 1976; Georgakakos *et al.* 1988; Gan and Burges 1990), developed by Burnash *et al.* in 1973, in National Weather Service Sacramento, for California River Forecast Center use (Peck 1976). A Dutch version of this model (by Hymos software) is usually applied on a daily time step in the Itaipu Hydroelectric Power Plant. In this study it was used in order to calculate the runoff volume.

With the use of Sacramento Model, sub–process and physical mechanisms, which govern the hydrologic cycle, can be internally modelled (see Figure 6). With the 'soil moisture account–ing routine' soil field capacity and change in soil moisture storage due to rainfall and evapo–transpiration can be calculated; while with the runoff generation routine water from the soil moisture zone to runoff can be transformed.

Figure 7 shows in deep detail how the modelling of the hydrologic cycle is done. Further–more, the model is a semi–distributed conceptual model because the referential basin is split into several sub–basins where the hydrology model is applied.

The model parameters are determined through a calibration process, where the parameters are adjusted until simulated and observed runoff shows good agreement. Then, the calibrated model can be used as a simulation tool in numerous applications.

Figure 6. The water cycle by the US Geological Survey
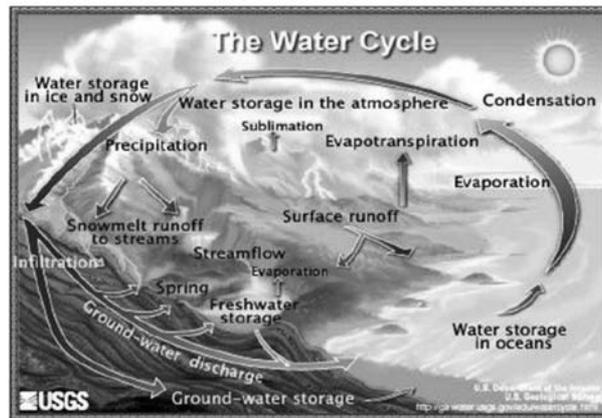
Figure 7. Rainfall–runoff process in each sub–basin inside the Sacramento model
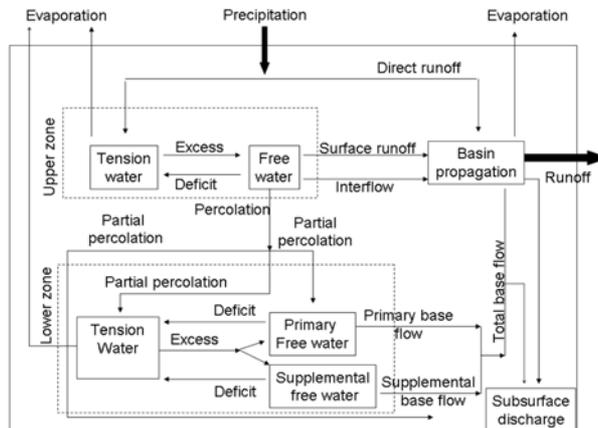
The Sacramento model has been applied to a wide range of applications including, for example, analysis of extreme floods and effects of climate change. In this study only the rainfall-runoff process was used because stochastic time series for each sub-basin were temporally and spatially independent: this is an element which is essential to obtain for river flows since the rainfall-runoff process has to be used (channel routing model).

4.6.2 Applications in the study area

The Itaipu incremental basin, 147,000 km² of drainage area wide, was split into 29 sub-basins (also called 'segments'), in order to represent in a deeper detail each river's sub- basin (especially the Ivai and Piquiri rivers), as shown in Figure 8, and in order to improve the simulated river flow.

Figure 8. Sub-basins boundaries of the Itaipu incremental basin in order to run the rainfall-runoff model (29 segments).
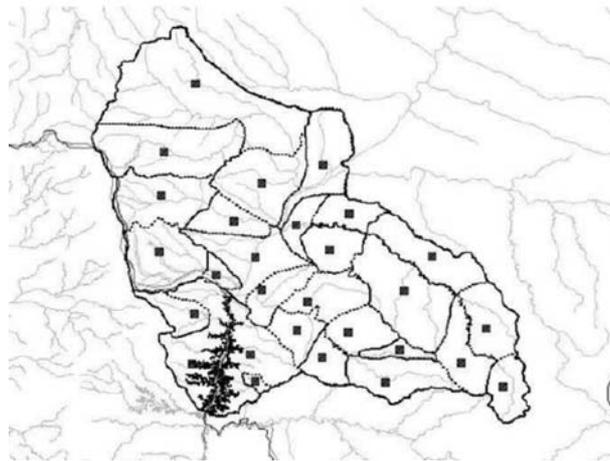
For each segment, spatial mean precipitation and the evaporation have been calculated, since required by the Sacramento model running. The nearest neighbour's method (Thiessen 1911) was used to obtain spatial mean precipitation, for this purpose specific software, developed within the Itaipu Power Plant centre, has been used.

The evaporation data, used for all the sub-basins, belongs to the monthly evaporation recorded by the Guaira Porto evaporation gauge. In fact evaporation data are not available within data collection network. This monthly climatic data was converted to daily time series. This simplification is also used in the model operation phase. The same assumption was also used during this study (one evaporation series data for each scenario).

4.6.3 Performance of hydrologic model applications

Twenty seven years of daily river-flow data between 1980 and 2006 were used for the performance model. The performance model results are described in Figure 9 and show the total flow which has been calculated by the discharges sum of five river-flow gauges (observed vs. simulated): Porto Paraiso do Norte (Ivai river), Balsa Santa Maria (Piquiri river) on the left side of the Paraná river, Ivinheima (Ivinheima river), Florida (Amambai river) and Iguatemi

Figure 9. Model performance total flow sum from 5 rivers of Itaipu incremental basin. The table shows square correlation coefficients by river
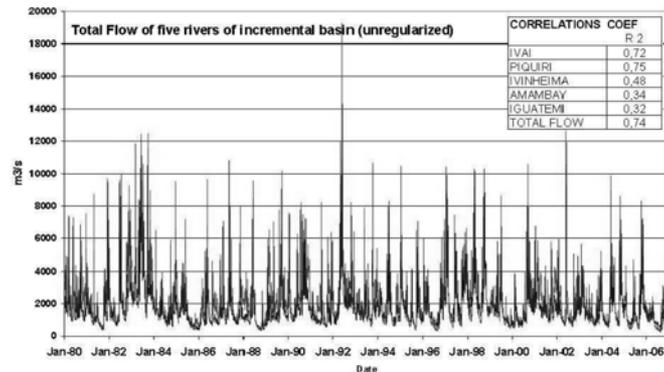
Table 2. Detailed data for each sub–basins

No.	Name	River	Area km2	Lat degree	Long degree	Altitude mamsl
1	Guaìra	Parana	6400	–23.600	–54,000	230
2	Amambai (Florida)	Amambai	7090	–22.867	–55,121	350
3	Amambai Confluencia	Amambai	3300	–2 3.173	–54,257	250
4	Balsa do Cantu	Piquiri	1482	–24.700	–52,300	600
5	Porto Guaranì	Piquiri	5291	–25.089	–52,465	600
g	Novo Porto 2 MD	Piquiri	3939	–24.491	–52,905	500
7	Novo Porto 2 Ml	Piquiri	2701	–24.793	–53,208	500
8	Balsa Santa Maria MD	Piquiri	4615	–24.129	–53,383	400
9	Balsa Santa Maria Ml	Piquiri	2969	–24.474	–53,513	400
10	Piquiri Confluencia	Piquiri	3330	–23.984	–53,930	250
11	Iguatemi (Estrada)	Iguatemi	7225.	–23.536	–55,139	450
12	Iguatemi Confluencia	Iguatemi	1330	–23.808	–54,463	300
13	Carapà	Itaipu lateral	3100	–24.275	–54,718	350
14	Area Embalse MD	Itaipu lateral	8000	–24.871	–54,749	400
15	San Francisco Falso	Itaipu lateral	570	–25.080	–54,000	450
16	Area Embalse Ml	Itaipu lateral	7800	–24.762	–54,055	500
17	Reservorio	Reservoir	1400	–24.971	–54,445	225
18	Caiuà	Parana	7000	–22.500	–53,200	250
19	Tereza Cristina	Ivai	3500	–25.143	–51,074	800
20	Ubà do Sul MD	Ivai	5131	–24.451	–51,272	600
21	Ubà do Sul Ml	Ivai	4499	–24.856	–51,571	600
22	Porto Paraiso do Norte MD	Ivai	6064	–23.587	–51,912	400
23	Porto Paraiso do Norte Ml	Ivai	10186	–24.003	–52,244	400
24	Novo Porto Taquara MD	Ivai	2518	–23.089	–52,893	300
25	Novo Porto Taquara MI	Ivai	3326	–23.518	–53,122	300
26	Ivai Confluencia	Ivai	2050	–23.219	–53,523	300
27	Ivinhema Ml	Ivinhema	21200	–21.527	–54,714	500
28	Ivinhema MD	Ivinhema	10100	–22.350	–55,089	500
29	Ivinhema Confluencia	Ivinhema	7850	–22.715	–53,928	300

mamsl meters above mean sea level

(Iguatemi river) on the Paraná river right side. In box table of Figure 9 performance results per gauge, with square correlation coefficients, can be visualized.

The performance of the hydrologic model is acceptable for the total flow, and also for the left side of the Paraná River: Ivai and Piquiri rivers. But on the right side (Ivinheima, Amambai and Iguatemi rivers) the performance is much lower. These performance results are easily to understand since the station network availability and sub–basin divisions are not numerous within Paraná River right side.

However, we must remember that the hydrologic model is used only to obtain the change in runoff considering several climate scenarios.

5. Climate change scenarios

5.1 Socioeconomic IPCC/ SRES scenarios - Greenhouse gas emission

The Special Report on Emission Scenarios (SRES) was a report prepared by the Intergovernmental Panel on Climate Change (IPCC) for the Third Assessment Report, on future emission scenarios to be used for driving global circulation models to develop climate change scenarios. Because projections of climate change depend heavily upon future human activity, climate models are running against scenarios (with different assumptions for future greenhouse gas pollution, land–use, etc) (http://en.wikipedia.org).

The scenarios are organized in families. In summary, there are four scenario groups which produce: high (A1), medium high (A2), medium low (B1) and low (B2) anthropogenic emissions of greenhouse gases and aerosols; according to technical development, environmental and social conscience, demographic development and cooperation within the countries (see Figure 10).

In deeper detail:

- the A1 family scenarios is one of most integrated scenarios of world, and is characterized by: rapid economic growth, a global population that reaches 9 billion of people in 2050 and then gradually declines, the quick spread of new and efficient technologies and a convergent world (income and way of life converge between regions, extensive social and cultural interactions worldwide).
- the A2 family scenarios is one of the most divided scenarios of world, and is characterized by: a world of independently operating, self-reliant nations, continuously increasing popu-

Figure 10. Dimensions of SRES/IPCC greenhouse gas emission scenarios
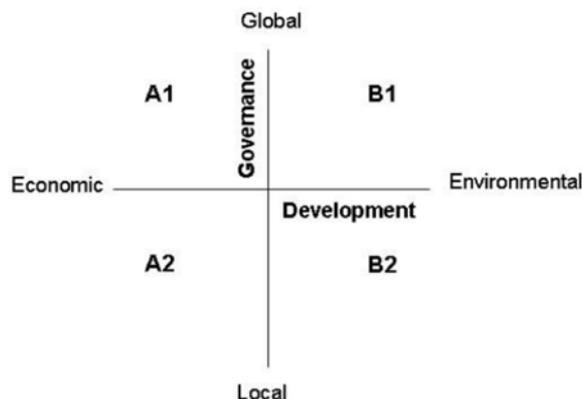
lation, regionally oriented economic development and slower and more fragmented technological changes and improvements to per capita income.
- the B1 family scenarios is one of the most integrated and ecologically friendly of the world, and is characterized by: rapid economic growth as in A1, but with rapid changes towards a service and information economy, population rising to 9 billion in 2050 and then declining as in A1, reductions in material intensity and the introduction of clean and resource efficient technologies (an emphasis on global solutions to economic, social and environmental stability).
- the B2 family scenarios is one of the most divided of the world, but more ecologically friendly, and characterized by: continuously increasing population, but at a slower rate than in A2, emphasis on local rather than global solutions to economic, social and environmental stability and intermediate levels of economic development (less rapid and more fragmented technological change than in B1 and A1).

5.2   Selected scenario

As mentioned before, this study used the Coupled Global Climate Model (CGCM2) of the Canadian Centre for Climate Modelling and Analysis, which has a daily output of meteorological data with 'A2' and 'B2' SRES/IPCC emission scenarios, and which was only used with 'A2' SRES/IPCC emission scenario.

The CGCM2-A2 output has daily data availability for the time period from 1961 to 2100. Usually, the climate baseline period (present scenario) is a 30-year 'normal period' as defined by the WMO, for 1961-1990, but in this study was used between 1980 and 2006 (27 years) because the observed data sets availability was much more consistent.

The climate change scenarios which have been selected are: a) scenario CGCM2-A2 period 2010/2040 (scenario 2010/2040) and b) scenario CGCM2-A2 period 2070/2100 (scenario 2070/2100).

The synthetic spatial mean precipitation series (for each sub-basin) were generated for the present scenario and climate change scenarios by the LARS-WG model, using the process explained above (Downscaling techniques).

The monthly evaporation observed data were perturbed (within each scenario) using the relative change of monthly evaporation output of CGCM2-A2 in grid point 'PR' (in which its trend is similar to the trend of monthly data observed). This perturbed monthly evaporation data were converted to the daily step in order to be used within hydrologic model (see Table 3).

6. Hydrologic impact of climate change

6.1   Precipitation

Precipitation changes are analyzed from the monthly precipitations near to CGCM2 grid points ('PY', 'PR' and 'MG'), and are calculated averaging monthly observed precipitation values, recorded by the closest stations to each grid point. These averages are then perturbed by the relative change of the monthly precipitation CGCM2-A2 model output. The results found were the following:

Scenario 2010/2040
Figure 11 (a, b and c) shows that monthly precipitation changes are low and dispersed. Analysing all the trends we can state that: in the 'PR' and 'MG' regions the autumn precipitation trend decreases (AMJ), whereas the spring one increases.

Table 3. Relative change in the evaporation

	CLIMATOLOGY USED IN SACRAM.	CGCM2_A2 – GRID POINT: PARANA				
		Present (1980/2006)	Scenario 2010/2040		Scenario 2070/2100	
	mm/m	mm/m	mm/m	Relative change	mm/m	Relative change
Jan	150,2	134,5	135,0	1,00	134,6	1,00
Feb	117,3	124,1	127,4	1,03	118,9	0,96
Mar	90,4	129,1	129,8	1,01	121,1	0,94
Apr	68,3	99,3	104,7	1,05	102,1	1,03
May	52,2	79,5	79,7	1,00	81,7	1,03
Jun	42,1	57,2	57,2	1,00	60,1	1,05
Jul	38,1	59,9	59,9	1,00	62,2	1,04
Aug	40,2	74,2	72,7	0,98	74,9	1,01
Sep	48,4	89,8	88,5	0,99	84,6	0,94
Oct	62,5	118,6	118,9	1,00	106,0	0,89
Nov	82,7	127,8	123,4	0,97	118,8	0,93
Dec	108,9	135,6	136,8	1,01	130,3	0,96
Annual	901	1230	1234	1,00	1195	0,97

Scenario 2070/2100

Also Figure 12 shows monthly precipitation changes: in this scenario a trend decrease has been encountered principally during summer and autumn seasons, while in spring monthly precipitation decrease is lower.

6.2   Runoff

Before runoff analysis comment, it is important to remind statistical characteristic of monthly observed river flow for the study area (Itaipu incremental basin).

Figure 13 shows the mean, maximum, minimum, quantile statistics (q33% and q66%). Through these information we can get data concerning the available runoff (mean), extreme event periods, dry (minimum and q33%) and wet (minimum and q33%) periods.

The mean river flow has a low variation. Wet events usually occur in May, June (autumn) and October (spring) (regarding maximum and q66%); while dry periods occur during all months of the year, but especially in August (winter) (regarding minimum and principally q33%).

Therefore, with the goal of knowing the available runoff change, it will be necessary to analyse the mean runoff taking into account the annual, and seasonal (summer, autumn, winter and spring) periods for each sub-basin. Wet extreme events will be shown only within the annual statistic and during autumn season when there is a greater runoff. Dry extreme events will be shown only within the annual statistic and during winter season, when there is a lower runoff.

The runoff analysis has been carried out within each sub-basin because the stochastic series data are not spatially correlated on a daily scale, where daily river flow is necessary to know.

The scale adopted for trend analysis is: without trend and low/medium/high trend for positive change (runoff increase) or negative (runoff decrease).

Figure 11a. Precipitation change for grid point 'PY' in Scenario GCM2–A2 2010/2040
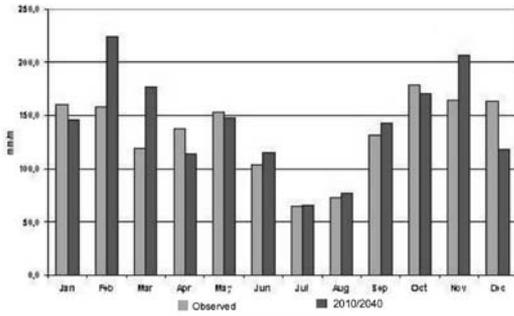
Figure 12a. Precipitation change for grid point 'PY' in Scenario 2070/2100
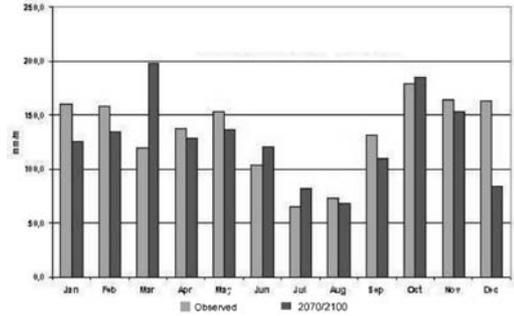
Figure 11b. Precipitation change for grid point 'PR' in Scenario GCM2–A2 2010/2040
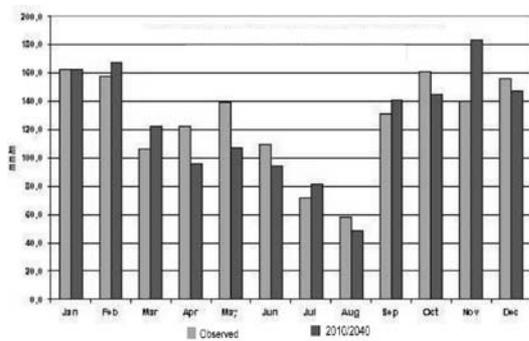
Figure 12b. Precipitation change for grid point 'PR' in Scenario 2070/2100
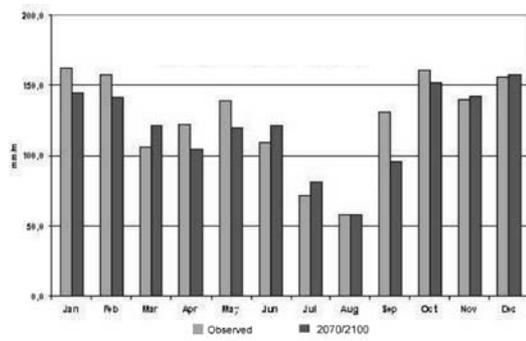
Figure 11c. Precipitation change for grid point 'MG' in Scenario GCM2–A2 2010/2040
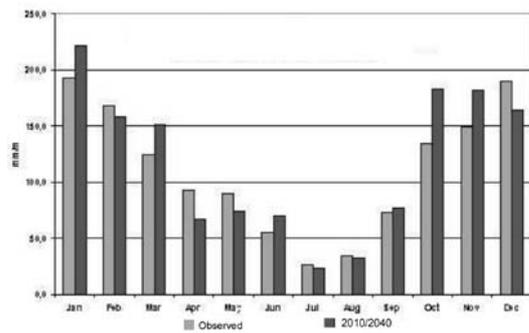
Figure 12c. Precipitation change for grid point 'MG' in Scenario 2070/2100
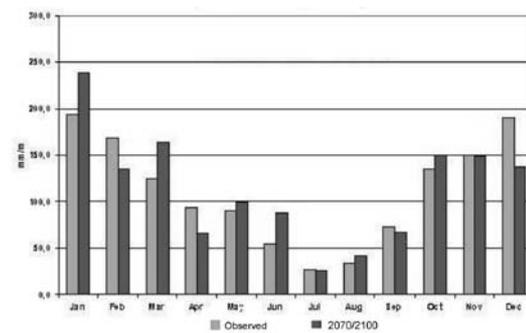
6.3   Scenario 2010/2040

6.3.1 Mean runoff change

Figure 14 shows that mean runoff has a decrease trend in the left side of the Paraná River, on the opposite an increase trend in the right side occurs.

In summer there is an increase trend in most of the sub-basins, but many of them have scattered results (see Figure 15). In autumn there is a decrease trend in left side of the Paraná

Figure 13. Total flow monthly statistic of the incremental basin rivers. Calculated from adding observed flow rivers of the flow station (P.P. do Notres, B.S. Maria, Invinheima, Florida and E. Iguatemi)
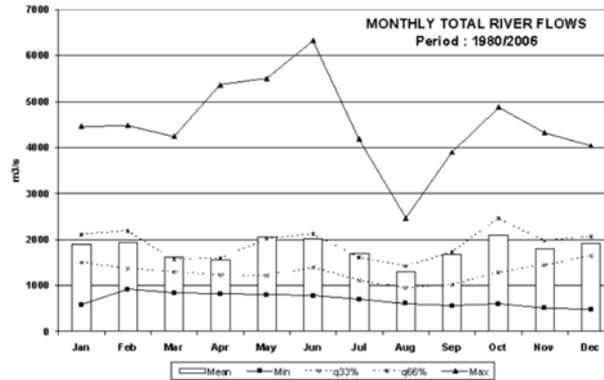
Figure 14. Changes in mean annual runoff in scenario CGCM2–A2 2010/2040 by sub-basin
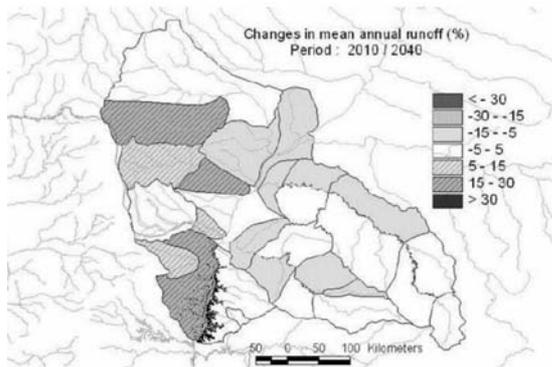
Figure 15. Changes in mean annual runoff in scenario CGCM2–A2 2010/2040 by season
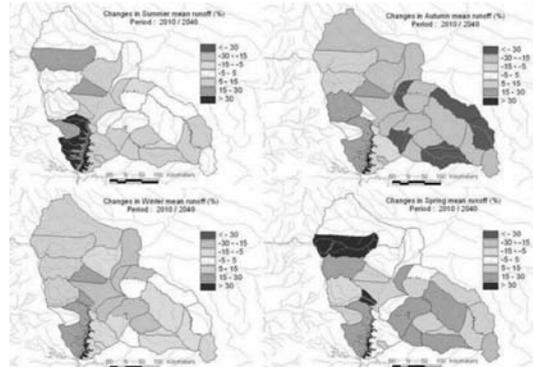
River, while there is an increase trend in the south of the right side (influenced by grid point 'PY'). In winter there is a decrease trend in the left side, while there is an increase trend in the right side. In spring, there is an increase trend in most of the sub-basins, but one sub-basin is characterized by a scattered result.

6.3.2   Extreme events change

Figure 16 shows that monthly maximum runoff has a decrease trend in the left side of the Paraná River while an increase trend has been noted in the right side. Many of the sub-basins show scattered results. Analysing the autumn season, when a greater runoff occurs, a decrease trend in most of the sub-basins occurs and many sub-basins have scattered results.

Likely, Figure 17 shows that monthly minimum runoff has a decrease trend in the left side of Paraná River, while this one has an increase trend in the south of the right side, but also in this case many sub-basins have scattered results. In winter time the same trend is also seen.

The scattered result could be due to the fact that the stochastic precipitation series were created through a random process; therefore these series are spatially independent with each other. Another problem could concern with data consistency.

Figure 16. Changes in monthly maximum runoff in scenario CGCM2–A2 2010/2040 by sub-basin
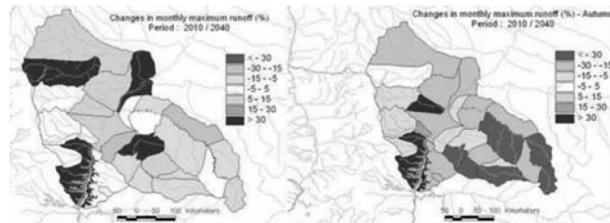
Figure 17. Changes in monthly minimum runoff in scenario CGCM2–A2 2010/2040 by sub-basin
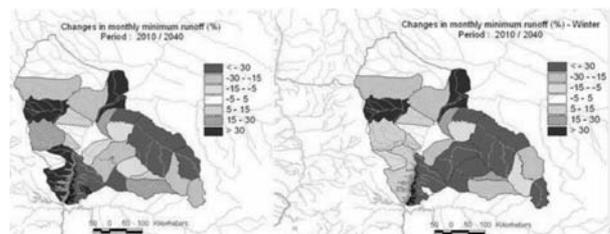
6.4   Scenario 2070/2100

6.4.1 Mean runoff change

Figure 18 shows that mean runoff has a decrease trend in most of the sub–basins, but two sub–basins have scattered results.

In summer time there is a decrease trend in most of the sub–basins, but many sub–basins have scattered results (see Figure 19). In autumn there is a decrease trend in the left side of the Paraná River, while there is an increase trend in the south of the right side (influenced by grid point 'PY'). In winter there is a decrease trend in most of the sub–basins. In spring, there is a decrease trend in most of the sub–basins; in the left side this trend is very low. However, in all seasons many sub–basins have scattered results.

6.4.2 Extreme events change

Figure 20 shows that monthly maximum runoff has a decrease trend in the left side of the Paraná River, while it presents an increase trend in the right side, but many sub–basins have scattered results. In the autumn season there is not any clear trend.

In the same way, Figure 21 shows that monthly minimum runoff has a decrease trend in most of the sub–basins. In winter the same trend is seen. However many sub–basins have dispersed results.

The scattered results could probably be due to the fact that the stochastic precipitation series were created through a random process; therefore these series are spatially independent.

6.4.3 Monthly frequency

With regard to the monthly frequency of the Itaipu incremental basin total runoff (for all scenarios) (see Figure 22) a runoff decrease trend occurs.

Figure 18. Changes in mean annual runoff in scenario CGCM2-A2 2070/2100 by sub-basin
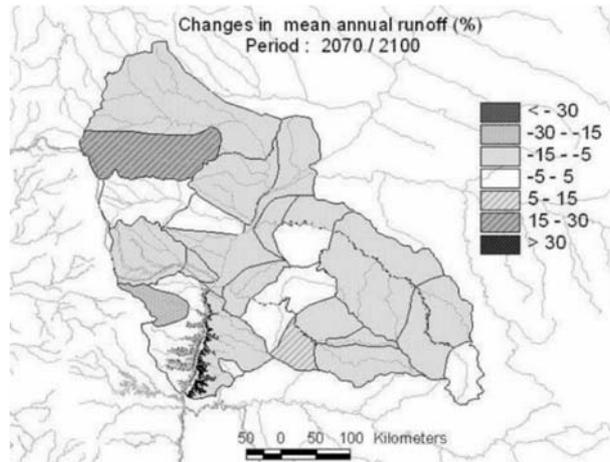
Figure 19. Changes in mean annual runoff in scenario CGCM2-A2 2070/2100 by season
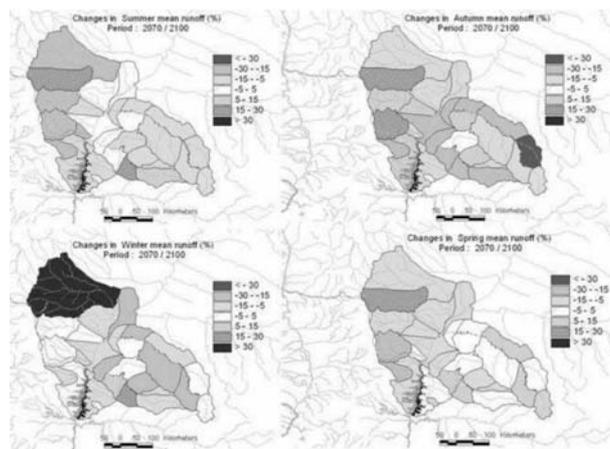
In Figure 22 the runoff variability is more clearly shown. The mean and mode values have both a decrease trend.

Monthly maximum runoffs have a decrease trend in terms of value and frequency and also the monthly minimum one shows then same decrease trend.

7. Summary and conclusions

Many of the found results were scattered. Hence, a good non–stationary analysis of the data sets is recommended, especially when the statistical downscaling method is used. It may also be interesting to verify if there is a random variance within observed data (Semenov *et al.* 2002).

The Sacramento hydrologic model shows a good performance in the left side of the Paraná River, but its performance is very low in the right side probably because the station network is not significant.

The development a performance analysis of several GCMs models which regard to both spatial and temporal performance and, principally, the qualitative performance since these models are only used to obtain climate change parameters.

Figure 20. Changes in monthly maximum runoff in scenario CGCM2-A2 2070/2100 by sub-basin
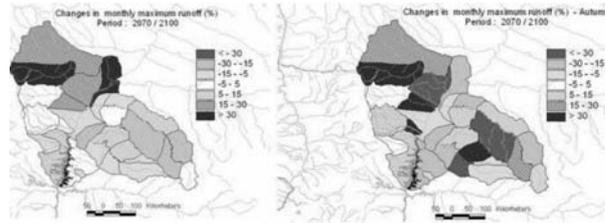
Figure 21. Changes in monthly minimum runoff in scenario CGCM2-A2 2070/2100 by sub-basin
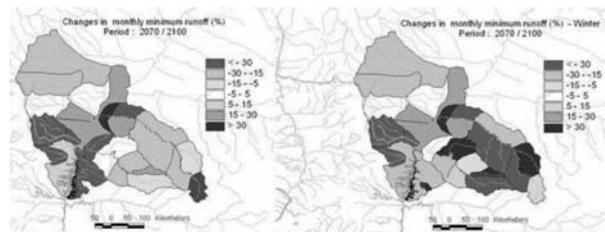
Figure 22. Frequency of monthly total runoff of Itaipu incremental basin by scenario
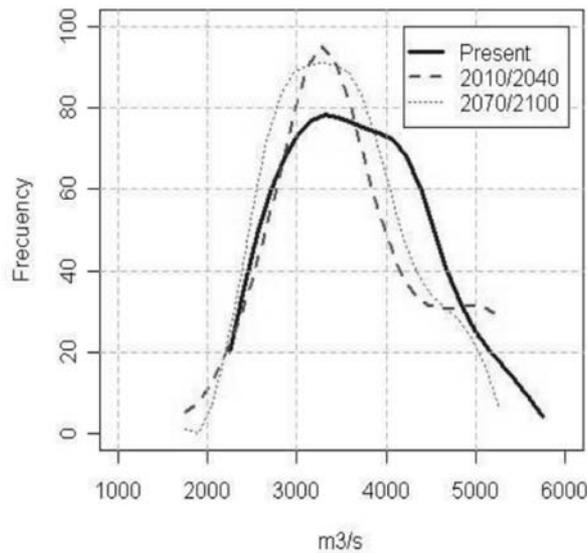
The stochastic generation, independently for which sub-basin, produces time series data without a spatial correlation. This is outlined by Wendy Merritt: «Clearly, an opportunity exists for the development or enhancement of stochastic models capable of performing the spatial interpolation of generated climate series and spatial correlation of synthetic time series» (Merritt *et al.* 2001).

With the methodology and the climate change scenarios that were used (CGCM2-A2), some trends of possible impact of climate change on the runoff in the Itaipu incremental basin were found:

• The mean precipitation decrease trend is very low
• In summer and spring there is a precipitation increase trend

- In autumn there is a precipitation decrease trend
- Mean runoff has a decrease trend, especially in autumn.
- Runoff maximum events decrease, especially in the left side of the Paraná River.
- In autumn, when runoff maximum events usually occur, a runoff decrease trend is observed, but this trend disappears in the scenario 2070–2100.
- Runoff minimum events decrease.

This study was only developed with climate change scenarios using one CGCM model in a learning process. However, it is recommended to use many "contrasting Scenarios", in order to explore the uncertainty of the future consequences.

References

Burnash, R.J.E., Ferral, R.L. and McGuire R.A. (1973). *A Generalized Streamflow Simulation System.* Joint Federal–State River Forecast Center, Sacramento, CA.

Carlsson B., Graham L.P., Andréasson J., Rosberg J., 2005. Exploring the range of uncertainty in climate change impacts on runoff and hydropower for the Luleälven River. In: *Proceedings of the 15th International Northern Research Basins Symposium and Workshop, Luleå to Kvikkjokk, Sweden, 29 August − 2 Sept. 2005*: 9-19.

Gan, T.Y. and Burges, S.J. (1990). An assessment of a conceptual rainfall–runoff model's ability to represent the dynamics of small hypothetical catchments, 1, Models, model properties, and experimental design. *Water Resour. Res.*, 26(7): 1595-1604.

Georgakakos K.P. and Bras R.L. (1984). A hydrologically useful station precipitation model. 1. Formulation. *Water Resour. Res.*, 20(11): 1585–1596.

Lofgren, B.M., Quinn F.H., Clites A.H., Assel R.A., Eberhardt A.J. and Luukkonen C.L. (2002). Evaluation of potential impacts on Great Lakes water resources based on two GCM climate scenarios. *J. Great Lakes Res.*, 28: 537-554.

Merritt W.S., Alila Y., Barton, M. Taylor, B, Cohen S. (2001). *Exploring impacts of climate change on the hydrology of the Okanagan Basin.* Department of Forest Resources management. University of British Columbia and others Institute, Canada.

Miller N.L., Bashford K. and Strem E. (2003). Potential Impacts of Climate Change on California Hydrology. *Journal of American Water Resources Association (JAWRA),* 39(4):771-784.

Nguyen V.T.V. (2005). *Downscaling methods for evaluating the impacts of climate change and variability on hydrological regime at basin scale.* McGill University,Department of Civil Engineering and Applied mechanics, Montreal. Canada.

Peck E.L. (1976). *Catchment Modeling and Initial Parameter Estimation for the National Weather Service River orecast System. NWS HYDRO-31.* NOAA, NWS, Office of Hydrology, Silver Spring, MD.

Racsko, P., Szeidl, L. and Semenov M. (1991). A Serial Approach to Local Stochastic Weather Models. *Ecological Modelling*, 57: 27-41.

Richardson C.W. and Wright D.A. (1981). *Wgen: A model for generating daily weather variables.* Department of Agriculture Research Service, Washington USA.

Semenov M.A. and Barrow E.M. (2002). *LARS-WG. A Stochastic Weather Generator for Use in Climate Impact Studies. Version 3.0. User manual.* Rothamsted Research, Harpenden, UK.

Semenov M.A., Brooks R.J., Barrow E.M. and Richardson C.W. (1998). Comparison of the WGEN and LARS–WG stochastic weather generators in diverse climates. *Climate Research*, 10.

Tebaldi C., Mearns L.O., Nychka D. and Smith R.L. (2005). Hydrologic impact of climate change in the Saguenay watershed: comparison of downscaling methods and hydrologic models. *Geophysical Research letters*, 31.

Van Rheenen N.T., Wood A.W., Palmer R.N., Lettenmaier D.P. (2004). Potential implications of PCM climate change scenarios for Sacramento–San Joaquin River basin hydrology and water resources. *Climate Change*, 62: 257-281.

Wilby R.L., Conway D. and Jones P.D. (2002b). Prospect for downscaling seasonal precipitation variability using conditioned weather generator parameters. *Hydrological Processes*, 16.

Wilby R.L., Dawson C.W. and Barrow E.M. (2002a). SDSM – a decision support tool the assessment of regional climate change impacts. *Environmental Modelling & Software*, 17.

Yonas B. D. and Coulibaly P. (2005). Hydrologic impact of climate change in the Saguenay watershed: comparison of downscaling methods and hydrologic models. *Journal of Hydrology*, 307:145–163.

Internet references

<http://en.wikipedia.org/wiki/Special_Report_on_Emissions_Scenarios/>.
<http://www.cccma.bc.ec.gc.ca/eng_index.shtml>.
<http://www.itaipu.gov.py/>.
<http://hidroweb.ana.gov.br/>.

PRECIPITATION AND TEMPERATURE TREND EVALUATION IN PARAGUAY USING BRAMS MODEL

Alejandro Max Pastén
Facultad de Ciencias y Tecnología
Universidad Católica Nuestra Señora de la Asunción
Paraguay

Tutors: Prof. J. Baez, Prof. L. Lugo, Prof. H. Ribeiro da Rocha
Department of Atmospheric Sciences
Universidade de São Paulo
Brasil

1. Introduction

Undoubtedly one of the major problems which the humanity faces is the global heating especially in the last 150 years, as consequence of the emissions of greenhouse gases.

Measurements made of weather and climate trends during the last decades of the twentieth century increase concern that global temperatures are rising not in response to natural cyclic fluctuations (see Figure 1), but rather in response to increasing concentrations of atmospheric gases that are critical to the natural and life-enabling greenhouse effect (infrared re-radiation, mostly from water vapor and clouds, that warms the earth's surface).

According to the Intergovernmental Panel on Climate Change (IPCC) «Global atmospheric concentrations of carbon dioxide, methane and nitrous oxide have increased markedly as a result of human activities since 1750 and now far exceed pre-industrial values determined from ice cores spanning many thousands of years. The global increases in carbon dioxide concentration are due primarily to fossil fuel use and land use change, while those of methane and nitrous oxide are primarily due to agriculture».

IPCC shows how the observed increasing in temperatures in the last century can only be reproduced much better the observation, when included the anthropogenic forcing.

The observed increasing in temperatures since 1900 in South America, for example, reveals that this temperature trend associated with other factors such as changes in land use and coverage, will have a significant impact on the agricultural sector and production energy in Latin America.

Global Climate Models (GCM) are a very used tool, specially for the generation of climatic scenes. Assessing the ability of these models to reproduce observed atmospheric circulation given the lower boundary conditions, and thus its ability to predict climate, has been a recurrent concern.

In general, the outputs provided by GCMS do not have a good spatial resolution to be applied in regional assessment of climate change impacts; several methods have been then developed to generate regional scenarios based on GCMs with an improved resolution. These procedures are known as downscaling and these techniques have been designed to bridge the gap between the information that the GCM can currently provide and that required by the impacts research community (Wilby and Wigley 1997). Downscaling techniques are generally divided into spatial and temporal classes. Spatial downscaling techniques can be divided into empirical/statistical methods, statistical/dynamical methods generally incorporating weather typing techniques, and higher resolution modeling.

1.1   Paraguay Present Climate

Paraguay is located in the central region of South American region, between Andes Moun-
tain on the west and south Brazilians hills on the east. The country has little elevation, rang-
ing from 50 m on the wetland in south region to 300 m on the west, border with Bolivia. On
the northeast, there is the Amambay hill where the elevation is not above to 500 m. Only in
the central region, Department of Guairá and Caazapa, the hills reach 850 m. The country has
two big rivers, Paraguay and Paraná, both tributaries of La Plata River and all the country is
located in the La Plata Basin. This particular physiographic configuration plus the atmospheric
circulation associated, favors the occurrence of great rainfalls and thunderstone in all country.

Thus, the annual cycle of rainfall in the Eastern region has two maximum, one in April–
May and the other one in October-November (Figure 1), reaching values of 180 mm in some
places. In the Western region (Chaco) the precipitation annual cycle has a different behavior,
having only one maximum during summer season, December to March. The minimum precip-
itation occurs during winter season, particularly in July, when in some locations of the western
part of Chaco, the precipitation during this month is null. The maximum annual mean rain-
fall in the country in the east, at departments of Alto Paraná and Itapua, with values of 1800
mm and the minimum on the west, as low as 400 mm (Figure 2a). During El Niño events,
these values can raise two or three times, producing floods in low lands (Grimm *et al.* 2000).

The average temperature has only 10 °C between summer and winter, almost in all loca-
tions. The annual mean temperature ranges between 21°C in the south-east region to 25°C in
the center and north of the Chaco, Figure 2b. The mean annual maximum temperature in the
Chaco region is 32 °C, while the mean minimum is of 15°C. In the Eastern region the mean
maximum temperature varies from 26 °C to 30 °C.

Paraguay is under the influence of the subtropical anticyclone of the Atlantic Ocean. This
system, which center ranges seasonally between 20 ° S and 30 ° S, is responsible for transport-
ing mass of warm and moist air from lower latitudes on this country as a result of the move-
ment of prevailing winds from North and Northeast, composing part of the South American
monsoon. This is disturbed in winter months by the entry of cold fronts that transport mass
of cold and dry air deriving from the winds of the south, being the winds of the south–east.

Figure 1. Annual cycle of rainfall over Paraguay (source: Direction of Meteorology and Hydrology)
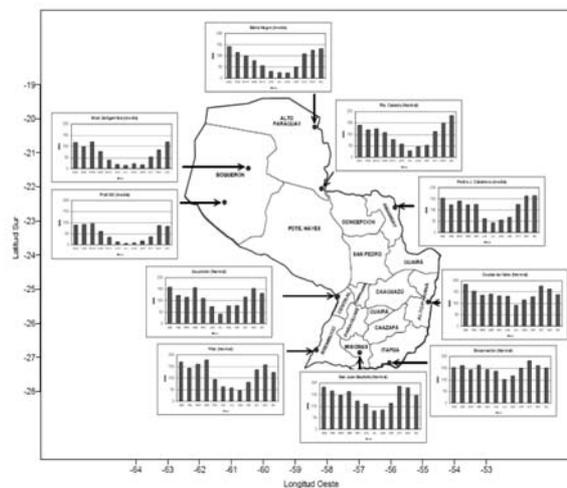
Figure 2a. The rainfall change from a minimum of 400 mm in the northwest of the Chaco to more than 1800 mm in the east of the Oriental region. (Source: Analysis of the trend of the Rainfall in the Paraguay)

Figure 2b. The annual mean temperature ranges between 21°C in the south-east of the Oriental region to more of 25°C in the center and north of the Chaco. (Source: Analysis of the trend of the temperature in the Paraguay)
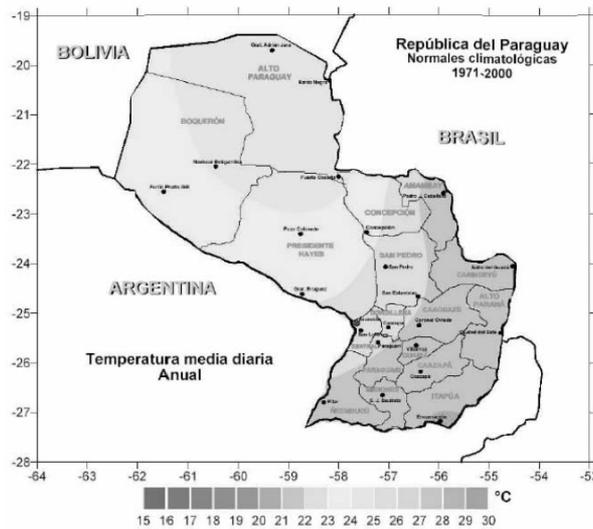
Other important systems are of meso-scale as the lines of turbon and isolated storms that pro-duce variable winds and high intensity.

2. Methodology

To reproduce the climate in Paraguay it was used the Brazilian Regional Atmospheric Modeling System (BRAMS 4.0 – http://www.cptec.inpe.br/brams/). BRAMS was originally developed to facilitate research into predominately mesoscale and cloud-scale atmospheric phe-nomena, but has been extended to larger scales over the last decade (Cotton *et al.* 2002). This

model is fully three–dimensional, non hydrostatic, include telescoping, interactive nested grid capabilities, supports various turbulence closure, short and long wave radiation, initialization, and boundary conditions schemes (Pielke *et al.* 1992).

The model was running in the cluster of the Laboratory of Meteorology Applied to Systems of Regional Weather (MASTER – Meteorologia Aplicada a Sistemas de Tempo Regionais) of the San Pablo University, but previously several procedures were perfomed.

It was used the data set generated from Eder Vendrasco, during his stage at Catholic University. This data were acquired from the Global Hadley Centre from the Brazilian Center for Weather Forecasting and Climatic Studies (CPTEC). The data were used as initial and boundary conditions in the BRAMS model.

It was used some software in Fortran, Shell Script, and Grads Script for reading the global data and writing files with the BRAMS input data format. These were created and collected for Eder Vendrasco.

Some simulations were realized to check the applied procedures. The aim of this step was to find some probably spurious errors and fix them.

Table 1. Data available for this project obtained from Hadley Centre global model (HadCM3)

Type	Members	Availabel Period
Present time	Member 1	1980–1984

After completing all the previous requirements, the BRAMS model was run. This step consists in running the model for the present time (1980-1984 period, member 1).

2.1　Region for downscaling

The region selected for the downscaling is shown in the Figure 3 and Table 2.

The principal reason for choosing this area is because is centered over Paraguay, focus of study and including the principal river Paraná where is located the biggest hydroelectric power plant in the world. This area is inside of the area used by Eder Vendrasco in his work to be able to compare the obtained results.

For the first one, the model was run with 80 km to realize the first tests, after that it was used a grid with 40 km resolution. The vertical resolution for both was the same (Table 3).

3. Results

Figure 3 shows the selected area for the study as well as 7 locations (see Table 2) that serve as checkpoints for the release of this model.

It was obtained the average of temperature and accumulated precipitation for the period 1980-1984, for every month (see Figures 4 and 5). It is also shown, the averages of observed data from (DMH) in order to obtain adjustment of the model. Besides, it was calculated the time correlation between them.

The figures 8 to 15 show fields of seasonal average temperature and monthly rainfall accumulated (model output and NCEP/NCAR reanalysis). It is shown that the temperature distribution of the model output shows slightly higher than those of the reanalysis, although it may be noted that this difference becomes smaller in autumn and winter. The field of precipitation

Figure 3. Region where the downscaling was performed and some key locations
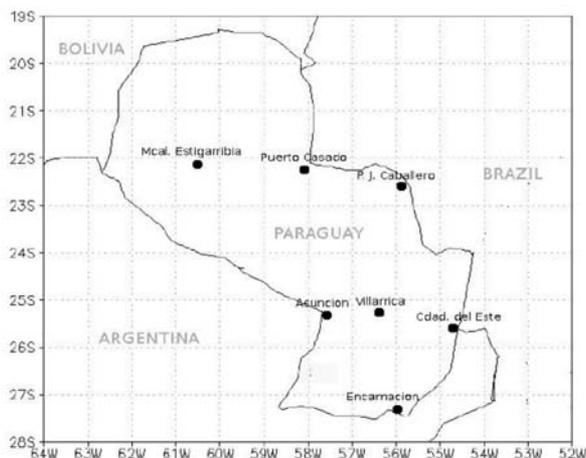
Table 2. List of 7 locations that serve as checkpoints for the release of the model output

Ref.	Longitude	Latitude	Locations
MES	–60,61	–22,03	Mcal. Estigarribia
PCA	–58,09	–22,21	Puerto Casado
PJC	–55,90	–22,58	Pedro Juan Caballero
ASU	–57,66	–25,18	Asunción
VIL	–56,40	–25,25	Villarrica
CDE	–54,82	–25,40	Ciudad del Este
ENC	–56,00	–27,20	Encarnación

Table 3. BRAMS setup

Simulation	Present time
Simulation time (years)	5
Number of grids	1
Spatial resolution (horizontal)	40 Km
Spatial resolution (vertical)	100 m
Δz	1,2 until 1000m and constant above
Number of points (x,y,z)	(34, 20,34)
Number of points for lateral boundary nudging	5
Nudgin time for lateral boundary	1800
Nudgrid time for top domain	10800
Lateral boundary scheme	Klemp e Wilhelmson (1978)
SW and LW radiation	Chen e Cotton (1983)
Cumulus parametrization	Grell (1993)
Turbulence parametrization	Anisotropic deformation (Smagorinsky 1963) based on modifications of Hill (1974) and Lilly (1962)

does not show a very good fit in that part of Chaco, however, in the Eastern region values are more consistent and are closer to the values of the reanalysis.

Figure 4. Monthly mean temperature [°C] for all locations (see map in fig. 3). The mean was retrieved of daily mean temperature (daily mean has been calculated using tmed=(tmax+tmin)/2, where tmin is the minimal temperature of the day and tmax is the maximum). The straight line is the average over all months. The red line represents the observation and the black one is the model. It is also show the correlation between them. Observations from DMH (Direccion de Meteorologia e Hidrologia de Paraguay)
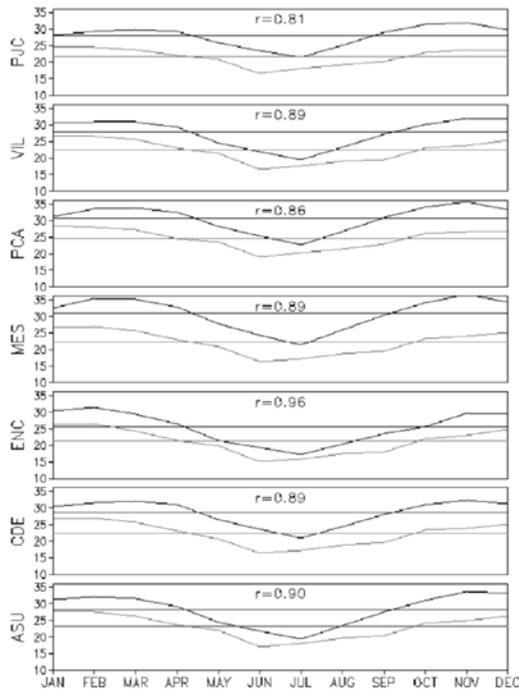
Figure 5. Monthly accumulated precipitation [mm/month] for all locations (see map in Fig. 3). The red line represents the observations and the black bar is the model. It is also shown the correlation between them. Observations from DMH (Direccion de Meteorologia e Hidrologia de Paraguay)
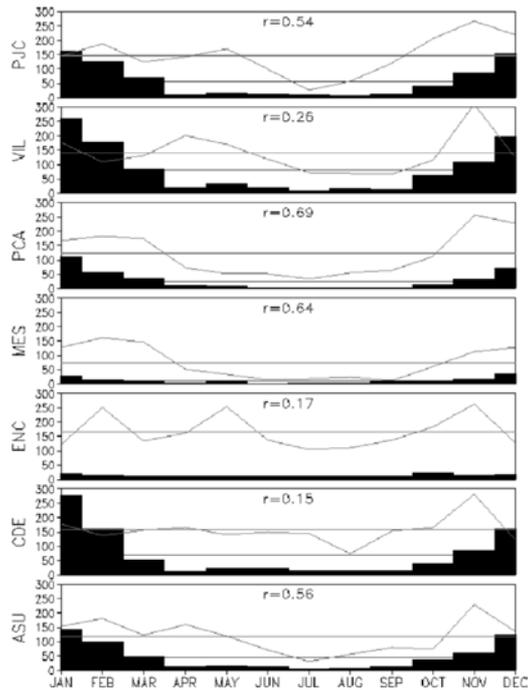
Figure 6. Seasonal mean of temperature for summer in Southern Hemisphere, (a) model and (b) NCEP/NCAR reanalysis – [°C]

(a)   (b)
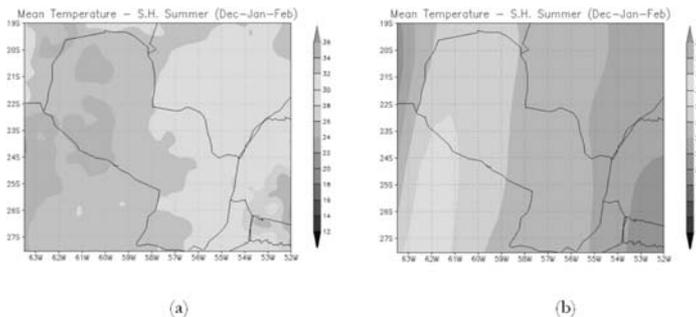
It can be noted that the temperature obtained from the model is hotter than the observed data in all localities analyzed. In the locations of Asuncion (ASU), Villarrica (VIL), Encarnacion (ENC) and Ciudad del Este (CDE) the results were better where temporary correlations were between 0.89 and 0.96. In all cases the time correlation was higher than 0.80. With regard to the cumulative monthly rainfall, was observed that in most locations the

Figure 7. Seasonal mean of temperature for Autumn in Southern Hemisphere, (a) model and (b) NCEP/NCAR reanalysis – [°C].
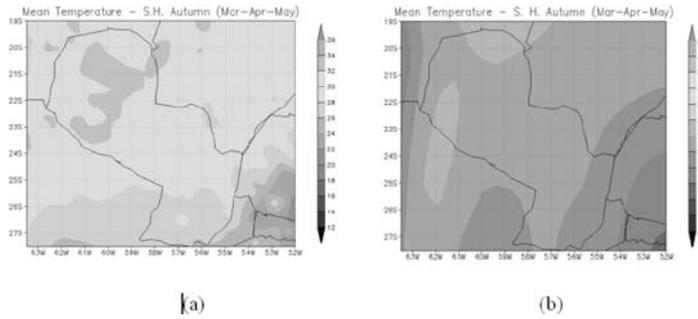
Figure 8. Seasonal mean of temperature for Winter in Southern Hemisphere, (a) model and (b) NCEP/NCAR reanalysis – [°C].
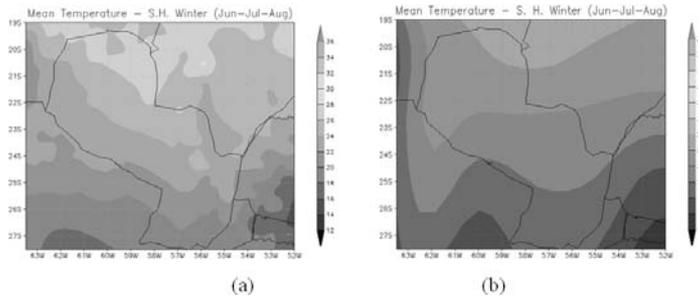
Figure 9. Seasonal mean of temperature for Spring in Southern Hemisphere, (a) model and (b) NCEP/NCAR reanalysis – [°C].
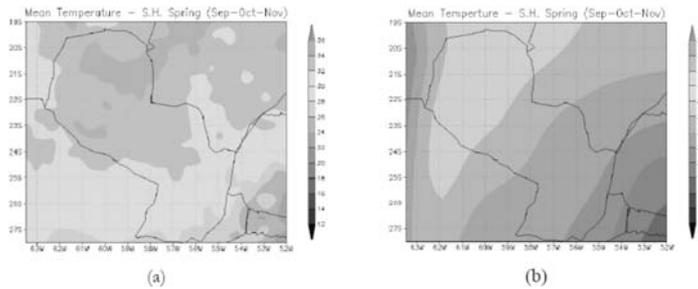
Figure 10. Seasonal mean of month accumulated precipitation for Summer in Southern Hemisphere, (a) model and (b) NCEP/NCAR reanalysis – [mm/month].
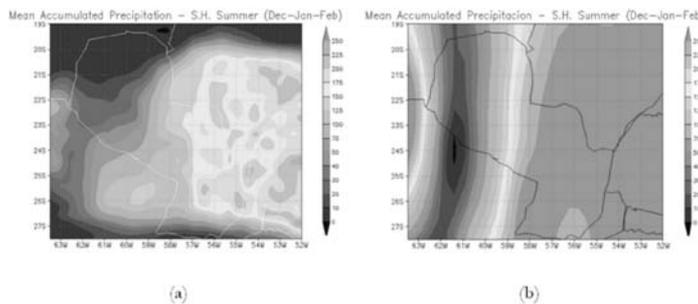
Figure 11. For Autumm in Southern Hemisphere, (a) model and (b) NCEP/NCAR reanalysis − [mm/month].

Figure 12. Seasonal mean of month accumulated precipitation for Winter in Southern Hemisphere, (a) model and (b) NCEP/NCAR reanalysis − [mm/month].
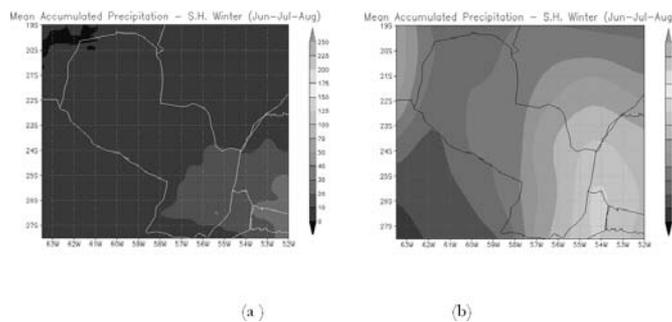
Figure 13. Seasonal mean of month accumulated precipitation for Spring in Southern Hemisphere, (a) model and (b) NCEP/NCAR reanalysis − [mm/month].
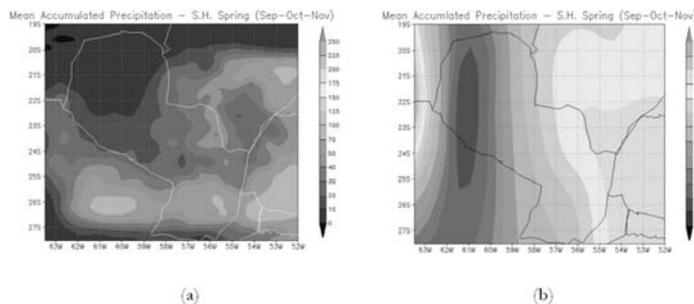
model gave higher values than those observed except in VIL and CDE, the time correlation reaching 0.69 in PCA.

The Figures 6 to 13 show the fields of seasonal averages of temperature and monthly accumulated precipitation (model output and reanalysis). It shows that the distribution of temperature and Precipitation model is similar to reanalysis, however, the absolute values are not so close to the reanalysis, especially in precipitation.

References

Chen C. and Cotton W.R. (1983). A one-dimensional simulation of the stratocumulus-capped mixed layer. *Boundary-Layer Meteorol*, 25: 289–321.

Cotton W.R., Pielke R.A., Walko R.L., Liston G.E., Tremback C.J., Jiang H., Mcanelly R.L., Harrington J.Y., Nicholls M.E., Carrio G.G., Mcfadden J.P. (2002). RAMS 2001: Current status and future directions. *Meteorol. Atmos. Phys.*, 82, 5–29.

Grell G.A. (1993). Prognostic evaluation of assumptions used by cumulus parametrization. *Mon. Wea. Rev.*, 121: 764-787.

Grimm A.M., Barros V.R. and Doyle M.E. (2000). Climate Variability in Southern South America Associated with El Niño and La Niña Events. *J. Climate*, 13, 35–58.

Hill G.E. (1974). Factor controlling the size and spacing of cumulus clouds as revealed by numerical experiments. *J. Atmos. Sci.*, 31: 646-673.

Intergovernmental Panel on Climate Change (2008). Climate Change 2007: The Phisycal Science Basis. Working Group I, <http://www.ipcc.ch/>.

Klemp J.B. and Wilhelmson R.B. (1978). The simulation of three-dimensional convective storm dynamics. *J. Atmos. Sci.*, 3: 1070-1096

Lilly D.K. (1962). On the numerical simulation of buoyant convection. *Tellus*, 2: 148-172.

Pielke R.A., Cotton R.L., Walko W.R., Tremback C.J., Lyons W.A., Grasso L.D., Nichols M.E., Moran M.D., Wesley D.A., Lee T.J., Copeland E.J.H. (1992). A comprehensive meteorological modelling system – RAMS. *Meteorol. Atmos. Phys.*, 49: 69-91.

Smagorinsky J. (1963). General circulation experiments with the primitive equations: 1. The basic experiment. *Mon. Wea. Rev.*, 91: 99–164.

Wilby R.L. and T.M.L. Wigley (1997). Downscaling General Circulation Model Output: A review of methods and limitations. *Progress in physical geography*, 1997; 21: 530-548.

EXPLORING LAND USE IN THE *LITORAL ARGENTINO*, BY REMOTE SENSING TECHNIQUES APPLIED TO THE CLASSIFICATION OF SAC C SATELITE IMAGERY

Marta L. Stiefel
Facultad de Ingenieria, geoecología y medio Ambiente
Universidad Católica de Santa Fé
Argentina

Tutors: Prof. M.A. Gilabert Navarro Dr. Joaquín Meliá Miralles
Departament de Física de la Terra i Termodinàmica
Universidad de València
Dr. Moliner, 50. 46100–Burjassot (Spain)

1. Introduction

1.1 Justification

Historical records of the Argentinean land use show an increase of 5,5 millions ha in the surface dedicated to annual crops, across the period 1988–2002 (Figure 1). This increase is located both in existing cultivated areas by means of more intensive exploitation, and expanding agriculture over naturally vegetated soils. Soy cultivation is the major responsible of agricultural land expansion.

The World Bank report No. 32763–AR (June 06) «Argentina – Agriculture and Rural development: selected Issues» highlights some processes, such as the expansion of cultivated land, the increasing farm size, and states that such trends are very likely to continue in the future.

The environmental impact of agriculture increases when also natural vegetation lands are cultivated (National Secretariat for Environment and Sustainable Development).

For instance, the 86% of the agricultural land increases in the period 1988–2002 in the provinces of Chaco and Santiago del Estero, due to the occupation of naturally vegetated areas.

According to the data showed in Figure 2, while in the 50 years in the period 1937-1987 the total loss of native forests reached 2.355.308 Ha, during the last 17 years it reached 5.321.001 Ha. This confirms that Argentina is currently experiencing the fastest deforestation in the Country history, basically due to the expansion of agricultural land over native forest lands (National Secretariat for Env. and Sust. Dev. 2006).

The expansion of the agricultural land across the western and northern borders of the traditional agricultural land is manly due to market and technology factors, but also the climate changes occurred in the Region, such as rainfall increasing, have also their influence. This spontaneous adaptation needs to be timely addressed, in order to face the problems and reduce their negative impacts (National Secretariat for Env. and Sust. Dev. 2006).

The present study has been led in the administrative provinces of Santa Fe, Entre Ríos and Corrientes. In these areas since many years, and especially since the '90s, agricultural land has increasingly being expanding over lands that historically were left to the natural vegetation, as well as to other uses, such as extensive livestock keeping, especially in ecologic transition areas (ecotones).

Reports issued by the Ministry for Production of Santa Fe (2004) underline that intensive agriculture of the Province is expanding, at the same time of a reduction in the crops variety, that are basically turning into one-crop (i.e. soybean).

Nowadays, many environmental and social indicators point out un-sustainability of this expansion.

Figure 1. Land use change graph in Argentina: 1988 – 2002 (source: Censo Nacional Agropecuario. Instituto Nacional de Estadisticay. Ministero de Economia y Produccion)
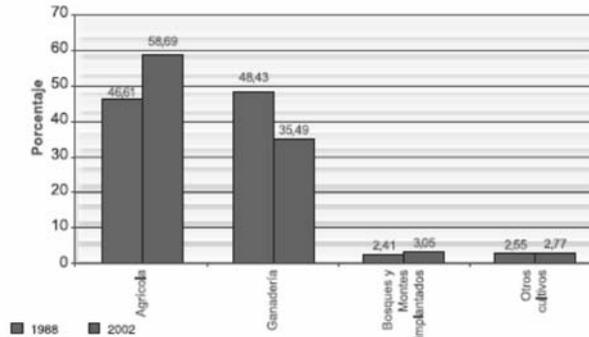
Figure 2. Native forest surface, 2004. Argentina. (Source: year 1937, Censo Nacional Agropecuario; year 1987, Estimaciones del Instituto Forestal Nacional – IFNOA; year 1998–2004 Unidad de Manej del Sistema de Evaluacion Forestal – UMSEF. Direccion des Bosques. Sedretaria de Ambiente y Desarollo Sustentable. Jefatura del Gabinete de Ministros)
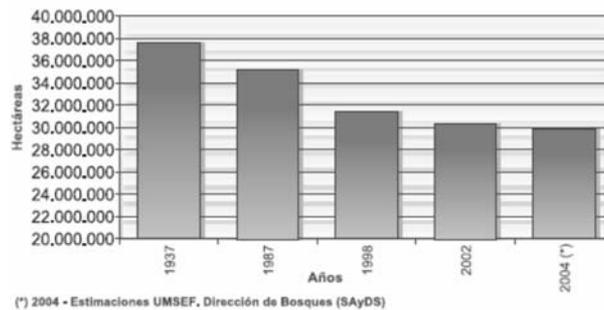
1.2   Background

The expansion of agriculture, and its environmental impact, is one of the core issues of climatic change debate, and many recent researches have been carried out on this subject.

Remote sensing is an undoubtedly a useful tool to be used for land surface and dynamics studies. Nowadays several ate the advanced sensors that can be used, as well as processing technique to be applied.

In Argentina, the National Commission for Aerospace Activities (CONAE) is in charge of the operatively of the SAC C satellite, working since late 2000, whose products were used for this study, considering that both spatial and spectral resolution meet the needs of the research (García and Chuvieco 2002; Carñel 2004).

1.3   Objectives

Within the frame of a broader project, whose goal is to analyse the changes in soil use in the last years in Argentina, this research aims at identifying the different types of soil use characterizing the study area

The main objectives are:

• to examine the soil cover over the last 10 years, by means of radiometric characterization.

- to use remote sensing techniques as a research tool, and particularly MMRS (Multispectral Medium Resolution Scanner) imagery from SAC C satellite, as main source of data.

1.4   Study area

The region examined is located between 58° – 62° W (long) and 27° – 34° S (lat), for an approximated surface of 161.200 sqkm, enclosing lands from the administrative boundaries of Santa Fe, Entre Ríos and Corrientes provinces (Figure 3). It is fully covered by orbit path 226 of SAC C.

Characterization

The study area includes parts of the geographic regions called *llanura chaqueña*, *llanura pampeana* and *llanura mesopotámica*. This flatland region is originated by crystalline rocks from the Brasilia Horst, overlapped by a thick sedimentary layer, including *loess pampeano* and marine sediments (variable in different areas), finally covered by a humus layer of extraordinary fertility.

The flatlands called *llanura chaqueña* and *llanura pampeana* form a single geological unit, so called *llanura chacopampeana*. *Chaco* and *Pampa* are distinguished for climatic and ecological characters. While the *Pampa* region is characterized by 4 well-separated seasons, and mean annual temperatures from the temperate range, the *Chaco* region has only 2 seasons, a dry one (with precipitation minimum values around July) and a humid one (highest precipitation values around January) with high temperatures.

Two different biomes can be identified:

- In the Chaco region, vegetation is dominated by forest trees (wood, forest and natural areas) at side of grasslands and wetland landscapes, called *cañadas* and *esteros*;
- The Pampa region is dominated by grasslands and grass steppe, at side of small xerophillous shrubs landscapes, with some sparse forest spots.

The *Llanura Mesopotámica* makes part of the *Mesopotamia Argentina*, the region surrounded by the rivers Paraná and Uruguay; within this area, the study reaches the *esteros correntinos*, the *lomadas entrerrianas* and the *planicie deltaica*. The climate is temperate (hotter in the North) and precipitation values are high.

Figure 3. Study area
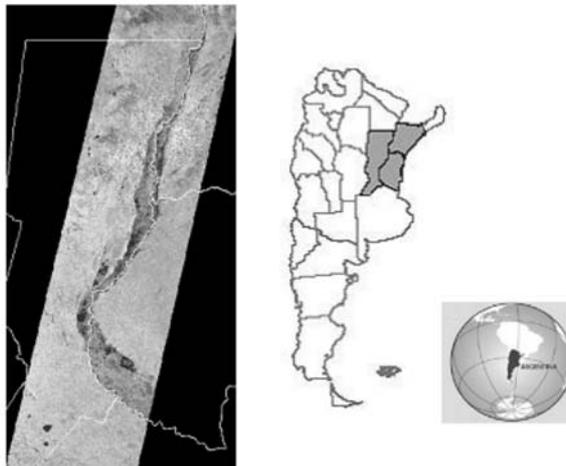
The *esteros correntinos* are represented by a depressed region, originated over sedimentary deposits, whose aspect is a typical marshland landscape.

In the Entre Ríos area, the ground is gently undulating, and it is ploughed by many rivers and streams; soil texture is dominated by clay. The limits of the *delta* flatland are marked by two faults, bordering a subsided block where the delta of Paraná river flows. The constant deposition of sediments by this river causes the origin of many islands, whose edges (*albardones*), slightly elevated, protect the surface from normal high tides. The dynamics of the delta formation slow but permanent, cause a constant change in shape and size of these islands.

The land of Entre Ríos province is covered by a relevant rate of naturally vegetated areas.

The study area is also characterized by large areas used for extensive agriculture, dominated by non-irrigated cultures of temperate and semi-tropical climate; furthermore it is also one of the most important Argentinean regions for milk production, and livestock breeding for meat production (Figure 4).

In Table 1 data referred to the amount of land occupied by cultivated land at province level for year 2002 are reported (INDEC – National Institute of Statistics and Census – Instituto Nacional de Estadística y Censos).

Figure 4. Land Use. CIOMTA 2004
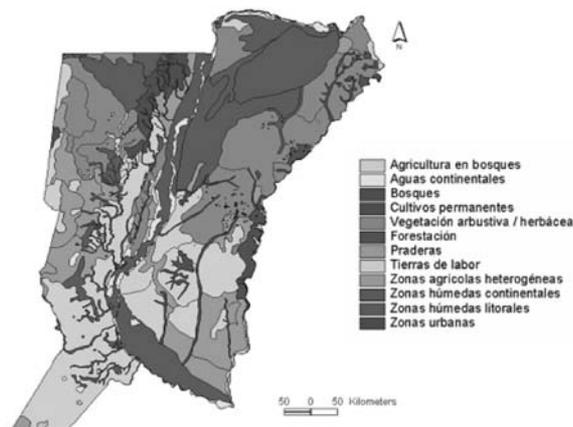
Table 1. Seeded surface (ha). National Agricultural Census 2002.

Surface (ha)	Corrientes	Entre Ríos	Santa Fe
Province	8.819.900	7.878.100	13.300.700
Implanted	126.700	1.929.948	5.343.661
% implanted	1 %	24 %	40 %
Mais	8.899	172.688	433.362
Wheat	338	372.432	967.465
Other cereal	58.267	69.216	112.855
Sunflower	–	25.698	80.172
Soya bean	5.801	870.767	2.603.147
Other oilseed crops	221	3.491	640
Fodder	53.174	415.656	1.146.020

INDEC

1.5 Methodology

This study was carried out through the following steps:

a) Preliminary analysis and collection of references
b) Data collection:
    b.1. field data
    b.2. geographic information of the study area
    b.3. satellite imagery
c) Design of the methodology and data processing
d) Discussion of the results
e) Conclusions

2. Tools

2.1 Software

Many software were used: IDRISI Andes, ENVI 4.1, IDL 6.1, ArcView GIS 3.2 and Ms Excel 2003.

IDRISI, ENVI and IDL compilator were used for satellite data processing, numeric data processing and figures were made by using Ms Excel, and for the geographic data two GIS applications were chosen: IDRISI Andes and ESRI ArcView.

2.2 Data

The geographical information to be used for georeferencing the satellite data, was extracted by both vector files and imagery. For this purpose were used the Geodesic Reference System POSGAR 94, and GCP (Gauss-Kruger Conformal Projection), obtained from CIOMTA (Centro de Investigación, Observación y Monitoreo Territorial y Ambiental, UCSF – Universidad Católica de Santa Fe), from the Province Authority of Santa Fe Province through its IDESF agency (Infrastructure for Aerospace Data of Santa Fe), and from the Military Geographic Institute of Argentina (IGM).

Field data: some areas were identified, with particular cultivations and its corresponding phase, to be used as sample in the analysis of remote sensing data, in 2 different periods. These were obtained from the Rafaela Station (Santa Fe) of INTA (National Institute for agricultural technology) and from ProArroz (Rice producers association of Entre Ríos).

Satellite images were provided by CONAE. Twelve MMRS scenes, selected from the SAC C catalogue published in the CONAE website (<http://www.conae.gov.ar>), Path 226. In order to select the images, cloud coverage was considered, as well as the crops phenological cycle: soy, maize, wheat, sorghum, rice, sunflower.

Features of the MMRS imagery:

• Spatial resolution: pixel size 175 m.
• Size of the scene: approx. 3.000 columns by 30.000 rows. Each band is stored in a file of approximately 116 Mb.
• spectral resolution: 5 bands (Table 2).
• storage format: BSQ (Band–Sequential).

In Table 3 a list is reported of the satellite images provided by CONAE to realize this study.

Table 2. Spectral bands of MMRS images

Band 1	$480 - 500$ nm – blu greenish
Band 2	$540 - 560$ nm – green
Band 3	$630 - 690$ nm – red (RED)
Band 4	$795 - 835$ nm – near IR (NIR)
Band 5	$1550 - 1700$ nm – mean short waves IR (SWIR)

Table 3. Selected scenes

Period	Scene date
2001 – 2002	24/08/2001
	28/11/2001
	16/02/2002
2005 – 2006	18/07/2005
	19/11/2005
	17/02/2006

3. Methodology and data processing

According to the research objectives, two periods were taken into account, encompassing key-dates for phenological variations of the main crops and vegetation of the region.

The main assumption of the methodology is based on the fact that different elements over the Earth surface do have different answer to the sunlight, and these answers can be recorded by remote sensors.

Based on the knowledge of the study area, some categories of land cover were selected, after their relevance (for the great extension reached, or for some specific feature), these land cover categories (classes) are characterized by the values and magnitude recorded in the satellite images.

Five spectral bands were used as radiometric range to characterize the vegetation classes, as well as the NDVI (Normalized Difference Vegetation Index).

Periods examined

The periods examined in this study are 2001–2002 and 2005–2006: winter and spring in 2001 and 2005, and summer in 2002 and 2006.

These periods were chosen following the objectives and considering the availability of re-liable data provided by SAC C, i.e., the time span from the first data collection until a trouble in sensors calibration (<http://www.conae.gov.ar/>).

3.1   Origin of the data used in this study

One of the objectives is to apply remote sensing techniques for land use studies, so that the very raw data used are satellite images.

Following the plan of the research, the available images were examined, and 3 scenes for each period have been chosen. Each scene corresponds to winter and springtime 2001, and to summer 2002 and 2006. By this selection, it is expected to detect different phenological states of the main vegetation classes.

3.2 Data processing

The images to process were taken by the MMRS sensor of SAC C satellite. Since the original files had already been very slightly corrected (<http://www.conae.gov.ar/>) it was firstly necessary to adapt them. Some processing and adaptation is always necessary, when the same land is examined using remote sensing data taken in different moments (Chuvieco E. 2002).

Geometric correction

Geometric corrections (geo-reference) are made in order to re-orient the position of the pixels based on a given reference system.

In this case, the geo-reference was necessary to overlay different images of the same region and to locate field data in the corresponding pixel of the satellite images.

It is known that geometric correction imply the introduction of some errors in the radiometric values. Nevertheless, it was decided to make this correction as a first processing operation, considering the importance of a correct location of the field data, required to identify land cover classes.

First of all, a single scene was georeferenced and then used as a reference for all the other images.

The correction procedure was applied by the RESAMPLE module included in IDRISI Andes, after having digitized the requested control points. The parameters that were set were *polynomial 2°* for Geometric Transformation, and nearest neighbourhood for *resampling*, in order to keep the radiometric value as close as possible to the original data (Eastman R. 2006).

Each image was cut, following the borders of the study area that was generated and defined with polygon features, since a perfect matching in geographic location, resolution, number of rows and columns is absolutely necessary to be able to operate with raster data.

Each image/band of the area is composed by 2.186 columns and 4.486 rows, whose pixel size is 175m for approximately 9,5 Mb (Figure 5).

Radiometric corrections

This generic definition stands for all the techniques that are used to modify the original DN (digital number) of a pixel, in order to bring them near to the value of an ideal image, with no noise. This procedure therefore includes the correction of radiometric errors caused by sensor failures, obtaining physical magnitudes, and atmospheric correction of the data (Chuvieco 2002).

It is very useful to convert the DN into standard values of a physical variable, this facilitates the comparison of time series of images taken by the same sensor or different sensors, and to integrate remote sensing with data from other sources.

The formulas and the values for this research were taken from the references given by CONAE (www.conae.gov.ar).

The radiometric calibration of the image MMRS consists in converting DN into radiance values Lk, applying to each band the following equation:

Figure 5. Soybean, February 2006. Radiance (left) and reflectance (right) values of the 5 spectral bands

$L^K[mW/sr.cm^2] = [(L^K_{max} - L^K_{min})/(DN_{max})] \star DN^K + L^K_{min}$
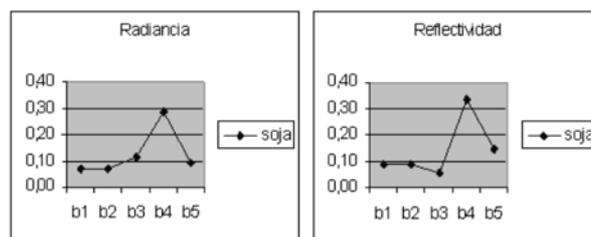
where:

k: band (k: 1, 2, 3, 4, 5)
DN_{max}: maximum DN (254)
L^k_{max}: radiance corresponding to $DN^k = DN_{max}$, for k: 1,2,3,4,5
L^k_{min}: radiance corresponding to $DN^k = 0$, for k: 1,2,3,4,5

Image calibration was performed by the *IDRISI Andes* IMAGE CALCULATOR module with the above mentioned equation proposed by CONAE, resulting into 29 images with radiance values.

Conversion into values of apparent reflectance

Reflectance is the ratio between the reflected and incident energy, whose value varies in the range 0 (totally absorbing surface) − 1 (totally reflecting surface) (Chuvieco E. 2002). It is known that the reflectance of any land cover depends from physical and chemical features, as well as from the observation conditions.

Reflectance values changes according to the considered range of spectral bands, and for this reason it is also called «spectral reflectance», referring to the measure of a given wavelength range; in fact, this variation across different wavelengths allows to identify different land covers.

The conversion of DN into reflectance takes two steps: first, the conversion of DN into radiance values, then, the estimation of apparent reflectance values, considering the solar radiance and the date of data gathered (Figure 5 and Figure 6).

The formula and the values that have been used in this process were taken from CONAE (Box 1).

Box 1. Calculation of reflectance at sensor MMRS level

The study kept on working with the specifics parameters that were chosen according to the specific metadata annexed to each scene, as shown in Table 4.

Irradiance values were corrected considering the day of the year (CONAE).

The images were processed trough IDRISI Andes, in order to obtain 29 final images showing apparent reflectance values. After each image processing, the resulting values were constantly checked out (Figure 7).

Table 4. Metadata about images, used for calculation of apparent reflectance

	Scenes					
Centre of the image (–30.8, –60)	47399	47402	47404	47405	47406	47409
Scene time series	24–08–2001	28–11–2001	16–02–2001	18–07–2005	19–11–2005	17–02–2006
Julian day	236	332	47	199	323	48
Time GTM	13:56:43	13:57:58	13:58:35	13:36:07	13:30:28	13:23:52
Time GTM (decimal)	13:93	13:95	13:96	13:60	13:50	13:38
Local time	10:56:43	10:57:58	10:58:35	10:36:07	10:30:28	10:23:52
Sun elevation angle (1)	38.5	63.4	53.6	27	57.6	46.4
Zenital Angle	51.5	26.6	36.4	63	32.4	43.6
COS Zenital angle	0.62251299	0.89415375	0.80489292	0.45398821	0.84432722	0.72417063

(1) Data obtained through a web application: http://www.jgiesen.de/azimuth/

Figure 6. Scene from 15/02/2002 (band 4), by DN, radiance and reflectance
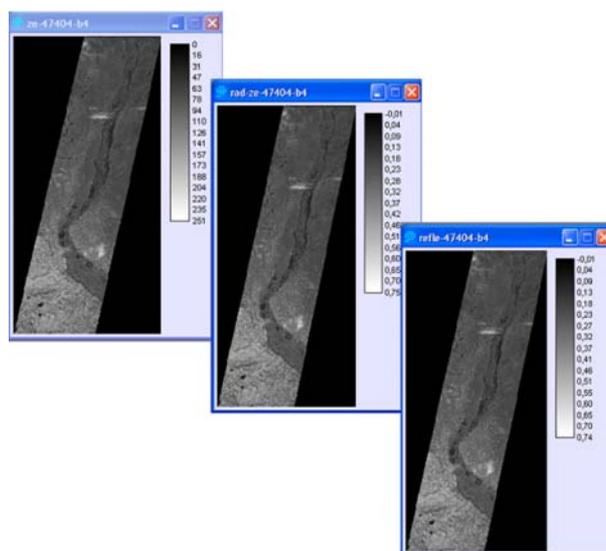

Figure 7. Spectral reflectance of a pixel corresponding to alfalfa cover.
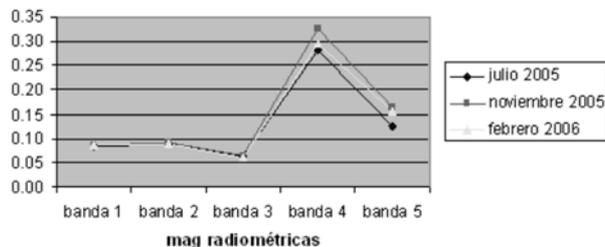
(Peyrano District, Department of Constitución, Santa Fe)

Normalized Difference of Vegetation Index: NDVI

Indexes (resulting from calculations operated on 2 or more spectral bands of the same im-age) are used to distinct the various vegetation classes having very different reflectance in the

bands considered by the index. This kind of process is based on the different radiometric behaviour of vegetation.

Among all the indexes normally used in remote sensing, NDVI is one of the simplest and about the most used (Chuvieco E. 2002).

NDVI is calculated with the following formula:

NDVI = NIR − RED / NIR + RED

where

NIR is the reflectance value of the Near Infrared Band
RED is the reflectance value of the Red Band
NDVI: the calculation was performed by using the VEGINDEX module of IDRISI Andes, entering the images corresponding to band 4 (RED) and 5 (NIR).

Results were validated by checking the output values with some training areas on the ground (Figure 8).

The same was done for 6 scenes, obtaining the corresponding NDVI values (Figure 9).

3.3   Radiometric characterization

Soil Cover CLASSES.

The soil cover classes to be identified in the images were selected on the base of previous field experience in the same area and on available field data sets.

Vegetation types showing the same structure, composition, phenological cycles and spectral behaviour were joined in the same class. In this way, after having examined all the types

Table 5. Vegetation types and classes

Class Cover	Spectral Class	
Wheat	1	Winter cereals
Green		
Soybean Stubble		
Mais stublle	2	Soil nude
Plowed field		
Alfalfa	3	Alfalfa
pastures c/alfalfa		
pastures s/alfalfa	4	Pastures
Good pastures		
Bad pastures		
Natural field		
Low	5	Natural vegetation
Natural mountain		
Sojabean	6	Sojabean
Rice	7	Rice
Mais	8	Mais
Sorghum	9	Sorghum
Urban	10	Urban
Water	11	Water

Figure 8. NDVI evolution in an alfalfa pixel. (Peyrano District, Department of Constitución, Santa Fe)
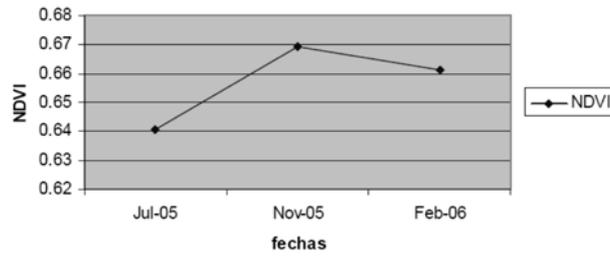
Figure 9. NDVI images from July 2005, Nov. 2005 and Feb 2006
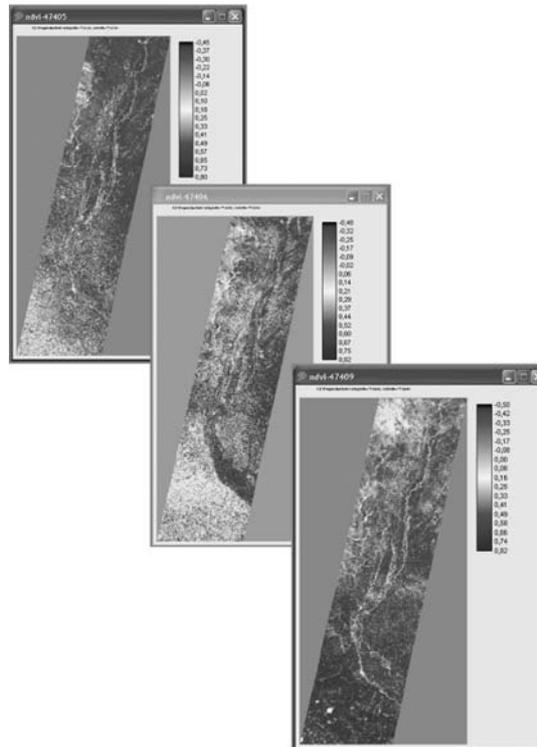
of vegetation of the study area, 11 spectral classes were defined for the classification, whose features are shown in detail in Table 5.

The following classes include several vegetation types:

- winter cereals: this class includes wheat, oats, barley, rye and so-called *verdeos* (cereal cover crops sowed shortly before wheat and used for feeding cattle);
- bare soil: class for areas with little vegetation in winter, including ploughed land and stubble
- grasslands: permanent grasslands with or without alfalfa;
- natural vegetation: naturally vegetated (non agricultural) fields, shrubs and lowlands, channels of seasonal rivers and minor pathways.

In order to define training sets for the classification, for each cover, the pixels were associated to the corresponding vegetation class (Tables 6 and 7).

For each period, the corresponding scene was classified using training sets defined with vector data maps: pixels with homogeneous values where carefully located, without considering border areas. In fact, border areas generally usually increase the real variability of a given class, due to contamination by different vegetation types.

The selection of the samples and of the training fields is performed on the basis of a visual identification of each cover class, taking into account the date of the image. Also field data availability must be considered, distant and scattered areas are privileged, in order to include the whole range of behaviour for a same crop. Different behaviours are probably due to changes in soil, climate condition, management, and the different seeding date, which is normal in such a broad area.

The information about rice was taken from Entre Ríos and Santa Fe; while all the other data came from areas in the Centre and South of Santa Fe Province.

In the study area, changes in crops, as well as crops rotation is a common agriculture practice: the cover of plots used for agriculture changes from year to year. In mixed used areas (both agriculture and animal breeding), the rotation is a common practise as well. This means that across longer periods, a change is possible from harvest crops to grassland for extensive grazing, and vice-versa. In the case of rice, rotation is not as frequent as for the other crops. In order to define the training sets for classification, it has been important to use field data in time coincidence with the satellite image scenes (Table 6).

For water and urban cover classes as well as for naturally vegetated and shrub land areas, and for lowlands, the same training pixels were used for all of the periods.

For urban areas, samples from big cities, with dense cover, were selected. The same was done for small towns, with minor density.

For the class *water*, samples from rivers were selected as well as from wetlands, in order to include different kind of areas (water motion, depth, sediment).

Table 6. Training fields, period 2001-2002

Cover	Surface (ha)	Number of training sites
Wheat	217,42	4
Green	12,25	1
Soybean Stubble	21,43	1
Mais stublle	107,18	2
Plowed field	238,87	4
Alfalfa	67,37	2
pastures c/alfalfa	33,68	2
pastures s/alfalfa	18,37	1
Bad pastures	15,31	1
Natural field	24,5	1
Low	474,68	2
Natural mountain	18,37	2
Sojabean	287,87	4
Rice	1.307,67	3
Mais	128,61	4
Sorghum	64,30	3
Urban	1.081,04	4
Water	4.890,80	4

Table 7. Training fields, period 2005–2006

Cover	Surface (ha)	Number of training sites
Wheat	36,74	3
Plowed field	15,31	2
Alfalfa	27,55	3
Good pastures	52,05	3
Bad pastures	42,87	3
Natural field	24,5	1
Low	474,68	2
Natural Mountain	18,37	2
Sojabean	168,43	4
Rice	281,73	4
Mais	174,54	4
Sorghum	39,81	4
Urban	1.081,04	4
Water	4.890,80	4

The field data, obtained as described in detail in annex II.2, represent a constraint which can alter the reliability of the results, due to the surface covered (which is not representative enough of the whole study area) the spatial distribution (covering small zones instead of the whole area) and the change in soil cover class across the 2 time periods examined (Table 7).

Radiometric Characterization Data

Each scene was separately processed. For each of them and within the 5 spectral bands, reflectance and NDVI were calculated.

The following statistic parameters were calculated: the minimum value, maximum value total, mean, range and standard deviation.

Mean values were used to characterize all the scenes.

Several maps were then produced:

Reflectance of each single spectral band and NDVI for all the training sets / classes / scene.

Reflectance of all the spectral bands for all the training sets / classes / date scene.

Changes in NDVI values across the period for each class, calculated from 3 values, one for each scene.

Distribution of NDVI values for each the cover classes of all scenes.

4. Results

With the analysis of tables and maps produced, the radiometric characteristics of each class was determined for all the scenes; for this reason both NDVI values and apparent reflectivity of each class in all bands was calculated.

Since the results of the two study periods fall within the same range of time, we can state that they are multi–temporal representative.

In the following figures, the characteristics of all the classes are reported, by showing their representative spectre for each scene (Figures .a), a comparative figure is also provided of the correspondent values found in the training sets (Figures .b).

The reference time was considered 2005–2006, because the 5 spectral bands are available for all of the scenes, while for 2001–2002 band 5 is missing in the image taken in August.

4.1   Winter cereals

The vegetative cycle of this class occurs in winter and springtime, so that the characterization was made in July and November (Seasons of the southern Hemisphere).

Winter – July

Figure 10.1.a. Winter cereals spectrum, July
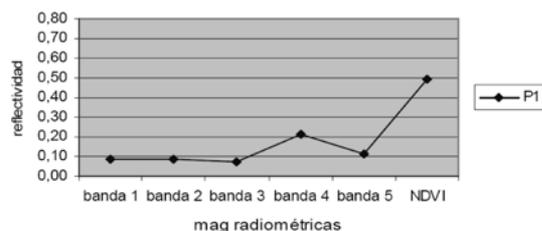
Figure 10.1.b. Comparative with training sites
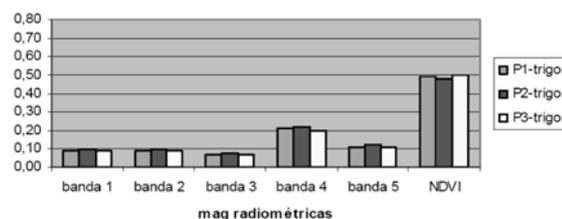
Spring – November

Figure 10.2.a. Winter cereals spectrum, November
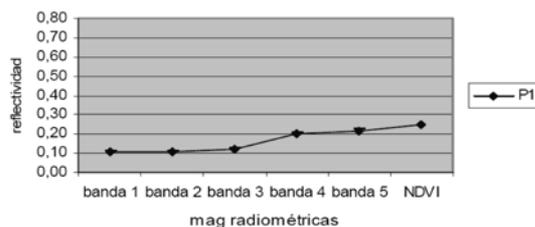
Figure 10.2.b. Comparative with training sites
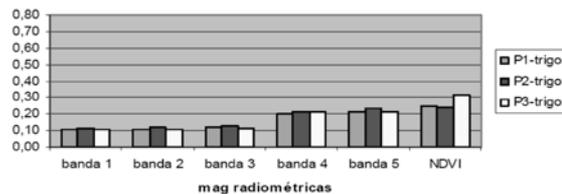
The difference found in P3 during November can be due to the variety of wheat cultivated (different cycles), or to its location in a lowland: a greater soil moisture, and as a consequence, a greater density of leafs would occur in November. This could explain lower values of reflectance in Band 5, and higher NDVI values.

The spectral behaviour of winter cereals during winter season is quite homogeneous, for this reason we can assume that winter cereals are characterized by a well identifiable and specific reflectance.

4.2   Bare soil

The *Bare soil* class was taken only in winter, and includes ploughed soils (both recent, and worked in previous months) and stubble of crops from the previous summer.

Winter − July

Figure 11.1.a. Spectre Bare soil, July
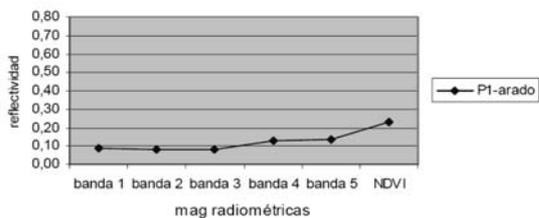
Figure 11.1.b. – Comparative with training sites
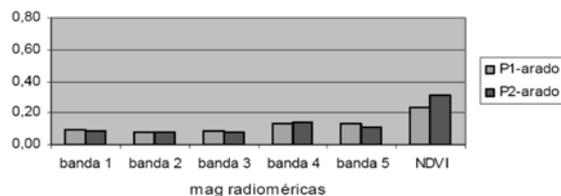
P2 plot is located in a site (lowland, *bajo*) with higher humidity, which makes easier the growth of spontaneous vegetation, therefore higher NDVI values are produced.

Bare soil spectral answer is characteristic in winter.

4.3   Alfalfa

Winter − July

Figure 12.1.a. Spectre Alfalfa, July
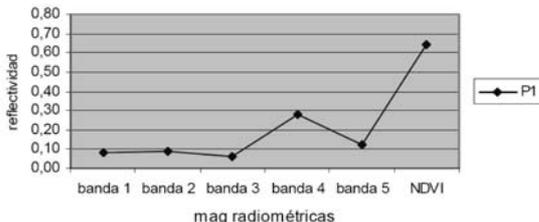
Figure 12.1.b. Comparative with training sites
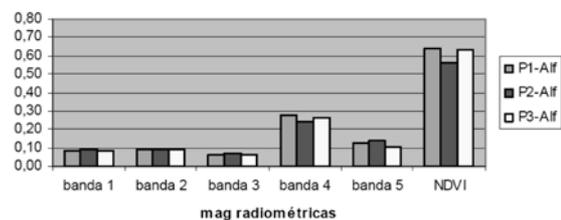
Spring − November

Figure 12.2.a. Spectre Alfalfa, November
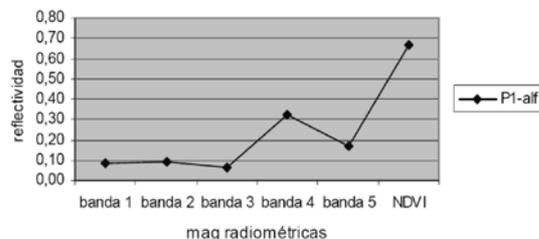
Figure 12.2.b. Comparative with training sites
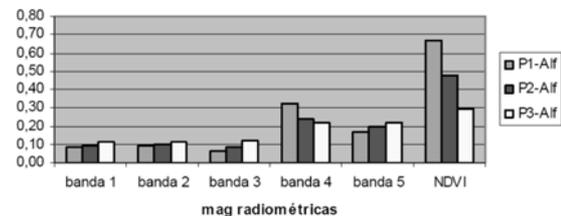
The spectral results derived from November images processing are not homogeneous at all. This can be due to differences in soil and crop management, which in many cases implies major cuts of the foliage.

Summer −February

Figure 12.3.a. Spectre Alfalfa, February
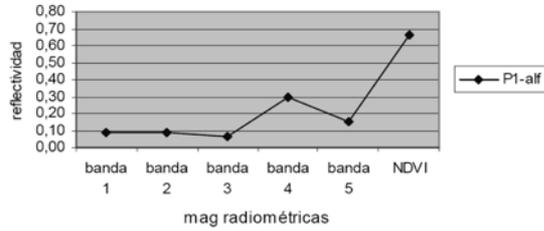
Figure 12.3.b. Comparative with training sites
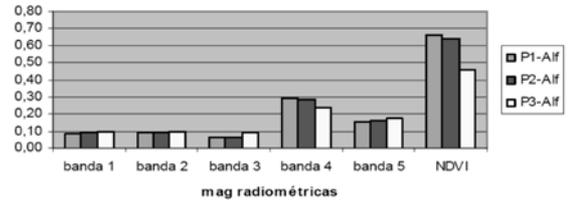
The spectral answer of class Alfalfa, derived from July and February image processing, had a characteristic reflectance.

4.4   Grasslands

Winter − July

Figure 13.1.a. Spectre Grasslands, July
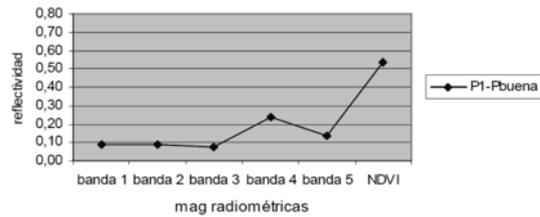
Figure 13.1.b. Comparative with training sites
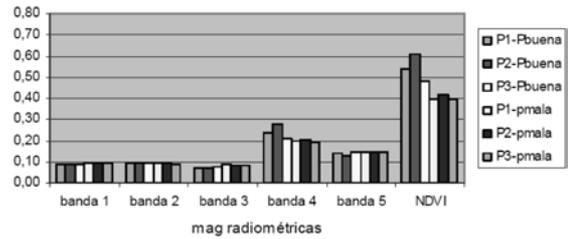
Spring − November

Figure 13.2.a. Spectre Grasslands, November
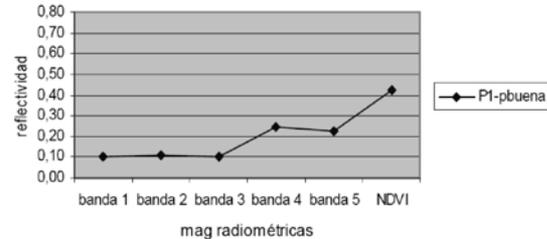
Figure 13.2.b. Comparative with training sites
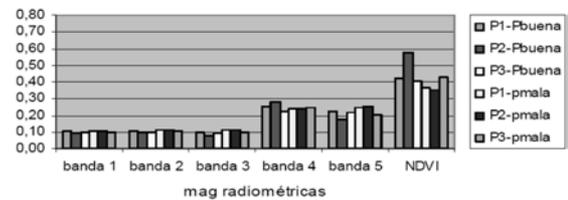
Summer – February

Figure 13.3.a. Spectre Grasslands, February
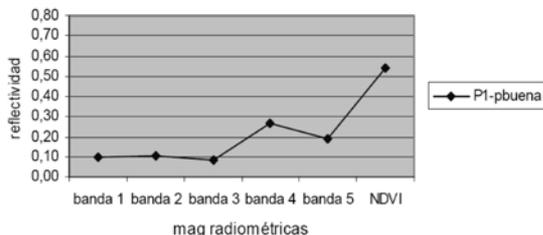
Figure 13.3.b. Comparative with training sites
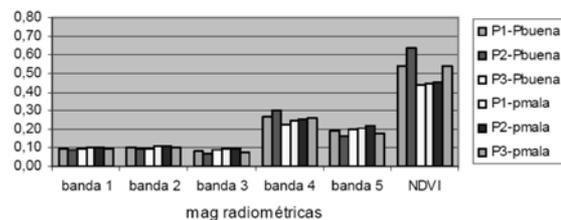
La reflectance of *Grasslands* class is conditioned by the heterogeneity in composition of the species (fodder species) and by state of growth the plants. In addition, factors like soil, climate and management, could also influence the results.

4.5 Natural Vegetation

Winter – July

Figure 14.1.a. Spectre Natural Vegetation, July
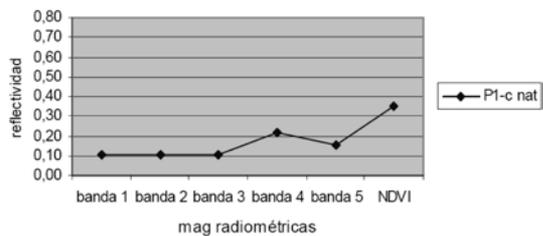
Figure 14.1.b Comparative with training sites
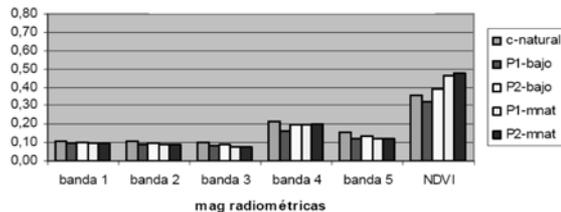
Spring – November

Figure 14.2.a. Spectre Natural Vegetation, November
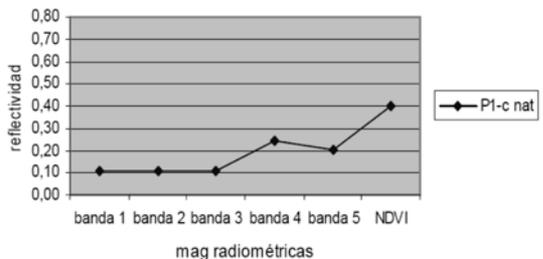
Figure 14.2.b. Comparative with training sites
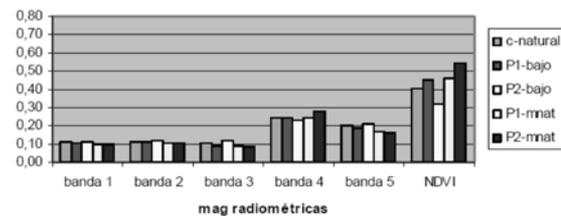
Summer – February

Figure 14.3.a. Spectre Natural Vegetation, February   Figure 14.3.b. Comparative with training sites
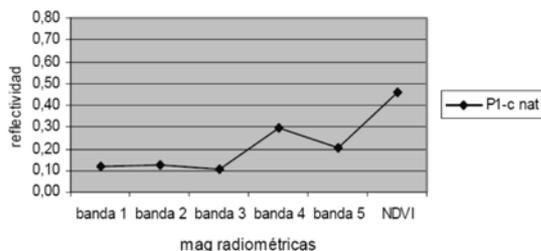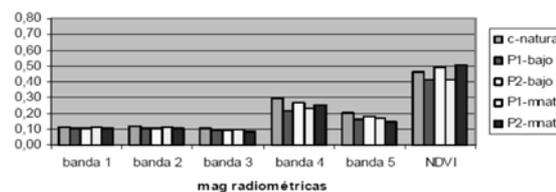
The *Natural Vegetation* class spectral response was very heterogeneous and this could be due to several land uses and to high variability of plant species; in addition, factors like soil, climate and production system could also be influent Moreover, it must be noted that the NDVI values of natural shrublands are always higher than natural pastures and lowlands.

4.6   Soybean

The vegetative cycle of this class occurs in springtime and summer, therefore its spectral characterization can be observed in November and February.

Spring – November

Figure 15.1.a. Soybean Spectre, November   Figure 15.1.b. Comparative with training sites
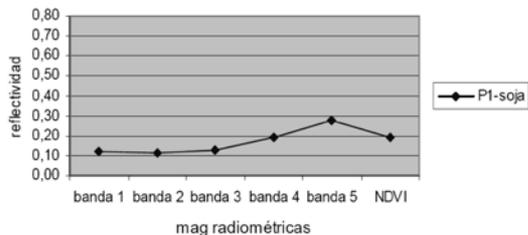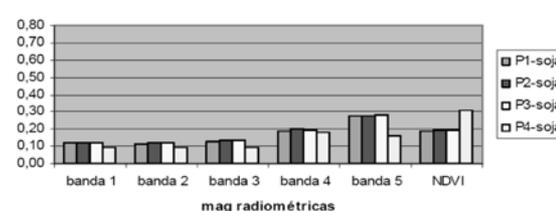
Summer – February

Figure 15.2.a. Soybean Spectre, February   Figure 15.2.b. Comparative with training sites
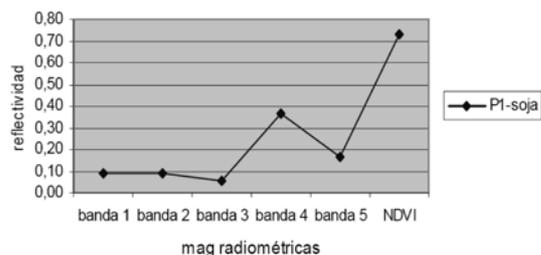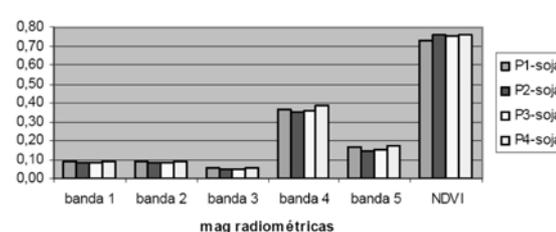
Soybean spectral answers are homogeneous in February, while differences in November are visible probably due to the date of the seeding. There are two main seeding periods for Soybean: even in the cases when the first seeding date is quite distant in time from the second, the two classes reach the same green area coverage in February-March.

For this reason, we can state that the spectral respond in February represents the significant reflectance of the class *Soybean*.

4.7   Rice

The vegetative cycle of rice occurs in springtime and summer, therefore it's most significant spectral response occurs in November and February.

Springtime − November

Figure 16.1.a. Rice Spectre, November
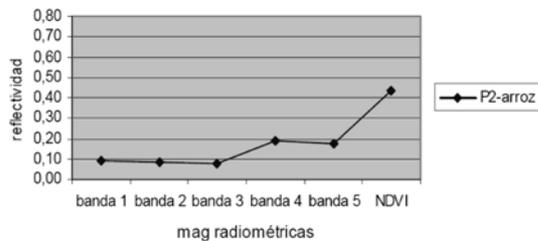
Figure 16.1.b. Comparative with training sites
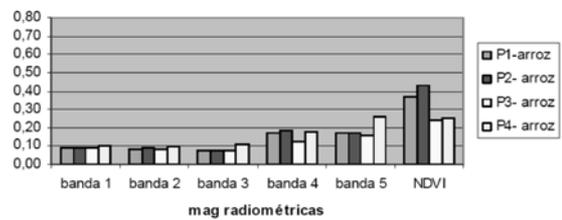
Summer − February

Figure 16.2.a. Rice Spectre, February
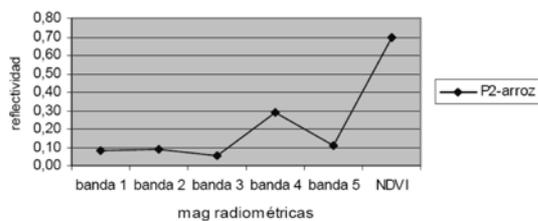
Figure 16.2.b. Comparative with training sites
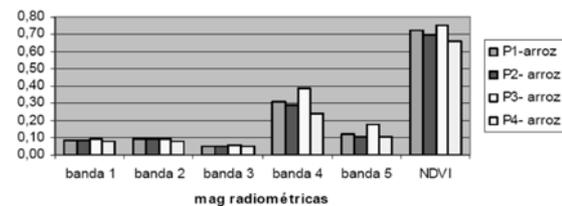
The differences found out in November are probably due to management factors. February is the best month to characterize *Rice* class under the spectral reflectance point of view.

4.8   Corn

*Winter – July*

Figure 17.1.a. Corn Spectre, July
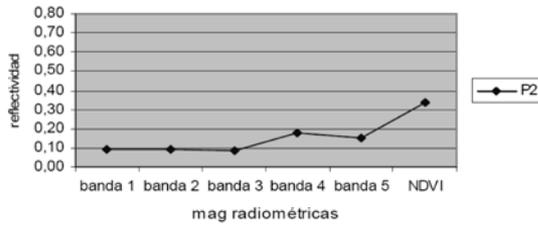
Figure 17.1.b. Comparative with training sites
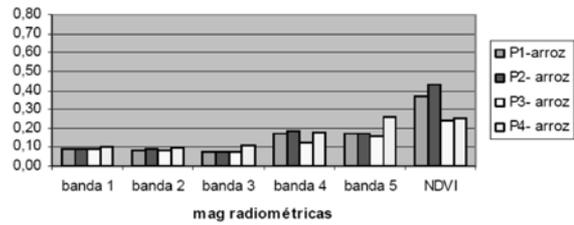
Spring – November

Figure 17.2.a. Corn Spectre, November
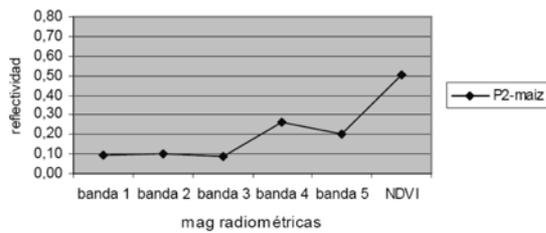

Figure 17.2.b. Comparative with training sites
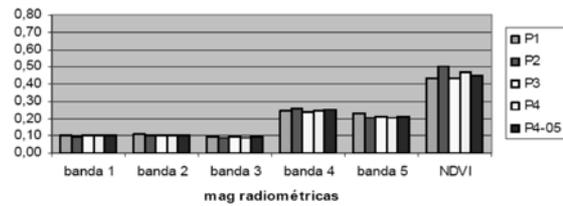
Summer – February

Figure 17.3.a. Corn Spectre, February
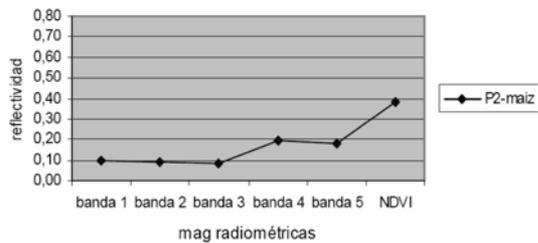
Figure 17.3.b. Comparative with training sites
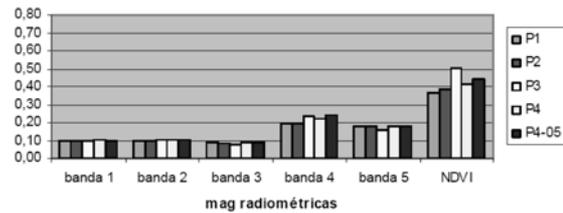
The heterogeneous values in July may depend upon the great variability in seeding dates, with a consequent difference of growth maturity in February. P1 shows the highest NDVI value in July, while, the lowest occurs in February.

November and February are the best months to spectral discriminate *Corn* class

4.9   Sorghum

*Winter – July*

Figure 18.1.a. Sorghum Spectre, July
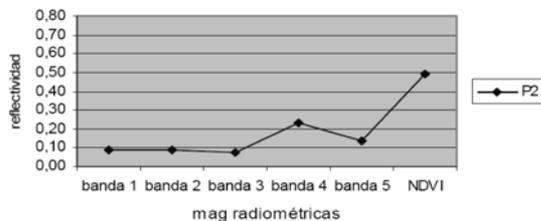
Figure 18.1.b. Comparative with training sites
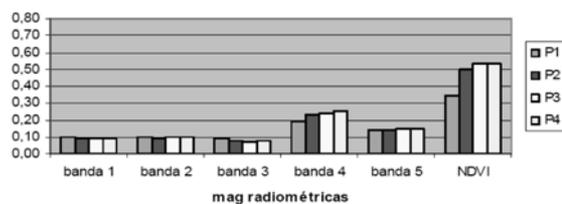
*Spring – November*

Figure 18.2.a. Sorghum Spectre, November
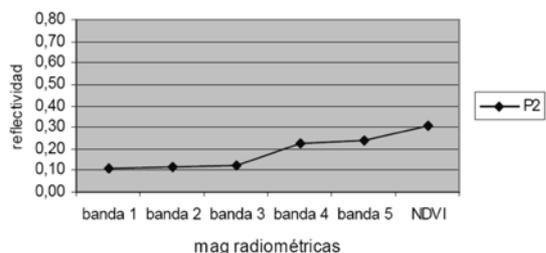
Figure 18.2.b. Comparative with training sites
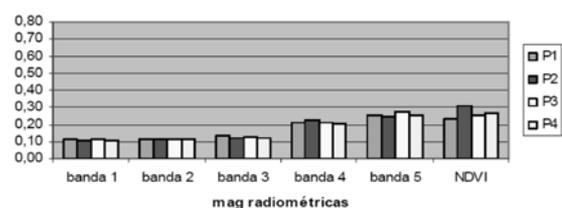
Summer – February

Figure 18.3.a. Sorghum Spectre, February
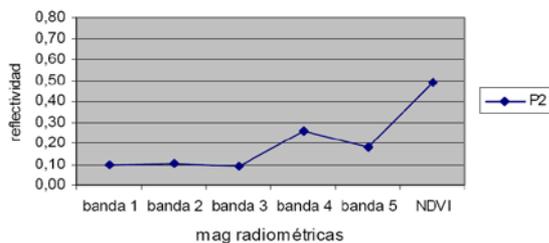
Figure 18.3.b. Comparative with training sites
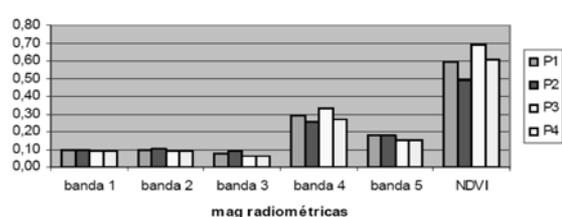
The difference observed in values in February depends upon de maturity level of the crop, as a consequence of management (seeding date) and climate.

The spectral answer obtained for *Sorghum* class represents its significant reflectance.

4.10   Urban

Winter − July

Figure 19.1.a. Urban spectre, July
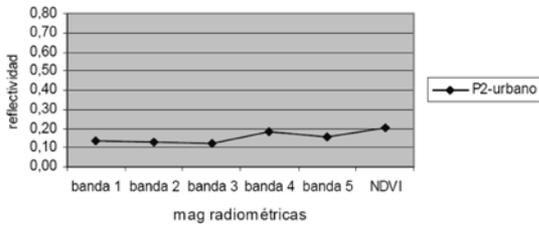
Figure 19.1.b. Comparative with training sites
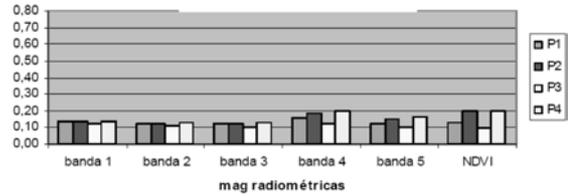
Springtime − November

Figure 19.2.a. Urban spectre, November
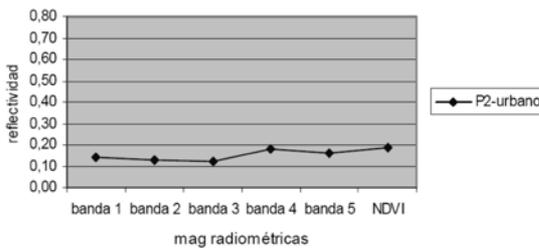
Figure 19.2.b. Comparative with training sites
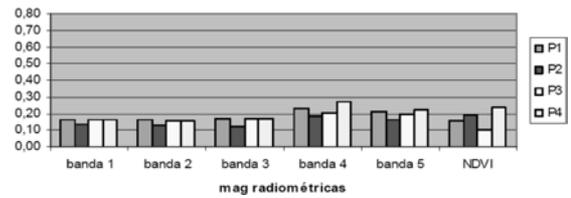
Summer − February

Figure 19.3.a. Urban spectre, February
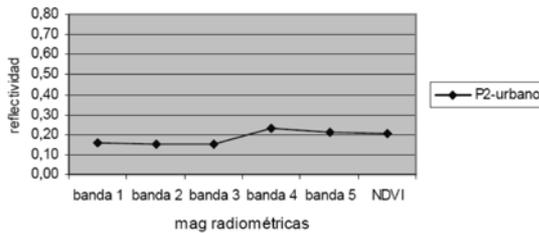
Figure 19.3.b. Comparative with training sites
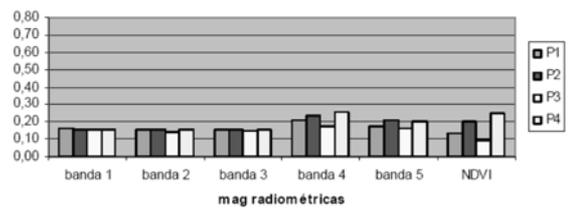
The differences observed in the plots of urban areas are manly due to different patterns which have been considered in the sample set, namely: compact, open, residential vegetated areas.

The spectral answer obtained in the *Urban* class represents its significant reflectance.

4.11   Water

Winter – July

Figure 20.1.a. Water spectre, July
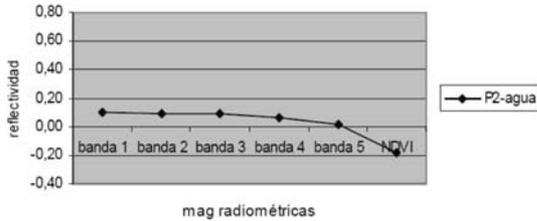
Figure 20.1.b. Comparative with training sites
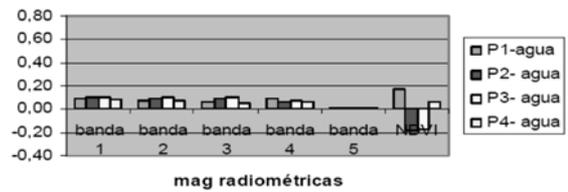
Springtime – November

Figure 20.2.a. Water spectre, November
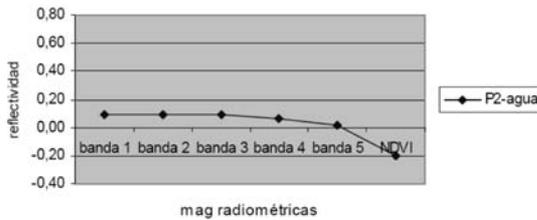

Figure 20.2.b. Comparative with training sites
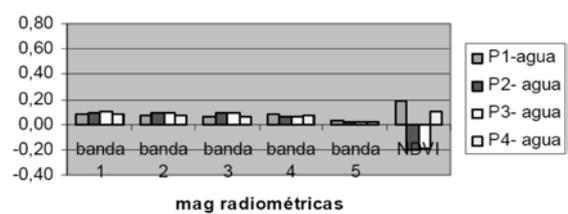
Summer – February

Figure 20.3.a. Water spectre, February
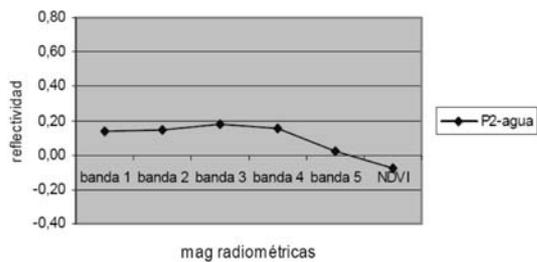
Figure 20.3.b. Comparative with training sites
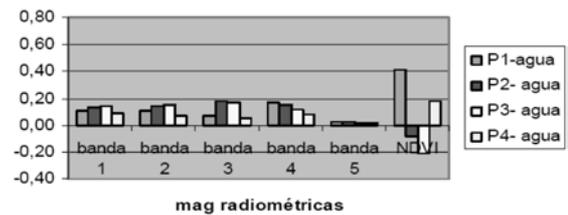
The different values of *Water* class probably derive from the different features of water bodies (deepness, motion or flows, and vegetation). It is possible to assume the existence of several differences in water spectral reflectance, therefore a split into two classes was necessary.

The training plots for «water» with NDVI values greater than 0, correspond to shallow water marshes (*laguna Melincue* and *laguna La Loca*, both located in Santa Fe province), with little water motion we refer to water surfaces partly occupied by water plants (cane, esparto grass). NDVI values of this class correspond to the cycle of aquatic vegetation.

5. Conclusions

As specified in the objectives of this research, the purpose of this study was the identification of different types of cover in a given area, through a supervised classification of available satellite imagery.

5.1 Characterization

Through the values recorded in images, taken at different times, real-time spectral signatures and single crops growth tracking can be extracted. Using multi-timing images, more classes of landuse can be distinguished by their spectral answer which can be different from season to season (Badhwar 1982).

Furthermore, the mean values of the spectral answers of each class at different time, for all the examined periods, are shown in Table 8, 9 and 10, and Figures 22, 23 and 24.

Here below are reported the different possibilities to discriminate spectral classes.

Spectral answer of the classes in Winter

Table 8. Spectral answer of the classes in winter

AUGUST 2001						
Class	band 1	band 2	band 3	band 4	band 5	NDVI
Winter cereals	0,09	0,10	0,07	0,30		0,62
Bare soil	0,11	0,10	0,11	0,17		0,24
Alfalfa	0,09	0,10	0,08	0,26		0,53
Pastures	0,10	0,11	0,09	0,24		0,44
Natural vegetation	0,09	0,10	0,08	0,19		0,38
Mais	0,11	0,11	0,11	0,22		0,32
Sorghum	0,10	0,11	0,10	0,22		0,35
Urban	0,14	0,13	0,13	0,18		0,15
Water	0,09	0,08	0,07	0,06		–0,01
July 2005						
Class	band 1	band 2	band 3	band 4	band 5	NDVI
Winter cereals	0,09	0,09	0,07	0,21	0,12	0,49
Bare soil	0,09	0,08	0,08	0,14	0,12	0,27
Alfalfa	0,09	0,09	0,06	0,26	0,12	0,61
Pastures	0,09	0,09	0,08	0,22	0,14	0,47
Natural vegetation	0,10	0,09	0,08	0,19	0,13	0,40
Mais	0,10	0,09	0,09	0,17	0,16	0,33
Sorghum	0,09	0,10	0,08	0,23	0,14	0,48
Urban	0,13	0,12	0,12	0,17	0,14	0,16
Water	0,09	0,08	0,08	0,07	0,01	–0,03

Figure 21. Spectral answer of the classes in winter
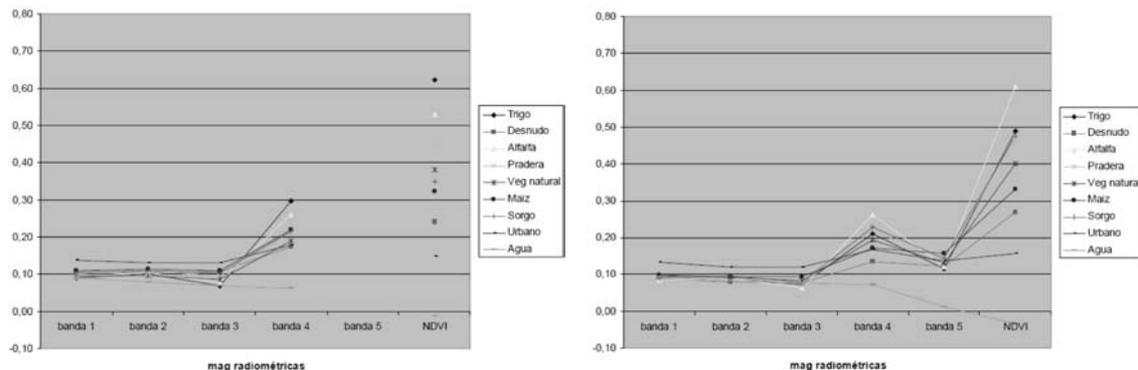
Spectral answer of the classes in Springtime

Table 9. Spectral answer of the classes in springtime

NOVEMBER 2001						
Class	Band 1	Band 2	Band 3	Band 4	Band 5	NDVI
Winter cereals	0,12	0,13	0,15	0,25	0,25	0,26
Alfalfa	0,09	0,11	0,09	0,31	0,18	0,57
Pastures	0,10	0,12	0,10	0,31	0,20	0,53
Natural vegetation	0,06	0,07	0,07	0,18	0,12	0,27
Soyabean	0,13	0,14	0,15	0,26	0,28	0,26
Rice	0,11	0,09	0,09	0,16	0,17	0,28
Mais	0,09	0,10	0,07	0,35	0,16	0,65
Sorghum	0,11	0,12	0,11	0,28	0,22	0,42
Urban	0,17	0,18	0,18	0,26	0,22	0,18
Water	0,10	0,09	0,09	0,09	0,03	0,03
NOVEMBER 2005						
Class	Band 1	Band 2	Band 3	Band 4	Band 5	NDVI
Winter cereals	0,11	0,11	0,12	0,21	0,22	0,27
Alfalfa	0,10	0,10	0,09	0,26	0,19	0,48
Pastures	0,10	0,11	0,10	0,25	0,22	0,43
Natural vegetation	0,10	0,11	0,10	0,25	0,18	0,44
Soyabean	0,11	0,11	0,12	0,19	0,25	0,22
Rice	0,09	0,09	0,08	0,16	0,19	0,32
Mais	0,10	0,10	0,09	0,25	0,21	0,46
Sorghum	0,11	0,11	0,12	0,21	0,26	0,27
Urban	0,16	0,15	0,16	0,22	0,20	0,17
Water	0,09	0,08	0,07	0,07	0,02	–0,03

Figura 22. Spectral answer of the classes in springtime
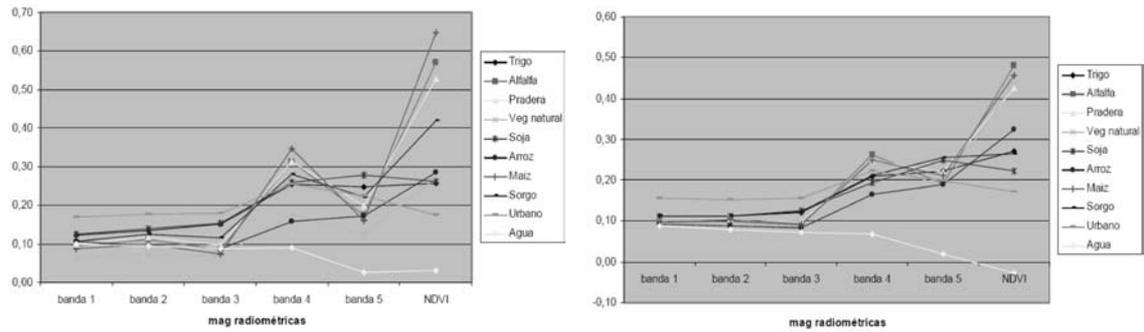
Spectral answer of the classes in Summer

Table 10. Spectral answer of the classes in summer

FEBRUARY 2002						
Class	band 1	band 2	band 3	band 4	band 5	NDVI
Alfalfa	0,11	0,11	0,10	0,30	0,20	0,49
Pasture	0,12	0,13	0,12	0,29	0,24	0,42
Natural veg	0,10	0,11	0,10	0,27	0,17	0,48
Soy bean	0,09	0,11	0,07	0,43	0,18	0,71
Rice	0,09	0,09	0,05	0,25	0,12	0,65
Maís	0,10	0,11	0,11	0,30	0,21	0,46
Sorghum	0,11	0,13	0,11	0,32	0,21	0,48
Urban	0,17	0,17	0,17	0,24	0,20	0,18
Water	0,11	0,11	0,11	0,12	0,02	0,06
FEBRUARY 2006						
Class	band 1	band 2	band 3	band 4	band 5	NDVI
Alfalfa	0,09	0,09	0,07	0,27	0,16	0,59
Pasture	0,10	0,10	0,08	0,26	0,19	0,51
Natural veg	0,11	0,11	0,09	0,25	0,17	0,46
Soy bean	0,08	0,09	0,05	0,36	0,16	0,75
Rice	0,09	0,09	0,05	0,31	0,13	0,71
Maís	0,10	0,10	0,09	0,22	0,17	0,42
Sorghum	0,09	0,10	0,07	0,29	0,16	0,60
Urban	0,16	0,15	0,15	0,22	0,19	0,17
Water	0,12	0,11	0,12	0,13	0,02	0,07

Figura 23. Spectral answer of the classes in summer
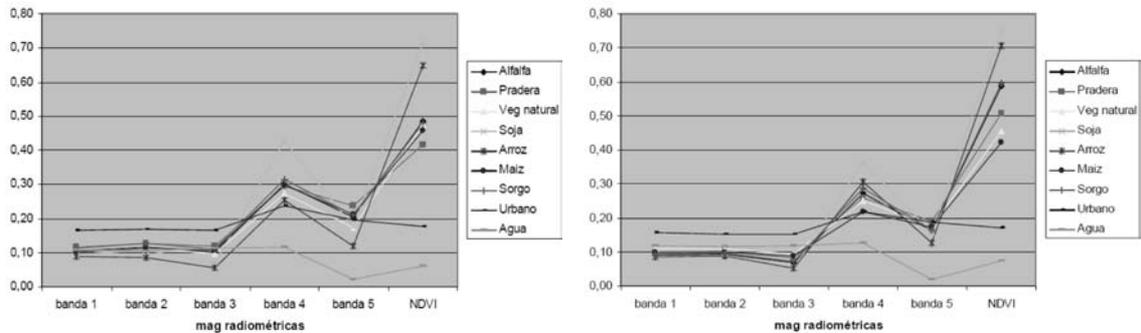
5.2   Winter Cereals

In winter (August 2001 and July 2005) NDVI value stands around 0,60. Even in this period these values look similar to those from alfalfa and grasslands; in November NDVI from cereals falls under 0,30 and the values from alfalfa and grasslands do not follow the same trend: their value increases, or remains around the previous average.

5.3   Bare soil

In winter, the NDVI value for stubble or ploughed parcels is lower than 0,30.

5.4   Alfalfa, grasslands, natural vegetation

Within similar NDVI values, the alfalfa answer (except for the case of cuts in the parcels) is always higher, followed by grasslands and Natural Vegetation that have always lower NDVI values. It is worth here to underline that natural shrublands, as well as winter species, have the same values as alfalfa in this season.

Winter NDVI values from alfalfa range between 0,50 and 0,60, grasslands 0,40 and 0,50 and Natural Vegetation between 0,30 and 0,40.

November NDVI from alfalfa ranges around 0,60, grasslands 0,50 Natural Vegetation around 0,40.

In February, NDVI from alfalfa ranges between 0,50 and 0,70, grasslands 0,40–0,55 and Natural Vegetation 0,40–0,50.

5.5   Soybean

NDVI values from Soybean in November average around 0,30 and in February they are higher than 0,60.

In February, the values from Soybean look similar to alfalfa, unlike the other dates, when NDVI value from alfalfa presents higher values.

5.6   Rice

The values from rice are similar to those from Soybean, being a little lower in February.

5.7   Corn

In winter, the NDVI values from corn are low, since it's the time for preparing the soil; in November the values are high, between 0,50 and 0,70, and in February between 0,40 and 0,60.

5.8   Sorghum

The values from sorghum are similar to those from corn, with lower value in November and higher one in February.

Both sorghum and corn, in November and in February there can confusion with alfalfa, but in winter NDVI value from alfalfa is always higher.

5.9   Urban

NDVI values of all the dates are in the range 0,15 – 0,20.

5.10 Water

The results for this class show two groups of NDVI values, corresponding to two types of cover. One of them identifies the absence of vegetation, with NDVI values between –0,10 and –0,20, while the other one shows the presence of vegetation with NDVI values between 0,10 and 0,25.

6. Recommendations

The possibility to separate the defined classes depends on three factors: their radiometric characterization, the distribution and shape of patterns across the region and the spatial resolution of the images.

The study area is very broad, with relevant differences in environmental and climatic characters, production systems, in addition to several distribution and shape patterns.

The great spatial variability of the crops and Natural Vegetation, and its evolution over time, implies that different vegetal covers show similar spectral answers, depending from the development reached at the moment when the images are taken.

Another limiting factor concerns the relatively low resolution of MMRS images.

In such situation, it is very difficult to identify any crop on the basis of a single scene, making thus necessary to count on several scenes to process, so to be allowed to analyze different phenological development of the crops.

If the time spectral path allows to track different phases of the phenological development of a crop, then it is possible to separate those crops whose time spectral path is different (Badhwar 1982).

Considering the situation described above, and after having analyzed the NDVI values presented by the classes, we can infer that this index is not accurate enough to identify the classes. According to Gilabert *et al.*, (1997) the spectral bands corresponding to the range of green, red, near infrared and shortwave infrared are mostly used, because of the reflectance of the complex formed by soil, water and vegetation. The ranges mentioned allow the best identification of these elements, and the study of their behavior.

With the aim of identifying crops and covers by means of classifying MMRS mages from SAC C satellite, we can affirm that, in addition to NDVI, it is necessary to add band 2 (green) and 5 (shortwave infrared).

Cases where the use of the only NDVI can lead to mix classes

Water
After having analyzed the answers from this class, it should be recommended to split it in two classes.

Water – Urban
One of the cases where NDVI values correspond to mixing classes is *urban* and *water*. The NDVI values of the shallow water marshes range around 0,20, similar to those of the *urban* class.

Urban – Bare soil, or with little vegetation
The towns edges, as well as urban areas with low population density, are frequently characterized by a relevant presence of vegetation, like trees, shrubs, areas with low building density (empty spaces, green plots) occupied by natural vegetation, showing similar reflectance as bare soils at plowing time, and natural areas.

Soybean – rice
It is recommended to select scenes from dates matching with inundation periods of the *rice* crop, especially at the beginning of this phase, when its green cover does not hide the water, allowing to separate it from *Soybean* class. Band 5 can be useful to make this discrimination.

This research is supposed to be a contribution to the knowledge of soil covers of the *litoral argentino* region; the radiometric characterization realized here could be applied for the creation of inventories and studies about the soil use and its evolution over time, which will be the object of the next step.

References

Badhwar G.D. *et al.* (1982). A semi-automatic technique for multitemporal classification of a given crop within a Landsat scene. *Pattern Recognition*, 15, 3: 217-230

Carñel G., Farías G., Crotti CH. (2004) Utilización de Imágenes SAC–C para estudios regionales. CIOMTA.

Ciomta (2004). Análisis territorial de ocupación del suelo – Período enero – marzo 2004. *Boletín Informativo*, 1, 4, December.

Chuvieco E. (2002). *Teledetección ambiental. La observación de la Tierra desde el Espacio.* Barcelona. Ariel Ciencia.

Eastman R. (2006). *Idrisi Andes. Guide to Gis and Image Proocessing.* Clark Labs, Worcester–USA.

García M., Chuvieco E. (2002). *Assessment of the potential of SAC- C/MMRS imagery for mapping burned areas in Spain*. Department of Geography, University of Alcala.

Gilabert *et al.*, (1997). Acerca de los índices de vegetación. *Revista de Teledetección, vol*. 8.

Indec. Censo Nacional Agropecuario (2002).

Research Systems Inc (2000). ENVI.

Research Systems Inc (2004). IDL.

Internet references

<http://www.inta.gov.ar/cuenca/info/documentos/sig-teledet/patrones.pdf>.
<http://www.conae.gov.ar/>.

DETERMINATION AND ANALYSIS OF THE STANDARDIZED PRECIPITATION INDEX (SPI) AS DROUGHT INTENSITY INDICATOR FOR PARAGUAY – A FIRST APPROACH

Jorge A. Vidal
Facultad de Ingenieria, geoecología y medio Ambiente
Universidad Católica de Santa Fe
Argentina

Tutors: Prof. J. Baez and Prof. L. Lugo
Facultad de Ciencias y Tecnología
Universidad Católica Nuestra Señora de la Asunción
Paraguay

1. Introduction

Drought is a normal and recurrent property of climate. Sometimes it is considered as an infrequent and contingent phenomenon. Drought occurs virtually in almost every climatic zone, even when its characteristics vary significantly among regions.

It is widely known that drought is a phenomenon of gradual development (OMM– n. 799), which starts and finishes in a not well-defined way and whose impacts are diverse. It affects wide areas for months and even years. It has an impact on food production and decreases the life expectancy and economic development of big regions and whole countries.

There are two kinds of definitions of droughts: conceptual and operational.

The conceptual definitions help to understand the meaning of drought and its effects. For instance, drought is a long period of deficient precipitation, which causes great damage to crops and leads to yield loss.

The operational definitions help to identify the beginning of drought, its end and severity degree. In order to determine the beginning of drought, the operational definitions specify the deviation degree of the average precipitation during a certain period of time. This is usually carried out by comparing the current situation with the historical average. The threshold identified as the beginning of drought (for example, 75% of average precipitation during a specific period of time) is usually established arbitrarily.

The operational definitions are used to analyse the frequency of drought, severity and duration for a given historical period. However, such definitions require atmospheric data about hour, day, month and other time scales which may have impact on other data (such as crop yields).

A common term in all definitions is «rainfall shortage» as regards its «normal» occurrence, and «normal rainfall» value refers to an average historic value obtained from a certain length series. However, when considering this «normal» value as immutable in time, the constant climate evolution is being eluded, so another topic for discussion is that the reference rainfall sheet should be dynamic and reflect the «evolution of climate» (Makarau 1992).

For operative purposes, it is necessary to have reliable and feasible techniques and procedures which allow to identify when drought begins, characterize its evolution in time and space and forecast its end. Sazónov (1989) stated that 'the crucial matter for those who study drought and its formation in time and space is how to define it and keep track of its evolution'.

When there is a period of drought, agriculture is normally the first sector to be affected due to its great dependence to the water stored in the ground.

This is why drought identification and intensity is of importance: to prevent the contingencies it arises regarding food production, ecosystems and all the social and economic activities of the region in question. They also constitute the base for the development of prediction models with scientific basis on this topic.

1.1   Types of Drought

Although there is not a universal definition of drought, it could be referred to it as 'a sufficiently long period of time when there is a deficit in fresh water availability in a certain place'.

As an adverse phenomenon, its effects are most destructive than the effects of floods, whereas these are almost exclusive in very small areas –river valleys in general- and for short periods of time. Droughts affect big areas and the periods of time are long.

Different types of drought can be distinguished depending on the discipline from which the phenomenon is analysed: meteorological, agricultural, hydrological and socio-economic drought.

The meteorological drought is based on climatic values. In general, it reflects the deviation of the precipitations regarding a mean, although other factors also interfere such as temperature and evaporation, among others. There is a very big dependence on the geographical area in most definitions.

The agricultural drought takes place when there is not enough humidity in the soil for a certain crop to develop. Since it is closely related to the type of crop and soil, the relationship with the meteorological drought is very variable.

Regarding the hydrological drought and related to the superficial water flow, apart from the registered precipitation, it directly depends on the ability to manage the hydric resources. In general it is underdeveloped if it is compared to the meteorological drought and if precipitation increases in a short time, it is sometimes not manifested. In a time sequence, the meteorological drought would come first, then the agricultural one and finally the hydrological one.

 The socio-economic drought is produced when the water shortage can cause damage to economy or people; therefore, the dependence of the state of the economic development is huge. In a developing country whose economy is based on agriculture, a slight drought can provoke significant economic imbalances.

Hereinafter, this report focuses on the study, spatial and temporal distribution and magnitude of meteorological droughts, considering only the precipitation data of the localities of Ciudad del Este and Encarnación in Paraguay.

The results of the application of a methodology of drought monitoring by means of the SPI indicator will be presented. This indicator allows to establish its global diagnosis and this is why the determination and analysis of the obtained data with the application software are carried out.

2. Materials and methodology

2.1   Standardized Precipitation Index

In 1993 McKee *et al.* developed the Standardized Precipitation Index (SPI) which enables to determine the beginning and end of drought as well as its intensity. The SPI was designed to quantify the deficit of precipitation for several time scales, assuming that the humidity conditions of the soil respond to the anomalies of precipitation in a short period of time. Meanwhile, for the subterranean water, the stored water and the water currents, the impact is reflected on

anomalies of precipitation in long periods of time. For these reasons, the SPI was originally estimated for periods of 3, 6, 12, 24 and 48 months.

This index is estimated with the precipitation accumulated on a monthly basis of a sufficiently long series of data (minimum 30 years) A new series of precipitations accumulated in periods of X months is generated in a way that the precipitation of a certain month represents the precipitation accumulated of the X previous months. As the accumulated precipitation does not distribute regarding a normal distribution, a function of the precipitation is defined and, once typified, is adjusted to a distribution of this kind.

To each value of the accumulated precipitation a value of the function is assigned and the probability of occurrence of this function is determined, which coincides with the probability of precipitation (SPI of the datum of accumulated precipitation)

The value of the SPI represents the probability of occurrence of a certain accumulated precipitation. It corresponds to the number of times that a concrete value of the accumulated precipitation of a period in time separates from the mean of the series, measured in units of typical deviation.

Keyantash and Dracup (2002) carried out a comparison between the drought indexes in Oregon, USA, and concluded that the SPI is the one that best estimates drought severity.

Komuscu (1999) highlights the SPI because of its rapidity, great approximation in drought analysis, simplicity and minimum data requirements. This author also claims that for large scales, lower drought frequency results but with more prolonged effect. In another way, for 3-month scales the drought frequency increases and its duration decreases. Lastly, he points out that the SPI responds quickly to humidity or drought periods, which means that each month has a strong influence on the global behaviour of precipitation.

Currently, the SPI is utilized to monitor drought in the United Status of America through The National Centre of Mitigation against Drought, The Climate Forecast Center in the USA, the Centro de Investigaciones sobre la Sequía del Instituto de Ecología in Mexico and the Servicio Meteorológico Nacional in Argentina, among other institutions.

2.2 SPI Estimation

The SPI is estimated with basis in the utilization of a precipitation data record that is adjusted to a function of gamma probability which transforms into a distribution of standardized normal probability. So the medium value of the SPI is zero and the variance is one. Positive values of the SPI are higher than the median and negative values are lower.

Precipitation is far from having a normal distribution, since its most frequent value (mode) does not coincide with the arithmetic mean of a series of data but is lower, emphatically for months of dry years.

The accumulated probability H(x) is transformed into the normal variable Z (with mean zero and variance one), which represents the value of the SPI. This is a transformation of equiprobability proposed by Panofsky and Brier (1958) and cited by McKee et al (1993), who established that the crucial characteristic of transformation of a random variable with gamma distribution to a random variable with pre-established distribution –in this case standard normal- resides in the similarity of behaviour of the probability of having the same or a lower given value than the random variable, both in the gamma distribution and in the transformed one.

With the purpose of facilitating the obtention of the McKee indexes, the values of Z can be estimated through an approximation that converts the accumulated gamma probability into a standard normal or Z variable probability value.

Standardization with mean zero and variance one allows to make comparisons between sites and in different time scales. The SPI represents the accumulated probability of the occur-

rence of a deviation of precipitation in relation to a basis period for which the gamma param-eters were estimated.

Finally, McKee *et al.* (1993) used a classification system to define drought intensity, which is shown in Table 1. They also defined the criteria in cases of drought episodes in any time scale.

A drought episode occurs if the SPI is constantly negative and reaches an intensity of –1,0 or lower.

A drought event ends when the SPI is positive.

Each drought event has a duration defined by its own beginning and end and an intensity for each month that the event lasts.

The totality of the SPI for all the months in a drought event is its magnitude.

Table 1. Classification of dry and humid periods in function of the SPI

Classification of the SPI	
2,0 or more	Extremely humid
1,5 to 1,99	Very humid
1,0 to 1,49	Moderately humid
–0,99 to 0,99	Almost normal
–1,0 to –1,49	Moderately dry
–1,5 to –1,99	Severely dry
–2,0 or less	Extremely dry

The advantage of this index is that it assigns a unique numerical value and these values are comparable in different climatic zones.

To determine the drought periods, the data of the series of daily precipitations of two me-teorological stations of Paraguay have been taken as basis.

Ciudad del Este.
Location: 25° 32′ South Latitude and 54° 36′ West Latitude.
Daily series considered: January 1966 to December 2005.
Encarnación.
Location: 27° 20′ South Latitude and 55° 50′ West Latitude.
Daily series considered: January 1951 to December 2005.
To estimate the SPI, the SPI_SL_6 software was used, which is available on The National Drought Mitigation Centre (NDMC) website of the Nebraska-Lincoln University.

The SPI estimated for the above mentioned localities corresponds to six temporal scales: 1, 3, 6, 12, 18 and 24 months. Such results were processed by computer in order to be graphi-cally depicted and subject to statistical validation tests such as estimation of trend models, least squares and polynomial, significance test on the straight of linear adjustment and calculation of the coefficient of determination.

4. Results and discussion

Hereinafter, the results obtained from the processing of the SPI values estimated with the SPI_SL_6 programme are graphically shown.

The graphs refer to six time scales: SPI-1 month (Figures 1 and 2), SPI–3 months (Figures 3 and 4), SPI–6 months (Figures 5 and 6), SPI–12 months (Figures 7 and 8), SPI–18 months (Figures 9 and 10) and SPI–24 months (Figures 11 and 12).

Figure 1. Ciudad del Este SPI–1

$y = 0,0003x - 0,2732$
$R^2 = 0,0014$

$y = -4E-15x^4 + 2E-11x^3 - 6E-08x^4 + 9E-05x^3 - 0,0731x^2 + 31,478x - 5614,6$
$R^2 = 0,0203$
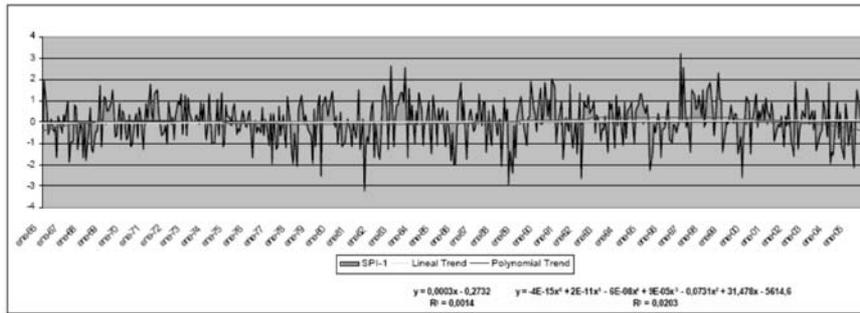
Figure 2. Encarnaciòn SPI–1

$y = 0,0002x - 0,0526$
$R^2 = 0,001$

$y = -3E-15x^5 + 6E-12x^5 - 5E-09x^4 + 2E-06x^3 - 0,0003x^2 + 0,0251x - 0,5262$
$R^2 = 0,0142$
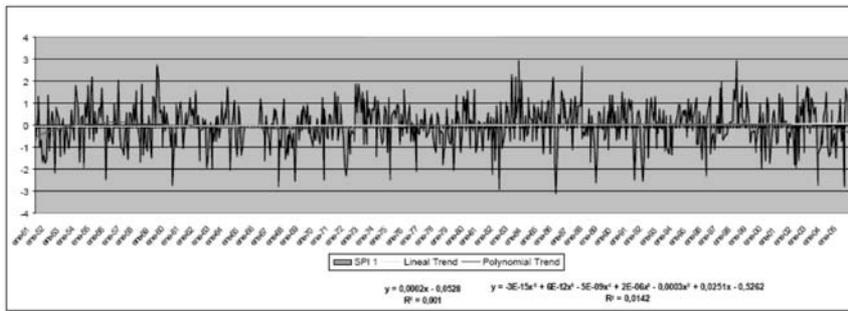
Figure 3. Ciudad del Este SPI–3

$y = 0,0008x - 0,7925$
$R^2 = 0,0112$

$y = -3E-15x^6 + 3E-11x^5 - 9E-08x^4 + 0,0001x^3 - 0,1057x^2 + 45,953x - 8262,6$
$R^2 = 0,0401$
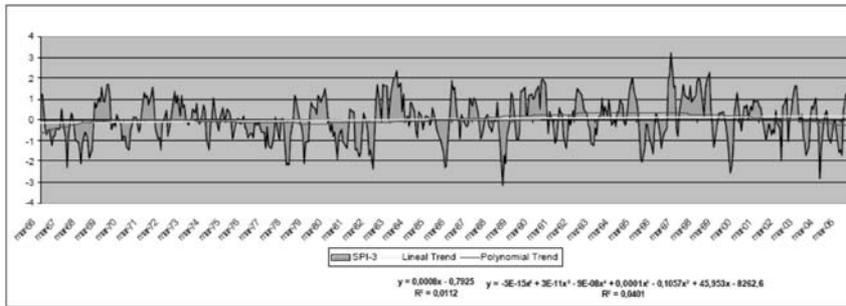
Figure 4. Encarnaciòn SPI–3

$y = 0,0003x - 0,1194$
$R^2 = 0,0039$

$y = -5E-15x^5 + 1E-11x^5 - 8E-09x^4 + 3E-06x^3 - 0,0006x^2 + 0,0436x - 0,8262$
$R^2 = 0,044$
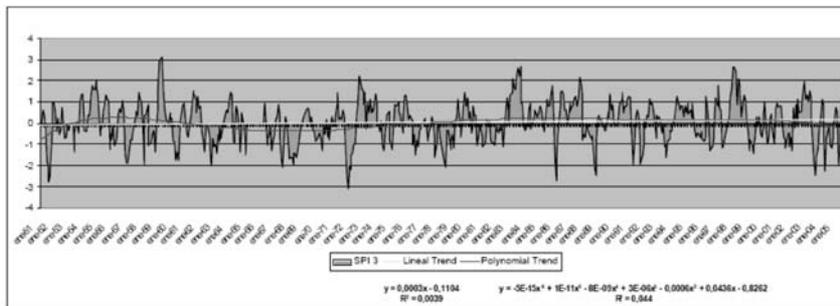
Figure 5. Ciudad del Este SPI–6
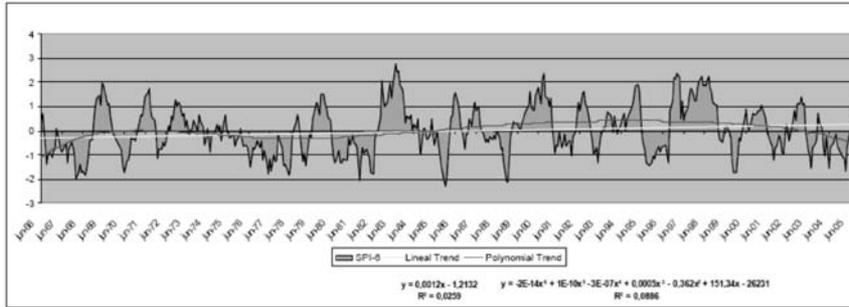
Figure 6. Encarnaciòn SPI–6
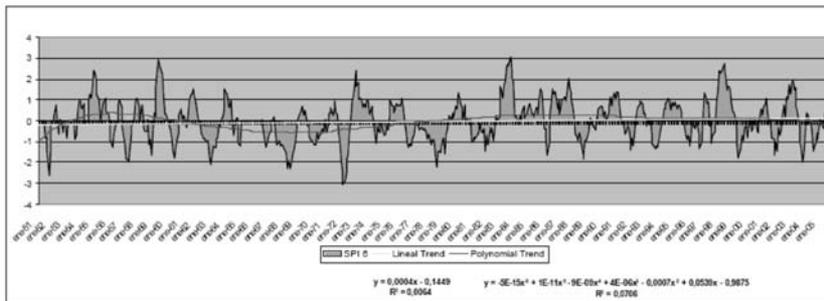
Figure 7. Ciudad del Este SPI–12
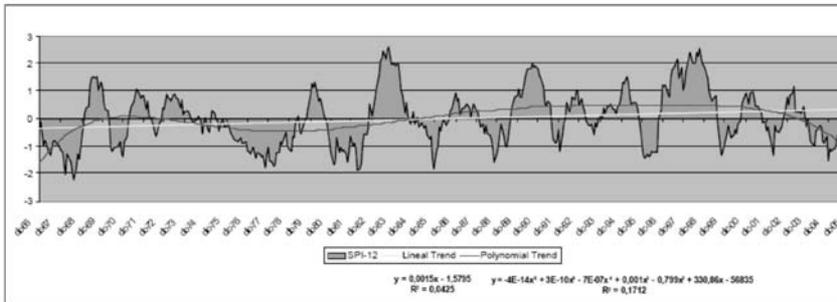
Figure 8. Encarnaciòn SPI–12
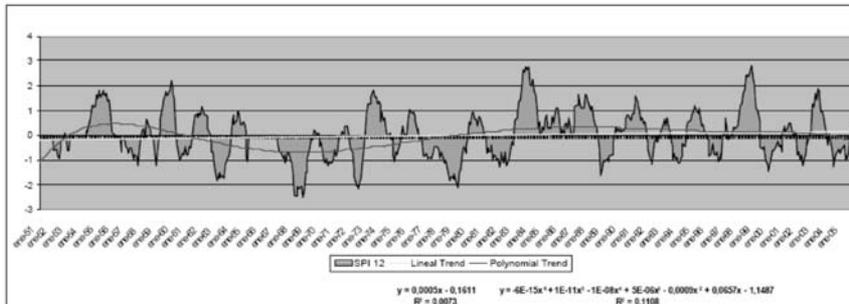
Figure 9. Ciudad del Este SPI–18
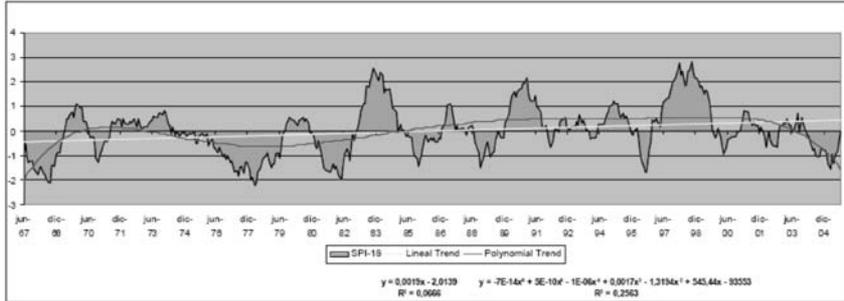
Figure 10. Encarnaciòn SPI–18
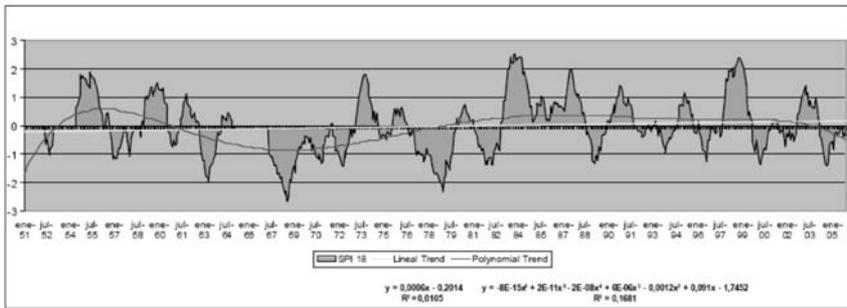
Figure 11. Ciudad del Este SPI–24
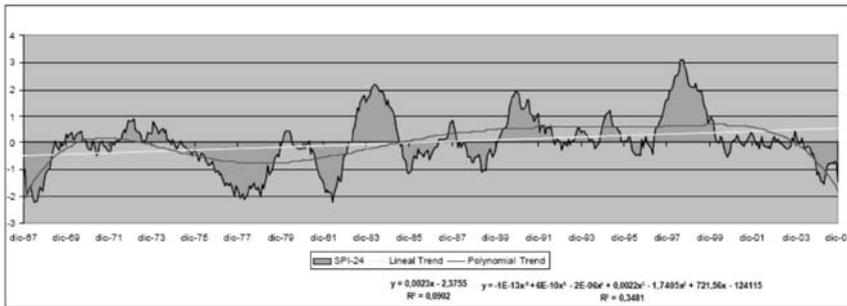
Figure 12. Encarnaciòn SPI–24
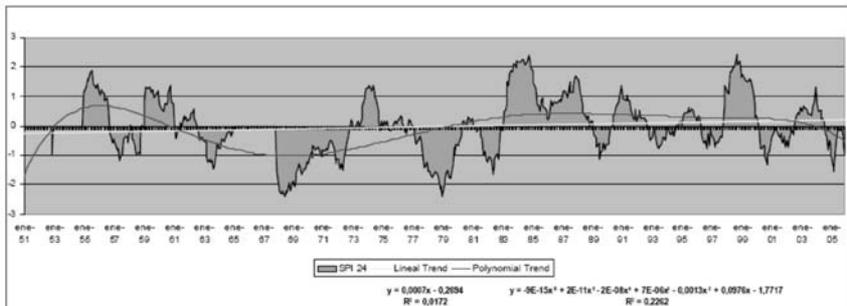
In the graphs, the areas comprised by the SPI values for the considered time scale, the straights of lineal and polynomial trend of 6th order, their formulae and the R^2 value that indicates the adjustment of these straights with the processed data are presented.

The polynomial trend was used as it was originally used by Nuñez (2005).

Both, for the case of Ciudad del Este and for the case of Encarnación, the graph for the negative SPI is added for the time scale of 3, 12 and 24 months, which indicates in a clearer way the considered drought periods.

These two graphs show the obtained values of the monthly SPI for both localities. When working with this 1 month scale, it was observed that the slope of the straight of the lineal trend becomes practically 0. The significance test of the adjustment straight indicated that the model of minimums seems not to be significant for any of the two localities (p CRITICAL = 0,42 for Ciudad del Este and 0,41 for Encarnación). In the same way, the R^2 values also showed a poor adjustment between the observations and the predicted values by the straight, being 0,0014 for Ciudad del Este and 0,001 for Encarnación.

When using the polynomial adjustment curve, it is observed that for both localities the trend evidently descends towards the end of the considered period.

The importance of the estimation of the SPI-3 resides in the fact that different authors quote this time scale as an approximation of the SPI for establishing Agronomical Droughts.

In the case of the two localities, the same statistical treatment was done.

In these cases, an ascending lineal trend is observed, which is significant in a p CRITICAL = 0,02 for Ciudad del Este and a p CRITICAL = 0,11 for Encarnación according to the significance test carried out on the lineal model, being the slope coefficients near 0. Nevertheless, the determination coefficients are very low regarding what was expected, finding for Ciudad del Este R^2 = 0,0112 and for Encarnación, R^2 = 0,0039.

In this time scale a bigger adjustment of the polynomial trend curve is observed. The R^2 values are low, but evidently the polynomial curve adjusts better than the lineal one and even more when increasing the quantity of equation terms –R^2 = 0,0401 and R^2 = 0,044 for Ciudad del Este and Encarnación respectively.

The two preceding graphs correspond to the SPI-6 for both localities and an ascending lineal trend is observed, which is significant for p CRITICAL = 0,0004 and p CRITICAL = 0,044 for Ciudad del Este and Encarnación respectively according to the significance test carried out on the lineal model. The slope coefficients are still near 0 in the same way as the determination ones, finding R^2 = 0,0259 for Ciudad del Este and R^2 = 0,0064 for Encarnación.

In this time scale a bigger adjustment of the polynomial trend curve is observed. Besides, there is a clear difference of the descending of the curve towards the end of the series if the first graph is taken with respect to the second one, being the first the most significant case.

The R^2 values are low but it is evident that the polynomial curve adjusts better than the lineal one and even more when increasing the quantity of the equation terms - R^2 = 0,0886 and R^2 = 0,0706 for Ciudad del Este and Encarnación respectively.

These two graphs correspond to the SPI-12 for the two localities and a bigger representativeness for the dry and humid periods is observed regarding the considered time scale.

When doing the statistical analysis of the trend models, it can be appreciated that the lineal trend in both cases appears as ascendant and significant for p CRITICAL = 6,77x10-6 for Ciudad del Este and p CRITICAL = 0,034 for Encarnación according to the significance test carried out on this lineal model. The slope coefficients are still near 0, the same as the determination coefficients, finding for Ciudad del Este R^2 = 0,0425 and for Encarnación, R^2 = 0,0073.

Although the precipitation series taken for the estimation of the SPI is bigger for the case of Encarnación than for the case of Ciudad del Este, in this temporal scale of the SPI of 12 months, a bigger adjustment of the curve of polynomial trend is still observed. Besides, in the

first graph a much more pronounced descent of this curve is observed towards the end of the series. Meanwhile, in the second graph the curve is descendant but not so pronouncedly.

The R^2 values are still low but it is evident that the polynomial curve adjusts better than the lineal one and even more when increasing the quantity of the equation terms: $R^2 = 0,1712$ and $R^2 = 0,1108$ for Ciudad del Este and Encarnación respectively.

These two graphs present the results of the SPI in a time scale of 18 months in which the analysis done to the obtained data is even more marked.

For these two cases, the model of lineal trend is ascendant for p CRITICAL = $1,91 \times 10^{-8}$ for Ciudad del Este and p CRITICAL = 0,012 for Encarnación according to the significance test carried out on this lineal model, which makes it significant. The slope coefficients are still near 0, the same as the determination coefficients, finding for Ciudad del Este $R^2 = 0,0666$ and for Encarnación, $R^2 = 0,0105$.

The curve of polynomial trend is also present and it can be noted that it possesses a better adjustment to the data. Moreover, it can still be appreciated in the graph for Ciudad del Este that this trend model presents a more marked descent towards the end of the series with respect to the graph of Encarnación for this time scale of 18 months.

The R^2 values are still low but it is evident that the polynomial curve adjusts better than the lineal one and even more when increasing the quantity of the equation terms: $R^2 = 0,2563$ and $R^2 = 0,1681$ for Ciudad del Este and Encarnación respectively.

The statistical analysis for these two localities –taking as time scale 24 months– is the following:

The model of lineal trend is ascendant for p CRITICAL = $5,53 \times 10^{-11}$ for Ciudad del Este and p CRITICAL = 0,016 for Encarnación according to the significance test carried out on this lineal model. In spite of the slope coefficients being near 0, it is significant.

The determination coefficients are near 0; Ciudad del Este presents $R^2 = 0,0902$ and Encarnación, $R^2 = 0,0172$ for the same lineal model.

In the model of polynomial trend, the R^2 values remain low, but it is evident that the polynomial curve adjusts better than the lineal one and even more when increasing the quantity of the equation terms: $R^2 = 0,3481$ and $R^2 = 0,2262$ for Ciudad del Este and Encarnación respectively.

It is also observed a marked descent of the curve of this trend towards the end of the series in the graph for Ciudad del Este, contrarily to the observed in the graph of Encarnación, where the descent is more maintained towards the end of the series.

In conclusion, in this part of the analysis it is important to highlight that although the ascendant lineal trend is significant in every case, it does not happen when working with a scale of 1 month. What is more, the increasing trend becomes more significant as the time scale increases too. This can be validated with the significance test.

Several curves of polynomial trend were applied to the graphs, varying the quantity of terms (from 2 to 6 polynomials) and for each case the curve equation and the determination coefficient were determined, which is a measurement of the association or correlation degree that exists between the data and the curve, opting for the one of bigger order. This coefficient varies between 0 and 1 and in the first case of the lineal trend, the association is almost non-existent and in the second case of trend the association is very significant.

Although the values for all the R^2 graphs are low, it is evident that the polynomial curve adjusts better than the lineal one and even more when increasing the quantity of the equation terms.

It is also significant that the polynomial trend is marked when the time scale increases and it can be appreciated that for every considered case, this trend decreases towards the end of the considered period for both localities, being that descent more marked for Ciudad del Este than for Encarnación as the time scale increases.

In order to detail this analysis, the frequency of the occurrence of droughts and excesses was calculated, according to the above mentioned categories.

The percentage frequencies for Ciudad del Este can be observed in the following tables (Tables 2, 3).

The estimation allows to observe that the higher percentages of occurrence are recorded for the Almost Normal category, increasing when the time scale of the SPI also increases.

The SPI–3 shows the highest percentage for a moderately humid condition (10,3) and for an extremely dry one (3,1); nevertheless, the occurrence of these periods is still very low.

The second highest percentages are observed in the Moderately Dry category for all the SPI for values raging between 14,5 and 10,8, being very little significant if compared with the main category.

Next, the percentage frequencies are presented for Encarnación through the following tables (Tables 4 and 5).

Although for this locality the series of pluviometric data is bigger (1951–2005), the obtained results do not vary much with respect to the previous locality.

The higher percentages of occurrence are still present in the Almost Normal category with values between 68,6 and 62,6 for all the considered SPIs.

The second highest percentages of occurrence are observed as similar in the Moderately Dry category and Moderately Humid for all the SPIs, for values between 9 and 12,8 as the highest percentage. Nevertheless, they are little significant compared to the main category and in this locality in particular, these values are distributed in a more uniform way between these two categories than in the previous case.

Next, the negative periods are analysed, considered as drought for the SPI, of the two localities and with a time scale of 3, 12 and 24 months for considering them as the most significant in those periods (figures 13-18)

Table 2

	SPI values	TIME SCALE (in months)					
		1	3	6	12	18	24
Extremely Dry	< –2	10	15	6	2	4	9
Very Dry	–1,99 to –1,5	27	15	21	18	27	31
Moderadately Dry	–1,49 to –1	52	39	50	68	49	32
Almost Normal	–0,99 to 0,99	324	324	311	309	317	322
Moderadately Humid	1 to 1,49	42	49	46	31	22	19
Very Humid	1,5 to 1,99	18	28	28	24	21	26
Extremely Humid	> 2	7	8	13	17	23	18
TOTAL		480	478	475	469	463	457

Table 3

	PERCENTAGES					
	SPI 1	SPI 3	SPI 6	SPI 12	SPI 18	SPI 24
Extremely Dry	2,1	3,1	1,3	0,4	0,9	2,0
Very Dry	5,6	3,1	4,4	3,8	5,8	6,8
Moderately Dry	10,8	8,2	10,5	14,5	10,6	7,0
Almost Normal	67,5	67,8	65,5	65,9	68,5	70,5
Moderately Humid	8,8	10,3	9,7	6,6	4,8	4,2
Very Humid	3,8	5,9	5,9	5,1	4,5	5,7
Extremely Humid	1,5	1,7	2,7	3,6	5,0	3,9

Table 4

	SPI Values	TIME SCALE (in months)					
		1	3	6	12	18	24
Extremely Dry	< –2	20	15	10	12	8	14
Very Dry	–1,99 to –1,5	25	26	24	24	21	28
Moderately Dry	–1,49 to –1	57	60	67	52	70	50
Almost Normal	–0,99 to 0,99	448	445	435	428	398	384
Moderately Humid	1 to 1,49	62	60	54	46	49	57
Very Humid	1,5 to 1,99	23	20	21	35	27	26
Extremely Humid	> 2	12	15	21	17	23	19
TOTAL		647	641	632	614	596	578

Table 5

	PERCENTAGES					
	SPI 1	SPI 3	SPI 6	SPI 12	SPI 18	SPI 24
Extremely Dry	3,2	2,4	1,6	2,1	1,5	2,7
Very Dry	3,9	4,2	3,9	4,1	3,8	5,4
Moderately Dry	9,0	9,6	11,0	9,0	12,8	9,6
Almost Normal	68,6	68,6	67,7	67,9	63,9	62,6
Moderately Humid	9,8	9,6	8,9	7,9	8,9	11,0
Very Humid	3,6	3,2	3,4	6,0	4,9	5,0
Extremely Humid	1,9	2,4	3,4	2,9	4,2	3,7

These negative SPIs are presented in a graph for each time scale and for both localities.

Later, the duration of the episodes is estimated without discriminating, that is to say, they are determined regarding the established categories, the quantity of consecutive months in which the SPI is negative.

These graphs contain the estimation of the negative SPIs for the three mentioned time scales.

The aim of this analysis is to complement and clarify the duration of the dry episodes exposed in the previous graphs.

In Table 6, the months and the times in which the SPI results negative in the considered series of data are shown.

It is observed that for the Negative SPI–3, 60 cases of drought are present for the considered series, being the duration of 1, 2 and 3 consecutive months of dry episodes the one which has a bigger quantity and it descends as the time periods increase.

For the Negative SPI–12 fewer cases of dry episodes are present –21 in total– recording more episodes as the time periods increase, which in this case are bigger than 10 consecutive months. However, these episodes very rarely take place. They stand out when a dry episode with several consecutive months of duration occurs, among them, the two periods of 18 consecutive months which extend from March 1985 to August 1986 and from February 1988 to July 1989. In three occasions, periods of 26 consecutive months occurred in dry episodes such as the one from December 1966 to January 1969, the one from September 1980 to October 1982 and the one from November 2003 to December 2005. At the same time, it is important to highlight the longest period of dry episodes for this time series from November 1975 to April 1979, which comprises 42 consecutive months of negative SPI.

Figure 13. Ciudad del Este SPI–3 (negative)
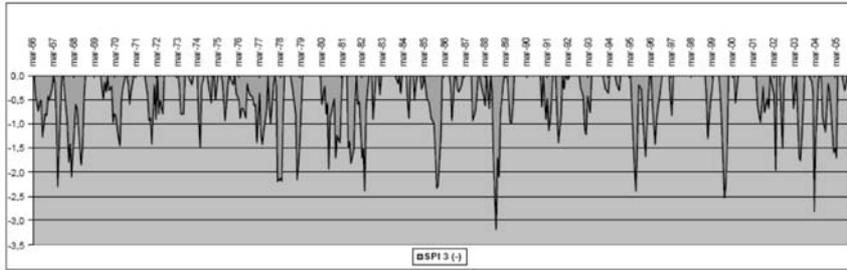
Figure 14. Encarnaciòn SPI–3 (negative)
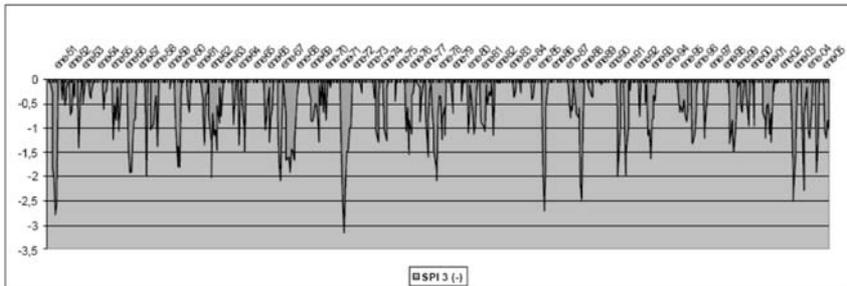
Figure 15. Ciudad del Este SPI–12 (negative)
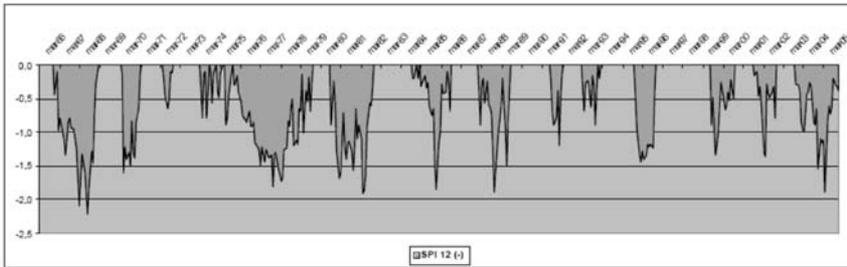
Figure 16. Encarnaciòn SPI–12 (negative)
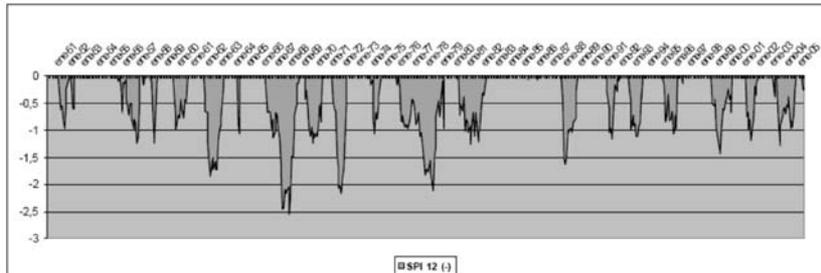
Figure 17. Ciudad del Este SPI-24 (negative)
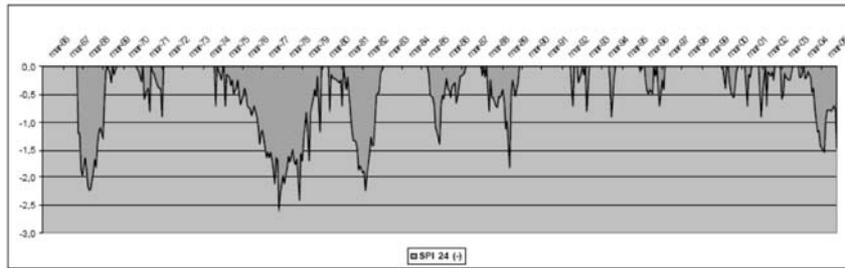
Figure 18. Encarnaciòn SPI-24 (negative)
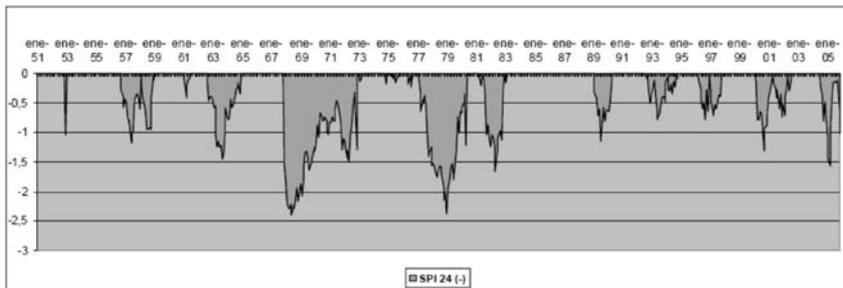
Table 6

Ciudad del Este – Duration of the Drought Periods																			
SPI	Cases	Months																	
		1	2	3	4	5	6	7	8	9	10	12	13	14	18	20	22	26	42	56
3	60	12	11	13	5	5	4	2		3	2	2			1					
12	21	2	1	2	3		1		2			2	1	1	2			3	1	
24	32	10	3	5	2	3		2		1					2	1	2			1

For the Negative SPI-24, 32 cases of dry episodes are observed, concentrating the biggest quantity in a one–month period with a total of 10 months. The longest period of the series is from May 1975 to December 1979 with 56 consecutive months, where the SPI is recorded as negative.

In the following table (Table 7), the months and times in which the SPI results negative in the series of data for Encarnación are shown.

It is observed that for the Negative SPI-3, 69 cases of drought were present for the considered series, being the duration of 1 and 3 consecutive months of dry events the one with higher quantity. It practically disappears as the time periods increase, recording only one time and period of 18 consecutive months of SPI, which comprises from August 1977 to January 1979.

For the Negative SPI-12 fewer dry events are present–33 in total– recording a bigger uniformity in their distribution regarding quantity. However, these events are very occasionally present, being the biggest quantity of episodes one month, with 8 cases during the series. The longest period of dry episodes of this time series is from June 1976 to September 1979 and comprises 40 consecutive months of negative SPI.

For the Negative SPI–24, 24 cases of dry episodes are observed, concentrating the biggest quantity in a one–month period with a total of 9 times. Two important periods of dry episodes

Table 7

SPI	Cases	Months																								
		1	2	3	4	5	6	7	8	9	10	11	12	13	14	15	16	17	18	21	22	24	25	28	29	40	59
3	69	15	7	13	8	5	2	5	3	4	1	1	4						1								
12	33	8	5	2			1			2	1	1	1	2	1	1	1	1	2	1		1		1	1		
24	24	9			1	1	2			1							1	1	1	1		1	1		1	1	1	1

Encarnación – Duration of the Drought Periods

in the series stand out, which comprise from January 1977 to April 1980 with a quantity of 40 consecutive months and from December 1967 to October 1980 with a quantity of 59 consecutive months, where the SPI is recorded as negative.

Finally, the magnitude of these dry episodes is determined, which according to McKee et al (1993) can be defined as the sum of the SPIs of the considered period.

In this sense, the biggest periods of consecutive months with negative SPI were taken, being the period of 42 and 56 months for Ciudad del Este and the two periods of 40 and the one of 59 months for Encarnación.

The magnitude of these periods and their average are shown in Table 8:

Table 8

Periods	Magnitude	Average
Ciudad del Este		
42 (SPI–12 negative)	–42,82	–1,02
56 (SPI–24 negative)	–65,83	–1,18
Encarnación		
40 (SPI–12 negative)	–39,07	–0,98
40 (SPI–24 negative)	–48,89	–1,22
59 (SPI–24 negative)	–76,83	–1,30

It can be observed that the average for these periods of considered dry episodes fluctuates within the category of the SPI corresponding to Moderately Dry.

5. Conclusions

The establishment of the SPI through the SPI_SL_6 programme with data of precipitation of two meteorological stations of the Meteorological Service of Paraguay situated in the localities of Ciudad del Este and Encarnación has proven to be an indicator of meteorological droughts suitable for the identification and monitoring of the dry episodes in Paraguay.

The obtained results in this project can be considered for other regions of the country. However, according to the consulted bibliography, some inconveniences can arise in regions with markedly seasonal systems in precipitation.

Although they have not been analysed in this study, the SPI identifies the humid episodes with the same importance than the droughts, becoming a very useful tool for their monitoring.

When applied to the considered series of precipitation for these two stations, it enabled to visualise a descendant polynomial trend towards the end of the series for the two stations. Ciudad del Este presents a much more pronounced descent than Encarnación as a bigger time scale is taken into account. Besides, this trend model is the one with the highest adjustment of data.

It was also determined for the two stations the frequency, duration and magnitude of the SPIs, finding that the frequency of the events corresponds to the Almost Normal category. Nevertheless, their duration allowed to establish the highest concentration of consecutive months with drought in the range between 1 and 3 months, observing the existence of very long periods where the SPI was negative from 18 to 59 consecutive months, but it does not exceed 3 occurrences in the considered series. Regarding its magnitude, it was determined for these long periods and it was observed that the one for these dry episodes is very big, recording an average in the Moderately Dry category of the SPIs estimated with this methodology.

This chosen indicator to determine meteorological droughts provides good services and has been very useful in this first approach to the studies of these events in Paraguay, where up to the present time no projects have been done in this respect, turning it into a positive contribution with extrapolation possibilities to other regions of the country.

Due to its simplicity for estimation and interpretation, the SPI has a high implementation potential in an operative way by the Meteorological Service of Paraguay for regions of interest and, eventually, for all its national territory.

References

Keyantash J. and Dracup J.A. (2002). The quantification of drought: an evaluation of drought indices. *Bulletin of the American Meteorological Society*, 83(8):1167–1180.

Komuscu A.U. (1999). Using the SPI to analyze spatial and temporal patterns of drought in Turkey. *Drought Network New*, 11(1): 7–13.

Makarau P. (1992). Drought, desertificaction and their mitigation technology in the world. Report of the CCL Repporteur on Drought and Desertification to the Eleventh session of the Commision of Climatology. In: Lapinel Pedroso B. and Planos Gutiérrez E., *Visión de la Sequía en Meso América y El Caribe: Diagnóstico, Impactos y Mitigación*", <http://www.met.inf.cu/sequia/paginas/contribuciones.html>.

Mckee T. *et al.* (1993). *The relationship of drought frequency and duration to time scales*. Preprints 8th Conference on Applied Climatology, California.

Núñez S. *et al.* (2005). El índice estandarizado de precipitación como herramienta para la caracterización y el monitoreo de la sequía: una prueba de concepto. Abstract submitted to Congremet IX, 9th Argentine Congress of Meteorology, Buenos Aires, Argentina, 3-7 October.

Panofsky H. and Brier G.W. (1958). *Some Applications of Statistics to Meteorology. Earth and Mineral Sciences Continuing Education, College of Earth and Mineral Sciences*, The Pennsylvania State University, University Park, Pennsylvania.

Sazonov. B.J. (1989). *Lucha contra los efectos de la sequía. Informe del ponente sobre sequía y Desertificación en los climas fríos*. Organización Meteorológica Mundial. Comisión de Climatología, Décima Reunión, Lisboa, Abril de 1989. In: Lapinel Pedroso B. and Planos Gutiérrez E., *Visión de la Sequía en Meso América y El Caribe: Diagnóstico, Impactos y Mitigación*, <http://www.met.inf.cu/sequia/paginas/contribuciones.html>.

AN INVESTIGATION OF VARIATION IN VEGETATION CANOPY WITH HEMISPHERICAL PHOTOGRAPHY AND SATELLITE DATA

Ebenezer Yemi Ogunbadewa
School of Environment and Life Sciences
University of Salford
United Kingdom

Tutor: Prof. H. Ribeiro Da Rocha
Department of Atmospheric Sciences
Universidade de São Paulo
Brasil

1. Introduction

Understanding the impact of climate change on natural and agricultural ecosystems requires an insight into a number of ecophysiological processes in vegetation canopies such as photo-synthesis, evapotranspiration, and respiration (Gower *et al.* 1999). The knowledge about these processes can be understood better by estimation of vegetation biophysical parameters that are indicators of change; these estimations can be made through ground-based measurements of leaf area index (LAI) and by deriving a normalized difference vegetation index (NDVI) from satellite remote sensing data.

1.1   USLE Model Application

1.1.1 Ground based measurement

The leaf component as a quantitative biophysical property of vegetation can be estimated on the ground by its structural attribute of leaf area index (LAI). Leaf Area Index is defined as the one-sided leaf area per unit ground area (Chen and Black 1992). The ratio of leaf surface area to unit ground cover is an integrative measure of carbon and water balance in plants, it describes the potential surface area available for leaf gas exchange, it can be correlated with net primary production (NPP), gross primary production (GPP) and evapotranspiration because changes in LAI indicates changes in the whole-plant photosynthetic activity and canopy-level compensatory response to climate change. Any research concerning the response of vegetation to climate change therefore requires reliable LAI estimations (Gower *et al.* 1999).

The techniques of LAI estimation are broadly categorized into direct methods and indirect methods. Examples of direct methods include destructive sampling, litter-fall collection, allometric techniques and inclined point quadrat technique.

Destructive sampling cannot preserve canopy properties; it is labour intensive, often impracticable in some inaccessible areas and requires numerous safety precautions (Chason *et al.* 1991). Litter-fall collections are slow, and they depend on the longevity of individual foliage. It is not compatible with long-term monitoring of spatial and temporal dynamics of leaf area development for evergreen forests where the litter-fall may be only weakly related to new growth. The litter traps are not accurate measurements for species that can replace their leaves during the growing season, such as for example poplars (Law *et al.* 2001). For instance, the inclined point quadrat technique requires a large number of insertions of needles at least 1000

in order to obtain a reliable assessment, and it is difficult to implement in tall vegetation types, particularly in canopies higher than 1.5 m. Allometric equations require knowledge of sapwood area/leaf area relationships; it is stand–specific and dependent on season, site fertility, local climate, and canopy structure (White *et al.* 1997). All direct methods have very limited spatial extent, and in particular, they may not be suitable for regional studies and temporal sampling is often infeasible (Table 1).

In contrast to direct methods, indirect techniques are based on the measurement of light transmittance through gap fraction of plant canopy to derive LAI (Table 2). It allows rapid and low-cost measurements (Pierce and Running 1988).

A major limitation of the gap fraction–based approach is that it does not distinguish photosynthetically active leaf tissue from other plant elements such as stem, branches or flowers or dead non–photosynthetic material and clumpiness.

Hemispherical photography method has the advantage of being able to differentiate between leaves and other plant elements. It can be used to perform other biophysical measurements, for example, fractal dimension, architecture and light regime below the canopy (Beaudet and Messier 2002). Hemispherical photography method may overcome the shortcomings of direct and indirect techniques because of advances in digital colour photography, software development and computer technologies that allow LAI to be derived with reasonable result when compared with existing measurement. Hemispherical photographs were used in this study because it is non destructive, simple, cheap, preserves canopy structure in terms of pictures, provides fast and instantaneous measurements of LAI in a wide range of daylight conditions, and does not require high computer resources to get the desired result.

Table 1. Direct methods estimating leaf area index (LAI)

Direct Methods	Description
Destructive sampling.	Involves physical contact with canopy elements and destructive harvesting of all or part of canopy by sampling.
Litter-fall collection.	The collection of all or part of canopy litter or use of litter traps.
Allometric techniques.	Based on correlation coefficients derived from relationships between leaf area and plant element carrying the green leaf.
Inclined point quadrat technique	Determination of LAI by piercing vegetation canopy with a long thin needle (point quadrat) or laser ray or fibre optics probe or plumb bob based on radiation penetration model equations.

Table 2. Indirect methods estimating leaf area index (LAI)

Indirect Methods	Description
SunScan	Gap fraction or sunflecks are used to measure direct and diffuse PAR 64 PAR-sensors distributed along a 1-m rod to estimate LAI.
AccuPAR	Gap fraction or sunflecks are used to measure total PAR 80 PAR-sensors distributed along a 0.90-m rod to estimate LAI.
LAI-2000	Gap fraction for each zenith angle is acquired simultaneously with diffuse blue light to estimate LAI.
DEMON	Gap fraction zenith angles from the sun at different angles to the vertical direct sun beam are used to estimate LAI.
Hemispherical photography	Gap fraction is estimated using photographs with hemispherical (fisheye) lens from beneath the canopy or placed above the canopy looking downward.
Tracing Radiation and Architecture of Canopies (TRAC).	LAI is estimated by using transmitted PAR and sunfleck length to determine sunlit foliage area and separates leaves from bark.

1.1.2 Remote sensing and vegetation change

Remotely sensed data has become an important tool in the studies of spatio-temporal variations of structural and functional attributes of vegetation by derivation of various vegetation indices (Jacquemoud *et al.* 2000). The vegetation signal of reflected energy in the visible spectrum is very low as a result of high absorption by photosynthetically active pigments with maximum sensitivity in the blue (470 nm) and red (670 nm) wavelengths. Nearly all of the near–infrared radiation is scattered (reflected and transmitted) with very little absorption, in a manner dependent upon the structural properties of a canopy (LAI, leaf angle distribution, leaf morphology). As a result, the contrast between red and near-infrared responses is a sensitive measure of vegetation amount, with maximum red and near-infrared differences occurring over a full canopy and minimal contrast over targets with little or no vegetation. For low and medium amounts of vegetation, the contrast is a result of red and near-infrared changes, while at higher amounts of vegetation only the near-infrared contributes to increasing contrasts as the red band becomes saturated due to chlorophyll absorption.

Remote sensing data are usually transformed into the vegetation indices derived from spectral reflectance signatures of leaves resulting in the development of many vegetation indices (Table 3).

NDVI is most commonly used to indicate green leaf biomass and LAI because it is a simple, fast and convenient method for identifying vegetation changes (Tucker *et al.* 1995). NDVI can be expressed mathematically as follows:

NDVI=(NIR–RED)/ (NIR+RED)

Table 3. Types of vegetation indices

Vegetation indices	Description
Simple Ratio (SR).	The ratio of Near-Infrared/Red bands. SR has infinite range.
Normalized Difference Vegetation Index (NDVI).	The ratio of the difference between the Near-Infrared and Red a band by their sum. It eliminates effects of broad-band Red – Near-Infrared albedo through normalization. NDVI values ranges from–1 to +1.
Perpendicular Vegetation Index (PVI).	These non-ratio vegetation indices utilize a soil line concept for site specific background corrections, which are a baseline value of zero vegetation over a wide brightness range of soil backgrounds from which vegetation can be measured in Near-Infrared space, relative to the baseline.
Infrared Perpendicular Vegetation Index (IPVI).	Assumes that only the sum of Near-Infrared and Red is the important use of the red band in the NDVI.
Renormalized Difference Vegetation Index (RNDVI).	Combines the advantages of linearlizes the relationships with surface parameters that are nonlinear.
Modified Simple Ratio (MSR).	An improvement on RNDVI by linearlizing the relationship between RNDVI and biophysical parameters.
Soil-Adjusted Vegetation Index (SAVI).	Includes a canopy background adjustment factor using narrow band in minimization of soil optical properties on vegetation reflectance.
Modified Soil-Adjusted Vegetation Index (MSAVI).	An improvement on SAVI using hyperspectral band.
Modified Soil-Adjusted Vegetation Index (MSAVI).	An improvement on SAVI using hyperspectral band.
Soil and Atmospherically Resistant Vegetation Index (SARVI)	Uses corrected red radiance for aerosol effect by incorporating the blue channel. Minimizes canopy background and atmospheric effects.
Global Environment Monitoring Index (GEMI).	Minimizes atmospheric effects specific to AVHRR data sets.
Enhanced Vegetation Index (EVI).	Uses the atmospheric resistance concept (blue/red) in the enhanced VI (EVI) to aid with highly variable aerosol conditions, such as smoke from biomass burning.

Where RED and NIR represent the spectral reflectance measurements acquired in the red and near–infrared regions. These spectral reflectance are themselves ratios of the reflected over the incoming radiation in each spectral band individually, NDVI values vary between –1 and +1: –1 indicates no vegetation while +1 indicates dense vegetation canopy.

NDVI temporal variations are related to the seasonal changes in the amount of photosynthetic tissues, it increases when the vegetation greens up in spring and decreases when the vegetation changes colour in autumn (Huete *et al.* 2002). However, NDVI have been known to correlate reasonably well in medium to low vegetation abundance with various biophysical parameters such as LAI or green leaf biomass, but in certain environments specific types of changes in vegetation may not be accurately depicted by NDVI. This is because of the inherent non–linearity in the relationships between vegetation abundance and ratio based indices. There is an asymptotic (saturated) signal once NDVI reaches a threshold level over high biomass (complex forest structures) conditions, mutual shadowing in mature stands, aging forests may show a decrease in NDVI while actual biomass increases. The correlation between LAI and NDVI is generally strong enough to accurately predict LAI levels between 3.0 to 4.0; however the estimation becomes problematic when the LAI is over 4 (Baret and Guyot 1991). In practice, LAI prediction from remotely sensed data faces two major difficulties; there is no unique relationship between LAI and a VI of choice, but rather a family of relationships, each a function of chlorophyll content and/or other canopy characteristics (Jacquemoud *et al.* 2000). The problem of saturation is being addressed by the current generation of satellite instruments, such as the MODIS–enhanced vegetation Index (EVI) data product; it does not become saturated as easily as the NDVI when viewing rainforests and other areas of the Earth with large amounts of chlorophyll. The EVI is more responsive to canopy structural variations including leaf area index (LAI), canopy type, plant physiognomy, and canopy architecture, but coarse spatial resolution of 1km of EVI data restricts its wide usage (Huete *et al.* 2002).

Monitoring vegetation change using NDVI data is also faced with the problem of trade–offs between the spatial and temporal resolution of satellite image data because fine spatial resolution data are generally only recorded a few times each year and in cloudy regions; it may not be possible to get a cloud free image for the whole year. Medium to low spatial resolution data may be recorded more frequently but may be more difficult to interpret for local scale application.

Despite the drawback, NDVI is still the most widely used VIs and its relationships with vegetation parameters have been established for a wide variety of ecosystems. This is, in part, due to its rationing properties, which enable the NDVI to cancel out a large proportion of signal variations attributed to calibration, noise, and changing irradiance conditions that accompany changing sun angles, topography, clouds/shadow and atmospheric conditions (Huete *et al.* 2002). The MODIS–NDVI data product is used in this study because it has high temporal resolution of 1–2 days, spatial resolution of 250m and is available free of charge.

1.2   Aims of the research

This research is aimed at estimating LAI with hemispherical photography and extracting NDVI data from Moderate resolution imaging spectroradiometer (MODIS) satellite sensor in sugarcane plantation, eucalyptus and cerrado vegetation canopies in Sao Paulo State of Brazil.

2. Study sites

The study sites are a sugar cane (*Saccharum officinarum*) plantation; eucalyptus (*Eucalyptus saligna*) and cerrado (*woodland-savanna*) with dominant tree *Tabebuia chrysantha* as ipê–*amarelo* in Sao Paulo State of Brazil. The sugarcane plantation is situated at latitude 21^0 38'13.4"S and lon-

gitude 47^0 47' 24.9"W in flat terrain of about 700m above the sea level. The sugarcane plants are planted closely to each other in a row of 1m apart while the height varies from plot to plot (2 to 5m) according to ages and time of planting. Eucalyptus is situated at latitude 21^0 35'0.6"S and longitude 47^0 36' 8.3.9"W in flat terrain also 700m above the sea level. These trees are planted in row of 3m and space of 2m, and their heights and diameter vary from 6 to 30m and 0.18 and 0.4m respectively. Cerrado is situated at latitude 210 37'10.1"S and longitude 470 38' 59.69"W is a close canopy. They were chosen to represent contrasting vegetation canopies, ranging from evergreen to woodland to agricultural ecosystem.

## 3. Description of methods

3.1   Hemispherical photography

Hemispherical photography was used in this study with the aim of planning field campaign strategies and testing the efficacy of hemispherical photography in the estimation of LAI. To achieve this aim the following objectives were set.

Using Canon camera with locally developed fisheye lens and the data processed with FV2000, Hemisfer with Canopix software and Interface Definition Language (IDL) programme with application of clumping factors of 0.70 0.80 0.90 1.00.

Using Nikon DX 40 camera with fisheye lens from the manufacturer and the data with Interface Definition Language (IDL) programme.

The first experiment was carried out with intensive measurement for 10 days from 21st of May to 31st of May, 2007 in eucalyptus and cerrado vegetation canopies. 250 pictures were taken with the Canon camera using locally made fisheye lens and 180 pictures were selected (Figure 1).

Figure 1. Hemispherical photographs

| Canon camera | | Nikon DX 40 camera |
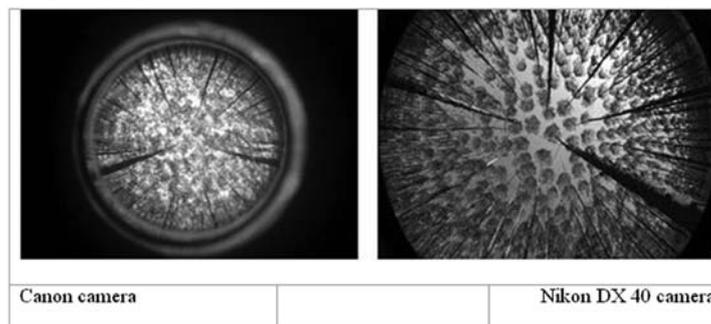
The second experiment was carried out on 10th and 11th of October, 2007 with a Nikon DX 40 camera using fisheye lens from the manufacturer and data processed with IDL programme. 180 pictures were taken with Nikon DX 40 with cropped frame of the camera lens at the angle of 1800 on a tripod of 1m high and 160 (see Figure 2).

The digital photographs were processed using Adobe Photoshop by changing the image format from jpg to bmp and reducing the image size to width of 640 and height of 426 pixel resolution. Images were then adjusted using a channel mixer by changing the pictures from coloured to monochrome (black and white) before deriving the LAI values using the IDL programme.

Figure 2. Field experiment with fisheye lens Nikon DX 40 camera

Figure 3. Moderate Resolution Imaging Spectroradiometer (MODIS)-NDVI data

3.2   *Moderate Resolution Imaging Spectroradiometer (MODIS)*

The Moderate Resolution Imaging Spectroradiometer (MODIS) 250-m NDVI 16-day product was used in this study and 134 NDVI data sets for year 2001 to 2006 were downloaded from National Aeronautics and Space Administration (NASA) websites (http://modis.gsfc. nasa.gov/) while 4 data sets were missing (2 each for the year 2001 and 2003). The data set were re-projected for geometric correction with MODIS Re-projection Tool (MRT). Corrected to UTM zone 23 of Brazil and imported into Erdas Imagine software for extraction of NDVI values (see Figure 3).

There are some problems with MODIS 250-m NDVI 16-day product, this includes removal of the data from the File Transfer Protocol (FTP) after 24hrs by the provider (NASA) even when downloading is underway, the large size of 0.5 Gigabyte requires large computer space and memory for storage and processing. The data requires re-ordering and re-downloading of the same file repeatedly due to the fact that at most times the files get corrupted easily, when copying to CD or DVD it is more likely to become even more affected.

4. *Results*

The LAI results of the first experiment were not so good, even after selection of the pictures that were not affected by the reflections from aluminium around the lens when the data were processed with software (FV2000, Hemisfer with Canopix and IDL programme). However, when clumping factors of 0.70, 0.80, 0.90, and 1.00 were applied to the IDL programme the results conform to the existing LAI indirect measurement in the similar vegetation canopies in Brazil (see Figure 4 and 5). In eucalyptus plantation, the mean ranged from 2.79 to 3.98 with standard deviation that ranged from 1.57 to 2.25. In cerrado plantation, the mean ranged 1.31 to 0.92 and the standard deviation ranged from 0.62 to 0.88. The mean varies according to the clumping factors applied; the lower the clumping factor the higher the LAI and standard deviation.

The second experiment was more promising as the result of the new camera and IDL processing programme. The aim was to test the variation of LAI with height using hempherical photography in eucalyptus and sugarcane. Trees with height of 6m, 20m and 30m were chosen in eucalyptus while 2m and 5m were used for sugarcane, the mean LAI results ranged from

Figure 4. Mean estimated Leaf Area Index values in eucalyptus using hemispherical photography (n = 90 standard deviation)
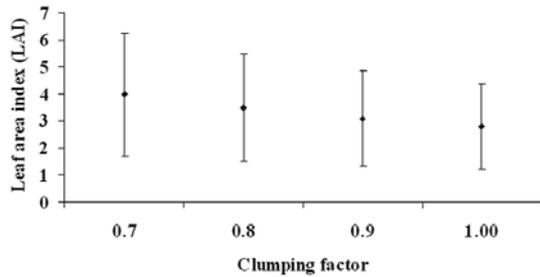
Figure 5. Mean estimated leaf area index values in cerrado using hemispherical photography (n = 90 standard deviation)
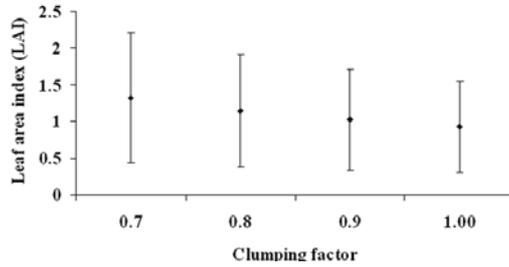
Figure 6. Leaf area index in eucalyptus (n = 90 standard deviation)
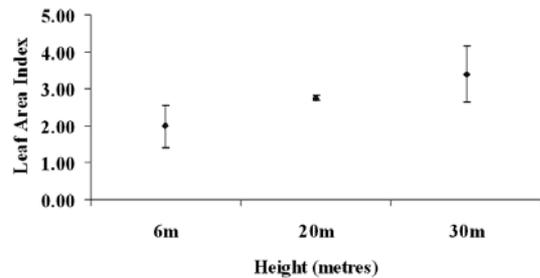
Figure 7. Leaf area index in sugarcane (n = 90 standard deviation)
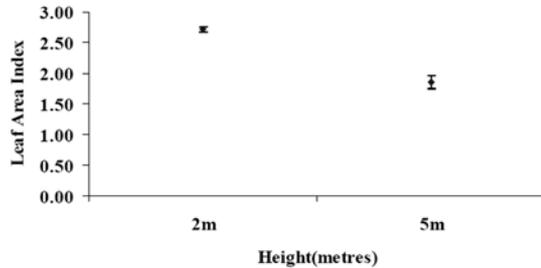
Figure 8. Normalized vegetation index (NDVI) in sugarcane
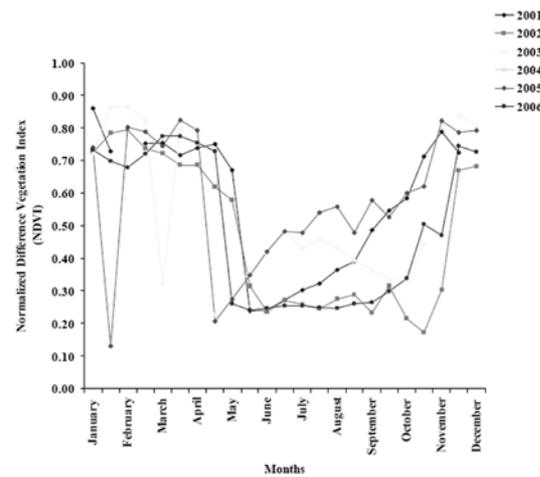
Figure 9. Normalized vegetation index (NDVI) in eucalyptus
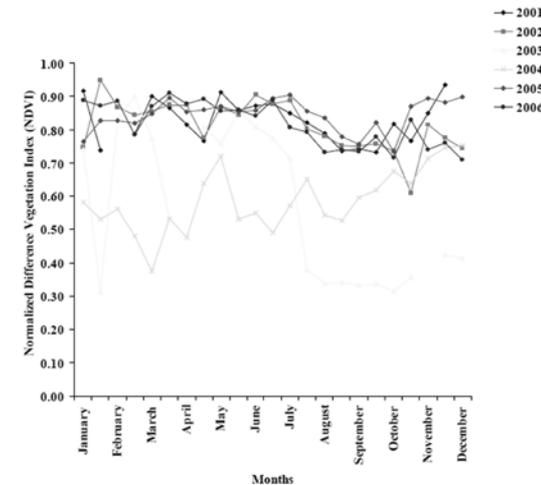
1.98 (6m) to 3.40 (30m) in eucalyptus and 2.71 (2m) and 1.84 (5m) in sugarcane. The standard deviation for eucalyptus ranged from 0.57 to 0.76 for sugarcane 0.03 to 0.10. LAI was derived for different heights and the results show that LAI varies with height (see Figure 6 and 7).

Figure 10. Normalized vegetation index (NDVI) in cerrado
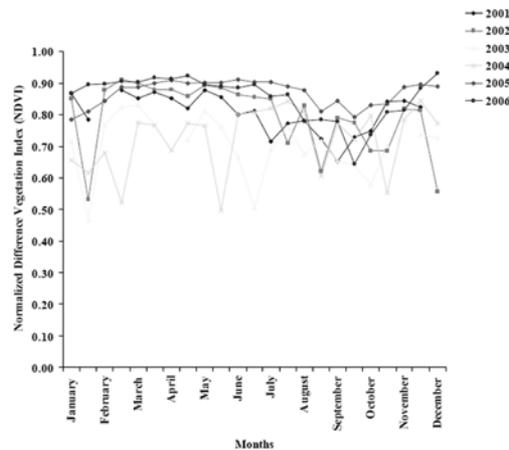
The NDVI values were extracted from 2001 to 2006 for sugarcane, eucalyptus and cerrado (see Figure 8, 9 and 10). Sugarcane NDVI indicates the harvesting period April, May and June, and the re-growth pattern from harvesting until December when this vegetation index usually stabilizes. June seems to be the harvesting planting period because the growth rate is increasing at a steady state from June. Low values were for January and December this may be due to irrigation in 2002 and 2005 November and January. For eucalyptus and cerrado the vegetation cover indicates stability except for the year 2003 which is very low; these anomalies this may be due to clearing, forest fire, and drought or plant disease. But by the year 2004 there is re-growth which may be due to reforestation.

5. Conclusion

The result of this study shows that hemispherical photos processed with IDL program, give good results in estimating LAI, in particular when clumping factor is applied to the photos from the Cannon camera with locally made lens. The NDVI data from the MODIS satellite sensor offers a very rapid method of retrieving vegetation change information when there has been no ground data available or it has been insufficient in the study area. Also the NDVI result appeared to be realistic for regional application.

It is not possible to relate ground based LAI to MODIS–NDVI in this study because satellite data were not available during the time of the experiment. Finally the results of this investigation can be incorporated into the current work on climate change and surface-vegetation models research group in the Universidade de São Paulo, Brazil.

members of the Laboratório de Clima e Biosfera in the Universidade de São Paulo, Brazil, for their cooperation during his stay in Brazil Mr Osvaldo M R Cabral and Mr Marcos V. Ligo (Embrapa Meio Ambiente) for providing Nikon DX 40 camera for the field experiments. Finally thanks to Prof M Bindi Coordinator of ICONE project and staff.

References

Baret F. and G. Guyot (1991). Potentials and Limits of vegetation indices for LAI and APAR assessment. *Remote Sensing of Environment*, 35:161-173.

Beaudet M. and Messier C. (2002). Variation in canopy openness and light transmission following selection cutting in northern hardwood stands: an assessment based on hemispherical photographs. *Agriculture and Forest Meteorology*. 110: 217-228.

Chason J.W., Baldocchi D.D., Huston M.A. (1991). Comparison of direct and indirect methods for estimating forest canopy leaf-area. *Agriculture and Forest Meteorology*. 57: 107-128.

Chen J.M. and Black T.A. (1992). Measuring leaf-area index of plant canopies with branch architecture. *Agriculture and Forest Meteorology*, 57: 1-12.

Gower S.T., Kucharik C.J. and Norman J.L. (1999). Direct and indirect estimation of leaf area index, fAPAR, and net primary production of terrestrial ecosystems. *Remote Sensing of Environment*. 70: 29–51.

Huete A., Didan K., Shimabukuro Y.E., Batana P., Saleska S., Hutyra L. *et al.* (2002). Amazon rainforests green–up with sunlight in dry season. *Geophysical Research Letters*, 33, p. L06405

Jacquemoud S., Bacour C., Poilvé H. and Frangi J.-P. (2000). Comparison of four radiative transfer models to simulate plant canopies reflectance – direct and inverse mode. *Remote Sensing of Environment*, 74: 471-481.

Law B.E., Cescatti A., Baldocchi D.D. (2001). Leaf area distribution and radiative transfer in open–canopy forest: implications for mass and energy exchange. *Tree Physiology*. 21: 777-787.

Pierce L.L. Running S.W. (1988). Rapid estimation of coniferous forest leaf area index using a portable integrating radiometer. *Ecology*, 69: 1762-1767.

Tucker C.J., Slayback D.A., Pinzon J.E., Los S.O., Myneni R.B. and Taylor M.G. (1985). Higher northern latitude normalized difference vegetation index and growing season trends from 1982 to 1999. *International Journal of Biometeorology*, 45: 184-190.

White M.A., Thornton P.E. and Running S.W. (1997). A continental phenology model for monitoring vegetation responses to interannual climatic variability. *Global Biogeochemical Cycles*, 11: 217-234.

CHARACTERIZING DROUGHT EVENTS IN CUIABÁ, MT, BRAZIL, WITH STANDARD PRECIPITATION INDEX (SPI)

Indriati Ilse Nangoi
Department of Atmospheric Sciences
Universidade de São Paulo
Brasil

Tutor: Prof. Simone Orlandini
Department of Agronomy and Land Management
University of Florence
Italy

1. Introduction

Drought phenomena occur in all the geographic regions of Brazil. Besides of the regular events which mainly occur in the north–eastern Region of the country, sporadic occurrences have also been harmful in central–western Region, where they have a strong impact in agriculture. During the drought event of 2005/2006, this sector lost about 135 million reais, something like about 64 million dollars, only in this region (AEN 2008). In the Southern Region, it was considered the worst drought occurrence of the last fifty years (Aguiar 2005).

Recently, in many countries, the damages caused by these phenomena have highlighted the vulnerability of the society towards this hazard. The secretary–general of World Meteorological Organization, Mr. M. Jarraud, in the foreword of the book «Natural disasters and extreme events in agriculture» (Sivakumar 2005), declared that the growing concern with the possible impact of natural disasters and extreme events on agriculture and forestry has created new demands of information that should be provided by agrometeorologists. Both the need of reorienting meteorological information (fine–tuning of climatic analysis), the way of presentation of the problem which could be suitable for agricultural decision–maker and helpful to marginal farmers in order to cope with the adverse impact of natural disasters and extreme events, were becoming more and more pressing.

An United Nations Development Program (UNDP) report states that drought is the most complex and less known natural hazard, which affects more people than any other disaster (UNSO 1999). Since it is a creeping event, it is difficult to identify its onset and its ending time. This climatic hazard occurs in almost every region of the world. Its consequences concern physical suffering, economic losses, and environmental degradation. Costs amount and misery increment caused by drought events are more than those one which occur after typhoons, earthquakes, and all other sudden climatic hazards (Mavi and Tupper 2004). A survey concerning with agriculture extreme weather and climate events impacts reports the hazards assessed by most of the 57 countries around the world and includes drought (91 per cent), local severe storms (83%), floods (79%), frost (74%) and high winds (72 %) (Sivakumar 2005).

Within all the Brazilian regions, various are the definitions given to drought; the most accepted is «the period, normally about month or years, in which the rainfall decreases considerably out of the expected» (Palmer 1965). On the other hand, considering the huge variability of this phenomenon, for Mckee *et al.* (1995), none valid definition of drought can be given for all regions and for all activities.

Drought can be classified as a meteorological, hydrological, agricultural and socioeconomic event (Byun and Wilhite 1999). The agricultural drought occurs when soil moisture is not

enough to meet the needs of the crops at a particular time, while the hydrological drought refers to surface and subsurface water supplies deficit (Mavi and Tupper 2004). All definitions include meteorological aspects which have to be characterized by their beginning and ending time. Definitions of meteorological drought must be considered at a regional scale since the atmospheric conditions that result in precipitation deficit are highly variable from region to region. For example, some definitions of meteorological drought identify periods of drought on the basis of the number of days with precipitation, while other drought events terms use fixed thresholds (NDMC 2006).

For this reason, some drought indexes (for example, the Standardized Precipitation Index – SPI) were created in order to allow the comparison of two climatic different regions through the analysis of drought occurrences intensity.

The SPI is recommended as a drought index because it is simple, spatially consistent (invariant) and probabilistic, therefore it can be used in risk and decision analysis, and linked to specific periods according to the user's interest (e.g., three months for the life of a crop, or several years for the water storage) (Guttman 1998). The SPI index is probability based and was designed to be a spatially invariant indicator of drought since it recognizes the importance of time scales in the analysis of water availability and water use (Guttman 1999).

Within this context, the objective of this project is the characterization of drought occurrences in Cuiabá, state of Mato Grosso (Brazil) and their impact on agriculture. the SPI index has been therefore analyzed in order to give an effort to the mitigation of drought impacts also in other states. The selected region has been considered as a case study area, and the reaction of one of the most important crop for the region, the soybean, has been studied.

2. Material and methods

2.1 Climatic Series Analysis

Daily rainfall data used in this study were provided by the Agência Nacional of Águas (ANA) for Cuiabá (15.4°S; 56.2°W; 240m) and Mato Grosso State (Brazil). The dataset referrers from 1972 to 2006 year. According to Köepen classification, the region of study is classified, as wet and dry tropical climatic area (Aw).

The Standardized Precipitation Index (SPI) was utilized to measure the intensity of a drought event.

The analysis of a possible existence of a trend in the series was carried out using the sequential Mann-Kendall test and its results were compared to those one obtained with the SPI index, considering 35 years.

The test was applied to the series from 1972 to 2006 for each month and each season of the year.

A sequential Mann-Kendall test was calculated under the statistical software R. The software SPSS, that gives predictive analyses, was also used to confirm a probable series trend.

2.2 Standardized Precipitation Index (SPI)

The Standardized Precipitation Index (SPI) is a relatively new drought index based only on precipitation data. It is simply the difference of precipitation from the precipitation mean referred to a specific period divided with precipitation standard deviation, where the mean and standard deviation are determined from past records (Mackee 1993).

The SPI can be used to monitor conditions on a variety of time scales. This temporal flexibility allows the SPI to be useful in both short-term agricultural and long-term hydrological

Table 1. SPI Classes (Mckee *et al.* 1993; Guttman 1999)

SPI value	Moisture category
≥ 2.0	Extremely wet
1,5 to 1.99	Very wet
1.00 to 1.49	Moderately wet
0 to –0.99	near normal (mild)
–1.00 to –1.49	Moderately drought
–1.50 to –1.99	Severely drought
≤ –2.00	Extremely drought

applications. The SPI index considers all the impacts that a precipitation deficit can occur on the groundwater, reservoir storage, soil moisture, snowpack, and stream flow.

Mathematically, SPI index corresponds to the cumulative probability of a certain precipitation event to happen in a determinate station. The standardized precipitation computational result is linearly proportional to the deficit of accumulated precipitation (Mavi and Tupper 2004). A classification system is used to define drought intensities resulting from the SPI index application (Table 1).

The Standardized Precipitation Index (SPI) was used to calculate the intensity of dry events and to identify drought occurrences. The SPI index quantifies precipitation deficits and surplus in different time scales, therefore it is useful within various hydrological availability studies. An event is defined as drought when the SPI value is equal or smaller than –1.0. A drought event starts up when SPI value is negative and ends when SPI turns back to positive values (McKee *et al.* 1993).

The SPI index computing includes the fitting of a gamma probability density function to a given frequency distribution of the overall precipitation for a specific climate station. First, the incomplete gamma distribution is calculated with the non-zero values, defined by its probability density function (Figure 1):

Figure 1

$$G(x) = \frac{1}{\Gamma(\alpha)} \cdot \int_0^x t^{\alpha-1} \cdot e^{-t} \cdot dt$$

$$\alpha = \frac{1}{4 \cdot A}\left(1 + \sqrt{1 + \frac{4 \cdot A}{3}}\right)$$

$$\beta = \frac{\bar{x}}{\alpha}$$

where alpha and beta parameters of the gamma probability density function are estimated by the maximum likelihood solutions, as demonstrated by Thom (1966), for each station, for each time scale of interest (1 month, 2 months, etc.), and for each month of the year.

This is an essential step to be verified, mainly for dry climatic regions – which have a great number of zeros values in the historical series of rainfall data – since the parameters of the gamma function are determined using the non-zero values of the series.

The probability of no rain (zero values) is then included in a cumulative probability by:

H(x)=q+(1–q).G(x)

where *q* is the probability of zero and it can be estimated by *m/n*, where *m* is the number of zeros in a range of time and *n* is the number of observations (Thom 1966).

The goodness of fitting of the rainfall series to a gamma distribution was evaluated with the Kolmogorov-Simirnov test. The cumulative probability H(x) values were then transformed to the standard normal random variable Z with mean zero and variance of one, which are the SPI values.

The analyses of length and frequencies were made with the evolution of SPI values during the referring time.

2.3 Trend Test

The non-parametric Mann–Kendall test was adopted to evaluate the presence of statistically significant trend. This test has been adopted by many authors in order to detect climate and hydrology time-series trends (Back 2001; Bonaccorso *et al.* 2005; Cannarozzo *et al.* 2006; Jónsdóttir *et al.* 2005; Modarres and Silva 2007). It can be stated most generally as a test for whether Y values tend to increase or decrease with time, also known as monotonic change (Helsel and Hirsch 2002). With this test it is possible to investigate the trend of long period rainfall data, without the need to make any assumption concerning its distributional properties. Moreover, as a nonparametric method, it is less influenced by the presence of outliers in the data (Lanzante 1996).

The Mann-Kendall test, proposed by Sneyers (1975), considers that, in a hypothesis of stability in a time series, both the sequence of values which occurred independently and the probability distribution, should be permanently the same (simple random series) (Back 2001). The test is able to reject what might appear to be trends over small time periods that may exhibit a short trend (Chabarek *et al.* undated).

Using Mann-Kendall test, the degree of similarity between two sets of ranks, given to a same set of objects, was evaluated. Each set of *N* object was decomposed into (½)*N*(*N*-1) ordered pairs and then compared through a Kendall approach. This number gives a *distance* between sets called the *symmetric difference distance*. The symmetric difference distance between two sets of ordered pairs P_1 and P_2 is denoted $d_\Delta(P_1, P_2)$ (Abdi 2007). Kendall correlation coefficient (τ) was obtained by the normalization of the symmetric difference according to the following equation (Figure 2):

Figure 2

$$\tau = \frac{\frac{1}{2}N(N-1) - d_\Delta(\mathscr{P}_1, \mathscr{P}_2)}{\frac{1}{2}N(N-1)} = 1 - \frac{2 \times [d_\Delta(\mathscr{P}_1, \mathscr{P}_2)]}{N(N-1)}$$

where *N* is the number of items in the set.

The τ value was then transformed into a *Z* value, with mean of 0 and a standard deviation of 1, and a significance test for a normal distribution was also applied. A possible trend was determined if $Z > 1.96$ or $Z < -1.96$. More details about the method can be found in Abdi (2007).

3. Results and discussion

The series had a good correlation with the gamma distribution and it was significant at 0.05 level of Kolmogorov–Simirnov test. This means that we can consider that the precipitation series of Cuiabá follows a known distribution: the complete gamma distribution. The Alfa and Beta parameters, calculated for each month, are reported in Table 2. In winter time – June, July and August – the (α) shape parameters are near to zero (0.5, 0.6 and 0.6, respectively) and the lower scale parameters (ß) confirm the driest occurrences expected for this period. The evolu-

tion of the monthly probability density of rainfall is illustrated in Figure 3. On the opposite, the highest α and ß values of summer period – December, January and February – produced soft curves, assuming that during this time a normal monthly precipitation occurs in the region. The other months are considered as transition time, with visible differences between the shapes of the curves. From March to May, during rainfall, the asymmetry of the curve shape becomes stronger approximating to the winter shape one.

According to the period analyzed for time scales which are shorter than one year, intra-annual variation has been determined. The analysis has been based on the consideration that the SPI value represents the difference, in numbers of standard deviations, from an observed rainfall data to the expected rainfall value (probable precipitation occurrence). The evolution of SPI values for 1, 3, 6 and 12 months are presented in Figure 4.

In larger scales, half-yearly and annual, longer and more frequent events of drought need to be determined within the hydrological concept. The first effects are the decrease of river, lakes and reservoirs water levels. On the opposite, under the agricultural point of view, in-

Table 2. Parameters of the Gamma distribution for each month from 1972 to 2006 in Cuiabá, MT, Brazil – Alfa (α), Beta (ß) – and percentage of months without rain (zero values occurrences)

Month	Alfa (α)	Beta (ß)	Freq. 0 values (%)
January	3.1	82.8	0.0
February	4.2	62.2	0.0
March	5.4	39.7	0.0
April	3.5	42.1	0.0
May	1.2	55.1	2.9
June	0.5	45.1	37.1
July	0.6	14.7	57.1
August	0.6	26.6	42.9
September	1.3	52.3	0.0
October	2.8	42.7	0.0
November	3.2	59.1	0.0
December	7.6	29.5	0.0

Figure 3. Monthly probability density distribution of rainfall for the period of 1972 to 2006, in Cuiabá, MT, Brazil
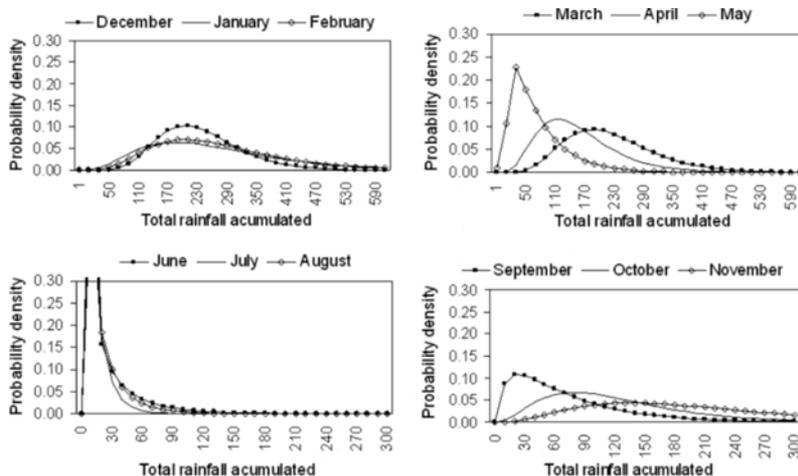
Figure 4. Evolution of SPI values from 1972 to 2006 in Cuiabá, MT, Brazil, calculated for 1, 3, 6 and 12 month time scales
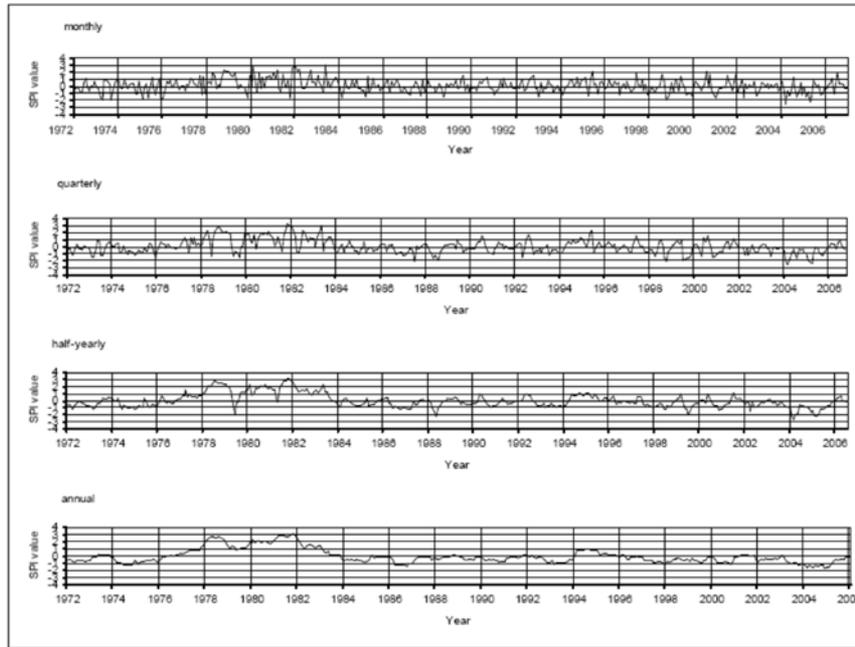
tense droughts are more frequent throughout a same period of record. This occurs mainly on agriculture activities due to the immediate necessity of water supply for the crops. Therefore, in this case, monthly and quarterly time scales are more recommended as drought indicators.

Besides, the beginning of a long-term event is determined by the effect of several short droughts. As shown in Table 3, the number of drought occurrences decreases with the increase of the time scale, while the duration becomes longer.

Table 4 gives deep information from an agricultural perspective. In agriculture, some specific periods are decisive for a crop outcome. For example, soybean cultivation, the most cultivated crop in this region, is very susceptible to water shortages in two periods: i) from sowing to emergency and ii) during grain filling. According to the soybean variety, these phases can respectively occur from October to December and from February to April. It is relevant that the highest number of droughts occur within the first month of the chosen time scale. Twenty one of thirty three events occur during the most vulnerable period for the crop. Although, the 3 month time scale doesn't detect the same risk, seven of the overall twenty one events occur. This fact highlights the importance of a shorter time scale to forecast and prevent an impact of drought.

Regarding to the trend test, any significant possibility of trend was found in none of the series. Samples of the results obtained through R software application are illustrated in the Figure 5. The horizontal line in the middle represents the mean, the limits of significance are represented by the other two horizontal lines of the graphics. An indication of trend is determined when the cross of the two curves occur besides the limit of the lines. This does not occur in all the graphics, therefore the null-hypothesis was not rejected and none conclusion can be made concerning with the presence of a significant trend. Neither a significant trend was found with the SPSS software.

In order to achieve more details, Mann-Kendall sequential values were overlapped to SPI values, considering one month time scale (Figures 6-11). The figure shows that a good correlation

Table 3. Number of drought events and its average durations, in months, for the period 1972 to 2006 in Cuiabá, MT, Brazil, for time scales of 1, 3, 6 and 12 months

	Time scale			
	1 month	3 months	6 months	12 months
n° drought occurrences	33	21	10	5
Average duration (months)	3.4	7.4	14.8	37.8

Table 4. Number of drought occurrences for the period 1972 to 2006 in Cuiabá, MT, Brazil, for the time scales of 1 and 3 months, in the period from October to December and from February to April

	Time scale			
	1 month		3 months	
	October–December	February–April	October–December	February–April
n° drought occurrences	12	9	3	4

Figure 5. Sequential Mann–Kendall test calculated for series from 1972 to 2006 in Cuiabá, MT, Brazil, for January, February, December and the summer
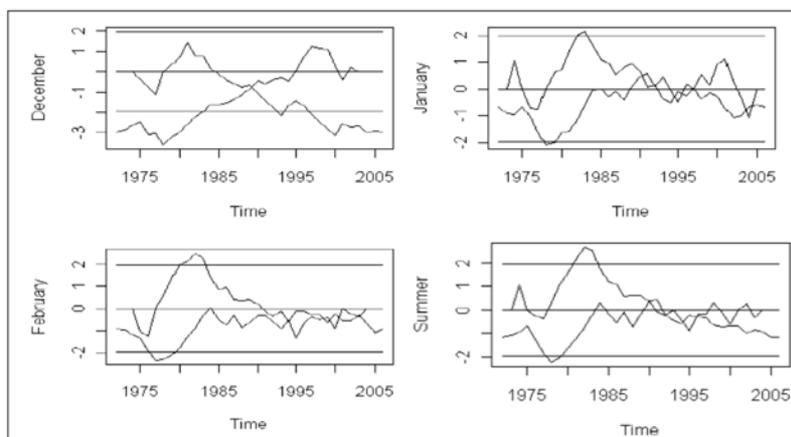

was found between SPI values and Mann–Kendall sequence, therefore a similar interpretation of the rainfall series can be given. The figure gives also information on the Mann–Kendall's curve shape which follows the oscillations of the SPI columns, These SPI oscillations occur when the soybean is more vulnerable to water shortages – from October to December and from February to April, between the 1972 and 2006 years. The u(t) and u★(t) values correspond to the *Z* values of the above mentioned Mann–Kendall test which was calculated before, respectively, from 1972 to 2006 and from 2006 to 1972 (ordered pairs of the set made from 1972 to 2006 and from 2006 to 1972, as shown in methodology).

Apart from December, the u(t) curves do never pass the inferior limit of –1.96 and, therefore, do not ever intercept the u★(t) curve on a region bellow this limit (–1.96). This means that any trend is observed (see Figures 6-11).

In December, from 1996 to 2005, the falling of u(t) curve coincides with the successive drought occurrences, reaching values bellow –1.96 with just one interruption in 2001 due to an extreme rainfall event. In the same period, the u★(t) curve (red from the left to right, from

Figure 6-11. Sequential Mann–Kendall test calculated for series from 1972 to 2006 in Cuiabá, MT, Brazil for the periods of December to October and February to April, overlapped by the SPI values for the same period
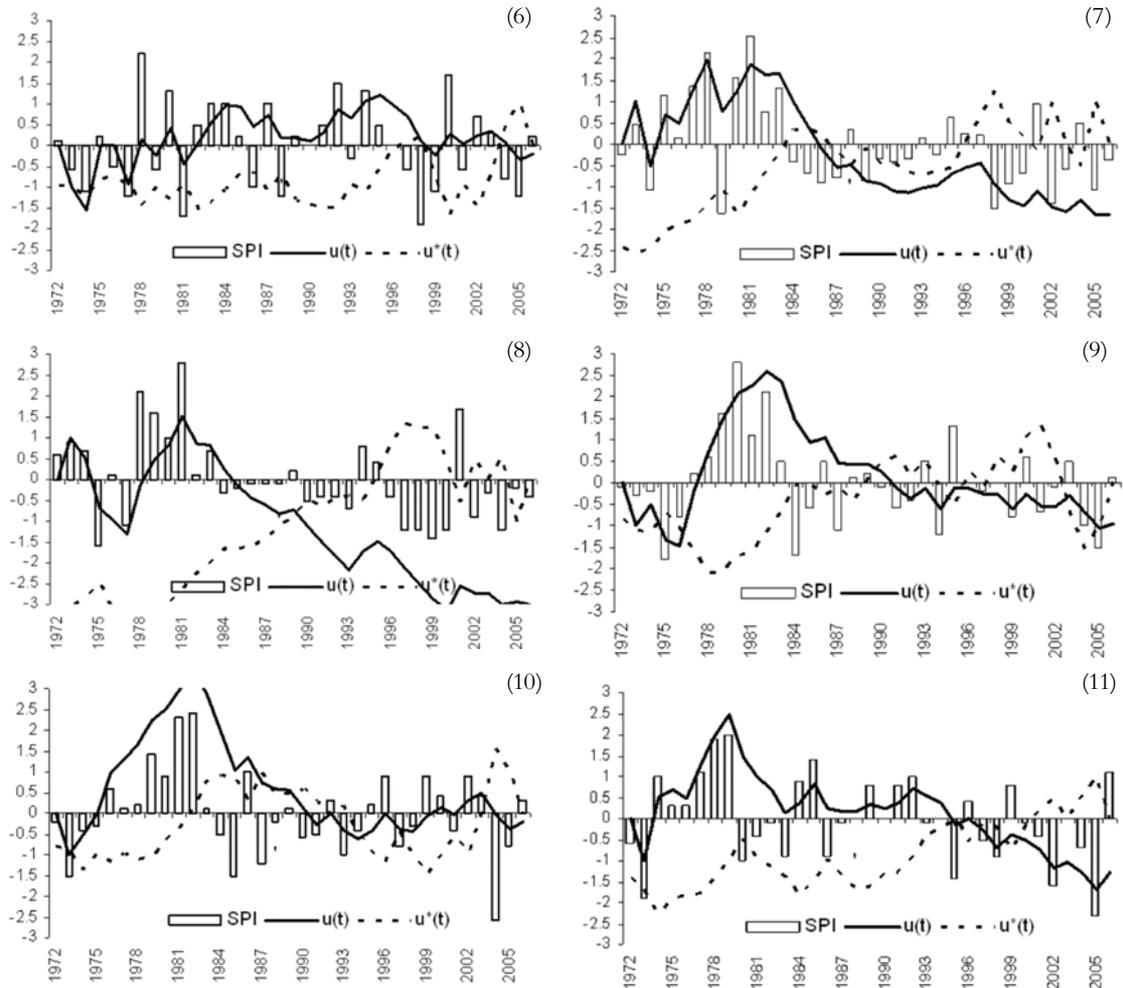
2006 to 1972), which should begin to fall from 2002, has an increment due to the precipitation event occurred in 2001 and crosses the u(t) line when it is still inside the limits of a no-trend; therefore any indication of tendency can be given.

In order to identify a trend, a longer series of precipitation data is necessary. These results agree with what found out also by other authors, who state in some regions that 30 years are not enough to characterize a water regime (Blain *et. al.* 2008).

4. Conclusion

Frequent droughts occurred on short periods (less than 1 month) in the region of Cuiabá, during the most vulnerable period of soybean growing.

The SPI index, right adjusted to the Cuiabá precipitation series, is useful to predict drought occurrences mainly for long time scales (3 months, 6 months and 1 year). For the agriculture, shorter time scales would be also necessary according to the vulnerability of the studied cultivation.

No trend was found in the Cuiaba monthly, seasonally and annually computed rainfall series. Longer time series of precipitation data are recommended in order to investigate a trend existence.

Acknowledgments

References

Abdi H. (2007). The Kendall rank correlation coefficient. In: Salkind N. (ed.). *Encyclopedia of measurement and statistics*. California: Sage Publications, Inc.

Agência Estadual de Notícias – AEN (2006). Seca já causou perda de 17,4% da safra de verão. Disponible in: <http://www.aenoticias.pr.gov.br/modules/news/article.php?storyid=17938>. Access on: 30 jun. 2008.

Aguiar R. (2005). Estiagem: como conviver com esse fenômeno? *Revista Extensão Rural e Desenvolvimento Sustentável*. 1, 4, nov/dez.

ANA (2000). *Precipitações diárias (1971-2006)*. Brasília.

Back A.J. (2001). Aplicação de análise estatística para identificação de tendências climáticas. *Pesq. Agropec. Bras.*, 36, 5: 717-726.

Blain G.C., Kayano M.T., Sentelhas P.C., Lulu J. (2008). Variabilidade amostral das séries mensais de precipitação pluvial na região de Campinas, São Paulo, Brasil (1890 a 2006). In: XV Congresso Brasileiro de Meteorologia. São Paulo. Aug. 2008. Anais, São Paulo.

Bonaccorso B., Cancelliere A., Rossi G. (2005). Detecting trends of extreme rainfall series in Sicily. *Advances in Geosciences*, 2: 7-11.

Byun H. and Wilhite D.A. (1999). Objective quantification of drought severity and duration. *Journal of Climate*, 12, 9: 2747-2756.

Cannarozzo M., Noto L.V., Viola F. (2006). Spatial distribution of rainfall trends in Sicily (1921–2000), *J. Phys. Chem. Earth*, doi:10.1016/j.pce.2006.03.022.

Chabarek J., Gesch D., Wirtala M. (undated). Lexical Trend Detection. Disponible in: <http://pages.cs.wisc.edu/~jerryzhu/cs540/project/report/trendy/MannKendall.htm>. Access on: 30 jun 2008.

Guttman N.B. (1998). Comparing the Palmer Index and the 'Standardized Precipitation Index". *Journal of the American Water Resources*, 16, 2: 113–121.

Guttman N.B. (1999). Accepting the standardized precipitation index: a calculation algorithm. *J. Am. Water Resour. Assoc.*, 35: 311–322.

Helsel D.R., Hirsch R.M. (2002). *Statistical Methods in Water Resources Techniques of Water Resources Investigations*, Book 4, chapter A3. U.S. Geological Survey.

Jónsdóttir J.F., Jónsson P., Uvo C.B. (2005). Trend analysis of Icelandic discharge, precipitation and temperature series. In: 15th International Northern Research Basins Symposium and Workshop Luleå to Kvikkjokk. Sweden. Aug/Sept.

Lanzante J.R. (1996). Resistant, robust and non–parametric techniques for the analysis of climate data: theory and examples including applications to historical radiosonde station data. *International Journal of Climatology*, 16: 1197.1226.

Mavi H.S. and Tupper G.J. (2004). *Agrometeorology: principles and applications of climate studies in agriculture*. Nova York: Food Products Press.

Mckee T.B., Doesken N.J., Kleist J. (1993). The relationship of drought frequency and duration to the time scales. 8th Conference on Applied Climatology, pp.179-184.

Mckee T.B., Doesken N.J., Kleist J. (1995). Drought monitoring with multiple times scales. Proceedings of the 9th Conference on Applied Climatology, Boston MA, U.S.A., 233-236 pp.

Modarres R., da Silva V. de P.R. (2007). Rainfall trends in arid and semi-arid regions of Iran. *Journal of Arid Environments*, 70: 344-355.

NDMC Home page (2006). Understanding and defining drought. Available in: <http://www.drought.unl.edu/whatis/concept.htm>. Access in Oct. 2007.

Palmer W.C. (1965). Meteorological drought. US Weather Bureau Res. n. 45. Washington, 1965.

Silva V.P.R. (2004). On climate variability in Northeast of Brazil. *Journal of Arid Environments*, 58: 575–596.

Sivakumar M.V.K., Motha R.P., Das, H.P. (2005). *Natural disasters and extreme events in agriculture*. The Netherlands*:* Springer. Cap. 1- 2.

Sneyers R. (1975). Sur l'analyse statistique des sites d'obsewations, *WMO Technical Note No. 143, World Meteorological Organization*.

Thom H.C.S. (1966). *Same methods of climatological analyses.* Geneva World Meteorological Organization, 1966 (WMO, 199; TP, 103; Technical note, 81.)

United Nations Development Program – Unso (1999).